Global and Time-dependent Modeling of Planetary Ions in Mercury's Magnetosphere

Anita Linnéa Elisabeth Werner

To cite this version:

Anita Linnéa Elisabeth Werner. Global and Time-dependent Modeling of Planetary Ions in Mercury's Magnetosphere. Planetology. Sorbonne Université, 2021. English. NNT : 2021SORUS527 . tel-03783493

HAL Id: tel-03783493

https://theses.hal.science/tel-03783493

Submitted on 22 Sep 2022

Sorbonne Université

Ecole Doctorale Astronomie et Astrophysique d'Ile de France

Laboratoire atmosphères, milieux, observations spatiales (LATMOS)

Global and Time-dependent Modeling of Planetary Ions in Mercury's Magnetosphere

Par Anita Linnéa Elisabeth WERNER

Thèse de doctorat de Physique Planétaire

Dirigée par François LEBLANC et Jean-Yves CHAUFRAY

Présentée et soutenue publiquement le 22 novembre 2021

Devant un jury composé de :
SAVOINI, Philippe, Professeur à la Sorbonne Université, Président du jury
DANDOURAS, Iannis, Directeur de Recherche au CNRS, Rapporteur
KRETZSCHMAR, Matthieu, Maître de Conférence à l'Université d'Orléans, Rapporteur
CASSIDY, Timothy, Chercheur au Laboratory for Atmospheric and Space Physics, Examinateur
FONTAINE, Dominique, Directrice de Recherche au CNRS, Examinateur
SÁNCHEZ-CANO, Beatriz, Chercheuse à l'University of Leicester, Examinateur
LEBLANC, François, Directeur de Recherche au CNRS, Directeur de thèse
CHAUFRAY, Jean-Yves, Chargé de Recherche au CNRS, Co-encadrant

Sol, Härre Konung, mäktig och grann,
vårhimlens lysande riddersman,
jordarnas fader och stjärnornas bror,
rund och varm och glad och god och stark och stor!

...

Närmast Merkurius, minstingen vek,
flyger kring gamlingen yr i lek

Karl-Erik Forsslund

✶

Till min fantastiska familj

ABSTRACT

The Hermean environment contains heavy ions which have their origin in Mercury's collision-less atmosphere (exosphere). The spatial distribution of the most abundant ion species has been characterized by the Fast Imaging Plasma Spectrometer (FIPS) on the MESSENGER spacecraft, which orbited Mercury between March 2011 - April 2015. Previous models of the planetary ion density distribution in Mercury's magnetosphere produce Na^+ densities which differ by 1-3 orders of magnitude from the FIPS observations. Only the Na^+ distribution has been modelled in the past.

This thesis describes the algorithm and application of a new ion density model, the Latmos IoniZed Exosphere model (LIZE). LIZE is coupled to a model of the exosphere (the Exospheric Global Model; EGM) and a hybrid magnetosphere model (Latmos Hybrid Simulation; LatHyS). I first use the LIZE model to reproduce the Na^+-group, O^+-group and He^+ ion density distribution observed by FIPS between 23 March 2011 to 30 April 2015. We account for the FIPS field-of-view and energy range, and also simulate the 3-D ion phase space density distribution. I then use the time-dependent LIZE model to study the response of planetary ion species to a strong solar flare event. We demonstrate that the response of the planetary ion population in Mercury's magnetosphere to the flare is non-linear with respect to species, energy, location inside the magnetosphere and the location of the flare source region with respect to Mercury.

The LIZE model offers several new capabilities for the analysis of FIPS data and will provide needed context to the ion measurements which will be made during the BepiColombo mission, which will be made from two different positions in space and by instruments with different spatial, temporal and energy coverage.

RÉSUMÉ

Mercure est la plus petite et plus interne planète de notre système solaire. La planète a une atmosphère non-collisionnelle (une exosphère limitée par une surface) qui est composée d'atomes d'hydrogène, d'hélium, de sodium, de potassium, magnésium, calcium, manganese, fer et aluminium (Bida et al., 2000 ; Bida et Killen, 2017 ; Broadfoot et al., 1974 ; McClintock et al., 2008 ; Potter et Morgan, 1985, 1986 ; Vervack et al., 2016).

La planète a aussi un cœur très large et partiellement fondu composé principalement de fer qui induit un champ magnétique intrinsèque (Anderson et al., 2011). L'intensité du champ magnétique intrinsèque de Mercure est seulement 1% de celle du champ terrestre. Malgré cela, le champ magnétique est suffisamment intense pour protéger la planète du vent solaire en le déviant autour de la planète. Comme la Terre, ce mécanisme créé une poche de plasma autour de Mercure appelée magnétosphère. La faiblesse du champ magnétique de Mercure, l'absence d'une ionosphère conductrice et l'intensité du vent solaire et du champ magnétique interplanétaire à l'orbite de Mercure créé un couplage très fort entre la surface, l'exosphère et la magnétosphère.

Mercure a été visité par deux missions spatiales : Mariner 10 qui a fait 3 passages (1974-1975) près de Mercure et « MErcury Surface, Space ENvironment, GEochemistry, and Ranging (MESSENGER) » qui a orbité autour de Mercure entre 2011 et 2015. La mission BepiColombo, avec ses deux satellites, en route vers Mercure fera son premier passage au plus près de la planète en octobre 2021 pour une mise en orbite en 2025.

MESSENGER avait à son bord deux instruments dédiés à la mesure des particules chargées. Le « Fast Imaging Spectrometer (FIPS; Andrews et al., 2007) était un spectromètre de masse à temps de vol qui a mesuré les ions du vent solaire et planétaires dans une gamme de rapport masse charge entre 1 et 60 uma/e et une gamme en énergie entre 50 eV/e et 20 keV/e (Raines et al., 2013). Cet instrument a quasiment un champ de vue hémisphérique de 1.4π, principalement limité par le bouclier thermique de MESSENGER (Gershman et al., 2013).

MESSENGER/FIPS a permis d'obtenir d'importantes informations sur l'abondance et la distribution spatiale des trois espèces ioniques ou groupes d'ions planétaire les plus abondantes dans la magnétosphère de Mercure. Le groupe des Na^+ ($m/q = 21-30$) qui comprend les ions Na^+, Mg^+ et Si^+ a été observé comme étant le groupe le plus abondant dans la magnétosphère de Mercure, suivi du groupe O^+

(m/q=16 – 20) qui inclut O^+ et les ions moléculaires et atomiques associés à la molécule d'eau et enfin l'ion He^+. Ces espèces sont peu abondantes dans le vent solaire et sont donc très probablement originaires de la photo-ionisation de l'exosphère neutre. Les observations orbitales de l'instrument FIPS entre le 25 mars 2011 et le 31 décembre 2011 ont mis en évidence que les groupes ions Na^+ et O^+ sont distribués spatialement de manière non-uniformes. Dans la gaine de plasma de la magnétosphère, la distribution spatiale est caractérisée par deux pics de densité localisés le matin (6-12h en heure locale) et le soir (18-22h). L'échelle de hauteur de la densité de ces ions est différente entre ces deux pics. Le pic du matin est limité à des basses altitudes tandis que le pic du soir a une distribution plus étendue en altitude jusqu'à 1500 – 6000 km. Le pic de densité dans le secteur du soir peut s'expliquer par des mécanismes d'accélération centrifuge sur des grandes échelles spatiales originellement proposés par Delcourt et al. (2002, 2003) et Delcourt (2013). He^+ est caractérisée par une distribution plus uniforme par rapport aux autres espèces ioniques, suggérant une source sans doute différente des autres espèces ioniques. Les densités de ces 3 espèces dans la région subsolaire étaient relativement faibles, possiblement indiquant une population ionique de faible énergie potentiellement non observée par FIPS.

Il existe un certain nombre de modèles de type test-particules qui ont été utilisés pour étudier la distribution spatiale des ions planétaires dans la magnétosphère de Mercure (Delcourt, 2013 ; Delcourt et al., 2002, 2003 ; Paral et al., 2010 ; Sarantos et Slavin, 2009 ; Seki et al., 2013 ; Yagi et al., 2010, 2017). Ces modèles sont typiquement couplés à un modèle d'exosphère neutre (Gamborino et al., 2019 ; Leblanc et Johnson, 2003 ; Mura et al., 2007) et utilisent pour décrire le champ électrique stationnaire et le champ magnétique dans la magnétosphère de Mercure soit une description analytique (Delcourt et al., 2003), soit déduit d'un modèle magnétohydrodynamique (Sarantos et Slavin, 2009 ; Seki et al., 2013 ; Yagi et al., 2010, 2017) ou d'un modèle magnétosphérique hybride (Paral et al., 2010). Les études précédentes se sont essentiellement focalisées sur les caractéristiques des ions Na^+ comparées aux observation par FIPS lors des deux premiers passages de la sonde MESSENGER à Mercure.

Mais, exosphère et magnétosphère sont en fait extrêmement variables temporellement. On peut donc raisonnablement se demander comment cette variabilité impacte les distributions spatiales des ions planétaires dans la magnétosphère de Mercure. Par exemple, FIPS/-MESSENGER a observé un cas très intéressant de variation des ions He^{2+}, d'origine solaire et He^+ d'origine planétaire lors du passage d'une éjection de masse coronale solaire à Mercure (Raines et al., 2018). Cet événement a aussi mis en évidence le couplage entre le vent solaire, la surface de Mercure, son exosphère et son ionosphère.

Un modèle décrivant la densité des ions planétaires dans la magnétosphère de Mercure basé sur une description réaliste de l'exosphère neutre est nécessaire pour pouvoir interpréter ce type d'événement. Ce modèle doit aussi être couplé à un modèle de la magnétosphère de Mercure décrivant à la fois les frontières magnétosphériques comme le choc et la magnétopause et les champs électriques et magnétiques autour de Mercure pour n'importe quelle configuration du vent solaire. Enfin, ce modèle doit être capable de décrire des variations temporelles pour prendre en compte la variabilité du vent solaire et/ou du flux radiatif solaire et leur impact sur l'exosphère de Mercure. De pouvoir reconstruire la distribution des vitesses de ces ions dans quelques régions clefs de la magnétosphère est aussi essentiel pour comprendre les mécanismes d'accélération des ions et être capable de comprendre l'impact du champ de vue forcément limité et de la couverture en énergie des instruments plasma qui ont observé et vont observer la distribution de ces ions autour de Mercure.

Au cours de ma thèse de doctorat, j'ai développé un tel modèle que j'ai appelé Latmos Ionized Exosphere model (LIZE) couplé au modèle Exospheric Global Model (EGM; Leblanc et al., 2017 ; Leblanc et Johnson, 2010) et LATMOS Hybrid Simulations (LatHyS; Modolo et al., 2018 ; Modolo et al., 2016). LIZE a tout d'abord été appliqué pour décrire la densité des ions He^+, O^+ et Na^+ dans la magnétosphère de Mercure. Les principaux résultats obtenus par ce modèle ont été comparés en détails aux observations de l'instrument MESSENGER/FIPS pendant la phase orbitale de la mission. J'ai aussi étudié la fonction de distribution des vitesses dans 4 régions particulières de la magnétosphère de Mercure. Ces résultats ont été établis pour différentes conditions de vent solaire et du champ magnétique interplanétaire.

Grâce à ces travaux, j'ai montré tout d'abord que le modèle LIZE couplé aux modèles EGM et LatHyS parvenaient à reconstruite correctement la distribution spatiale des ions Na^+, O^+ et He^+ telle qu'observée par MESSENGER/FIPS (Werner et al., 2021a). Deux modèles magnétosphériques ont été utilisés pour confirmer ces calculs : AIKEF (Müller et al., 2012) et LatHyS (Modolo et al., 2018 ; Modolo et al., 2016). Mais les densités modélisées sont globalement entre 2 à 20 fois plus grandes que celles observées (Werner et al., 2021a). Les simulations précédentes de la densité des ions Na^+ donnent d'ailleurs les mêmes ordres de grandeur que LIZE (Delcourt, 2013 ; Delcourt et al., 2002, 2003 ; Paral et al., 2010 ; Sarantos et Slavin, 2009 ; Seki et al., 2013 ; Yagi et al., 2010, 2017). En fait, une autre approche a été aussi utilisée pour estimer la densité des ions Na^+ à partir des mesures du magnétomètre MAG de MESSENGER en analysant le champ magnétique et l'impact de ces ions sur celles-ci (James et al., 2019). Limité aux régions de champ magnétique fermé, cette approche a permis d'estimer une densité des ions beaucoup plus proche de celle modélisée que la densité suggérée par les mesures MESSEN-

GER/FIPS (Werner et al., 2021a). En fait, mon étude a surtout considéré des conditions de vent solaire nominales à l'aphélie et un champ magnétique orienté vers le Nord dans un repère MSO. J'ai donc aussi montré que ces conditions particulières tendent à surestimer la densité des ions par rapport à des conditions de vent solaire plus proches de celles rencontrées le long de l'orbite de Mercure.

J'ai aussi utilisé LIZE pour modéliser la fonction de distribution des vitesses des différentes espèces ioniques dans 4 régions : à basses altitudes à midi heure locale, dans la queue magnétosphèrique côté soir, près de la surface côté matin et dans la magnétogaine côté matin. La distribution est relativement similaire dans ces 4 régions. Mise à part dans la queue magnétosphérique où la distribution est quasi isotropique, dans les autres régions, la distribution est très concentrée dans des domaines de vitesse restreints proches de l'axe Vx dans le plan Vx-Vz (avec Vx>0 vers le Soleil et Vz>0 vers le Nord). Cette région particulière est en partie bloquée par le champ de vue de FIPS à cause du bouclier thermique de MESSENGER, ce qui implique qu'une partie de la fonction de distribution n'est pas mesurée par FIPS dans ces régions. Cette étude a démontré la capacité de LIZE de reproduire les observations de MESSENGER/FIPS. Il est donc possible d'explorer les régions de l'espace des phases non accessibles par FIPS et de prédire ce qui sera observable par les instruments de BepiColombo.

Dans une seconde étude (Werner et al., 2021b), j'ai utilisé la version dépendante du temps du modèle LIZE pour étudier la réponse de plusieurs espèces ioniques à un événement solaire de type flare, plus précisément à un événement de classe X9.3 qui a eu lieu le 6 septembre 2017. Cet événement a été le plus intense flare solaire du cycle solaire précédent. Ses effets sur l'atmosphère et ionosphère de la Terre et de Mars ont été observés. Pour cette étude, j'ai utilisé un modèle simulé du spectre solaire de ce flare avec le modèle « Flare Irradiance Spectral Model » pour calculer la variation temporelle du taux de photo-ionisation de Mg, Na, O and He à Mercure. Cet événement solaire radiatif a probablement eu peu d'effet sur la photo-ionisation de Na, mais pour O, He and Mg le taux de photo-ionisation a pu augmenter entre 40 à 80%. A partir de cette variation temporelle du taux de photo-ionisation, j'ai mis à jour le taux de production des ions ainsi produits toutes les 60 s pendant les premières 30 minutes du flare dans LIZE. J'ai ensuite étudié comment la densité des ions pour ces espèces a pu changer au cours du temps dans 4 régions particulières de la magnétosphère. Avant le début de l'événement solaire, la distribution des ions vers midi à basses altitudes est composée de deux populations avec différentes énergies. La partie basse énergie est probablement produite localement tandis que la composante plus énergétique fait partie d'une distribution ionique dont la circulation autour de la planète forme un anneau partiel ou non près de la surface. L'importance de cette population énergétique par rapport à la composante basse énergie est notamment plus grande pour des espèces ioniques de masse plus faible comme He^+. Côté nuit, les distributions énergétiques ne contiennent que des ions dont l'énergie est autour du keV.

Côté jour, la population ionique de basse énergie atteint un maximum juste 2 minutes après le moment où le taux de photo-ionisation est maximum. La population de haute énergie est maximum dans cette même région 14 à 15 minutes plus tard. Parce que la population des He^+ a une composante de haute énergie plus importante, la densité de ces ions décroît plus lentement qu'attendu pendant les premières 10 minutes après l'événement solaire. Le flux des ions impactant la surface suit la même évolution temporelle que la densité des ions. Quand la densité des ions atteint son maximum dans une des 4 régions magnétosphériques, le flux est maximum juste 2 minutes plus tard.

Un événement solaire de type flare est généralement composé de deux phases, une phase dite impulsive et une phase plus graduelle, toutes deux correspondant à des émissions dans des gammes spectrales différentes. A cause de la différence d'épaisseur optique de l'atmosphère solaire entre la gamme X et la gamme EUV, l'intensité de la phase graduelle (essentiellement dans l'EUV) dépend de la position de l'événement solaire sur le disque solaire vue par Mercure. Pour un événement solaire ayant lieu près du centre du disque visible depuis Mercure, le maximum du taux de photoionisation pour Mg est atteint avant celui pour He and O, dont le taux de photoionisation pendant la phase graduelle du flare est toutefois plus important. Par contre, si la source du flare est positionnée plus proche du bord du disque solaire, la composante EUV de cet événement est alors plus atténuée si bien que le maximum de taux de photoionisation est atteint en même temps pour ces trois espèces ioniques.

Suite à cette thèse, j'aimerais étudier les observations décrites par RAINES et al. (2018) grâce à LIZE. Une telle analyse nécessitera d'étudier la variabilité temporelle de l'exosphère de He tout comme la distribution de He^+ dans la magnétosphère. En fait, la capacité de décrire des variations temporelles dans le modèle EGM a déjà été implémentée et étendue au cours de cette thèse (intégration de la possibilité de prendre en compte un flux solaire radiatif variable dans EGM). La variation saisonnière de la densité des ions Na^+ a été brièvement discutée par RAINES et al. (2013) et étudiée par JASINSKI et al. (2021). La géométrie de l'orbite de MESSENGER implique qu'il n'y a quasiment pas de recouvrement en latitude, temps local et altitude entre des observations de MESSENGER/FIPS à différentes anomalies vraies. Des observations avec MESSENGER/UVS de l'exosphère de Na proche de l'aphélie manquent également à cause des limites du champ de vue de cet instrument. Pour ces raisons, il n'est pas si simple d'étudier les variabilités saisonnières des densités exosphériques de Na^+ à partir de ces observations seulement. Là aussi, LIZE pourrait être extrêmement utile pour combler les absences de données.

Le modèle LIZE et les résultats obtenus au cours de ma thèse m'ont permis de mettre en évidence une nouvelle approche originale pour l'analyse des données MESSENGER/FIPS qui aidera à l'analyse des observations à venir des instruments à bord de la mission BepiColombo. La mission BepiColombo avec à son bord les deux plateformes MPO et MIO emporte un très grand nombre de spectromètres de masse ionique qui couvriront une gamme en énergie bien plus grande. D'autre part, la configuration multi-satellites permettra de séparer les effets spatiaux et temporels. Enfin, l'orbite de ces deux plateformes permettra une couverture spatiale bien meilleure que la mission MESSENGER, notamment d'étudier des gammes d'altitudes au nord et au sud jamais explorées jusqu'à maintenant. Des modèles comme LIZE seront donc essentielles pour exploiter au mieux des jeux de données associant plusieurs points de mesure et des instruments plasma ayant des couvertures spatiales, temporelles et en énergie différentes.

SUMMARY

Mercury is the smallest and innermost planet in our solar system. The planet possesses a collision-less atmosphere (i.e. a surface-bounded exosphere) which consists of hydrogen, helium, sodium, potassium, magnesium, calcium, manganese, iron and aluminium (Bida et al., 2000; Bida and Killen, 2017; Broadfoot et al., 1974; McClintock et al., 2008; Potter and Morgan, 1985, 1986; Vervack et al., 2016).

The planet also has a large, partially-molten iron core which generates an intrinsic magnetic field (Anderson et al., 2011). The strength of Mercury's intrinsic magnetic field is only 1 percent of the Earth's. Despite this, the magnetic field is strong enough to shield the planet from the solar wind and divert it around the planet. Similar to Earth, this creates a pocket of plasma around the planet called a magnetosphere. Mercury's weak magnetic field, lack of a conductive ionosphere and the intense solar wind and interplanetary magnetic field at Mercury creates a strong coupling between the surface, exosphere and the magnetosphere.

Mercury has been visited by two spacecrafts: Mariner 10 which made three Mercury flybys (1974-1975) and MErcury Surface, Space ENvironment, GEochemistry, and Ranging (MESSENGER) which orbited the planet between 2011-2015. The upcoming two-spacecraft mission BepiColombo will make its first flyby past Mercury in October 2021 and enter into orbit around the planet in 2025.

MESSENGER carried two charged particle analyzer. The Fast Imaging Spectrometer (FIPS; Andrews et al., 2007) was a time-of-flight mass spectrometer which detected solar wind and planetary ions within a mass-per-charge range of 1-60 amu/e and an energy between 50 eV/e to 20 keV/e (Raines et al., 2013). The instrument had a nearly hemispheric field-of-view of 1.4π sr, mainly limited by the sunshade on the MESSENGER spacecraft (Gershman et al., 2013).

MESSENGER/FIPS have revealed important information into the abundance and distribution of the three most abundant planetary ions or ion groups in the magnetosphere. The Na^+-group ($m/q = 21-30$), which includes Na^+, Mg^+ and Si^+, was found to be the most abundant ion group in Mercury's magnetosphere followed by the O^+-group ($m/q = 16-20$), which includes O^+ and water group ions, and the third most abundant species was He^+. These species are unlikely to be found in great quantities in the solar wind and are likely to have been derived from photo-ionization of Mercury's exosphere. FIPS orbital observations between 25 March 2011 and 31 December 2011 revealed that the Na^+-group and O^+-group ions are not uniformly distributed in the magnetosphere. The spatial distribution in

the plasma sheet revealed two density enhancements located in the morning (6-12 h local time) and the evening sector (18-22 h). The scale height is different between the two enhancements. The morning enhancement is limited to low altitudes while the evening enhancement shows higher densities far away from the planet ($\sim 1500 - 6000$ km). The evening enhancement may be explained by large-scale heavy ion transport by the centrifugal ion acceleration mechanism first described by Delcourt et al. (2002, 2003) and Delcourt (2013). He^+ revealed a relatively smooth distribution compared to the other ion species, and it has been suggested that the He^+ ions may be derived from a different source. The ion densities of all observed ion species were low near the subsolar point, possibly indicating the presence of a large population of low-energy ions.

There exists a number of test-particle models which have been used to study the spatial distribution of planetary ions in Mercury's magnetosphere (Delcourt, 2013; Delcourt et al., 2002, 2003; Leblanc and Johnson, 2003; Paral et al., 2010; Sarantos and Slavin, 2009; Seki et al., 2013; Yagi et al., 2010, 2017). The models are typically coupled to a neutral model of the exosphere (Gamborino et al., 2019; Leblanc and Johnson, 2003; Mura et al., 2007) and uses a steady-state electric and magnetic field description from analytical (Delcourt et al., 2003), magnetohydrodynamic (Sarantos and Slavin, 2009; Seki et al., 2013; Yagi et al., 2010, 2017) and hybrid (Paral et al., 2010) models of Mercury's magnetosphere. These studies has focused on characterizing the ion density distribution of Na^+ and comparison has been made with FIPS observations of the Na^+-group taken during the first two Mercury flybys.

But both the exosphere and the magnetosphere are highly variable with respect to time. One might ask how this time-variability affects the distribution of planetary ions inside the magnetosphere. An interesting real case is the apparent time-variability of solar wind He^{2+}, planetary He^+ and neutral He in response to the passage of a coronal mass ejection as observed by MESSENGER (Raines et al., 2018). This also highlights the coupling between the solar wind, Mercury's surface, exosphere and planetary ion environment.

An ion density model which describes the global distribution of key planetary ions based on a realistic description of the neutral exosphere is necessary to provide context to such spacecraft observations. A magnetosphere model which successfully recreates the observed positions of the bow shock and magnetopause as well as the magnetic and electric fields in Mercury's magnetosphere is also required. Finally, the model would need to be time-dependent to account for the changing conditions in the solar wind and in the solar radiation flux, and their impact on the exosphere. It would also be useful to be able to model the phase space density distribution in some key magnetospheric regions, in order to understand the key pathways of plasma transport in the system and what an instrument with limited energy range and field of view might observe.

In this PhD, I have developed such a model named the Latmos IoniZed Exosphere model (LIZE). This model was coupled with Exospheric Global Model (EGM; Leblanc et al., 2017; Leblanc and Johnson, 2010) and Latmos Hybrid Simulation (LatHyS; Modolo et al., 2018; Modolo et al., 2016).

I first apply the LIZE model to describe the ion density distribution of He^+, O^+ and Na^+ in Mercury's magnetosphere. The results from the LIZE model are compared with the average ion density distribution observed by MESSENGER/FIPS observations during the orbital mission. I then study the 3-D phase space density distribution in four different region located inside the magnetosphere. I also study how the average ion density computed with LIZE compares for different sets of solar wind and interplanetary magnetic field (IMF) conditions.

I demonstrate that the spatial distribution of the Na^+-, O^+-group ions and He^+ as seen in the FIPS observations are reproduced by the LIZE model (Werner et al., 2021a). Two different magnetospheric models were used to confirm our calculations: AIKEF (Müller et al., 2012) and LatHyS (Modolo et al., 2018; Modolo et al., 2016).

But the absolute magnitude of the modeled ion density is overestimated by a factor of 2-20 compared to the observations. Previous simulations of the Na^+ density in Mercury's magnetosphere give similar estimates (Delcourt, 2013; Delcourt et al., 2002, 2003; Paral et al., 2010; Sarantos and Slavin, 2009; Seki et al., 2013; Yagi et al., 2010, 2017). Another estimate of the Na^+ ion density distribution in the magnetosphere has also been inferred from MESSENGER/MAG observations of magnetic field line resonance events (James et al., 2019). This type of estimate is limited to closed field-line regions in the magnetosphere, but gives an average ion density which is much closer to the LIZE estimate (Werner et al., 2021a). Actually, my study mainly considers nominal solar wind conditions at aphelion and strictly northward IMF conditions. I also show that such particular conditions tend also to overestimate the ion density with respect to the average solar wind conditions along Mercury's orbit.

I also use the LIZE model to study the phase space density distribution of the different ion species in four different regions: at low altitudes at noon, in the dusk magnetotail, near the surface at dawn and in the dawn magnetosheath flank. The phase space density shows a similar distribution in all four regions for the three different species. Apart from the far magnetotail, which has a relatively isotropic phase space density distribution, in all the studied regions the phase space density is highly concentrated to a narrow region near the v_x-axis in the $v_x - v_z$ plane (where $v_x > 0$ toward the Sun and $v_z > 0$ to north). This particular region is blocked from FIPS field-of-view due to MESSENGER's sunshade, meaning that only a fraction of the total ion density distribution is likely observed by FIPS inside these regions. This study has demonstrated the capability of LIZE to reproduce the MESSENGER/FIPS ion density observations with good results. This opens up the possibility to study parts of the energy distribution and field-of-view not accessible to FIPS, but which will be viewed by the ion instruments on the BepiColombo spacecraft.

In the second study (Werner et al., 2021b), I use the time-dependent version of LIZE to study the response of several planetary ion species to real solar flare event, the X9.3-class solar flare on 6 September 2017. This was the strongest solar flare of the previous solar activity cycle and its effects on the atmosphere and ionosphere was measured on both Earth and the planet Mars. I use a simulated solar irradiance spectra from the event in question computed with the Flare Irradiance Spectral Model to compute the time-dependent photo-ionization rate for several exospheric species, with special focus on Mg, Na, O and He. The studied solar flare event has very little effect on the photo-ionization rate of Na. For O, He and Mg the photo-ionization rate is raised by up to $40 - 80\%$. This information is used to update the 3-D ion production rate every 60 s during for first 30 minutes of the flare. I then study how the ion density distribution for the different species changes with time in three different regions inside the magnetosphere. Before the starting of the flare event, the ion density distribution two regions, both located on the dayside at noon and dawn, contains two ion populations with different energies. The low-energy ion population is likely produced locally, while the high-energy ions appear to belong to an ion ring distribution located near the surface in the equatorial plane. The relative intensity of the high-energy population is higher for low-mass ions such as He+. The nightside plasma sheet contains a single ion population at keV energies for all species.

On the dayside, the low-energy ion population reach its maximum intensity just 2 minutes after the time when the photo-ionization rate is at its highest. The high-energy ion population in the same region reaches its maximum intensity 14-15 minutes later. Because He^+ has a significant high-energy ion population, the He^+ ion density on the dayside is almost constant during the first 10 minutes after the main peak. On the nightside the maximum ion density occurs 7-8 minutes after the corresponding event on the dayside. The distribution of the surface impact flux follows the general evolution of the ion density distribution. When the ion density peaks in a given region, the impact flux peaks just ~ 2 minutes later.

Solar flares have an impulsive and a gradual phase, which correspond to emission at different wavelengths. Due to the difference in optical thickness of the solar atmosphere in X-ray and EUV wavelengths, the intensity of the gradual flare phase (i.e. EUV) depends on where the flare source region is located on the solar disk with respect to Mercury. If the flare occurs on the limb, the EUV emission is attenuated and He, O and Mg all reach their maximum photo-ionization rate at the same time. For flares which occur near the center of the apparent disk from Mercury, He and O reach their maximum photo-ionization rate a few minutes after the maximum Mg photo-ionization rate.

In the following, I would like to apply the time-dependent algorithm of LIZE to try to recreate the observations described in Raines et al. (2018). This would require a time-dependent study of both the He exosphere and the He^+ distribution in the magnetosphere. The time-dependent algorithm has already been implemented and extended during this PhD (capability to integrate a variable solar radiative flux in EGM).

The seasonal cycle of the Na^+ density has been briefly discussed in Raines et al. (2013) and studied by Jasinski et al. (2021). The geometry of MESSENGER's orbit meant that there is almost no overlap in latitude, local time and altitude between MESSENGER/FIPS observations taken at different true anomaly angles (TAAs). MESSENGER/UVVS observations of the Na exosphere are also missing near aphelion due to UVVS viewing geometry limitations. For these reasons it is not straight-forward to study the seasonal variation of the Na^+ population with observations alone. A model such a LIZE will therefore be useful to compensate the lack of observations in some portion of Mercury's orbital period.

This model and the described results provide a new and original analysis of MESSENGER/FIPS data and context to the ion measurements which will be made during the BepiColombo mission. The BepiColombo MPO and Mio carries several ion mass spectrometers which together will cover a much larger energy range than previous planetary ion observations. The multi-spacecraft configuration will make it feasible to separate spatial and time-dependent effects. The orbits of the two spacecraft are also better suited to study previously uncharted altitudes at the north and south pole. This also means that models as LIZE will be critical to properly analyze measurements made from two different positions in space and instruments with different spatial, temporal and energy coverage.

ACKNOWLEDGMENTS

These past three years have been nothing short of a roller coaster of emotions. At times I have felt like an old woman struggling to get up a hill, barely moving forward and afraid that I will never reach the end. Other times I have felt like a child stumbling down the same hill, running faster and faster without being able to stop. Terrified of falling down and not being able to pick myself up again. Somehow I am still standing on my feet after three years. I feel extremely fortunate to have had a solid support network of people on whom I could rely on when things got particularly tough. This is for you. Thank you so much.

First, I would like to thank my two superb supervisors, Francois and Jean-Yves. I am deeply grateful for everything that you have taught me, your guidance and for your unwavering support. Thank you for believing in me when I didn't believe in myself.

I would like to express my sincere gratitude to the committee members who took time out of their busy schedules to assess this work. Thank you!

I would like to thank my collaborators, Ronan Modolo, Sae Aizawa, Jim Raines, Lina Hadid, Carl Schmidt and Willi Exner, for their kindness, immense expertise and helpful comments.

Thank you to Dominique Delcourt and Dimitra Koutroumpa, who reviewed my work on several occasions during these past three years. I am thankful to Frédéric Daigne, Florence Durret, Thierry Fouchet and Jacques Le Bourlot at L'ecole doctorale astronomie et astrophysique d'ile de France for their help and encouragement. Thank you to Pierre, Jacques, Marc, Manuela, Faty and all of the residents at La maison des étudiants suédois for giving me a warm and welcoming home away from home.

I would also like to thank the incredibly sweet and considerate office mates I have had during the years: Marie, Adrien F, Antoine, Léa, Adrien V, Jinjin and Manuel. Special thanks to Audrey C who I first met at the IRF in Uppsala and who made me feel super welcome at Latmos. Thank you to Loïc, who held a great round-table discussion about the postdoc career path at the Journée des doctorants a few years ago, and who have always made me feel welcome at the few réunions jeunes planétos that I attended. To Claire, you're doing an amazing job and I wish you all the success in the world. A huge thank you to Nicolas, easily one of the most dedicated and ingenious people I have ever met! Big hugs to Audrey L and Lefteris, who always seem to know how to cheer me up. Love you guys!

I am fortunate to have had a large number of role models in my life. Thank you to Ouafi El Alami, the most inspiring and supportive physics teacher I've ever had. Thank you to Mikael Ingemyr, who I have always looked up to and whose leadership skills I greatly admire. Thank you to Ulf Torkelsson, for sharing your insight into the daily work of an astronomer with a stubborn little girl. It really inspired me to keep going. Thank you to John Rickert, an incredible tutor and the best presentation coach I've ever known. Thank you to Emiliya, a huge source of inspiration and who have always encouraged me to keep fighting. Thank you to Andrew, Andris, Mats, Anders and everyone at the IRF in Uppsala for guiding and inspiring me during my undergraduate studies.

Last but not least, I am immensely grateful for having such a caring and encouraging family: Mamma, Pappa and Alexandra. I love you more than anything.

CONTENTS

LIST OF FIGURES

LIST OF TABLES

ACRONYMS

AIKEF	Adaptive Ion-Kinetic Electron-Fluid
AU	The distance between the Sun and the Earth (149,600,000 km)
BELA	BepiColombo Laser Altimeter
CFL	Courant-Friedrich-Levy
CICLAD	Calcul Intensif pour le Climat, l'Atmosphère et la Dynamique
CIR	Co-rotating interaction region
CME	Coronal mass ejection
EGM	Exospheric Global Model
EPPS	Energetic Particle and Plasma Spectrometer
EPS	Energetic Particle Spectrometer
ESA	Electrostatic Analyzer
ESA	European Space Agency
ESD	Electron-stimulated desorption
EUV	Extreme ultraviolet
FIPS	Fast Imaging Plasma Spectrometer

FOV	Field-of-view
f10.7	The 10.7 cm solar flux
g-value	Photon scattering coefficient
IMF	Interplanetary magnetic field
IPS	Interplanetary scintillation
ISA	Italian Spring Accelerometer
JAXA	Japanese Aerospace Exploration Agency
K-H	Kelvin-Helmholtz
LatHyS	Latmos Hybrid Simulation
LIZE	Latmos IoniZed Exosphere
LOS	Line-of-sight
MAG	Magnetometer
MASCS	Mercury Atmospheric and Surface Composition Spectrometer
MDM	Mercury Dust Monitor
MERTIS	Mercury Radiometer and Thermal Infrared Spectrometer
MESSENGER	MErcury Surface, Space ENvironment, GEochemistry, and Ranging
MGF	Magnetometer
MGNS	Mercury Gamma-Ray and Neutron Spectrometer
MHD	Magnetohydrodynamic
Mio	Mercury Magnetospheric Orbiter (MMO; renamed after launch)
MIXS	Mercury Imaging X-Ray Spectrometer
MORE	Mercury Orbiter Radio-Science Experiment
MPO	Mercury Planetary Orbiter
MPPE	Mercury Plasma Particle Experiment
MSASI	Mercury Sodium Atmosphere Spectral Imager
M1	MESSENGER's first Mercury flyby
NetCDF	Network Common Data Form
n_{obs}	Observed number density
PHEBUS	Probing of Herman Exosphere by Ultraviolet Spectroscopy
PSD	Photon-stimulated desorption
PWI	Plasma Wave Investigation
SERENA	Search for Exospheric Refilling and Emitter Natural Abundances

SIMBIO-SYS	Spectrometer and Imagers for MPO BepiColombo Integrated Observatory System
SIXS	Solar Intensity X-Ray and Particles Spectrometer
SWS	Solar wind ion sputtering
S/N	Signal-to-noise ratio
TAA	True anomaly angle
THEMIS	Téléscope Héliographique pour l’Etude du Magnetisme et des Instabilité Solaires
TOF	Time-of-flight (spectrometer)
UVVS	Ultraviolet and Visible Spectrometer

1

INTRODUCTION

1.1 OVERVIEW

Mercury may seem like an unremarkable planet at first glance. Mercury has neither the seas of Earth, enormous volcanoes of Mars or icy rings of Saturn. However, you will find that this planet has countless of characteristics which makes it a unique and fascinating place in the solar system.

Mercury's diameter is just 40% larger than the Moon's (see Figure 1). This makes Mercury the smallest planet of the solar system and 10% smaller than the largest moon of the solar system, i.e. Ganymede. Mercury is the planet which is located closest to the Sun. The planet lacks a thick atmosphere however, which gives rise to a dayside surface temperature of 467 °C and −183 °C on the nightside. Mercury is also the fastest-moving planet of the solar system, completing a full orbit around the Sun in just 88 Earth days. Mercury has the most eccentric orbit in the solar system ($\epsilon = 0.2056$). This causes the planet's heliocentric distance to vary by over 40% between its farthest and closest point to the Sun.

Mercury's atmosphere is so thin that it is called an exosphere, that is, the collisionless part of the atmosphere. The exosphere mainly consists of metallic vapors (sodium, calcium, magnesium etc.) and gases one would normally find in the Sun's atmosphere (hydrogen and helium). Because of the planet's elliptical orbit Mercury's exosphere have been shown to exhibit strong "seasonal" variations. Ground-based observations have also indicated that Mercury's sodium exosphere may exhibit short time variations caused by changes in the magnetized plasma which flows from the Sun and fills the heliosphere (i.e. the solar wind).

Mercury has a large, partially molten iron core that generates a weak but persistent magnetic field. The magnetic field is highly compressed on the dayside due to the strong ram pressure exerted by the solar wind. Because Mercury's magnetic field is so weak, the planet takes up a relatively large part of the magnetosphere. Mercury's unique location in the solar system exposes it to intense solar radiation which ionizes a significant portion of its exosphere. The planetary ions are then "picked-up" by the electric field and magnetic fields surrounding Mercury.

Mercury has been visited by two spacecraft in the past; Mariner 10 (1974-1975) and MESSENGER (2008-2015). Only MESSENGER carried a science instrument capable of studying the distribution of plan-

Figure 1: Mercury as viewed by MESSENGER/WAC (NASA/JPL, 2008), the Moon photographed on Apollo 11 (NASA, 2017) and Earth by DSCOVR/EPIC (NASA/Karen Northon, 2017), all to scale.

etary ions in the Mercury environment, e.g. the Fast Ion Plasma Spectrometer (FIPS; Andrews et al., 2007). The distribution of the three most abundant planetary ions or ion groups have been characterized with respect to altitude, longitude and latitude (Raines et al., 2013). However, due to the limited mass resolution and field-of-view (FOV) of the instrument, little is known about the full ion distribution function of the observed species or the distribution of less abundant ion species. MESSENGER was a single spacecraft mission, and only limited information exists on temporal variations in the planetary ion distribution.

Ion density models can provide the global distribution of different ion species, which gives the needed context to separate temporal and spatial variations in the ion observations. Previous models of planetary ions in Mercury's magnetosphere have been limited to describing the distribution of Na^+ ions. Model-data comparison has been limited to MESSENGER's Mercury flybys. The FIPS observations made in orbit between 2011-2015 constitutes a much larger data sample, for a variety of orbital positions, solar wind conditions and with higher accuracy and coverage in local time. Models which account for time-dependent solar wind, IMF or solar radiation conditions have not been applied to Mercury to our knowledge.

BepiColombo is a two-spacecraft mission to Mercury which carries several ion mass spectrometers that will cover a much larger energy range than previous planetary ion observations. The multi-site observations will also make it possible to separate spatial and temporal variations in the planetary ion population. The model described in this thesis offers an original tool to analyze FIPS data and will provide crucial context to the future ion measurements which will be made during the BepiColombo mission.

1.2 OUTLINE OF THESIS

This thesis considers the development of a test-particle model to describe the global distribution of different planetary ion species in Mercury's magnetosphere. The model is first applied to reproduce the average ion density distribution of the most abundant ions and ion groups observed by MESSENGER/FIPS. It is then applied to predict the time-evolution of different planetary ion species in response to a real solar transient event.

Chapter 2 gives an overview of the planet Mercury and lays the foundation for the more exhaustive Chapter 3 and 4. The chapter begins with Mercury's orbital characteristics and then describes the planet from the core and outward: beginning with the internal structure and ending in the Mercury space environment. We then describe key concepts and techniques used in ground-based telescope observations of Mercury. Finally we give a brief overview of the spacecraft missions which have (Mariner 10 and MESSENGER) and will study Mercury in the near future (BepiColombo).

Chapter 3 describes the observations which have been made from the ground and from space of Mercury's exosphere (organized by species), the magnetosphere and the ion plasma environment.

Chapter 4 presents an overview of the techniques by which the Mercury environment has been modelled in the past. We first give a brief description of Chamberlain's exosphere theory and the principles behind test-particle Monte Carlo models. We then move on to describe the main sources, sinks, surface ejection processes and surface-exosphere interaction mechanisms which are important for Mercury's exosphere. We give the key equations and concepts of magnetohydrodynamic and hybrid models used to model Mercury's magnetosphere. Finally, we describe previous models of planetary ions at Mercury and some key results. The algorithm of the new Latmos IoniZed Exosphere (LIZE) model, which is the focus of this study, is described in detail at the end of this chapter.

Chapter 5 demonstrates the LIZE model's ability to reproduce MESSENGER/FIPS observations of planetary ions in Mercury's magnetosphere. The modeled ion density distribution of He^+, O^+ and Na^+ are compared with FIPS observations of the Na^+-group, O^+-group and He^+ collected during the entire MESSENGER orbital mission (2011-2015). In addition, we use the model of illustrate the phase space density distribution in four key regions in the magnetosphere.

Chapter 6 showcases the application of the time-dependent version of the LIZE model to describe the response of the Mg^+, Na^+, O^+ and He^+ ion density distribution to the strongest solar flare in solar activity cycle 23. We study the time-evolution of the energy distribution in three different magnetospheric regions and use these findings to discuss the non-linear response of the planetary ion distribution to the flare. The response is shown to depend on the species, location inside the magnetosphere, energy and the location of the flare source region relative to Mercury.

Finally, **Chapter 7** summarizes the main conclusions of this thesis and presents an outlook for future work on this topic.

2

THE PLANET MERCURY

2.1 ORBITAL PARAMETERS

Mercury is the innermost planet in our solar system located approximately 58 million kilometers or 0.4 astronomical units[1] (AU) away from the Sun. Mercury's orbit is elliptic and its distance from the Sun varies from 0.47 AU at its farthest point from the Sun (aphelion; New Latin: apo- "away from"; Greek: hēlios "sun") to 0.31 AU at perihelion (Greek: peri- "around").

Mercury is both the smallest and fastest planet of the solar system, and has many characteristics that makes it somewhat similar to the Moon (see Table 1). Mercury's radius is only 40% larger than the Moon's but it's mean density is more similar to that of Earth. This is due to the planet's large molten iron core, which takes up 60% of the planet's total volume.

Mercury is trapped in a 3:2 spin-orbit resonance with the Sun, which means that the planet spins exactly three times around its own rotation axis (i.e. diurnal rotation) in the time it takes to complete two laps around the Sun (sidereal rotation). One Mercury day (synodic rotation) does not equate an Earth day in the classical sense where the Sun rises in the East and sets in the West. Due to Mercury's highly elliptical orbit (see Table 1) there is a phase of the orbit surrounding perihelion where the planet's angular orbital velocity will exceed the planet's angular rotational velocity. In this region, the Sun's motion across the sky as seen from an observer on Mercury will appear to suddenly stop and then move in the opposite direction. When the planet has passed perihelion the Sun will eventually stop its retrograde motion and then resume its motion across the sky. This will make it appear so that the Sun repeatedly rises and sets in the same place at the horizon. This causes Mercury's synodic period to be larger than its sidereal period (see Table 1). Mercury's orbit is inclined 7% with respect to the plane of Earth's orbit around the Sun (i.e. the ecliptic), which causes Mercury-Sun transits to be relatively rare (see Figure 8).

2.2 INTERNAL STRUCTURE AND SURFACE

Mercury's solid core is believed to consist mainly of iron and nickel, while the molten core is likely infused with a lighter element to allow it to remain liquid under high pressure (Hauck et al., 2013). Above

---

[1] 1 astronomical unit (abbreviated as AU) is the distance from the Sun to Earth.

Table 1: Basic properties of Mercury, Earth and the Moon. Unless otherwise noted the properties listed here are evaluated at the surface (i.e. the temperature, gravity, escape velocity etc.) and at the equator (radius, gravity).

Property:	Mercury	Earth	Moon
Heliocentric distance [AU]	0.31-0.47	1	1
Radius [km]	2439	6378	1738
Mass [10^{22} kg]	32.9	597	7.35
Mean density [g/cm^3]	5.427	5.514	3.344
Core radius [km]	2074	3485	660
Maximum temperature [K]	750	330	396
Minimum temperature [K]	40	184	25
Solar irradiance [W/m^2]	6490-14291	1361	1361
Gravity [m/s^2]	3.70	9.78	1.62
Escape velocity [km/s]	4.3	11.2	2.38
Eccentricity	0.2056	0.0167	0.0549
Obliquity to orbital plane	0.034°	23.44°	6.68°
Inclination to ecliptic plane	7°	0	5°
Diurnal period [Earth days]	88.0	23.9	27.3
Sidereal period [Earth days]	58.6	365	-
Synodic period [Earth days]	116	365	-
Magnetic dipole moment	$195\ nT\ R_M^3$	$30,000\ nT\ R_E^3$	0

Mercury's core lies a thin silicate mantle that is enriched in different refractory and volatile elements. Mercury's surface is rich in sulfur and magnesium but depleted in iron, aluminium and calcium compared to the Earth's crust. The concentration of different refractory species on the surface show spatial variability and form so-called "geochemical terranes" which are rich and/or depleted in certain elements (Peplowski et al., 2015b; Weider et al., 2015). Mercury's surface is also relatively rich in volatile elements and has a similar surface concentration of Na, S, K and Cl to that of Mars (Nittler et al., 2018). Measurements of the K/Th and Cl/K abundance ratios, which probes the internal composition of volatiles relative to refractory species, confirms that not only the surface but the entire crust is rich in volatiles (Evans et al., 2015; Peplowski et al., 2011, 2012). This implies that Mercury, like Mars, may have formed after rapid accretion and limited meteoroid bombardment. Intense meteoroid bombardment during the planet's formation would otherwise act to strip the planet of volatile elements (Evans et al., 2015).

Mercury has a heavily cratered surface which indicates that it has not been geologically active for several billions of years. It was however likely geologically active in past just following its formation 4.6 billion years ago. At that time the craters left in the wake of meteoroid impacts would have been rapidly filled up with lava, leaving a smooth surface. The remnants of these relatively smooth surfaces (so-called mares) can now only be seen in the spaces between more recent meteoroid impact craters. Pyroclastic volcanism was also likely widespread on Mercury for much of its geological history (Robinson and Lucey, 1997).

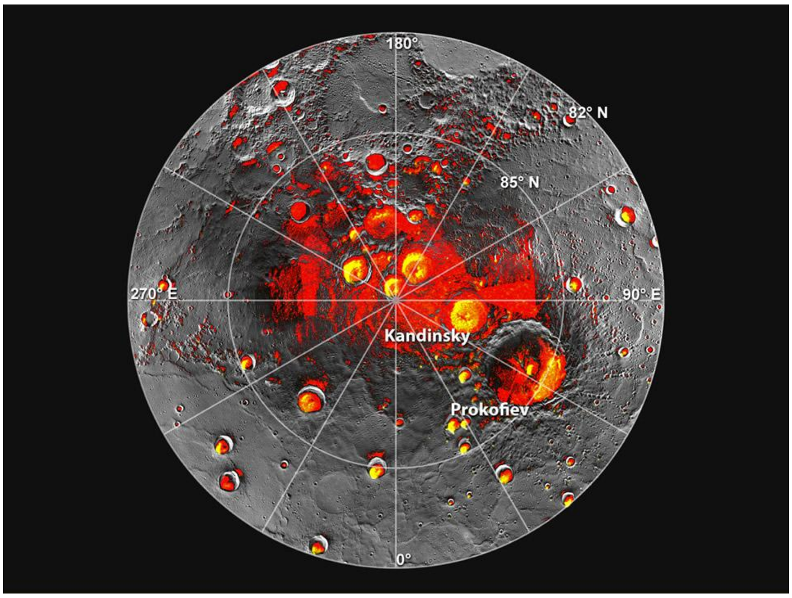

Figure 2: View of Mercury's north pole with red shadows showing regions which lie in permanent darkness and yellow highlights showing the location of the polar deposits imaged by Earth-based radars (Credit: Johns Hopkins University Applied Physics Laboratory).

Even though Mercury's surface can reach temperatures of up to 430°C or 700 Kelvin on the surface facing the Sun, its nightside is also one of the coldest places you can find in the solar system (-180°C or 90 K). There may exist water ice inside some of its craters. Mercury has a very low inclination with respect to its orbital plane, which causes some craters located close to the poles to lie in permanent shadow (see Figure 2). The temperature is low enough (-93°C) inside these craters to sustain water ice year round. The water may originally have came from the interior as water vapor that solidified when it travelled out through the crust of the surface, or from comets impacting the surface in the past.

2.3 ATMOSPHERE

Mercury is too small and located too close to the Sun to harbor an Earth-like atmosphere, but possesses a thin surface-bounded exosphere (i.e. a collision-less atmosphere). Mercury's exosphere is rich in gases of exotic elements like sodium, potassium, magnesium and calcium which are derived from the surface minerals or radioactive decay of heavier elements in Mercury's interior. The exosphere also contains lighter species (H, He) which have their origin in the magnetized plasma that flows from the Sun (i.e. the solar wind). Atoms and molecules in Mercury's surface layer are ejected and released from the surface by the intense solar radiation and continuous bombardment by solar wind ions and micro-meteoroids, sustaining the exosphere over time.

Hydrogen and helium were discovered in Mercury's exosphere by the Mariner 10 spacecraft. Ground-based telescope observations of resonance scattered sunlight off Mercury's exosphere later led to the discovery of sodium (Potter and Morgan, 1985). Potassium and calcium were later added to the inventory of exospheric species following ground-based observations by Bida et al. (2000) and Potter and Morgan (1986). Aluminium was first provisionally detected by Doressoundiram et al. (2009) and then detected alongside iron by Bida and Killen (2017). Magnesium and manganese was discovered in Mercury's exosphere with the MErcury Surface, Space ENvironment, GEochemistry, and Ranging (MESSENGER) spacecraft (McClintock et al., 2009; Vervack et al., 2016).

2.4 MAGNETOSPHERE

Mercury large metallic core is, similar to Earth's core, divided into a solid inner part and an outer liquid core (Genova et al., 2019; Margot et al., 2007). The molten rock in the outer core shifts and circulates as the planet moves in its highly elliptical orbit, which causes a dynamo effect like on Earth. This dynamo effect allows the planet to generate a weak but stable intrinsic magnetic field (Christensen, 2006). The strength of Mercury's dipole magnetic field is only 1 percent of the Earth's (Anderson et al., 2011). Despite this, Mercury's intrinsic magnetic field is strong enough to shield the planet from the solar wind and diverts it around the planet. This creates a magnetosphere similar to Earth's magnetosphere containing pockets of plasma with different kinetic and thermal properties separated by current layers (see Figure 3).

However, the lack of a thick atmosphere and extreme solar wind conditions give rise to a number of magnetospheric features which are unique to Mercury. The weak magnetic field and high solar wind dynamic pressure at Mercury causes the magnetosphere to be very

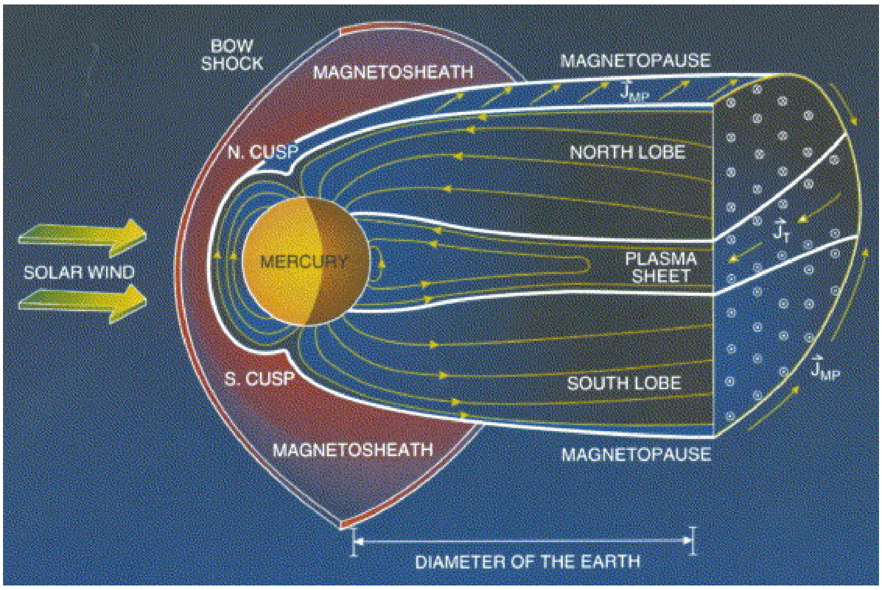

Figure 3: The large-scale structure of Mercury's magnetosphere (Slavin et al., 2003).

small compared to Earth. The magnetopause, which is the boundary layer which separates the magnetosphere plasma from the surrounding shocked solar wind plasma, is located just 1.45 R_M from the core (Winslow et al., 2013). Because Mercury lacks a conductive ionosphere, magnetospheric currents close through the upper layer of Mercury's iron core and give rise to induction currents that combat the compression of the magnetosphere by the solar wind dynamic pressure (Slavin et al., 2014). Solar wind plasma can interact directly with the surface regolith near the poles, which gives rise to the ejection of new neutrals into the exosphere through sputtering. The strong solar irradiance at Mercury also causes a significant portion of the heavy neutrals in the exosphere to become ionized and move into the magnetosphere and the solar wind. Once in the magnetosphere, the heavy ions are particularly susceptible to non-adiabatic acceleration and influence the large-scale transport of magnetospheric plasma.

2.5 SOLAR WIND CONDITIONS AT 0.4 AU

The solar wind is the expanding outer envelope of the Sun's atmosphere. The upper atmosphere (i.e. the corona) has a temperature of several million Kelvin and possesses a very high thermal and electrical conductivity. This causes the magnetic field to be "frozen-in" to the solar wind plasma. As the solar wind expands the magnetic field lines are dragged out with it, and as the Sun rotates the interplanetary magnetic field (IMF) forms a Parker spiral configuration (see Figure 4).

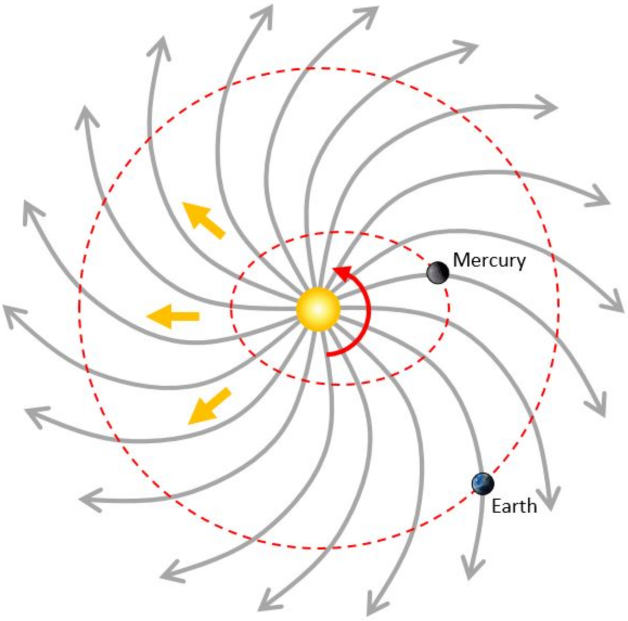

Figure 4: Schematic of the solar wind flow (yellow), the solar rotation (red) and the Parker spiral configuration of the interplanetary magnetic field (grey). As seen, the angle that the Parker spiral makes with the Mercury-Sun normal (and Earth-Sun normal respectively) is much smaller at Mercury ($\alpha = 20°$) compared to at Earth ($\alpha = 45°$).

The solar wind conditions in the inner solar system have been studied in the past by Helios 1, Helios 2, MESSENGER (James et al., 2017; Korth et al., 2011; Marsch et al., 1982; Pilipp et al., 1987; Sarantos et al., 2007) and, more recently, by Solar Orbiter and the Parker Solar Probe. Because Mercury is located closest to the Sun out of the planets in the solar system, it is exposed to highly variable, hot, dense solar wind and a stronger IMF compared to at Earth. The planet's highly eccentric orbit also means that the solar wind and IMF conditions vary over the timescale of the Mercury year (Russell et al., 1988). Burlaga (2001), Russell et al. (1988) and Sarantos et al. (2007) have characterized the solar wind and IMF conditions at Mercury from statistical analysis of data from Helios I and II (see Table 2).

The solar wind is characterized by the solar wind flow speed v_{sw}, density n, temperature T while the IMF is described by the IMF strength $|B|$, IMF direction, Alfvénic Mach number ($M_A = v_{sw}/v_A$, where V_A is the Alfvén speed) and the plasma β (the ratio between the plasma and magnetic pressure). The solar wind proton density varies strongly as a function of heliocentric distance r ($1/r^2$; Burlaga, 2001; Sarantos et al., 2007; Slavin and Holzer, 1981) and is approximately 5-10 times larger on average at Mercury compared to at Earth (see Table 2). The flow speed of the quiet solar wind is independent of heliocentric distance, but the speed variations imposed by co-

Table 2: Average properties of the solar wind and IMF at Mercury, separated by the typical values at perihelion and aphelion, and at Earth (Slavin and Holzer, 1981).

Property:	Mercury		Earth
Heliocentric distance [AU]	0.31	0.47	1
Flow speed [km/s]	430	430	430
Proton density [cm^{-3}]	73	32	7
Proton temperature [MK]	0.17	0.13	0.08
Magnetic field strength $\|B\|$ [nT]	46	21	6
Plasma β	0.5	0.9	1.7
Alfvén Mach number M_A	3.9	5.7	9.4

rotating interaction regions (CIRs) and coronal mass ejections (CMEs) will have a larger amplitude at Mercury compared to at Earth. The IMF strength vary as a function of heliocentric distance and is approximately 5 times larger at Mercury. The Parker spiral angle is only 20° at Mercury (compared to 45° at Earth), which means that the IMF direction is mainly sun- or anti-sunward.

2.6 MERCURY OBSERVATIONS FROM THE EARTH

Mercury is visible to the naked eye and has been observed by several ancient civilisations as a "wandering star", similar to the planet Venus. One of the oldest surviving records of Mercury are the MUL.APIN tablets, which were likely based on a much older transcript of observations made by Assyrian astronomers in 1370±100 B.C. (Schaefer, 2007). Mercury was given its current name after the Roman messenger god due to its fast movement in the sky. The first telescope observations of Mercury were made in the early 17th century by Galileo Galilei, who described Mercury and Venus as planets in "Sidereus Nuncius" in 1610. Giovanni Zupi later observed Mercury's phases in 1639.

Mercury's orbit changes orientation with time ("precesses") so that the perihelion changes location by 574 arc seconds every 100 years (see Figure 5). 92% of the displacement (531 arc seconds/century) is caused by the gravitational pull from the other planets in the solar system (Jupiter in particular), which leaves 42 arc seconds unaccounted for. Urbain Le Verrier, whose calculations led to the discovery of Neptune, was first to suggest in 1855 that the precession of Mercury's perihelion could not be explained by Newton's gravitation laws. At the time, Le Verrier proposed that the precession was caused by an undiscovered planet located inside Mercury's orbit ("Vulcan"). Mer-

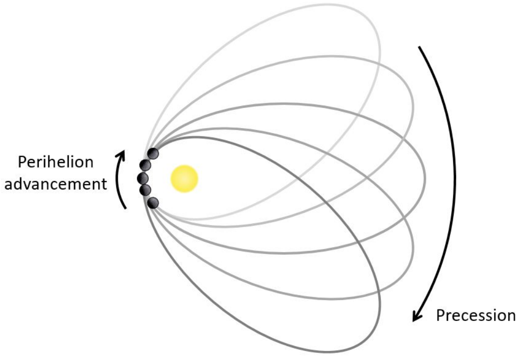

Figure 5: Illustration showing how the perihelion point changes location due to the precession of Mercury's orbit over time. A fraction of the total movement is due to the curvature of space-time close to the Sun.

cury's perihelion advancement was later explained by the curvature of space-time using the theory of general relativity proposed by Albert Einstein in 1915.

Mercury's 3:2 spin-orbit resonance was discovered by ground-based radar observations (Pettengill and Dyce, 1965). Later radar observations has also suggested the existence of water ice at Mercury's north pole (Slade et al., 1992).

Following the discovery of Na emission from Mercury's exosphere (Potter and Morgan, 1985), resonant scattering emission from exospheric species have been observed from the ground. Resonant scattering occurs when an atom (in its ground state) absorbs an incident photon, is excited and emits a new photon before returning to its ground state. The excited atom (or molecule) can only decay back to its ground state by emitting resonant radiation of the same wavelength as the transition. The resonant scattering emission from Mercury's Na exosphere comes from the strong Na D_1 and D_2 spectral absorption lines (wavelengths at rest: 589.0 and 589.6 nm), which are also present as Fraunhofer lines in the Sun's visible spectrum. Fine-structure splitting of the first excited state of sodium (P) gives rise to the two absorption lines (D_1 and D_2).

In an optically thin medium the intensity (I) of the resonant scattered emission is related to the total number of emitters along the line-of-sight,

$$4\pi I = gN \tag{1}$$

where g is the photon scattering coefficient (unit: photons/atom·s) and N is the column density along the line-of-sight (unit: atoms/cm^2; Hunten et al., 1956). I is commonly expressed in Rayleighs, which has the unit 10^6 photons/cm^2·s·sr. g, which is commonly referred to as the g-value, is proportional to the absorption cross section (unit: cm^2) and the incident solar irradiance at the rest wavelength of the transition (unit: photons/cm^2·s). Equation 1 rests on the assumption that light is scattered isotropically. The Na D_2 line is scattered according to a phase function which slightly favors forward and backward scattering (Chamberlain, 1961).

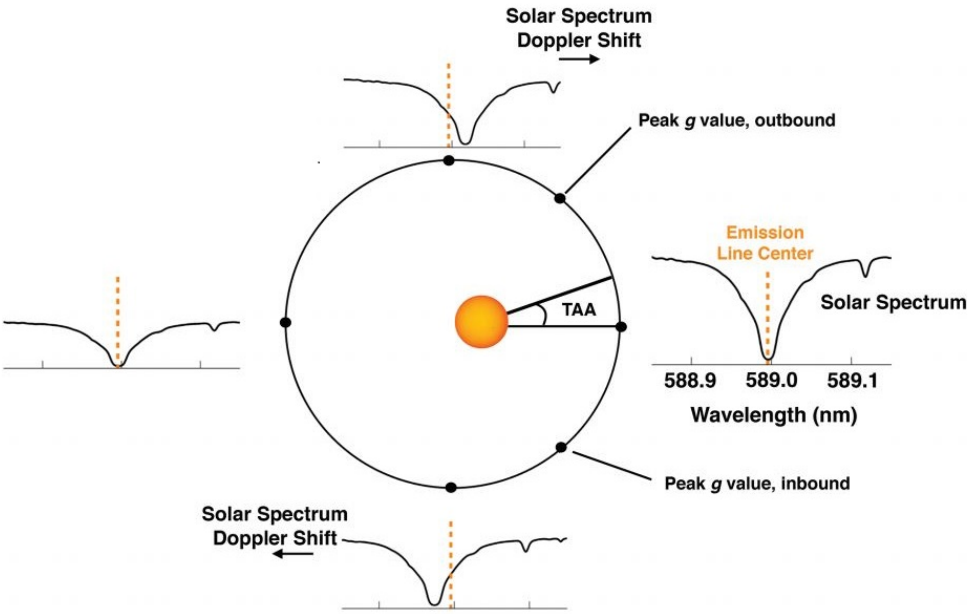

Figure 6: The solar spectral irradiance around the Na D_2 emission line at different points along Mercury's orbit around the Sun (McClintock et al., 2018, Figure 14.1). The solar spectra appears "flatter" at aphelion compared to perihelion in this figure because the solar intensity is lower due to the planet's larger heliocentric distance.

At perihelion, i.e. at true anomaly angle TAA = 0°, the solar spectrum exhibits a deep absorption feature (Fraunhofer line) near λ = 589.0 nm, which is the rest wavelength of the Na D_2 resonance transition (see Figure 6). Due to its elliptical orbit, Mercury experiences a large range of radial velocities. In the outbound leg of the orbit the planet's radial velocity begins to increase relative to the Sun and reaches a maximum at TAA = 90°. The planet's radial motion causes the solar spectrum to become Doppler shifted toward longer wavelengths (as seen from Mercury). Then, Mercury's radial velocity decreases until it reaches zero at aphelion (TAA = 180°). The planet's radial velocity increases during the inbound leg of the orbit but has the opposite sign compared to the outbound leg, reaching a maximum negative value at TAA = 270°. The Na D_2 g-value depends on both the Doppler shift and the heliocentric distance. This means that, although the radial velocity of the planet is maximum at TAA = 90° and TAA = 270°, the g-value reaches its maximum value slightly closer to the planet, at TAA = 60° and TAA = 300° (see Figure 7).

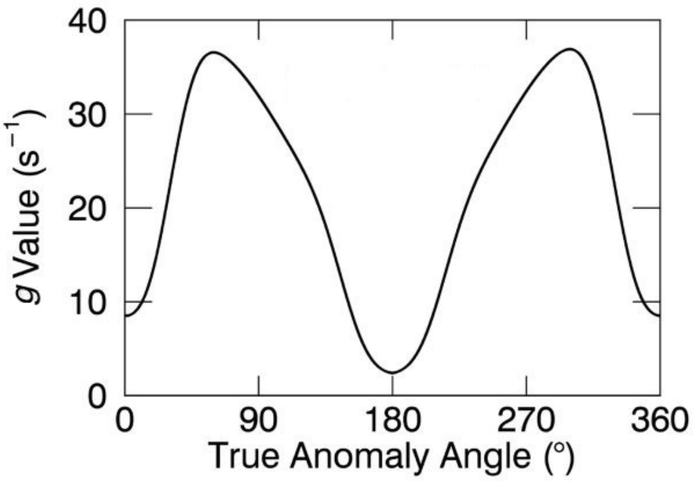

Figure 7: The photon scattering efficiency (g-value) of Na D_2 as a function of true anomaly angle (McClintock et al., 2018, Figure 14.1).

When the Fraunhofer line is shifted out of the rest wavelength of the Na D_2 line, the solar intensity as seen by the Na atoms at rest with respect to Mercury becomes higher than usual. This also means that the solar radiation pressure experienced by the Na atoms is higher. The radiation acceleration a_{rad} is proportional to the g-value (Killen et al., 2018; Smyth, 1983)

$$a_{rad} = \sum_i \frac{h}{m\lambda_i} g_i$$

where i is the resonant transition, h is the Planck constant, m is the atom mass, λ_i is the resonant wavelength and g_i is the g-value of the resonant transition. For Na D_2, the value of a_{rad} varies between 12 cm/s^2 at aphelion up to 2 m/s^2 (i.e. $\sim$ 54% of Mercury's surface gravity) near TAA=60° and 300°.

Doppler broadening of the Na D absorption lines can be used to infer the temperature of the emitting gas. Doppler broadening occurs because the atoms in a gas are not at rest, but are moving at different velocities. Each emitter contributes to a small Doppler shift Δf,

$$\Delta f = \frac{\Delta v}{c} f_0$$

where $f = (1 + \frac{\Delta v}{c}) f_0$ is the observed frequency, f_0 is the rest frequency and c is the speed of light. Δv is positive when the emitter is moving toward the observer. This means that the emission will be blue-shifted for an emitter moving toward the observer, and red-shifted when moving away from the observer. If the velocity distribution of the gas can be approximated by, for instance, a Maxwell-Boltzmann distribution, the gas temperature can be estimated from the total Doppler broadening caused by the thermal velocity of the atoms.

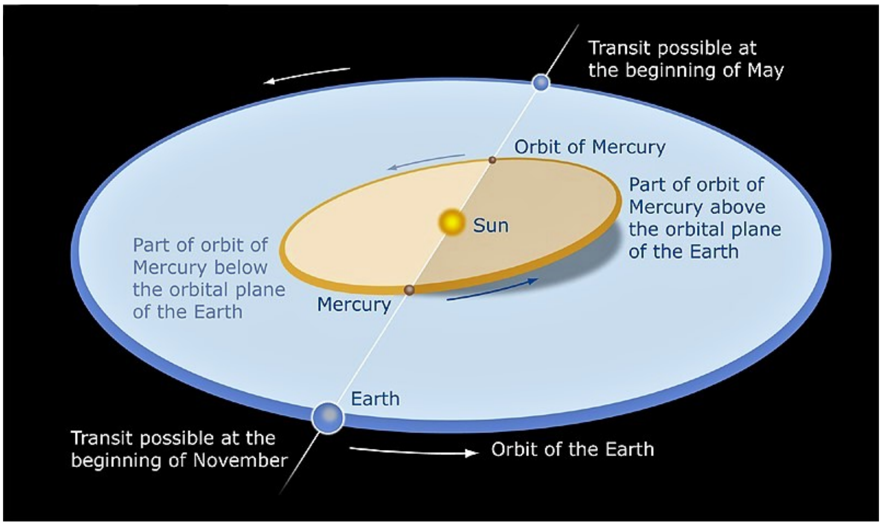

Figure 8: Geometry of Mercury-Sun transits (Credit: European Southern Observatory).

Mercury can also be observed during Mercury-Sun transits, which occur when Mercury moves across the solar disk as seen from Earth. Mercury-Sun transits are rare due to the 7° tilt of Mercury's orbital plane with respect to the ecliptic and occur $\sim 13 - 14$ times for every century. Mercury-Sun transits will only occur when Mercury is near the descending (8 May) or ascending node (10 November) when Mercury crosses the Earth's orbital plane (see Figure 8). The earliest recorded Mercury-Sun transit was observed on 7 November 1631 by Pierre Gassendi in Paris after a prediction made by Johannes Kepler in 1629 (van Helden, 1976). The last Mercury-Sun transit occurred on 11 November 2019 and the next transit will occur on 13 November 2032.

2.7 SPACECRAFT MISSIONS TO MERCURY

Mercury has been visited by two spacecraft: Mariner 10 which made three flybys past the planet in 1974-1975 and MESSENGER which orbited the planet between 2011-2015. BepiColombo will make its first flyby past Mercury in October 2021 and enter into orbit around the planet in 2025 (Dandouras et al., 2020).

2.7.1 *Mariner 10*

The first spacecraft to visit Mercury was Mariner 10, which made three flybys past Mercury between 1974-1975 (Broadfoot et al., 1976, 1974; Hunten et al., 1988). The space probe carried two television cameras, an infrared radiometer, two ultraviolet spectrometers, a magnetometer, an electron spectrometer and an electrostatic analyzer (see Figure 9). The spacecraft passed by Venus on 5 February 1974 en-route to Mercury and returned the first close-up images of Venus.

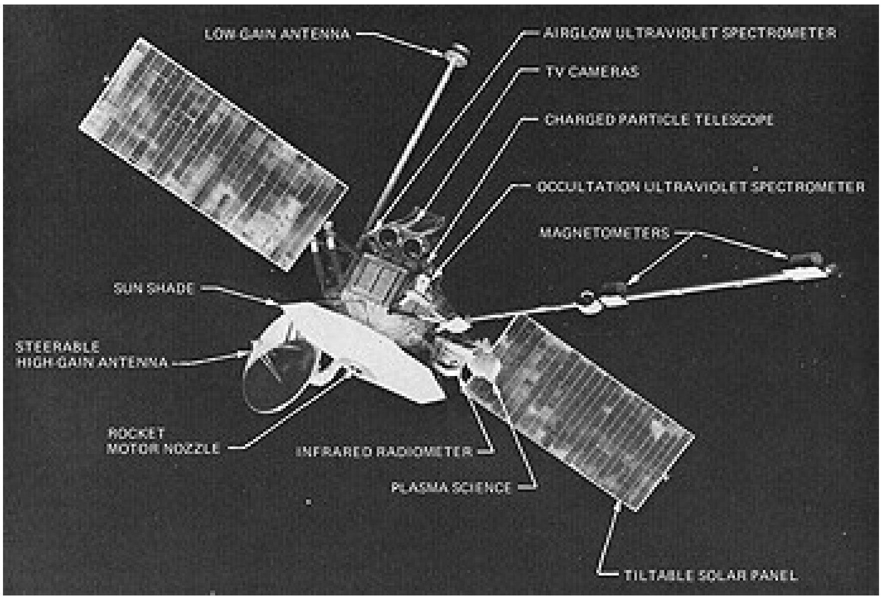

Figure 9: Location of the airglow and solar-occultation spectrometer on the Mariner 10 spacecraft (NASA Space Science Data Coordinated Archive, 2021).

The first flyby (29 March 1974) revealed a cratered Moon-like surface, a weak magnetic field and a thin exosphere consisting of hydrogen, helium and possibly oxygen. The spacecraft reached closest approach at an altitude of 703 km near the nightside plasma sheet. The second flyby occurred several months later on 21 September 1974 at a minimum altitude of 48,000 km. The third and last encounter with Mercury (16 March 1975) brought the spacecraft much closer to the planet (327 km), which allowed electron measurements indicating the existence of cold plasma (potentially of planetary origin) in the planet's shadow. Nearly half of Mercury's surface was imaged during the three flybys with an image resolution of up to 100 m in diameter.

Mariner 10 carried two ultraviolet spectrometers: an solar-occultation spectrometer which searched for atmospheric absorption lines in the solar radiation spectra and a a more sensitive spectrometer which measured the airglow (resonantly scattered sunlight; Broadfoot et al., 1976).

The solar-occultation spectrometer measured the extinction of extreme ultraviolet (EUV) solar radiation by the exosphere. The grazing-incidence spectrometer collected simultaneous measurements in four different spectral bands centered at 47.0, 74.0, 81.0 and 89.0 nm with ~ 7.5 nm bandwidth. The absorption cross section of the many common atmospheric species are large in the extreme ultraviolet (EUV) spectral range (30-90 nm). Therefore, the solar-occultation experiment would allow for detection of the total atmospheric extinction and identification of species like Ne, He, Ar, Xe. However, the occultation spectrometer did not detect any definitive absorption features.

The airglow spectrometer observed resonant scattering emission at set wavelengths which correspond to identified resonance transitions of different species that were believed to exist in Mercury's exosphere. The spectrometer had ten detectors in total, centered at 30.4 (He^+), 43, 58.4 (He), 74 (Ne), 86.9 (Ar), 104.8 (Ar), 121.6 (H), 130.4 (O), 148 and 165.7 (C) nm and had a 2 nm bandwidth. The spectrometer also carried two additional spectral channels to monitor the total incident EUV flux.

Space-based measurements of resonant scattering emission from Mercury's exosphere is typically made with limb scans, where the spectrometer views the exosphere along a line-of-sight (LOS) that passes above the surface (i.e. the limb). By repeating these observations for several tangent altitudes it is possible to characterize the density drop-off with altitude, producing so-called limb column density profiles. Equation 1 relates the observed intensity to the column density.

2.7.2 *MESSENGER*

Nearly 30 years after the end of the Mariner 10 mission, the MESSENGER spacecraft was launched from Cape Canaveral, set to reach Mercury in 2011. During the cruise phase, MESSENGER underwent a series of gravity-assist maneuvers around the Venus and Mercury to decelerate the velocity of the spacecraft relative to the planet Mercury and conserve fuel. MESSENGER made one Earth flyby, two Venus flybys and three Mercury flybys (14 January 2008, 6 October 2008, 29 September 2009) before entering into an orbit around the planet on 18 March 2011. MESSENGER had a highly elliptical polar orbit around the planet, which brought it as close as 200 km from the surface at the north pole. The initial orbit had a 12 h period, inclination of 82.5°, apoapsis at 15,200 km and periapsis at 200 km in altitude (see Figure 10a). After four Mercury years, the apoapsis was reduced to 10,000 km which caused the orbital period to be reduced to 8 h. The MESSENGER mission finally ended on 30 April 2015 with a controlled impact on the surface.

The spacecraft carried an imaging system, a magnetometer (MAG), a laser altimeter, a range of spectrometer including a gamma ray spectrometer, neutron spectrometer and X-ray spectrometer, atmospheric and surface composition spectrometer (MASCS), an energetic particle and plasma spectrometer (EPPS) as well as a radio science experiment (see Figure 10b).

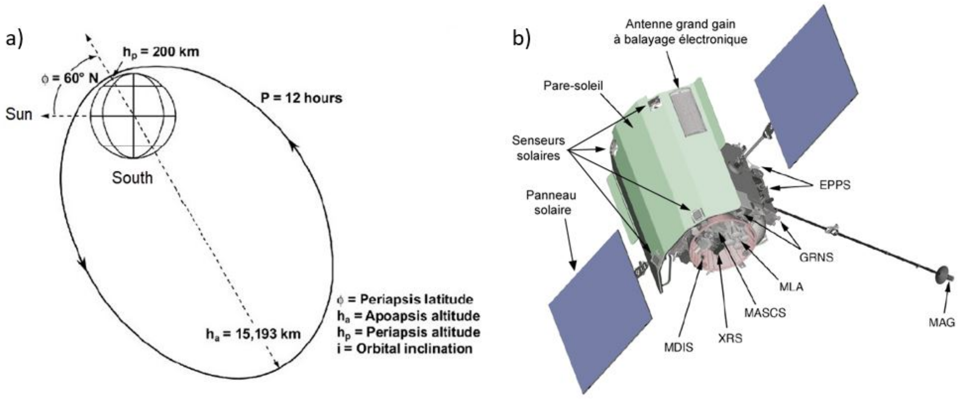

Figure 10: (a) The orbital characteristics of MESSENGER's orbit around Mercury and (b) the location of the different instruments on the spacecraft body.

The Mercury Atmospheric and Surface Composition Spectrometer (MASCS) carried an infrared and an ultraviolet spectrograph to decipher the composition of different surface minerals and exospheric gases. The Ultraviolet and Visible Spectrometer (UVVS) covered far ultraviolet (115-180 nm), mid-ultraviolet (160-320 nm) and visible (250-600 nm) wavelengths with an average spectral resolution of 0.6 nm. UVVS utilized a scanning grating, but was connected to three separate photomultiplier tubes which allowed the three different spectral ranges to be covered at the same time.

During the Mercury flybys, MESSENGER executed a series of partial roll maneuvers which swept the UVVS spectrograph slit from north to south during the approach. These spacecraft maneuvers made it possible to map the nightside exosphere along the north-south axis and the near-surface dawn region.

UVVS performed most of the orbital observations of the exosphere when the spacecraft was near apoapsis, which permitted observations of the widest range of local times. The local time coverage of the dayside was somewhat limited by the sunshade on the spacecraft. This effect varied depending on Mercury's orbital position. Near perihelion (TAA~ 0°) and aphelion (TAA~ 180°), UVVS observations were limited to local times near dawn and dusk. At other points along the orbit, the spacecraft was able to make small scan maneuvers in order for UVVS to sample local times near noon (12 h). The most complete local time coverage occurred at TAA 90° and 270°, when MESSENGER's orbit around the planet was aligned parallel to the Sun-Mercury line. Scans over the polar region were not made routinely. South pole observations were technically possible near TAA 0° and 180°, but even then the tangent points of the UVVS scans were mostly located near the equator.

MESSENGER also carried a charged particle instrument package, i.e. the Energetic Particle and Plasma Spectrometer (EPPS). EPPS was composed of two different spectrometers: the Energetic Particle Spectrometer (EPS) which measured high-energy electrons and ions and the Fast Imaging Plasma Spectrometer (FIPS) which measured low-energy ions. EPS was a time-of-flight (TOF) mass spectrometer covering an energy range of 25 keV to 1 MeV for electrons and 10 keV/nucleon to ~ 3 MeV/nucleon for ions (Andrews et al., 2007). FIPS was also a time-of-flight mass spectrometer which measured ions within a mass-per-charge range of 1-60 amu/e with an energy between 50 eV/e to 20 keV/e (Raines et al., 2013). FIPS had a nearly hemispheric FOV of 1.4π sr which was mainly limited by the sunshade on the spacecraft (Gershman et al., 2013).

MESSENGER's magnetometer (MAG) was a miniature three-axis ring-core fluxgate magnetometer mounted on a 3.6 m long aluminium boom. MAG measured fields between $\pm 1,530$ nT with a resolution of 0.047 nT resolution in the Mercury environment (Anderson et al., 2007). The EPPS and MAG coverage in local time and altitude were mainly limited by the elliptical orbit, which meant that the low-altitude region near the south pole could not be sampled.

2.7.3 *BepiColombo*

BepiColombo is a dual spacecraft mission to Mercury led by the European Space Agency (ESA) and the Japanese Aerospace Exploration Agency (JAXA). The scientific objectives of the mission include the study of Mercury's internal structure, surface, geology, exosphere and magnetosphere, the origin of the planet and its intrinsic magnetic field, the planet's evolution as well as to test Einstein's theory of general relativity. BepiColombo will provide a more complete set of measurements of the surface, exosphere and magnetosphere with higher temporal and spatial resolution than previous spacecraft missions to Mercury.

The BepiColombo mission consists of two planetary orbiters: the Mercury Planetary Orbiter (MPO) from ESA and the Mercury Magnetospheric Orbiter (MMO) by JAXA, which was renamed Mio after launch. The MPO carries 11 instruments which will primarily study Mercury's surface and internal structure, but will also sample the exosphere and magnetosphere at low altitudes. Mio carries 5 instruments or instrument packages that will study the exosphere and magnetosphere at a wide range of altitudes.

The spacecraft was launched on 20 October 2018 and will make its first flyby past Mercury on 1 October 2021. BepiColombo will make five more flybys before entering into an orbit around the planet between December 2025 and March 2026. The two spacecraft will be placed in two co-planar polar orbits but have different eccentricities, as shown in Figure 11. The periapsis of both spacecraft will be centered on the dayside equator at aphelion (as shown in Figure 11), and on the nightside at perihelion.

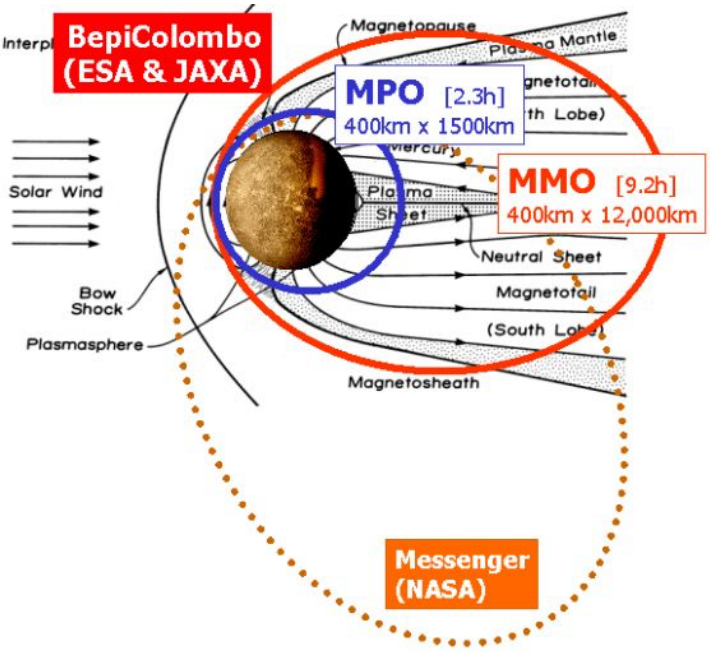

Figure 11: The orbital characteristics of MPO (blue) and Mio (red) compared to MESSENGER (ESA/Sebastian Besse, 2016).

MPO will orbit Mercury's south polar region at a much lower altitude than was possible with the MESSENGER spacecraft (see Figure 11). This will allow the MPO to image the south pole with higher resolution and to give more detailed observations of the magnetic field in this region. The dual viewpoints of MPO and Mio will also give a better understanding of solar driven magnetospheric dynamics.

The MPO carries a laser altimeter (BELA; see Figure 12), an accelerometer (ISA), a dual fluxgate magnetometer (MAG), infrared, ultraviolet, gamma-ray, neutron and X-ray spectrometers (MERTIS, PHEBUS, MGNS, MIXS, SIXS), a set of particle- and ion spectrometers (SERENA), a radio-science experiment (MORE) and a suite of optical cameras and spectrometers (SIMBIO-SYS). BELA and SIMBIO-SYS will study tectonics, volcanism and perform surface dating. MERTIS will provide information on the mineralogical composition of the surface, which is important for models of the planet's origin and evolution. The surface composition will be studied by several instruments, including the aforementioned MERTIS along with MGNS and MIXS. MGNS will also study the distribution of volatile deposits in the polar regions. MAG will characterize the structure of Mercury's intrinsic magnetic field and its origin. PHEBUS will study the UV emission from Mercury's exosphere as well as surface-exosphere interactions. SERENA will study both the exosphere and ion environment near the planet.

ISA and MORE measurements will be used to study the planet's internal structure, gravity field and test Einstein's theory of General Relativity.

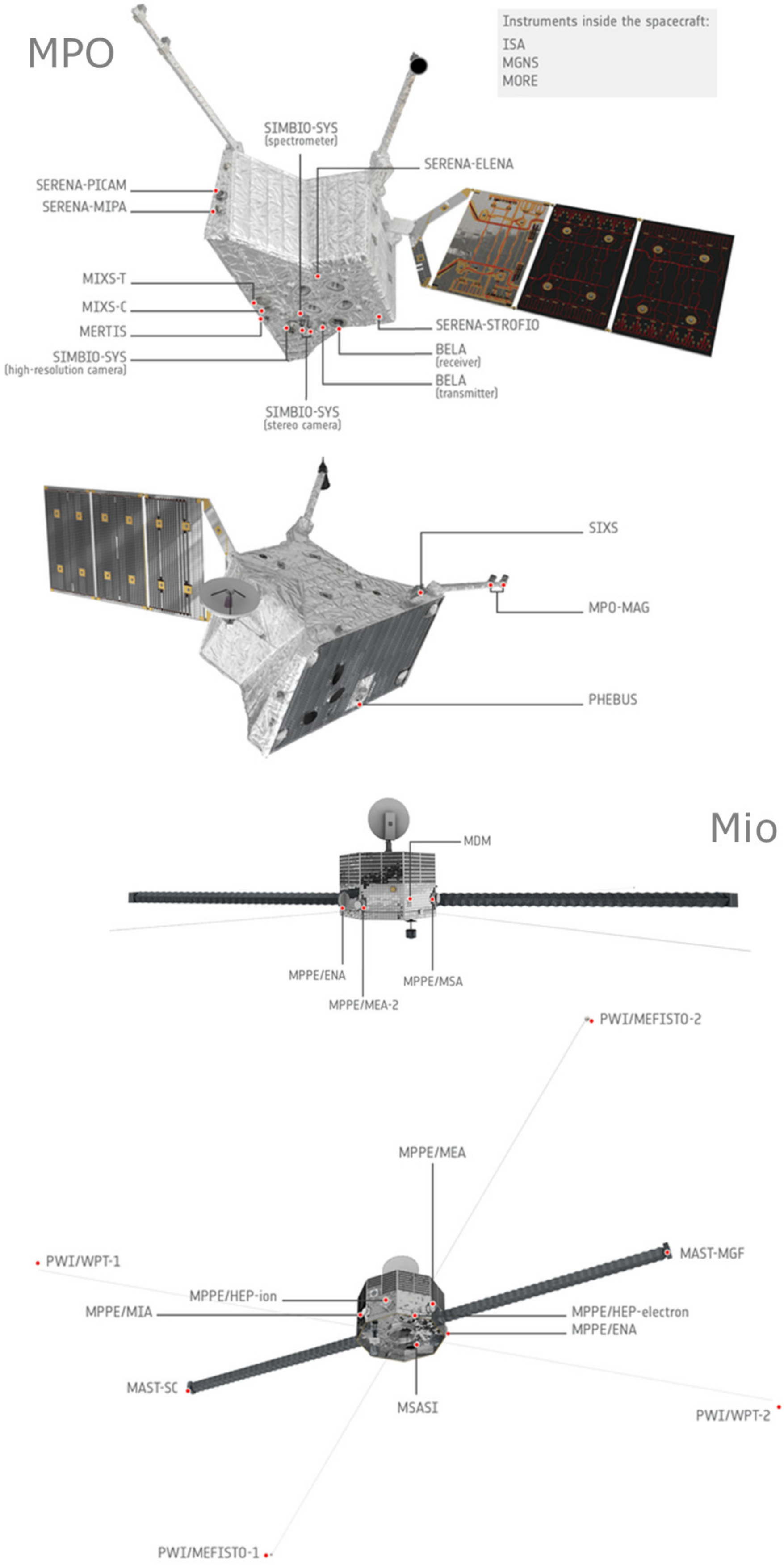

Figure 12: Location of the different science instruments onboard the BepiColombo/MPO and Mio (ESA/ATG medialab, 2020).

Mio carries a dust monitor (MDM; see Figure 12) that will study the dust environment near Mercury, a set of two fluxgate magnetometers which are mounted on a boom at different distances from the spacecraft (MGF-O and MGF-I), a plasma and particle package (MPPE), a specialized spectrometer which will measure the Na D_2 emission from Mercury's exosphere (MSASI) and a plasma wave instrument package (PWI) which will measure the electric field, plasma waves and radio waves in the Mercury environment. The setup of MGF will provide magnetic field measurements with high temporal resolution. This will be used to measure magnetic fluctuations that are indicative of plasma turbulence, which may be important for the heating and acceleration of the solar wind. Mio/MGF will also assist MPO/MAG in characterising the structure of Mercury's magnetic field. The MPPE provides several electron and ion analyzers mounted so as to provide a 4π FOV and a wide energy range. MPPE also carries an energetic neutral atom analyzer which will provide information on the escape of exospheric neutrals.

3

MERCURY OBSERVATIONS

3.1 MERCURY'S EXOSPHERE

A combination of ground-based and in-situ observations by Mariner 10 (1974-1975) and MESSENGER (2011-2015) have confirmed that hydrogen, helium, sodium, potassium, magnesium, calcium, manganese, iron and aluminium exist in Mercury's exosphere (Bida et al., 2000; Bida and Killen, 2017; Broadfoot et al., 1974; McClintock et al., 2008; Potter and Morgan, 1985, 1986; Vervack et al., 2016). Other species are expected (sulfur, chlorine, carbon, water, neon, argon etc.) based on observations of the surface composition (Evans et al., 2012, 2015; Nittler et al., 2011; Peplowski et al., 2012, 2015a) but have not been detected yet.

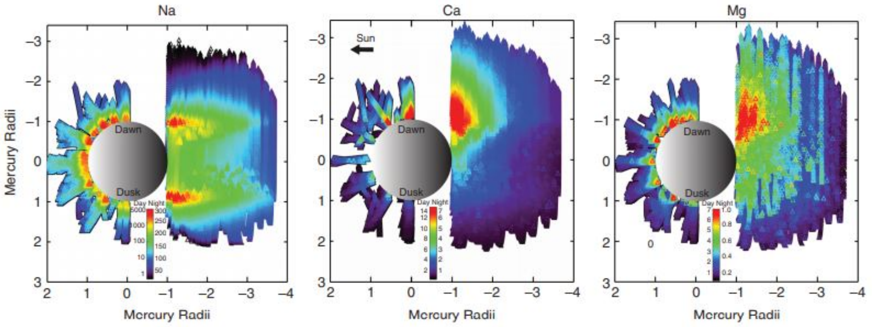

Figure 13: Distribution of the sodium, calcium and magnesium exosphere emission in the equatorial plane as determined from orbital MESSENGER UVVS observations (McClintock et al., 2018, Figure 14.47). Note that the color scale is different between each species and the day- and nightside.

The MErcury Surface, Space ENvironment, GEochemistry, and Ranging (MESSENGER) spacecraft made three flybys in 2008-2009 before entering a polar orbit around the planet in March 2011 where it remained until April 2015. MESSENGER Mercury Atmospheric and Surface Composition Spectrometer (MASCS) Ultraviolet Visible Spectrometer (UVVS; McClintock and Lankton, 2007) detected sodium, calcium, magnesium, hydrogen, aluminum, manganese and singly ionized calcium (McClintock et al., 2009; Vervack et al., 2016; Vervack et al., 2010) of which sodium, calcium and magnesium were observed regularly during the orbital phase. Subsets of UVVS data taken in orbit have been analyzed to describe the abundances of sodium, calcium and magnesium as a function of local time, latitude and TAA

(Burger et al., 2014; Cassidy et al., 2015; Merkel et al., 2017, see Figure 13).

The discovery of manganese and definitive detections of aluminium and singly ionized calcium was reported by Vervack et al. (2016) over a limited TAA range near the end of the mission. The spectral range of the UVVS instrument did not permit observations of helium or the potassium D-line transitions. Attempts to detect the less intense potassium emission lines located at 404.48 nm and 404.52 nm with the UVVS were unsuccessful. To date only Mariner 10 has been able to make observations of Mercury's helium exosphere.

Here follows a description of ground-based telescope and spacecraft observations of the different species present in the exosphere of Mercury since the Mariner 10 era up until the present time.

3.1.1 *Hydrogen*

Ly-α H emission (121.6 nm) radiances were detected above the subsolar limb during the first and the third Mariner 10 Mercury flybys. Broadfoot et al. (1976) found that the approximate scale height of the H emission changes abruptly from 1900 km to 70 km around 300 km in altitude. Following this observation, Shemansky and Broadfoot (1977) argued that the H exosphere consists of two different H populations: a hot component with a mean temperature that is consistent with the dayside surface temperature (420 K) and a cold component (110 K).

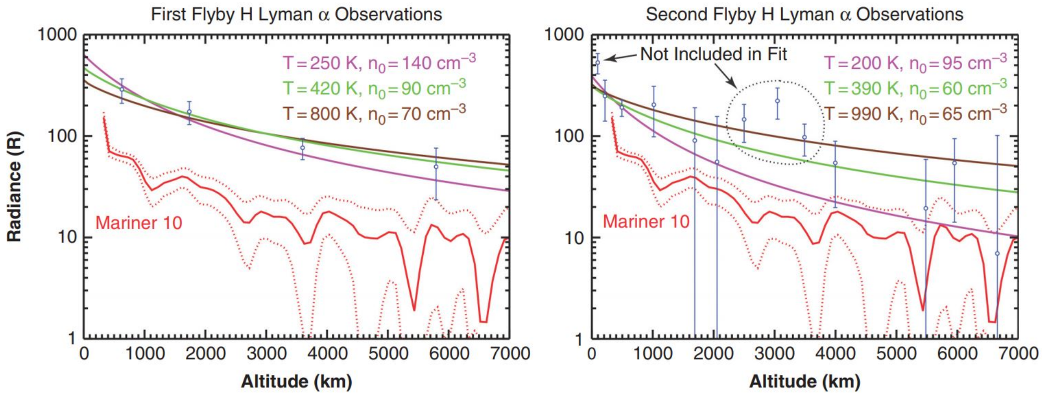

Figure 14: Chamberlain model fits to MESSENGER UVVS observations of Mercury's H exosphere (McClintock et al., 2018, Figure 14.38). The red curve shows the H radiances observed during the first Mariner 10 flyby (Broadfoot et al., 1976).

UVVS conducted dayside H observations during the first two MESSENGER flybys (Vervack et al., 2010). Vervack et al. (2009) fit a range of Chamberlain models to the UVVS observations to extract the source temperature of the H emission and the surface density, and found that the H column density was higher than what was previously detected by Mariner 10 (see Figure 14). Vervack et al. (2011) later measured H radiance-altitude profile during the orbital phase to search for the cold component reported during the Mariner 10 observations. Vervack et al. (2011) pointed out that sunlight scattered into the UVVS telescope from the planet's surface can mimic a cold component, and any possible artifact resulting from this effect had not been removed from their data. Thus, the existence of a cold component has not been conclusively verified by MESSENGER.

3.1.2 *Helium*

The airglow spectrometer on Mariner 10 detected He emission (58.4 nm) in numerous scans of the planet during the first and third flyby, including observations across the planetary disk above the south pole. The He radiance-altitude profile from the first flyby of the subsolar limb fit a single temperature distribution with a scale height that roughly corresponds to the dayside surface temperatures (575 K; see Figure 15a). The enhanced He emission below ~ 60 km is due to reflected sunlight off the surface.

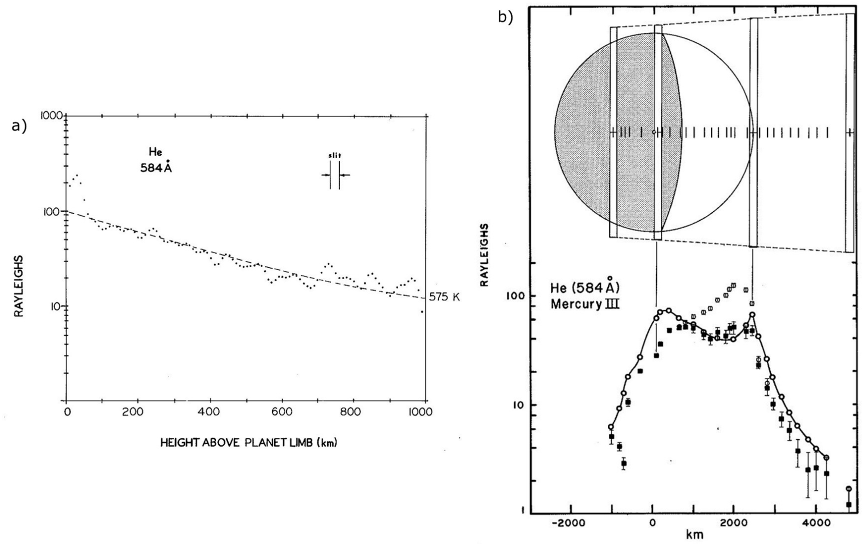

Figure 15: He radiance-altitude profiles from (a) the first and (b) the third Mariner 10 flyby (Broadfoot et al., 1976).

The He observations during the third flyby are shown in Figure 15b along with the projected FOV and slit size during the encounter. The open square markers show the uncorrected observations, the solid squares show the observations corrected for the planetary albedo. The solid line joined by open circles in the same figure shows a model exosphere profile by (Smith et al., 1978). Clearly it is difficult to achieve a good fit between the data on the nightside and the dayside, indicating a complex interaction between surface and exosphere not explained by said model.

UVVS did not cover the wavelengths of He emission.

3.1.3 *Sodium*

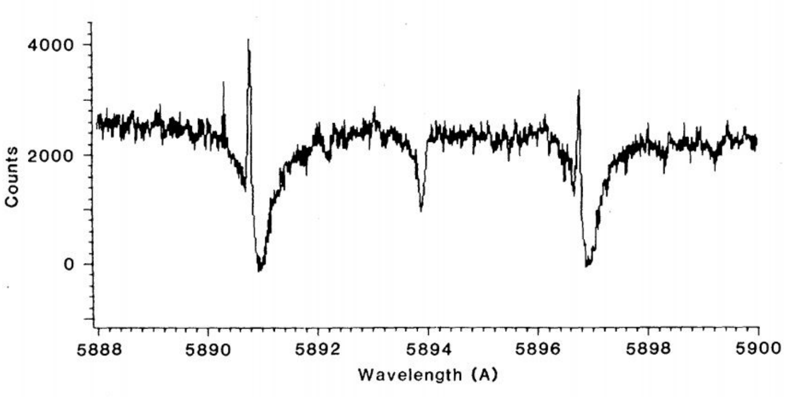

Figure 16: First observation of the resonantly scattered solar radiation spectra of Mercury's exosphere (Potter and Morgan, 1985).

Since its discovery (Potter and Morgan, 1985) sodium (Na) has been the most studied of the exospheric species, and has been observed both by ground-based telescopes and from space. Potter and Morgan (1985) first observed the doublet Na D_1 and D_2 of the resonantly scattered solar radiation spectra by Mercury's exosphere with the 2.7-m telescope at the McDonald Observatory on 3-6 January 1985 (see Figure 16). The authors determined an average Na column density of $8.1 \cdot 10^{11}$ Na/cm^2 and a Na density of $1.5 \cdot 10^5$ Na/cm^3 at the surface.

3.1.3.1 *Diurnal cycle*

It was early suggested (Killen et al., 1990; Potter and Morgan, 1990) that the Na emission from the exosphere may exhibit two different types of variation with time: a diurnal variation which is caused by the changing solar radiation pressure along Mercury's orbit and a more rapid variation due to changing magnetospheric activity on the time scale of a few days or less.

Sprague et al. (1997) analyzed a large set of Na observations between July 1985-May 1988 and found that the Na emission was typically enhanced at morning compared to afternoon at equatorial to mid-latitudes. Similarly, Hunten and Sprague (2002) reported up to 3-4x higher Na column densities in the morning compared to the afternoon based on analysis of a large set of Na emission observations. Deposition of the Na on the cold nightside, followed by its thermal desorption in the morning, has been suggested as a possible source mechanism for the observed morning enhancement (Hunten and Sprague, 2002; Sprague et al., 1997). In contrast a data set analyzed by Killen and Morgan (1993) showed very little diurnal variation, and even a small maximum in the afternoon.

Schleicher et al. (2004) observed Na absorption features from Mercury's exosphere for the first time during a Mercury-Sun transit on 7 May 2003. Yoshikawa et al. (2008) and Potter et al. (2013) made similar observations during the Mercury-Sun transit on November 8 2006. Schleicher et al. (2004) detected a small enhancement above the western limb (dusk), while no absorption was detected above the eastern limb (dawn). Yoshikawa et al. (2008) derived a 1.5x Na column density enhancement at dawn compared to dusk. To the contrary, Potter et al. (2013) reported less Na absorption at the dawn terminator compared to dusk.

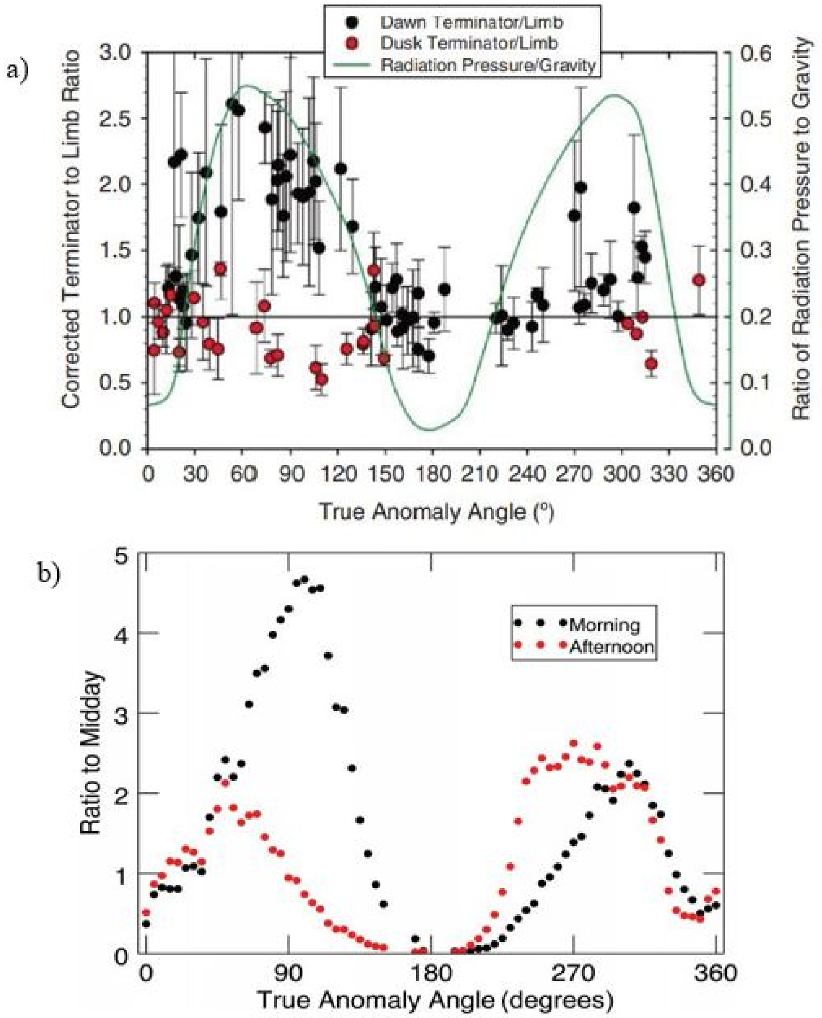

Figure 17: The morning-to-midday (black) and afternoon-to-midday (red) radiance ratio determined from (a) ground-based and (b) MESSENGER UVVS observations as a function of TAA (Cassidy et al., 2015; Potter et al., 2006) (McClintock et al., 2018, Figure 14.12 and 14.24).

Potter et al. (2006) studied the seasonal variation of the limb-to-terminator ratios in morning and afternoon using a large set of Na exosphere observations collected between 1997-2003 (see Figure 17). If the distribution of the Na exosphere is assumed to be spherically symmetric, the terminator-to-limb Na emission ratio should be close to unity. A ratio that is larger than unity is indicative of a Na enhancement at the terminator, while a ratio below 1 reflect a deficiency. When the dawn terminator was in view, Potter et al. (2006) found that the ratio was little above unity at small true anomaly angles and high (up to 2.5) at true anomaly angles up to 140°. Between TAA=180° and 240°, the ratio drops to unity or below. This seasonal pattern is consistent with two different effects: evaporation of condensed Na as the Sun rises above the dawn terminator, and radiation acceleration which sweeps Na away from the subsolar point toward the terminator. When the dusk terminator was in view, most of the ratios were below unity, which led Potter et al. (2006) to suggest that there exists a Na deficit at the dusk terminator.

Cassidy et al. (2016) did not find evidence for a sustained Na dawn-dusk asymmetry based on the near-equator Na limb scans made by MESSENGER/UVVS. As in the case of the Na ground-based telescope observations, the UVVS measurements show a strong morning enhancement for a large portion of the outbound leg of the orbit and no dawn-dusk asymmetry at perihelion (see Figure 17). Contrary to the ground-based observations, UVVS data show that the afternoon is brighter during the inbound leg of the orbit (180° $<$TAA$<$ 300°).

3.1.3.2 *Seasonal cycle*

Early modeling studies suggested that Na atoms in Mercury's exosphere could experience significant acceleration by the solar radiation pressure (Ip, 1986; Smyth, 1986). Ip (1986) and Smyth (1986) showed that Na atoms with an injection velocity at the surface of >2 km/s were able to reach escape energies (~ 4 km/s) and form an extended sodium tail on the nightside, similar to the sodium tails observed behind comets (Nguyen, 1960; Oppenheimer, 1980). Moreover it was predicted that the Na density will vary as a function of the changing solar radiation pressure along the eccentric orbit.

Potter and Morgan (1987) compared a set of 23 Na observations taken at different TAA, when the exosphere was exposed to different solar radiation pressure ($13-43\%$ of the gravitational acceleration at Mercury's surface) and found that the disk-averaged Na column density is anti-correlated with the solar radiation pressure. Sprague et al. (1997) did not find a relationship between the Na column density and the solar radiation pressure acceleration.

Potter et al. (2002) made the first mapping of the Na D_2 emission of the extended Na tail up to 40,000 km from the surface. Doppler shifts were measured at different points along the tail and Na atom velocities of up to 11 km/s could be detected. This would imply a surface ejection velocity of up to ~ 5 km/s (or ~ 4 eV). Later, Baumgardner et al. (2008), Potter and Killen (2008) and Schmidt (2013) also observed the extended Na tail.

Potter et al. (2006) confirmed from a large set of observations that the disk-averaged Na emission tends to be most intense at TAA=60° and 300°, when the g-value is maximum. Potter et al. (2007) analyzed the same set of observations as in Potter et al. (2006) but considered the effect of the solar radiation pressure on the Na emission. The authors proposed that there is a positive feedback loop in the outbound leg of the orbit such that the radiation acceleration increases the solar continuum intensity seen by the atoms, and a negative feedback loop in the inbound leg of the orbit (see Figure 6).

UVVS observed much lower Na emission in the tail during MESSENGER's third flyby (TAA = 331°) compared to the first and second flyby (TAA = 285°, 293°). This is consistent with the less extended Na tail near perihelion when solar radiation pressure acceleration of Na atoms is weak.

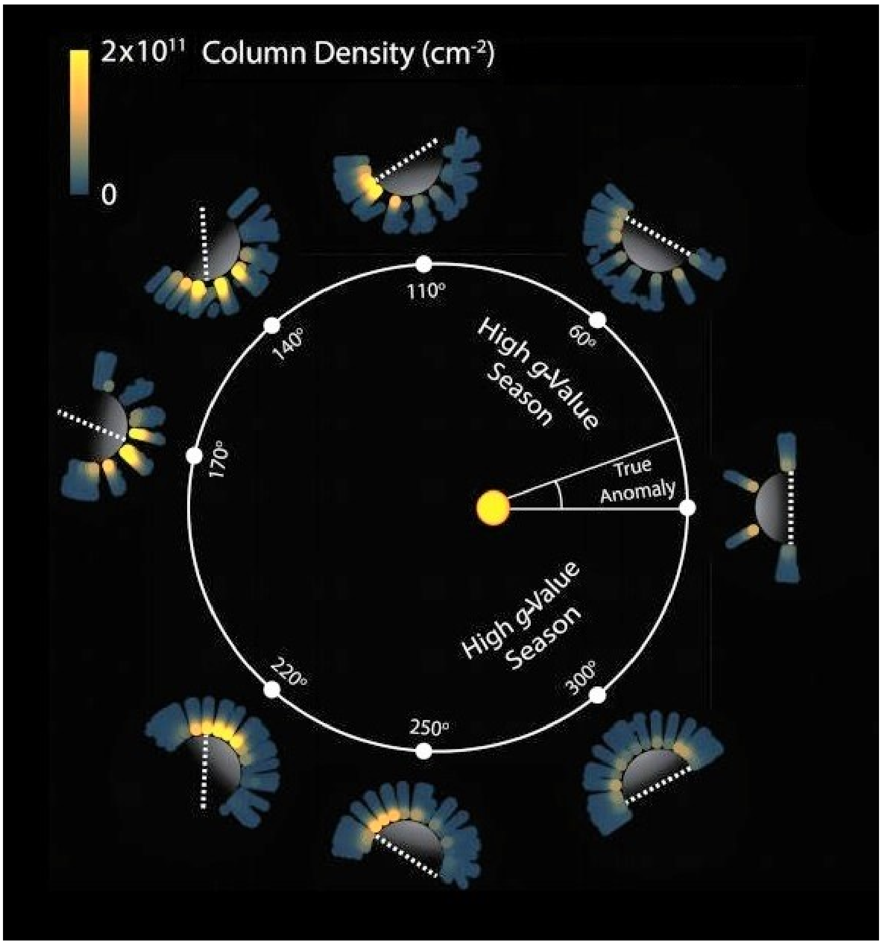

Figure 18: The dayside Na column density distribution near the equatorial plane as observed by MESSENGER UVVS at different points along Mercury's orbit (McClintock et al., 2018, Figure 14.23).

Cassidy et al. (2016) linked the TAA dependence of the subsolar Na density to the existence of so-called "cold pole" longitudes. Because of Mercury's 3:2 spin-orbit resonance with the Sun, there are pairs of invariant longitudes separated by 180° that sit at the subsolar point on alternating years. The cold longitude pair are located at the subsolar point when Mercury is at aphelion (TAA=180°).

The cold longitudes (indicated by the dashed white lines in Figure 18) are located near the terminators when Mercury is in the "high g-value season" ($TAA = 300 - 60°$), which is when the solar radiation pressure is at its maximum. Between $TAA = 270 - 90°$ the planet's rotation rate is comparable to the orbital angular rate. This implies that the terminators are nearly stationary at the cold pole longitudes. The strong anti-sunward transport of Na and nearly stationary terminators gives rise to the formation of temporary Na reservoirs in the regolith at the cold longitudes. When Mercury moves out of the high g-value season, the orbital angular rate is reduced and the terminators move again. This causes the cold pole longitude that was previously located at dawn to rotate onto the dayside. The accumulated Na is released into the exosphere and the Na emission at the dawn terminator and pre-noon sector is greatly enhanced. The Na emission from the cold pole decreases with time as the cold pole rotates from dawn to dusk and the reservoir of frozen Na is depleted. Finally the cold pole reaches the dusk terminator, the planet enters into the high g-value season, and the process begins anew. This mechanism can be used to understand the lack of a persistent Na dawn enhancement in the UVVS observations (Cassidy et al., 2015).

3.1.3.3 *Short-term variability*

Early attempts to characterize the latitudinal variation of Na across the planetary disk hinted toward possible enhancements in the polar regions and daily intensity variations (Killen et al., 1990; Tyler et al., 1987). Later studies that obtained two-dimensional images of the Na emission resulted in similar observations (Potter and Morgan, 1990; Potter and Morgan, 1997; Sprague et al., 1997). Potter and Morgan (1990) suggested that solar wind ion sputtering could account for both the high-latitude enhancements and their time-variability, consistent with a changing magnetic field topology in response to variations of the IMF.

Potter et al. (1999) linked an observed 3x increase of the total Na content over several days with three consecutive CME events. The authors suggested that the CME events may have affected the Na exosphere by enhancing the proton and electron impact flux. Killen et al. (2001) proposed that solar wind ion sputtering was the most likely source process responsible for the observed change of the total Na density based on estimates of the solar wind dynamic pressure from interplanetary scintillation (IPS) data and solar EUV flux observations during the specified time period in Potter et al. (1999).

Excess Na emission was observed at or above the north or the south pole during a third of the observations described in Potter et al. (2006). The high-latitude enhancements were observed to appear at either pole with no relation to the longitude or the TAA. Favorable IMF configurations for which solar wind ions can precipitate at high latitudes occur 30% of the time, strongly suggesting that solar wind ion sputtering is responsible for the Na emission at high latitudes.

The Na emission was occasionally found to be much stronger over the northern or the southern pole respectively (Potter and Morgan, 1990; Sprague et al., 1997). Potter and Killen (2008) observed higher Na emission in the north portion of the extended Na tail, and suggested that any north-south asymmetry in tail should match a similar asymmetry in the dayside exosphere (Potter et al., 2006). However, they also noted that the IMF could control the sense of the north-south asymmetry in the tail (Sarantos et al., 2001). Schmidt (2013) demonstrated from modeling that solar radiation pressure causes escaping Na atoms to drift to the opposite hemisphere of the tail. The higher Na emission in the northern part of Mercury's sodium tail previously reported by Baumgardner et al. (2008) and Potter and Killen (2008) was thus suggested to be due to enhanced Na production in the dayside southern cusp region.

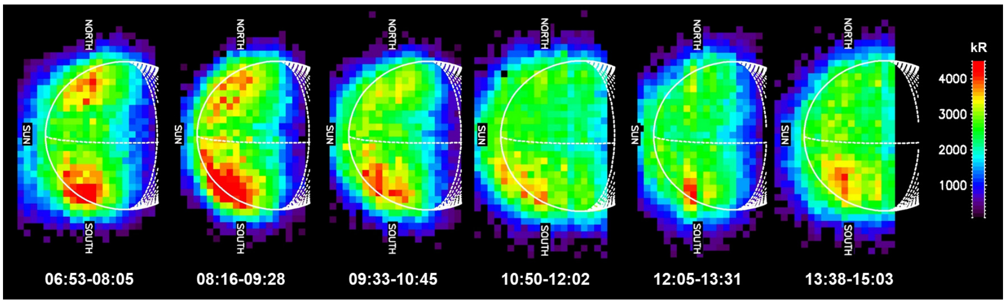

Figure 19: Six hour-long, consecutive scans of Mercury's Na exosphere collected by the THEMIS solar telescope on 13 June 2008 (Leblanc et al., 2009). The Na emission (here measured in kilo-Rayleighs) is most intense near one or both of the magnetic cusps. The Na emission also appears to become more intense and then fade over the course of a few (Earth) hours.

Two decades of Na exosphere observations with the French-Italian solar telescope THEMIS (López Ariste et al., 2000) have revealed emission patterns at high latitudes that change in shape and intensity over the course of a few (Earth) hours (see Figure 19; Leblanc et al., 2008, 2009; Mangano et al., 2009; Mangano et al., 2013, 2015; Orsini et al., 2018). Mangano et al. (2013) attributed observed changes in the Na emission at the equator and mid-latitudes over one (Earth) day to magnetospheric dynamics. They estimated that the variable Na component was on the order of 10% of the total emission. Mangano et al. (2015) suggested a correlation between the magnitude of the IMF southward component and the presence of mid-latitude Na emission peaks in a subset of the observations. Massetti et al. (2017) observed a series of in-phase intensity oscillations of the Na emission above both the northern and southern hemisphere on a time-scale of 10 minutes. Orsini et al. (2018) linked a THEMIS observation of diffuse Na emission over Mercury's dayside with the transit of two CMEs at Mercury as indicated by proton measurements with MESSENGER/FIPS and MESSENGER/MAG magnetic field data.

The observations during the first Mercury flyby (M1) by MESSENGER revealed bright emission at the poles, weak emission at the equator and a north-south asymmetry of the Na distribution in the tail (McClintock et al., 2008). The UVVS observations during the orbital phase mostly observed the equatorial region of Mercury's exosphere and did not regularly observe the southern pole (the northern pole not at all due to the observation geometry). Nonetheless, UVVS did not observe a significant short-term variation of the Na emission at high latitudes.

3.1.3.4 *Altitude dependence*

Potter and Morgan (1987) determined that the bulk of the observed Na emission was most consistent with a kinetic temperature of 500 K, which matches the temperature of the dayside surface. This would imply that the visible Na distribution is mainly injected into the exosphere by thermal processes. This was a surprising result considering the observed variation of the Na density with the solar radiation pressure. Shemansky and Morgan (1991) later re-analyzed the Na D2 line profile from Potter and Morgan (1987) and suggested that the existence of a secondary, non-thermal Na component could not be excluded due to the low signal-to-noise ratio (S/N) of the observation.

Potter and Morgan (1997) detected Na emission located as far as 10,000 km from the surface above the north and south pole. The authors interpreted the observation as evidence for a supra-thermal source capable of ejecting Na atoms to high altitudes. The characteristic temperature of the Na emission was estimated to 6,500 K. In a later set of Na exosphere observations Potter et al. (1999) employed images of Mercury's surface reflectance to account for the atmospheric seeing. Poor atmospheric seeing can otherwise blur the observed Na emission so that the source region of the emission on the disk can not reliably be determined. In effect, Potter et al. (1999) did not detect any Na emission above the limb and suggested that the high altitude Na emission observed by Potter and Morgan (1997) may be have been overestimated.

The UVVS fantail observations during M3 (with the UVVS slit sweeping from south through dawn to north) allowed for Na altitude scans to be made above both the north and south pole (Vervack et al., 2010). Fits of exponential functions to the Na altitude profiles led to the conclusion that Na is characterized by a two-component structure above the poles: one low-altitude component (<800 km) with an *e*-folding distance (or scale height) of 200 km and a high altitude component (>800 km) with an *e*-folding distance of 500 km (Vervack et al., 2010). The temperature of the observed Na emission can normally be derived from Doppler broadening in the case of ground-based telescope observations. Due to the relatively low spectral resolution of the MASCS instruments, this approach is not possible. Instead, the observations are typically fit to a simple Chamberlain model (Chamberlain, 1963) derived from Chamberlain's exosphere theory (see Section 4).

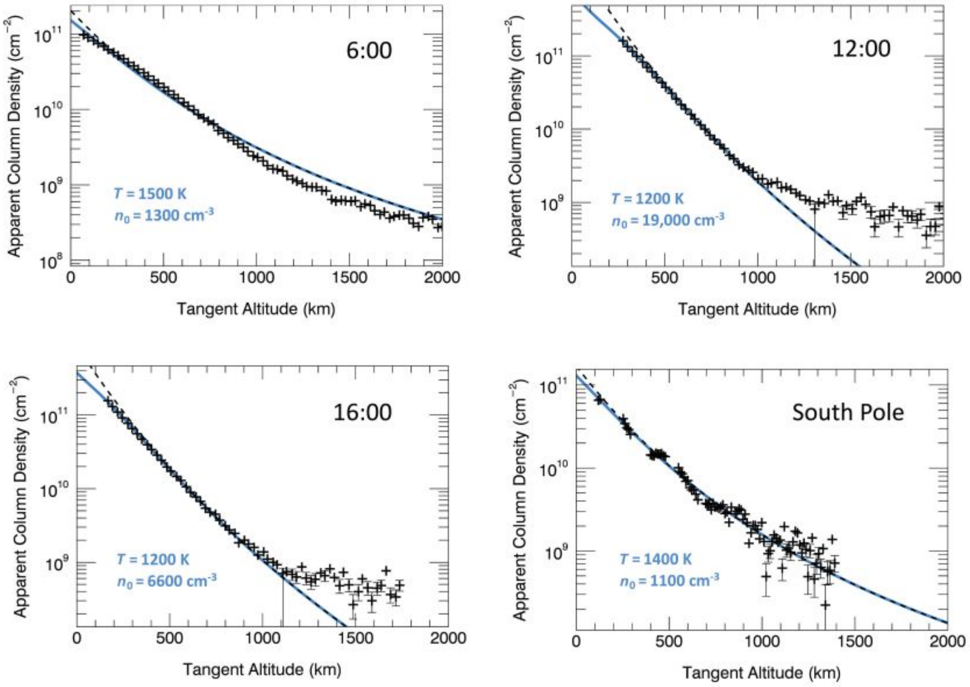

Figure 20: Example Chamberlain model fits (black dashed lines) to UVVS observations (black crosses) of the Na exosphere (Cassidy et al., 2015, Figure 6). The blue lines show the same model fits with optical depth correction. The UVVS limb scans shown here were taken at different local times near the dayside equatorial plane on 6 June 2012 and of the south polar region on 17 October 2011. The derived temperature and surface density are indicated in the lower left corner of each plot.

UVVS limb scans from the orbital phase with tangent points in the low-altitude equatorial region and above the south pole were fitted to Chamberlain altitude profiles (see Figure 20; Cassidy et al., 2015). The Na column density was best fitted using a two-component Chamberlain model with two different gas temperatures: a cold (1150 ± 50 K) Na component below 500 km in altitude and a hotter component with a temperature between $T = 5,000 - 20,000$ K in the altitude range 500-4000 km. The temperature of the hotter component could not be well constrained and may be consistent with a range of high-energy surface ejection processes.

3.1.4 *Potassium*

Because potassium (K) and Na have similar properties, they are likely ejected from the surface by similar processes. Potter and Morgan (1986) made the first discovery of K emission from Mercury's exosphere. The observed K emission was blue-shifted by 0.096 nm compared to the solar Fraunhofer line at 769.8 nm. This Doppler shift is sufficient to move the K emission line almost entirely out of the Fraunhofer absorption line into the solar continuum, which led to much higher K emission levels than would otherwise be expected. The K emission intensity was strongest above the polar regions and weakest near the equator, implying that the K exosphere exhibits high-latitude enhancements similar to the Na exosphere. The K column abundance was estimated to $0.5 - 1.6 \cdot 10^9$ cm^{-2}.

Apart from the low abundance of K relative to Na, ground-based observations of K is also further complicated by the fact that large Doppler shifts are necessary in order to avoid contamination from molecular lines in the Earth's atmosphere.

Potter and Morgan (1986) determined that the Na/K abundance ratio on Mercury (Na/K$= 80 \pm 1.7$) is substantially larger than that measured in lunar rocks and meteorites. Potter et al. (2002) later analyzed Na/K ratios determined from a larger set of spectroscopic observations of Mercury's exosphere. They found that the Na/K ratio is 100 on average and highly variable (Na/K$= 40 - 250$). Loss due to solar radiation pressure acceleration and photo-ionization were both deemed insufficient to explain the high Na/K ratio. Potter et al. (2002) instead suggested a combination of two effects: different photo-ionization rates and recycling efficiencies of the corresponding photo-ions. The higher mass of K (40 amu) compared to Na (23 amu) results in a smaller scale height and larger gyroradius, which would lead to a larger loss rate from the exosphere (see also Doressoundiram et al., 2010).

Shemansky and Morgan (1991) suggested a connection between observed variations of the average K column density and changes in the solar activity. They observed a strong correlation between the K column density and the 10.7 cm solar flux (abbreviated f10.7, which is a commonly used proxy for solar activity). Killen et al. (2010) found a weak correlation (r=0.66) between the solar UV flux and the K column density, supporting Shemansky and Morgan (1991)'s hypothesis.

3.1.5 *Magnesium*

Emission from Mercury's magnesium (Mg) exosphere was first detected by UVVS during the second flyby (McClintock et al., 2009). The Mg exosphere was initially observed to have a nearly uniform distribution on the nightside and a weak north-south asymmetry. Killen et al. (2010), Sarantos et al. (2011) and Vervack et al. (2010) made fits of the flyby Mg observations with a Chamberlain model, and determined that the inferred magnesium density distribution could not be derived with a single source process. A combination of a hot (>20,000 K) and a cooler source (<5000 K) to describe the near and far tail was suggested (Killen et al., 2010; Sarantos et al., 2011).

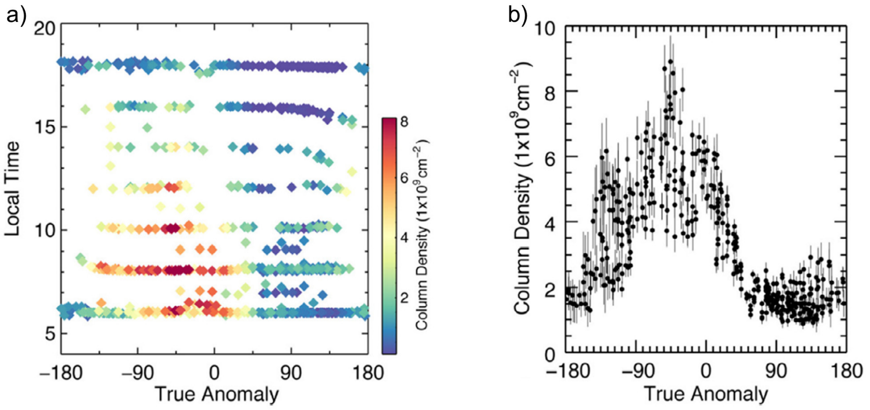

Figure 21: The (a) Mg column density derived from UVVS observations as a function of TAA and local time. The (b) average Mg column density between local times 06:00 - 10:00 h plotted as a function of TAA (Merkel et al., 2017, Figure 6c and 6d).

Merkel et al. (2017) analyzed a subset of the UVVS orbital observations (March 2013-April 2015) to determine the main characteristics of the Mg exosphere. Although (Sarantos et al., 2011) indicated the need for two distinct temperatures to characterize the Mg flyby data, Merkel et al. (2017) found that the orbital dayside Mg emission limb scans is typically well characterized by a single temperature (6000 K). Merkel et al. (2017) noted that a high-energy source ($T > 10,000$ K) may be active near the dawn terminator 15% of the time. The near-surface density varied between 5 cm $^{-3}$ up to 50 cm $^{-3}$. The authors derived Mg production rates and noted a persistent enhancement at dawn (local time: 6-10 h) peaking in the inbound leg of the orbit (TAA=315°; see Figure 21).

Merkel et al. (2018) later cross-correlated the MASCS observations with data from the MESSENGER X-ray spectrometer (XRS) and found a biennial cycle associated to a large Mg-rich region centered at 270° E, which places it at the dawn terminator near perihelion every other year.

3.1.6 *Calcium*

Bida et al. (2000) made the first discovery of Ca emission (422.7 nm) from Mercury's exosphere with the Keck I telescope. The Ca column abundance was very low, $1.1 \cdot 10^8$ cm^{-2} above the subsolar point, and the temperature high. This strongly suggests that a highly energetic ejection process is responsible for the bulk Ca distribution.

Killen et al. (2005) analyzed the results of four years of Ca emission observations from Mercury's exosphere. The observations revealed a variable, but consistent, Doppler blue-shift of the Ca emission. The temperature of the Ca gas was estimated to lie somewhere between $12,000 - 20,000$ K. They suggested that the most likely source of the hot Ca is ion sputtering or photo-dissociation of Ca in impact vapor produced by meteoroid impact vaporization of Ca-bearing molecules in the regolith.

During MESSENGER's first Mercury flyby (M1), Ca was observed at closest approach to the planet in the magnetotail and in the pre-dawn region up to the dawn terminator (McClintock et al., 2008). During M2 and M3 Ca was observed in the tail (McClintock et al., 2009; Vervack et al., 2010). Ca was also observed above the north and south pole during M3.

Burger et al. (2014) fitted UVVS limb scans from March 2011 - March 2013 of the dayside exosphere to a Monte Carlo model (Burger et al., 2010, 2012). The best-fit model to the Ca UVVS observations contained a hot Ca source (T=70,000 K) centered at dawn with a peak emission rate at TAA $= 20°$. The high temperature of the Ca source was attributed to molecular dissociation of Ca-rich molecules produced in the vapor left behind from meteoroid impact events.

Christou et al. (2015) and Killen and Hahn (2015) also studied the strong seasonal dependence of the Ca emission at dawn. Killen and Hahn (2015) suggested that the interplanetary dust disk and a secondary dust source at TAA $= 25 \pm 5°$ could together explain the enhanced Ca production at TAA $= 20°$ (see Figure 22). Christou et al. (2015) proposed that the cometary dust stream left in the path of comet Encke (which crosses the Mercury orbital plane at TAA $= 45°$) may account for the secondary dust source needed to explain the seasonal Ca dawn enhancement.

A later study using Burger et al. (2014)'s model showed that part of the energetic Ca source is located behind the terminator (Killen, 2016). This effectively rules out photo-dissociation as the source of energetic calcium. Direct impact vaporization remains as a likely ejection process for energetic Ca.

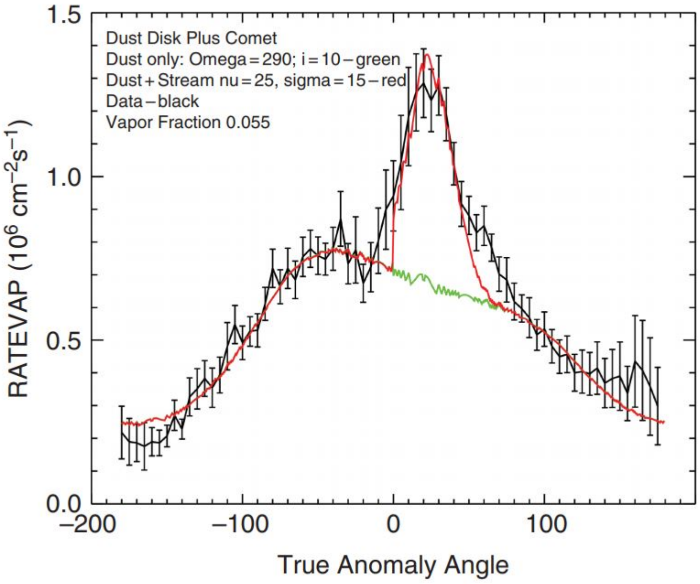

Figure 22: The Ca source rate estimated from UVVS observations (black) as a function of TAA (Killen and Hahn, 2015, Figure 7). The red curve shows the source rate from a model of the Ca exosphere with impact vaporization from two sources: interplanetary dust and comet 2P/Encke. The green line shows the same Ca exosphere model without the 2P/Encke dust source.

3.1.7 *Oxygen*

Mariner 10 made a "very tentative" O emission (130.4 nm) detection during the third Mercury flyby (Broadfoot et al., 1976). High noise levels preceded the measurement and the level of detection was uncertain (63-200 R; Broadfoot et al., 1976; Hunten et al., 1988). The low signal-to-noise level did not permit the derivation of an O scale height but it was possible to make an estimate of the O density above the subsolar point.

Attempts to observe the O exosphere were regularly made during the MESSENGER orbital phase, but no convincing O detection was made. In fact, Vervack et al. (2016) reported that O radiances consistent with those reported by Mariner 10 would have been easily detected by UVVS. The authors estimated a revised O radiance upper limit of 2 rayleighs, which corresponds to a tangent column density of $2 \cdot 10^{10}/\text{cm}^2$.

3.1.8 *Aluminum, iron and other species*

Doressoundiram et al. (2009) reported a tentative detection of aluminium (Al) emission (394.4 nm) from Mercury's exosphere but the poor signal-to-noise ratio prevented a clear detection. The upper limit Al column abundance was estimated to $7.8 \cdot 10^9$ cm^{-2}.

Bida and Killen (2017) later reported a definitive detection of Al and Fe in Mercury's exosphere. The observed Al tangent column densities ($2.5-5.1 \cdot 10^7$ cm^{-2} between 860-2100 km) were far lower than previously suggested by Doressoundiram et al. (2009). This confirms the suggestion laid forward by Doressoundiram et al. (2009) to treat the reported detection as an upper limit. Bida and Killen (2017) reported a Fe tangent column density of $9.4 \cdot 10^8$ cm^{-2} at 965 km.

Al, Ca^+ and Mn were detected by MESSENGER/UVVS in the predawn nightside region (2-5 h) over a limited TAA range ($0-70°$; Vervack et al., 2016) near the end of the mission only. The UVVS line of sight skirted Mercury's shadow during this set of observations, which prevented possibility of making complete radiance-altitude profiles. Instead, Vervack et al. (2016) converted the average observed radiances to column densities (Al: $7.7 \cdot 10^7/\text{cm}^2$, Mn: $4.9 \cdot 10^7/\text{cm}^2$). The Al column density is in reasonable agreement with the line-of-sight column densities reported by Bida and Killen (2017).

3.2 MERCURY'S MAGNETOSPHERE

Mariner 10 made the first in-situ measurements of Mercury's magnetic field. It was then revealed that Mercury has a magnetic field that is strong enough to stand off the solar wind plasma from reaching the surface and form a magnetic bubble surrounding the planet, i.e. a magnetosphere.

Mariner 10 sampled the magnetosphere during two of the three Mercury flybys. The magnetic field measurements during the flybys revealed a weak magnetic field with a similar magnetic topology to Earth's magnetic field (i.e. a southward directed dipole field). The dipole magnetic moment was eventually estimated to 350 nT R_M^3 (Ness et al., 1974, 1975, 1976). The first estimates of Mercury's dipole moment were made under the assumption that the dipole is centered on the planet, and higher-order multipole moments were not well constrained.

The strength, orientation and location of Mercury's magnetic moment could be re-evaluated later on thanks to the MESSENGER/-MAG measurements (see Figure 23). Magnetic field measurements during the first flyby confirmed that Mercury has an intrinsic field that can be well approximated by a dipole (Anderson et al., 2007). The dipole field was closely aligned with Mercury's rotation axis ($0.6° \pm 0.1$) and offset northward of the planet's center by 484 ± 4 km along the rotation axis. With these specifications, a dipole moment of 195 ± 10 nT R_M^3 best fitted the observations (Anderson et al., 2012). The dipole field has a negligible inclination with respect to Mercury's rotation axis ($\sim 1°$; Anderson et al., 2008).

The magnetopause stand-off distance from the surface was first estimated to 0.5 R_M from the Mariner 10 flyby observations (Ogilvie et al., 1977). Both the bow shock and the magnetopause were later mapped in detail during the orbital phase of the MESSENGER mission. Winslow et al. (2013) characterized the average location and shape of the two magnetospheric boundaries from three Mercury years of MAG observations. They showed that the bow shock moves closer to the planet as the solar wind Alfvén Mach number increases. Korth et al. (2015) made an updated estimate of the magnetopause shape from MAG data spanning seven Mercury years.

Mariner 10 observations showed that Mercury's magnetotail have properties similar to Earth's magnetotail and other magnetospheres in the solar system. The plasma sheet lies between the two tail lobes and is composed of high-energy (1-2 keV) plasma. The magnetic field strength is comparatively low in the central plasma sheet due to the high plasma density in this region (Jasinski et al., 2017). Because the Mercury's magnetic moment is directed southward (as for Earth), the magnetic field in the magnetotail is mainly directed toward north ($B_z > 0$).

Winslow et al. (2012) first determined the average location and extent of Mercury's northern cusp from two Mercury years of MAG data in orbit around the planet. This was possible by detecting diamagnetic depressions in the magnetic field magnitude near the cusp at every orbit. The cusp typically spans a region of 11° in latitude and 4.5 h in local time. Winslow et al. (2014) determined by a different method that the northern cusp is located at 76.4°N latitude, 12 h local time and extends 15.6° in latitude and 7.5 h in local time. MESSENGER's highly elliptical polar orbit prevented the necessary measurements of the southern hemisphere near the surface in order to pinpoint the southern cusp location. However, due to the northward offset of the planetary dipole, the extent of the southern cusp is expected to be larger than its northern counterpart.

The circulation of magnetic flux due to the large-scale plasma motion of the Dungey-cycle leads to a convection electric field and plasma drift. DiBraccio et al. (2015) observed this plasma drift directly as a persistent layer of anti-sunward flowing plasma with properties akin to the magnetosheath plasma inside and adjacent to magnetopause. The plasma drift velocity was measured to be $\sim 1-2$ orders of magnitude faster than the corresponding plasma drift at Earth. This indicates that the characteristic Dungey cycle time at Mercury is one the order of minutes instead of hours like on Earth (Slavin et al., 2009, 2010).

The behavior of charged particles in an electromagnetic field such as Mercury's depend on the ratio between the local gradient scale of the magnetic field and the gyroradius of the particle. If the magnetic field varies on scales much greater than the particle gyroradius, the first adiabatic invariant is conserved and the particle motion can be well described with a guiding center approximation. However, due to the small characteristic length scale of Mercury's magnetic field the magnetotail equator is characterized by non-adiabatic particle motion for which the guiding center approximation no longer holds. Non-adiabatic particle motion is prevalent for both protons and heavier ions in most of the magnetosphere, and stochastic processes may be important for plasma transport and heating (Korth et al., 2012). Electron motion is expected to remain adiabatic up to energies of hundreds of keV.

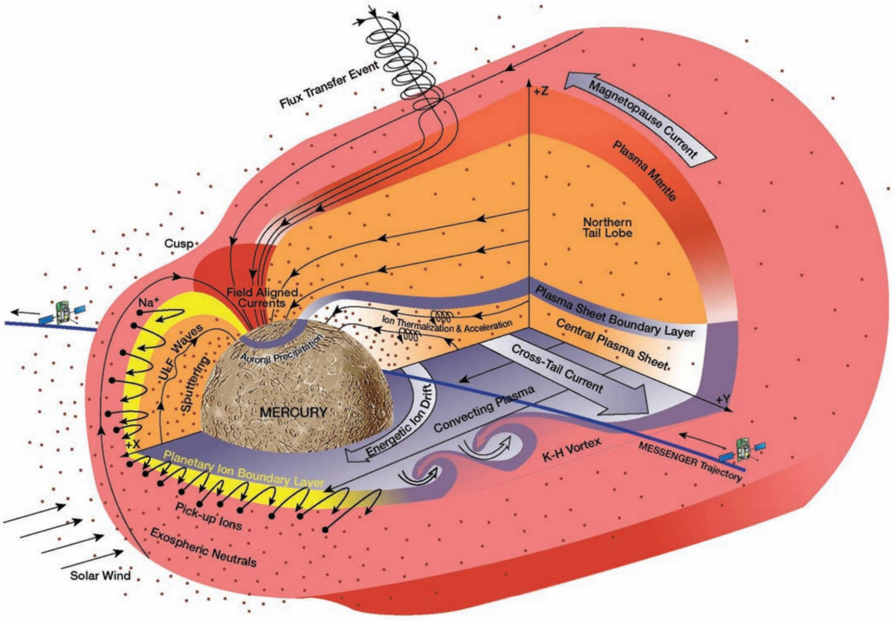

Figure 23: Schematic of Mercury's magnetosphere and the different features observed during MESSENGER's first flyby past Mercury (Slavin et al., 2008). The solar wind IMF was mainly directed northward ($B_z > 0$) and some of the observed features (i.e. K-H vortices, energetic ion population in the low-altitude nightside plasma sheet etc.) reflect typically quiet magnetospheric conditions.

Kelvin-Helmholtz (K-H) waves are large, sawtooth-like oscillations in density and magnetic field strength which may influence day-to-night plasma transport in Mercury's magnetosphere. K-H waves are driven by the formation of K-H instabilities and develop at boundaries separating two fluids with different streaming velocities, for example along the magnetopause (see Figure 23). A small perturbation of the boundary can develop into large-scale boundary waves and finally into rolled-up vortices. K-H vortices can promote interchange between magnetospheric and solar wind plasma across the magnetopause and contribute to the large-scale plasma convection of the Dungey cycle.

K-H waves were first detected at Mercury's magnetopause during MESSENGER's third flyby (Boardsen et al., 2010). The waves typically originate from the noon magnetopause and then propagate along the nightside magnetopause in the equatorial plane during time periods of strong, persistent northward IMF. K-H waves are rarely observed on the dawn magnetopause flank and during southward IMF (Liljeblad et al., 2014; Sundberg et al., 2012). The apparent dusk-dawn asymmetry in the formation of K-H waves (Sundberg et al., 2012) is believed to be due to kinetic effects caused by the large gyro radii of protons and Na^+ in the boundary layer relative to the width of the velocity shear layer (~ 350 km; Boardsen et al., 2010).

MESSENGER/FIPS observations have shown periodic injections of protons with magnetosheath-type properties inside the magnetopause (Raines et al., 2014). This observation indicates that K-H wave induced transport of magnetosheath plasma across the magnetopause boundary is indeed present.

3.3 MERCURY'S ION ENVIRONMENT

MESSENGER was the first spacecraft that explored the solar wind and planetary ion environment at Mercury. The protective cover of the Mariner 10 Scanning Electrostatic Analyzer did not open after launch (Ogilvie et al., 1974), which meant that no ion measurements could be made at Mercury before MESSENGER.

The Fast Imaging Plasma Spectrometer (FIPS; Andrews et al., 2007) was a low-energy (< 50 eV to 20 keV) ion spectrometer which was part of the Energetic Particle and Plasma Spectrometer (EPPS) package on the MESSENGER spacecraft. EPPS also consisted of a Energetic Particle Spectrometer (EPS), which measured both high-energy ions (> 5 keV/nucleon) and electrons (> 20 keV).

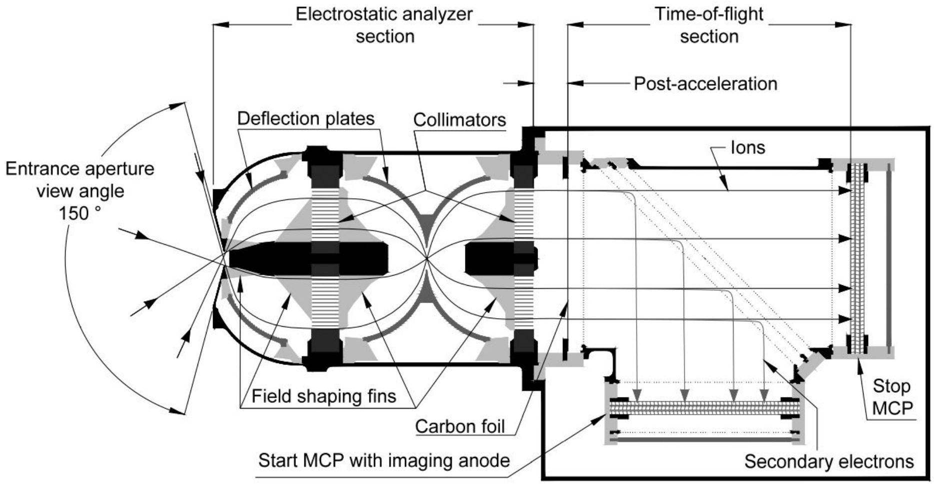

Figure 24: A cross-section of the FIPS instrument on the MESSENGER spacecraft (Andrews et al., 2007, Figure 5)

The key science objectives of EPPS was connected to the origin and structure of Mercury's magnetic field, inventory of exospheric species, including their sources and sinks, and determination of the radar-reflective material on Mercury's poles. The second objective was addressed specifically by FIPS, which would measure the mass, moments and angle distribution of low-energy accelerated magnetospheric ions in the whole Mercury environment.

FIPS consists of an Electrostatic Analyzer (ESA; see Figure 24) with a wide instantaneous FOV ($\sim 1.4\pi$ sr) and a time-of-flight (TOF) mass spectrometer. FIPS measured ions with an energy-per-charge of $E/q = 0.046 - 13.3$ keV/e and mass-per-charge ratio of $m/q = 1 - 40$ amu/e. The instrument used a nominal scan mode, during which all 64 energy channels were scanned in 64 s (1 s/channel), and a fast "burst" mode which made full E/q sweeps every 8 s (100 ms/channel). The instrument had an energy resolution of 10%, angular resolution of 20% and a mass resolution that is sufficient to separate C, N and O.

This meant that ions with similar mass-per-charge, such as Na^+ ($m/q = 23$) and Mg^+ ($m/q = 24$), could not be separated. Due to the limited mass resolution, and to improve the signal-to-noise ratio of the measurements, some ions were grouped together. The Na^+-group (m/q = 21-30 amu/e; including Na^+, Mg^+ and Si^+) and O^+-group (m/q = 16-20 amu/e; including O^+ and water group ions) are two such examples.

To derive the observed number density of a given species, a differential flux $(dJ/dE)_i$ (unit: $(\mathrm{keV/e})^{-1}\mathrm{sec}^{-1}\mathrm{cm}^{-2}\mathrm{sr}^{-1}$) is first derived from the observed counts C_i,

$$(\frac{dJ}{dE})_i = \frac{C_i}{(E/q)_i \tau_i g \eta_i \Delta\Omega}$$

where $(E/q)_i$ is the energy-per-charge at voltage step i, τ_i is the accumulation time and g is the energy-geometric factor ($g = 8.31 \times 10^{-5}$ mm^2 (eV/eV)). g represents the effective collection area of the sensor, and is determined by the physical aperture of the instrument and the E/q passband. η_i is the detection efficiency of protons (which typically dominates the observed spectra) and is a function of energy. $\Delta\Omega$ is the effective FOV, which has an approximate value of $\Delta\Omega = 1.15\pi$.

The differential flux can then converted to a phase space density f_i (unit: $s^3 m^{-6}$) using the relation,

$$f_i = 6.2414 \times 10^{19} \frac{m}{v_i^2} (\frac{dJ}{dE})_i$$

where v_i (unit: m/s) is the ion velocity and m (unit: kg) is the ion mass. Finally, f_i is integrated over all velocities v_i to yield the observed number density (n_{obs}),

$$n_{obs} = \sum_i f_i v_i^2 (\Delta v)_i (\Delta\Omega).$$

Note that n_{obs} does not reflect the full 3-D ion density distribution, but rather a slice of the distribution with size $\Delta\Omega$.

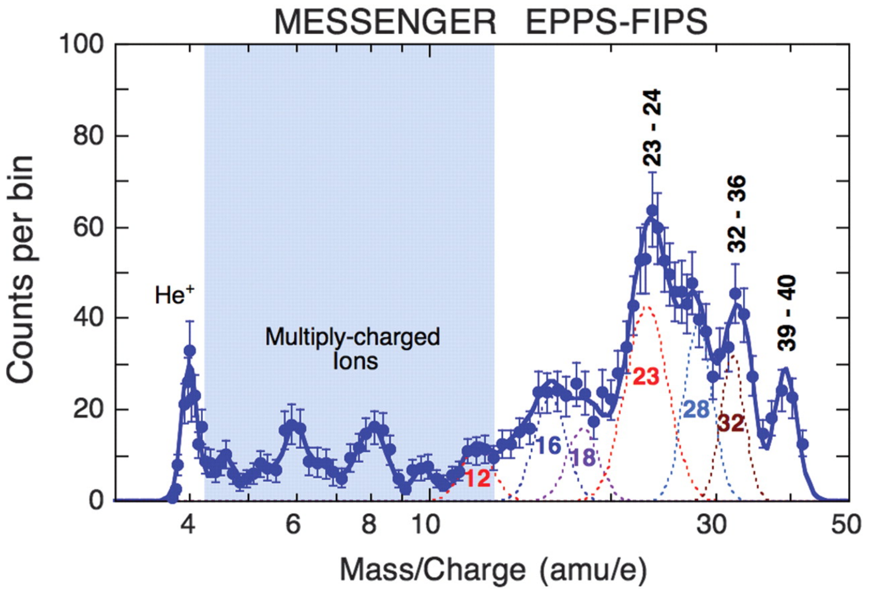

Figure 25: Counts (blue dots) per mass-per-charge ratio (m/q) observed by FIPS during MESSENGER's first Mercury flyby (Zurbuchen et al., 2008). The thick blue curve shows the sum of multiple Gaussian distributions that correspond to different ion species. The dotted curves show example Gaussian distributions for C^+ (m/q=12 amu/e), O^+ and water group ions (m/q = 16-18), Na^+ (m/q=23), Si^+ (m/q=28) and S^+ (m/q=32).

FIPS measurements during the first MESSENGER flyby revealed solar wind ions (i.e. H^+ and He^{2+}) and heavy ions (m/q = 4-40 amu/e) in the whole Mercury environment (see Figure 25; Zurbuchen et al., 2008). FIPS observations of the plasma sheet revealed that the plasma is dominated by H^+ with a density of $1-10\ \text{cm}^{-3}$, temperatures in the range $5-30$ MK and a thermal pressure of ~ 1 nPa. The solar wind ions were enhanced in the magnetosheath while the heavier ions, which are likely sourced from the planet itself, were more abundant in the plasma sheet compared to other regions inside the magnetosphere. Out of the planetary ions the Na^+-group, which includes Na^+, Mg^+ and Si^+, was the most abundant. Because Na is the most abundant species in the neutral exosphere and is easily photo-ionized, the Na^+-group is believed to be dominated by Na^+. The existence of multiply-charged heavy ions have been inferred in the FIPS observations (Zurbuchen et al., 2008).

The spatial distribution of protons in the plasma sheet has been mapped using both FIPS and MAG data with different techniques. The proton density in the plasma sheet is enhanced within a partial "ion ring" on the nightside that is centered on midnight local time and extends from dusk to dawn (Korth et al., 2014). The observations show that heavier ions do not form a complete ion ring distribution around the planet (i.e. a plasmasphere). The proton density is also enhanced near the magnetopause flanks, which indicates plasma transport of magnetosheath protons into the low-latitude boundary layer. Korth et al. (2012) estimated that the plasma pressure exhibits a weak dusk-to-dawn gradient in the magnetotail.

The spatial distribution of the plasma mass density in the plasma sheet can be derived from MAG observations of diamagnetic depressions (Korth et al., 2012). Diamagnetic depressions of the background dipole magnetic field occur in plasma enhancements regions. Here, the plasma thermal pressure is large, so in order to maintain the total pressure balance the magnetic pressure is decreased. Such estimates of the plasma mass density has the advantage that it is blind to the phase space density distribution of the plasma (FIPS limited FOV obstructs $\sim 65\%$ of the incoming plasma), but has the disadvantage of no mass resolution.

FIPS observations between 25 March 2011 and 31 December 2011 during the orbital phase revealed that Na^+-group ($m/q = 21-30$) and O^+-group ($m/q = 16-20$) ions are not uniformly distributed in the magnetosphere. Na^+- and O^+-group ions were in particular observed above the northern cusp and the nightside plasma sheet (Raines et al., 2013; Zurbuchen et al., 2011). He^+, which is mainly sourced from Mercury's He exosphere, revealed a relatively smooth distribution in the magnetosphere compared to the other ions. The ion densities of both protons, He^+, the O^+- and Na^+-group ions are low near the subsolar point compared to the plasma sheet (Raines et al., 2013). The planetary ions contribute up to 15% of the total plasma thermal pressure and 50% of the plasma mass density in the plasma sheet (Gershman et al., 2014).

As shown in Figure 26, the spatial distribution of the heavy ions in the plasma sheet have two enhancements near dawn and dusk. The scale height is different between the two enhancements, the ion density at dawn is limited to low altitudes while the enhancement at dusk shows higher densities far away from the planet ($\sim 1500-6000$ km; Raines et al., 2013). The nightside dusk enhancement may be explained by centrifugal ion acceleration mechanism first described by Delcourt (2013) and Delcourt et al. (2002, 2003). Through this non-adiabatic acceleration process heavy ions are preferentially transported into this altitude range in the dusk-side magnetotail.

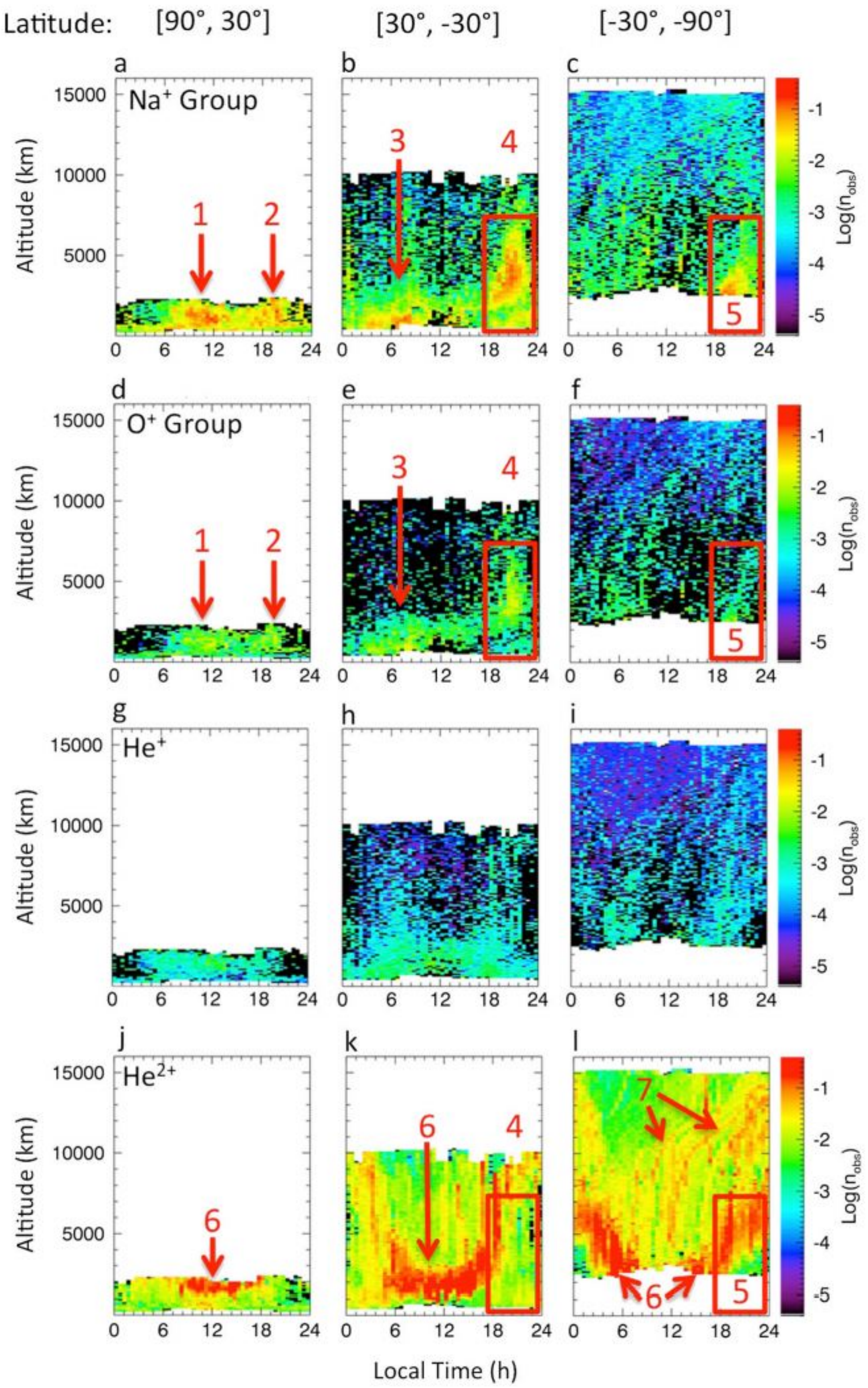

Figure 26: The average (a-c) Na^+-group, (d-f) O^+-group, (g-i) He^+ and (j-l) He^{2+} ion density observed by FIPS (Raines et al., 2013, Figure 3). The FIPS observations were collected between 25 March 2011 to 31 December 2011 and plotted as a function of local time and altitude. The data for each species is categorized into three regions with respect to latitude (north: $[90°, 30°]$, equator: $30°, -30°]$ and south: $-30°, -90°]$). Black points indicate regions were no counts were observed by FIPS and white regions show regions which were not sampled by FIPS due to MESSENGER's elliptical orbit. The red arrows, rectangles and numbers refer to different regions where the ion density is enhanced.

The main two pathways by which heavy ions produced outside the magnetopause can enter the magnetosphere is through the cusps during magnetopause reconnection or at equatorial latitudes during quiet magnetospheric conditions through Kelvin-Helmholtz wave formation (Raines et al., 2015).

The presence of heavy planetary ions in Mercury's magnetosphere cause diamagnetic depressions and has been shown to influence the size of Kelvin-Helmholtz vortices along the nightside magnetopause flanks. Gershman et al. (2015) found that the frequency of K-H waves in the pre-midnight region of the magnetosphere resonates with the Na+ gyrofrequency.

Analogously, a numerical study have shown that the formation of the K-H vortices is enhanced on the dusk flank (and suppressed in the dawn flank) when planetary Na^+ ions are included (Gingell et al., 2015). Another numerical study has shown that Na^+ ions may experience non-adiabatic energization when moving across large-scale K-H vortices (Aizawa et al., 2018).

During the first flyby an ion density enhancement was observed near the northern cusp centered at 12 h local time and 60°N latitude (Zurbuchen et al., 2011). The Na^+ density in the northern cusp is a factor of ~ 2 higher than the He^{2+} density, which may imply a significant Na density in the cusp produced by solar wind ion sputtering (Raines et al., 2013).

Raines et al. (2014) studied the distribution of protons and Na^+ group ions in the northern cusp as a function of pitch angle $\alpha = \tan^{-1}(\sqrt{W_\perp/W_\parallel})$, where $W_\perp$, $W_\parallel$ are the particle energies perpendicular and parallel to the magnetic field. The results showed that the precipitating proton flux ($W_\parallel > 0$) is larger than the flux of upwelling protons from the cusp ($W_\parallel < 0$). This implies significant proton precipitation at the cusps.

The Na^+ group ion population in the cusp has a mean energy of 2.7 keV but ranges between 800 eV up to 13 keV, which is the upper energy limit of the FIPS instrument (Raines et al., 2014). Planetary ions that have been produced locally in the cusp should have much lower energies initially (0.1-10 eV depending on the ejection process), implying that one or several different mechanisms are accelerating the ions to their observed energies. Raines et al. (2014) suggested that Na^+ group ions are accelerated to keV energies in the cusp have been produced from photo-ionized Na atoms beyond the magnetopause that are accelerated anti-sunward by the large-scale plasma convection.

MESSENGER/FIPS detected a ~ 10 minute enhancement of the Na^+-group ion density on 21 December 2013 at an altitude of 5300 km, when FIPS was located in the solar wind. The Na^+-group ion count rate peaked at 1.2 counts s^{-1} during this event, which is to be compared to the mean Na^+-group ion count rate detected by FIPS in the solar wind at < 0.01 counts s^{-1}. Jasinski et al. (2021) determined that the sudden Na^+-group ion enhancement was likely the result of a large meteoroid impact vaporization event, which caused a plume of exospheric Na at high altitudes.

The highest He^+ density observed to date by MESSENGER/FIPS occurred during the transit of a CME (Raines et al., 2018). FIPS first observed a large He^{2+} density enhancement in the northern cusp soon after the impact of the CME shock (> 0.1 cm^{-3}, which is in the top 1% of all cusp observations). This may indicate that the CME was enriched in He^{2+}. The northern cusp was also observed to be particularly large during said MESSENGER orbit, and together with the high He^{2+} flux, this indicates that the surface implantation and neutralization of He^{2+} may have been enhanced. During the following spacecraft orbits the He^+ content gradually increased, and reached a maximum value of ~ 0.1 cm^{-3} 36 hours after the CME shock impact. Raines et al. (2018) suggested that the favorable conditions for enhanced surface implantation of He^{2+} at the beginning of the CME transit caused neutral He to be released into the exosphere with an increased rate, eventually leading to an increased He^+ density due to photo-ionization and charge-exchange. Since MESSENGER/MASCS/UVVS did not study the He exosphere no measurements of the neutral He density were available.

Finally, UVVS detected emission from a single Ca^+ line (393.48 nm) in the low-altitude nightside plasma sheet (1-2 R_M) during the third MESSENGER flyby (Vervack et al., 2010). Two Ca^+ emission lines (393.48 and 396.96 nm) were detected during the orbital phase and the average tangent column density between 200-700 km in altitude could be estimated to $3.1 \cdot 10^7/\text{cm}^2$ (Vervack et al., 2016). A three-standard-deviation upper limit of the Ca^+ column density of $3.9 \cdot 10^6 \text{cm}^2$ at 1630 km altitude was later reported from ground-based observations (Bida and Killen, 2017).

3.4 SUMMARY

In this chapter we have described some key observations of Mercury's exosphere, magnetosphere and ion environment that have been made from the ground and space.

Mercury's exosphere is rich in volatile and refractory neutral species, each characterized by different abundances, scale height, spatial symmetry and temporal variations. Mercury's Na exosphere is especially complex and has a significant seasonal variability. The results from ground-based and spacecraft observations on the short-term temporal variability of the Na exosphere have been divisive. Ground-based telescope observations suggest the existence of high-latitude Na enhancements which change in intensity and latitudinal extent in the matter of minutes to a few hours. MESSENGER/UVVS observations have confirmed the existence of a seasonal Na cycle but did not find evidence for the short time-variations inferred from the ground-based observations.

Mercury has a small but dynamic magnetosphere, with high reconnection rates, large-scale flux tubes and Kelvin-Helmholtz instabilities driving plasma transport at equatorial latitudes. Ions have the special role of acting both as a source and a loss mechanism of the neutral exosphere, and a source of non-adiabatic effects in the magnetosphere. There are also strong indications that planetary Na^+ ions can both suppress and encourage formation of Kelvin-Helmholtz vortices, give rise to field line resonance events and make a significant contribution to the local plasma pressure in some regions. A few mechanisms of ion acceleration has been suggested but not yet been proven by observations.

MESSENGER/FIPS have revealed important information into the abundance and distribution of the three most abundant planetary ions or ion groups in the magnetosphere. The different spatial distribution of He^+ compared to the Na^+- and O+group ions is puzzling. It has been suggested that the He^+ ions are derived from a different source than photo-ionization of the neutral He exosphere, but it is unclear whether this is a viable explanation.

Both the exosphere and the magnetosphere are highly variable with respect to time. One might ask how does this affects the planetary ion distribution inside the magnetosphere? An interesting case is the apparent time-variability of He^+ in response to a CME impact event (Raines et al., 2018), and highlights the coupling between He^{2+} in the solar wind, He in the neutral exosphere and He+.

Models which can describe the global distribution of separate planetary ion species at different energies is necessary to provide context to spacecraft observations. In the following section, we will describe models of the neutral exosphere, magnetosphere and Mercury's environment, ending with LIZE.

4

MODELING OF THE MERCURY ENVIRONMENT

4.1 MERCURY'S EXOSPHERE

The exosphere of a planet, also known as a planetary corona, is defined as the collisionless region of the atmosphere (Chamberlain, 1963; Hunten et al., 1988). The boundary layer that separates the exosphere from the collisional atmosphere is termed the exobase. Mercury has a surface-bounded exosphere, which means that the exobase is located at the surface.

Two types of models have been mainly used to describe Mercury's exosphere: Chamberlain analytical models (first developed for the Earth; Chamberlain, 1963) and stochastic Monte Carlo models (e.g. Chamberlain and Campbell, 1967; Hodges, 1980). We will describe the basic concepts of both models in the following subsection.

4.1.1 *Chamberlain theory*

An often employed theory to describe the composition and temperature of an exosphere is Chamberlain's analytical model (Chamberlain, 1963).

The exosphere density n as a function of radial distance from the center of the planet r is described as

$$n = \zeta n_0 e^{-(U-U_0)/kT_s} \tag{2}$$

where

$$U = -GMm/r. \tag{3}$$

In equations 2 and 3, n_0 is the surface density, U is the gravitational potential energy, m is the particle mass, U_0 is the potential energy at the surface, k is Boltzmann's constant, T is the surface temperature, G is the gravitational constant at the surface and M is the mass of the planetary body. The coefficient ζ is the fraction of the initial isotropic Maxwellian distribution that is actually present at a given altitude. ζ can also be written as

$$\zeta = \zeta_{bal} + \zeta_{sat} + \zeta_{esc}$$

where ζ_{bal} are particles with ballistic orbits, ζ_{sat} are particles which move on so-called "satellite orbits" and finally, ζ_{esc} concerns particles on escaping orbits. Particles on satellite orbits do not intersect the critical level (i.e. the exobase), but are not energetic enough to escape the exosphere.

Chamberlain's theory was originally developed to describe the terrestrial exosphere, which is the upward extension of an atmosphere in approximate thermal equilibrium. In this model, the velocity distribution function is a Maxwellian distribution. The Chamberlain approximation is valid for a spherically symmetric exosphere in which only gravity acts on the particles and includes a single exosphere loss process (i.e. Jeans escape). In this case, ζ_{sat} should be equal to zero. However, as previously discussed for Na in Chapter 3, for some species a significant portion of the population can be accelerated to escape velocities by the solar radiation pressure.

Loss by solar radiation pressure acceleration was later included in Chamberlain's model (Bishop and Chamberlain, 1989). This is done through a modification of equation 3 to reflect the combined loss by gravitational and radiation pressure acceleration,

$$U = -GMm/r + mbr\cos\theta. \tag{4}$$

Here b is the net acceleration by photon pressure ($b = 20 - 200$ cm s^{-2} for Na) and θ is the solar zenith angle, i.e. the angle between the Mercury-Sun line and the local radius vector from the planet center.

At Mercury and the Moon, the surface is the exobase and the exosphere is populated by many components with different velocity distributions. Apart from Jeans escape and acceleration by solar radiation pressure, additional processes like surface adsorption and photo-ionization are also known to deplete Mercury's real exosphere. The Chamberlain model nonetheless provides a simple analytic description of the exosphere where the temperature is generally a free parameter which can differ from the surface temperature. It has been used to analyze the MESSENGER/UVVS Na observations (Cassidy et al., 2016) with surprisingly great success (see Figure 20).

4.1.2 *Monte Carlo models*

Chamberlain's theory relies on the assumption that the particle distribution at the exobase can be well described by a Maxwell-Boltzmann distribution. However, several non-thermal surface ejection processes are likely active in Mercury's exosphere.

Advances in numerical modeling in the last 25 years saw the emergence of test-particle Monte Carlo models and their application to model Mercury's exosphere. This type of model can be used to model several species and particle release processes independently. Several Monte Carlo models have been developed of Mercury's exosphere to describe the generation of the exosphere as well as the relative contribution of different ejection processes (Burger et al., 2010, 2012, 2014; Leblanc and Johnson, 2003; Leblanc and Johnson, 2010; Mura et al., 2009; Wurz and Lammer, 2003).

A set of so-called "test-particles", which each represent a large number of real particles, are ejected at the beginning of the simulation and then followed as they move under the influence of Mercury's gravitational field and the solar radiation pressure. The test-particles are followed until they leave the simulation box, reach escape velocity or collide and stick to the surface. Particles that stick to the surface can be re-ejected by a variety of ejection processes. Each surface ejection process is associated with a probability of ejection. The injection angle and velocity of the re-ejected test-particles is randomized from a velocity distribution specific to the selected surface ejection process. Finally, macroscopic quantities such as the density, velocity, temperature and pressure can be computed on a grid by summing over the test-particles located inside each cell. This type of model necessitates a large number of test-particles and require significant computational resources, and are therefore often parallelized.

4.1.3 *Sources and sinks*

A steady-state exosphere can only be maintained if there are sources and sinks to maintain continuity. This means that the global production and loss rate must be equal for each considered species. Since the exosphere is collisionless by definition, there is no significant interaction between gases of different species.

Mercury's short heliocentric distance gives rise to strong external forcing conditions, including high temperatures, solar irradiance and intense space weathering by solar energetic particles and meteoroids.

Space weathering of the surface by solar wind ions, interplanetary dust and meteoroids partake in "the gardening" of the surface regolith. Gardening acts to overturn the upper crust and expose fresh exospheric material to the external environment. These processes also act to divide the fresh surface grains into smaller components, which increases the available surface for diffusion and different surface ejection processes to act upon.

Sources of exospheric material are balanced by loss processes, which includes Jeans (thermal) escape, ionization and acceleration by the solar radiation pressure to escape velocity.

4.1.4 *Ejection processes*

Particles are released into Mercury's exosphere from the surface by a variety of physical mechanisms. The main surface ejection processes on Mercury are thermal desorption, solar wind ion sputtering, photon-stimulated desorption and meteoroid impact vaporization. Some species like H, He are almost exclusively ejected by thermal desorption, while all the mentioned processes are active for Na. The relative importance of the different ejection mechanisms may also vary depending on the local time, TAA and solar activity level. These different processes are described briefly below.

4.1.4.1 *Thermal desorption*

Exospheric species which are adsorbed to the surface can be desorbed thermally (Hunten and Sprague, 1997, 2002). The rate of thermal desorption (R_{TD}) is given by

$$R_{TD} = \nu_{TD} C e^{(-U/k_B T_S)}$$

where ν_{TD} is the vibrational frequency of the atom, C is the surface concentration, U is the surface binding energy, k_B is Boltzmann's constant and T_S is the surface temperature (Hunten et al., 1988).

Thermally desorbed species are typically assumed to be fully accommodated with the surface and their injection energy (E) is described by a Maxwellian-Boltzmann flux distribution ($f(E, \theta)$) given by,

$$f(E, \theta) = 2 \cos\theta \frac{E}{(k_B T_S)^2} e^{-E/k_b T_S}$$

where θ is the angle of the ejected atom relative to the surface normal.

TD is likely the main channel of ejection of light volatiles such as H and He (Hunten et al., 1988). Thermal desorption of Na has been invoked to explain the dawn-dusk asymmetry in ground-based observations of sodium (Leblanc and Johnson, 2003). The UVVS limb scans have not revealed a Na component with a temperature that matches the dayside surface temperature (Burger et al., 2012; Cassidy et al., 2015).

A possible explanation that has been invoked to explain this observation is that the surface binding energy may increases in response to continuous bombardment of energetic solar wind ions. Madey et al. (1998) found from laboratory studies that Na atoms released by TD from a substrate that has been exposed to bombardment of 1 keV He^+ ions tends to have a much higher temperature (1000 K). On the other hand it has been suggested that TD depletes the concentration of the adsorbed species from the surface layers of the regolith grains (Hunten and Sprague, 1997, 2002).

4.1.4.2 *Photon- and electron-stimulated desorption*

Photon-stimulated desorption (PSD) is an important surface ejection process for volatile elements and is considered to be one of the dominant ejection mechanisms of Na and K (Killen et al., 2001; Leblanc and Johnson, 2010; McGrath et al., 1986). PSD and the related process of electron-stimulated desorption (ESD) have been studied in laboratory experiments (Madey et al., 1998; Yakshinskiy and Madey, 1999; Yakshinskiy and Madey, 2005).

PSD produces higher temperature ejecta than TD, but less energetic than that produced by solar wind ion sputtering. Both PSD and ESD produce particles with an energy that can be approximated by the Sigmund-Thompson-type distribution $f(E)$, which has a core distribution reminiscent of a Maxwellian distribution with a high-energy tail (Johnson et al., 2002; Killen et al., 1999; Mura, 2012),

$$f(E) = \beta(1+\beta)\frac{EU^{\beta}}{(E+U)^{2+\beta}}$$

where U is a characteristic energy related to the binding energy and β is a free parameter (Burger et al., 2010).

4.1.4.3 *Solar wind ion sputtering*

Neutral atoms (and ions) can also be released from the surface as a result of direct interaction between the solar wind ions and regolith. Momentum carried by the impacting solar wind ions is directly transferred in an elastic collision, which can instigate a collision cascade (Johnson, 1994).

Solar wind ion sputtering (SWS) releases neutrals at high temperatures, which can reach several thousand kelvin. The SWS efficiency depends on the flux of the impacting ion and the surface concentration of the target species.

Wiens et al. (1997) estimated that the velocity distribution of Na atoms desorbed through ion sputtering would have a mean velocity of about 1.4 km/s, which is roughly comparable to 2700 K.

4.1.4.4 *Meteoroid impact vaporization*

Interplanetary dust and small meteoroids play a role in sustaining Mercury's exosphere by impacting the surface and releasing volatiles in the process. The release either occurs by vaporization of the bound surface atoms or through dissociation of molecules which have been released in the aforementioned vaporization. Entire meteoroid grains can also be vaporized and thereby contribute to the composition of the exosphere.

Fits of UVVS limb scans of Mg and Ca to Chamberlain models yield high surface temperature which are most consistent with meteoroid impact vaporization as the main source process.

The modeled Ca and Mg source rates (Burger et al., 2014; Merkel et al., 2017) have a seasonal variability that matches the predicted variation of the meteoroid impact flux with heliocentric distance (Killen and Hahn, 2015; Pokorný et al., 2018). Both the Ca and Mg emission exhibit a strong dawn-dusk asymmetry, which correlates with the dawn-dusk asymmetry of the meteoroid impact flux. This is because the dawn terminator faces the direction of the planet's motion around the Sun. Although meteoroid vaporization is the only ejection mechanism which is active over the whole surface of the planet, (Pokorný et al., 2017, 2018) showed that it is concentrated to a very limited part of the surface during large portions of the orbit.

At aphelion the impact flux is relatively evenly distributed over the surface while at other times along the orbit the impact surface can be very localized and the dawn/dusk-impact ratio may vary significantly (Pokorný et al., 2017, 2018).

Small meteoroids with a diameter between $10^{-6} - 10^{-3}$ m (Cremonese et al., 2005) is expected to impact Mercury so often that it can sustain an exosphere. However, meteoroid populations with large impact velocities may be more important for the total meteoroid vaporization flux than the populations responsible for the largest flux of meteoritic material to Mercury.

Rare impacts of large meteoroids (> 1 m in diameter) may be responsible for transient enhancements in the exosphere density (Mangano et al., 2007). Impact vaporization is an almost stoichiometric process, which means that all existing species are vaporized upon impact regardless of whether they are volatile or refractory. Large impact events could enable detection of rarer exosphere species such Si, which is expected to exist both in the surface and the exosphere but has not yet been detected by space- or ground-based telescope observations.

Such an enhancement was observed by FIPS (Jasinski et al., 2020). The ions were estimated to come from a neutral plume of impact vaporized surface material caused by 1 m sized meteoroid. The neutrals were then photo-ionized and became pick-up ions, which were then observed by FIPS. The pick-up ions were measured to be within a mass-per-charge ratio of 21-30 amu/e. which includes Na^+, Mg^+, $Al^+$and Si^+. Due to the long and short photo-ionization lifetimes of Mg and Al respectively, the main constituents of the plume were deemed to be Na and Si.

4.1.5 *Surface-exosphere interaction*

The energy exchange between atoms in the exosphere and the surface has been classically described with the accommodation coefficient α (Hunten et al., 1988) defined by

$$\alpha = \frac{E_{eje} - E_{imp}}{E_{th} - E_{imp}}$$

where E_{imp} is the mean energy of the atoms in the exosphere that impact the surface, E_{eje} is the mean energy of atoms which are ejected from the surface and E_{th} is the energy of atoms in thermal equilibrium with the surface (Grava et al., 2021; Leblanc and Chaufray, 2011; Shemansky and Broadfoot, 1977).

If $\alpha = 1$, particles that are ejected from the surface are on average fully thermally accommodated to the surface. This can be understood as the surface being fully saturated with atoms of the given species. Indeed, in that case, each surface impact is followed by the release of a previously adsorbed atom. Since the surface is already saturated, no actual net particle adsorption occurs in the regolith. This also means that the surface temperature fully determines the distribution of the exosphere. Atoms which are released from the hotter dayside surface will make longer ballistic "hops" than atoms which are released from the cold nightside surface. This will cause a net transport of exosphere atoms toward the day-night terminator, and the exosphere will become denser on the nightside compared to the dayside. This was initially believed to be the case for the Moon's and Mercury's He exospheres (Hodges, 1980).

Following the Mariner 10 observations of Mercury's He exosphere however, it was shown that a partial energy accommodation with the surface provided a better fit (Shemansky, 1980; Shemansky and Broadfoot, 1977; Smith et al., 1978). Leblanc and Chaufray (2011) showed that both the Moon and Mercury's He exospheres are best described by different thermal accommodation factors on the day- and nightside. Theoretical modeling work has demonstrated that the energy exchange in gas-surface collisions is limited by the Debye temperature of the surface (Kunc and Shemansky, 1981; Kunc and Shemansky, 1985). The value of the accommodation factor therefore does not only depend on the energy exchange during a single encounter, but is also related to the average number of collisions that the particle makes with the surface. The accommodation factor is also related to the residence time of adsorbed particles in the surface (e.g. Leblanc and Chaufray, 2011).

The rate of thermal accommodation is not the only process which affects the gas-surface interaction on Mercury. The nature of bond with the surface (i.e. chemisorption or physisorption) and availability of bond sites affect both the sticking probability and residence time in the surface (Domingue et al., 2007; Killen et al., 2018). The porosity of the surface, micro- and macroscopic irregularities produced by space weathering, the regolith grain size and lattice defects likely affects the thermal accommodation as well as the efficiency of the surface ejection processes listed above (Killen et al., 2018; Sarantos and Tsavachidis, 2020).

4.2 MERCURY'S MAGNETOSPHERE

The models that been used to model Mercury's magnetosphere can be divided into three categories: analytic (Delcourt et al., 2002; Ip, 1997; Killen et al., 2001; Korth et al., 2004; Luhmann et al., 1998; Lukyanov et al., 2001; Massetti et al., 2003; Sarantos et al., 2001), magnetohydrodynamic (MHD; Benna et al., 2010; Ip and Kopp, 2004; Ip and Kopp, 2002; Jia et al., 2015; Kabin et al., 2000, 2008; Zurbuchen et al., 2004) and hybrid models (Kallio and Janhunen, 2003, 2004; Modolo et al., 2018; Müller et al., 2012; Trávníček et al., 2010; Trávníček et al., 2007; Wang et al., 2010). The models have been used to provide context for the in-situ magnetic field and plasma measurements made by Mariner 10 and MESSENGER (see Section 3), to investigate the role of the solar wind and planetary ions for the global structure of the magnetosphere and plasma dynamics.

4.2.1 *Analytical models*

The very first models of Mercury's magnetosphere were typically obtained by scaling down pre-existing, analytical models of the Earth's geomagnetic field to fit the Mariner 10 magnetic field observations (Delcourt et al., 2002; Ip, 1997; Killen et al., 2001; Korth et al., 2004; Luhmann et al., 1998; Lukyanov et al., 2001; Massetti et al., 2003; Sarantos et al., 2001). These models do not account for the radial component (B_x) of the IMF, which dominates the external magnetic field environment at Mercury (Korth et al., 2004). The analytical models do not either account for variations of the magnetospheric boundaries due to changing solar wind conditions or magnetospheric dynamics (Korth et al., 2004; Lukyanov et al., 2001).

4.2.2 *Magnetohydrodynamic models*

The second type of models that characterized the large-scale structure of Mercury's magnetosphere were based on ideal magnetohydrodynamic (MHD) theory (Gombosi et al., 2000; Ip and Kopp, 2002; Kabin et al., 2000). Ideal MHD solves for the conservation of mass, momentum, energy and Faraday's law in order to give the particle density, bulk velocity and thermal pressure on a given grid. In conservative form, the dimensionless single-fluid ideal MHD equations reads as

$$\frac{\partial}{\partial t}\begin{pmatrix}\rho\\ \rho\mathbf{u}\\ \mathbf{B}\\ E\end{pmatrix}+\nabla\cdot\begin{pmatrix}\rho\mathbf{u}\\ \rho\mathbf{u}\mathbf{u}+p^{*}\mathbf{I}-\mathbf{B}\mathbf{B}\\ \mathbf{u}\mathbf{B}-\mathbf{B}\mathbf{u}\\ \mathbf{u}(E+p^{*})-\mathbf{B}(\mathbf{B}\cdot\mathbf{u})\end{pmatrix}=0 \tag{5}$$

where ρ is the mass density of the plasma, $\mathbf{u}$ is the velocity, p is the pressure, $\mathbf{B}$ is the magnetic field, $p^{*}=p+B^2/2$, $E=\rho u^2/2+p/(\gamma-1)+B^2/2$ is the total energy (kinetic, thermal and magnetic) where γ is the polytropic index and $\mathbf{I}$ is the unit 3×3 matrix. Only steady-state is considered, meaning that that induction in the conductive mantle of the planet and magnetospheric reconfiguration currents are neglected. Ideal MHD also does not account for multi-species plasma interaction, such as that between electrons, protons and other solar wind ions.

Multi-fluid or Hall MHD models have also been applied to describe Mercury's magnetosphere (Benna et al., 2010). In Hall MHD, the mass, momentum and pressure conservation equations for a set of ions s are

$$\frac{\partial \rho_s}{\partial t} + \nabla \cdot (\rho_s \mathbf{v_s}) = 0$$

$$\frac{\partial}{\partial t}(\rho_s \mathbf{v_s}) + \nabla(\rho_s \mathbf{v_s v_s} + p_s \mathbf{I}) = \rho_s \mathbf{g} + n_s q_s (\mathbf{E} + \mathbf{v_s} \times \mathbf{B})$$

$$\frac{\partial p_s}{\partial t} + \nabla \cdot (p_s \mathbf{v_s}) + (\gamma - 1) p_s \nabla \cdot \mathbf{v_s} = 0$$

where ρ_s and n_s are the mass and number density, $\mathbf{v_s}$ is the bulk velocity, p_s is the pressure, q_s is the electric charge of the ion species s, $\mathbf{E}$ and $\mathbf{B}$ are the local magnetic and electric fields and $\mathbf{g}$ is the local gravitational acceleration. The electrons are assumed to be a highly mobile and charge-neutralizing species in the presence of an electric current $\mathbf{J}$. The corresponding equations for electron dynamics are as follows,

$$n_e = \sum_s n_s$$

$$\mathbf{v_e} = \sum_s \frac{q_s n_s}{e n_s} \mathbf{v_s} - \frac{\mathbf{J}}{e n_e}$$

$$\frac{\partial p_e}{\partial t} + \nabla \cdot (p_e \mathbf{v_e}) + (\gamma - 1) p_e \nabla \cdot \mathbf{v_e} = 0$$

where n_e is the electron number density, $\mathbf{v_e}$ is the electron drift velocity, p_e is the electron pressure and e is the electron charge.

Because the Alfvén speed of the plasma is non-relativistic, the displacement current can be neglected and Ampère's law is written

$$\mathbf{J} = \frac{\nabla \times \mathbf{B}}{\mu_0}$$

where μ_0 is the magnetic permeability of free space. The magnetic field is governed by Faraday's law

$$\frac{\partial \mathbf{B}}{\partial t} = -\nabla \times \mathbf{E}.$$

The generalized Ohm's law can be written as

$$\mathbf{E} = -\frac{\nabla p_e}{e n_e} - \sum_s \frac{n_i}{n_e}(\mathbf{v_s} \times \mathbf{B}) + \frac{\mathbf{J} \times \mathbf{B}}{e n_e}$$

This formulation of Ohm's law expands the ideal Ohm's law used in ideal MHD to include the electron pressure gradient and the Hall term. The Hall term is necessary to achieve fast reconnection rates

(Birn et al., 2001) and the electron pressure gradient is important to drive field-aligned currents.

Hall MHD does not account for non-Maxwellian ion distributions. Finite gyroradius effects also restrict the use of MHD models. The gyroradius of a solar wind proton is less than 1% of Mercury's radius, which means that MHD theory can be freely applied to model solar wind protons. This is however not necessarily the case for the magnetospheric plasma at Mercury, which has a significant heavy ion component (i.e. Na^+).

4.2.3 *Hybrid models*

Hybrid models have been used to describe finite gyroradius effects and its impact on plasma dynamics (Kallio and Janhunen, 2003, 2004; Trávníček et al., 2007).

The Lorentz force acts on the ions

$$\frac{d\mathbf{x_i}}{dt} = \mathbf{v_i}$$

$$m_i \frac{d\mathbf{v_i}}{dt} = q_i(\mathbf{E} + \mathbf{v_i} \times \mathbf{B})$$

where m_i is the mass, $\mathbf{x_i}$ the position, q_i the charge and $\mathbf{v_i}$ the velocity of an ion of species i, $\mathbf{B}$ and $\mathbf{E}$ is the electric and magnetic fields.

The magnetic field is calculated from the Maxwell-Faraday induction equation:

$$\frac{\partial \mathbf{B}}{\partial t} = -\nabla \times \mathbf{E}$$

In hybrid models the ions are modelled as macro-particles, akin to cubic or spherical "clouds" with a homogeneous charge density and has the volume of a single grid cell. When the macro-particles changes position, they contribute to the mass density of all cells that it overlaps. The ion density n_i and ion bulk velocity $\mathbf{U_i}$ in a grid cell with position $\mathbf{r_k}$ is therefore given by

$$n_i(\mathbf{r_k}) = \frac{\sum_j \Delta w_i^j(\mathbf{r_k})}{\Delta V}$$

$$U_i(\mathbf{r_k}) = \frac{\sum_j \Delta w_i^j(\mathbf{r_k})\mathbf{v_i^j}}{\sum_j \Delta w_i^j(\mathbf{r_k})}$$

where j is all the macro-particles of species i which overlap the grid cell and ΔV is the volume of the grid cell.

In hybrid models a technique is often used which joins and splits macro-particles so that a certain number of (for example 10-20; Kallio and Janhunen, 2003) macro-particles per grid cell stays constant. This, and other techniques, are necessary to improve the performance of the computationally demanding hybrid models.

Quasi-neutrality of the electric charge is a valid assumption on spatial scales $L > \lambda_D \equiv \sqrt{\epsilon_0 k_B T/(n_e e^2)}$ where λ_D is the plasma Debye length. The mass-less electron fluid assumption means that electron particle effects are neglected as well as waves and instabilities which depend on the electron inertia.

The time step dt of the simulation is determined by the Courant-Friedrich-Levy (CFL) condition,

$$\frac{dx}{dt} \geqslant c_{max}$$

where dx is the grid cell size and c_{max} is the "maximum speed of information", i.e. the particle speed. Typically, a time step of $dt = 0.01$ s is sufficient to obtain a stable solution for a grid with a cell size of a few hundred km.

Recently, a cross-comparison was made between two MHD and two hybrid simulations of Mercury's magnetosphere for two example solar wind conditions (Aizawa et al., 2021). The models produced qualitatively similar results, including similar bow shock and the magnetopause positions. Both MHD and hybrid models commonly make use of adaptive mesh refinement to provide high spatial resolution near the surface, the magnetospheric boundaries and the magnetotail current sheet, and low resolution in the undisturbed solar wind. This is often a necessary approach to lighten the computational load of these types of models.

4.3 MERCURY'S IONIZED EXOSPHERE

Following the discovery of Mercury's Na exosphere Ip (1986) predicted that future in-situ measurements at Mercury would reveal the existence of heavy ions such as Na^+, Al^+, Fe^+, Ca^+ with their origin in Mercury's exosphere and surface.

Planetary ions can form through a variety of processes, including but not limited to photo-ionization, electron-impact excitation and charge-exchange. On Mercury these ions are mainly formed through photo-ionization of the exosphere and direct interaction processes with the surface regolith (Killen et al., 2007). Mura et al. (2005) estimated that less than 1% of the solar wind plasma inside Mercury's magnetosphere undergoes charge-exchange with exospheric neutrals. Photo-ionization, on the other hand, is responsible for upward of 50% of the loss of the exosphere and typically dominates over Jeans escape. Solar wind ion sputtering events can also lead to the ejection of positive or negative ions, but the probability is typically very small (Killen et al., 2007). The photo-ionization rate have been estimated for most species in Mercury's exosphere based on a combination of experimental laboratory studies and analytical modeling (see Table 3; Huebner et al., 1992; Huebner and Mukherjee, 2015).

Table 3: Photo-ionization loss rates and photo-ionization thresholds for different species calculated at Earth ($r = 1$ AU) and for quiet solar conditions (Huebner and Mukherjee, 2015).

Species	Photo-ionization rate [s^{-1}]	Photo-ionization threshold [nm]
Hydrogen	$7.30 \cdot 10^{-8}$	91.2
Helium	$5.64 \cdot 10^{-8}$	50.4
Carbon (^{3}P)	$5.63 \cdot 10^{-7}$	110
Oxygen (^{3}P)	$2.44 \cdot 10^{-7}$	91.0
Sodium	$7.26 \cdot 10^{-6}$	241
Magnesium	$6.49 \cdot 10^{-7}$	162
Aluminum	$1.20 \cdot 10^{-3}$	207
Silicon	$2.29 \cdot 10^{-5}$	152
Sulfur (^{3}P)	$1.37 \cdot 10^{-6}$	120
Potassium	$2.70 \cdot 10^{-5}$	286
Calcium	$3.05 \cdot 10^{-4}$	203
Iron	$8.20 \cdot 10^{-6}$	157

The photo-ionization rate is strongly dependent on the magnitude of the solar photon flux, which in turn is a function of the heliocentric distance. Therefore, for application to Mercury's exosphere it is necessary to scale the photo-ionization rates (τ_{Earth}) listed in Table 3 to Mercury's heliocentric distance (r_{Mercury}),

$$\tau_{\mathrm{Mercury}} = \tau_{\mathrm{Earth}} \cdot \left(\frac{1 \text{ AU}}{r_{\mathrm{Mercury}} \text{ [in AU]}} \right)^2 .$$

The solar photon flux also depends on the solar activity, which varies on both short (solar flares) and long (solar cycle) timescales. The values listed in Table 3 refer to the solar cycle minimum, but can be up to 50% higher at the solar cycle maximum (Huebner and Mukherjee, 2015).

4.3.1 *Models of Na$^+$ in Mercury's magnetosphere*

Monte Carlo test-particle models are also commonly used to model the distribution of planetary ions in the magnetosphere, where each test-particle represents a large number of real planetary ions. There exists a number of studies in which ion drift paths have been traced using such test-particle models (Delcourt et al., 2003; Leblanc et al., 2003; Paral et al., 2010; Sarantos and Slavin, 2009; Seki et al., 2013; Yagi et al., 2010, 2017).

The motion of planetary ions are, in contrast to neutral atoms which are mainly affected by gravity and the solar radiation pressure, only governed by the surrounding magnetic and electric fields. The path of the ions are determined by the Lorentz force,

$$\mathbf{F} = -q(\mathbf{E} + \mathbf{v} \times \mathbf{B}).$$

To compute the Lorentz force, the test-particle models typically use a static magnetic and electric field description from analytical (Delcourt et al., 2003; Leblanc et al., 2003), MHD (Sarantos and Slavin, 2009; Seki et al., 2013; Yagi et al., 2010, 2017), and hybrid (Paral et al., 2010) models of Mercury's magnetosphere.

The ion density distribution is determined by assigning weights to the test-particles which correspond to the local ion production rate. The ion production rate depends on the neutral density, which is estimated using a neutral model (Gamborino et al., 2019; Leblanc and Johnson, 2003; Mura et al., 2007) of the exosphere and the photoionization rate. Most of these studies have focused on the distribution of Na^+, which likely is the most common planetary ion species at Mercury (Raines et al., 2013).

Delcourt et al. (2002, 2003, 2012) studied test-particle trajectories of Na^+ ions using an analytical model of the Earth's magnetosphere (Luhmann and Friesen, 1979) scaled down to fit the Mariner 10 magnetometer measurements of Mercury's magnetic moment (Whang, 1977). Due to the small scale of Mercury's magnetosphere compared to Earth, the $\mathbf{E} \times \mathbf{B}$-drift paths are highly curved. This may cause ions that are formed near the cusps to experience strong centrifugal acceleration toward the nightside plasma sheet. Once located in the plasma sheet, the ions then drift toward the dusk flank magnetopause or return to the planet via Speiser-type orbits (Speiser, 1965). Since this process does not depend on the mass of the ion, it may be responsible for the enhancement of Na^+- and O^+-group ions in the pre-midnight plasma sheet as observed by MESSENGER/FIPS (Delcourt, 2013; Raines et al., 2013). The cyan part of the blue-cyan Na^+ trajectory in Figure 27 resembles the test-particle trajectories in Delcourt et al. (2003, Figure 2). The blue test-ion is launched near the north pole (see Figure 27a) and spends several minutes very close to the surface, where it gradually increases in energy to ~ 1 keV (see Figure 27b). Approximately ~ 4 minutes after its injection, the test-ion energy increases to ~ 10 keV and quickly moves toward lower latitudes and the dusk magnetotail. Both the evolution of the ion energy and the normalized magnetic moment (see Figure 27d) between $t = 3 - 5$ minutes is very similar to the red, green and blue curves in Delcourt et al. (2003, Figure 2).

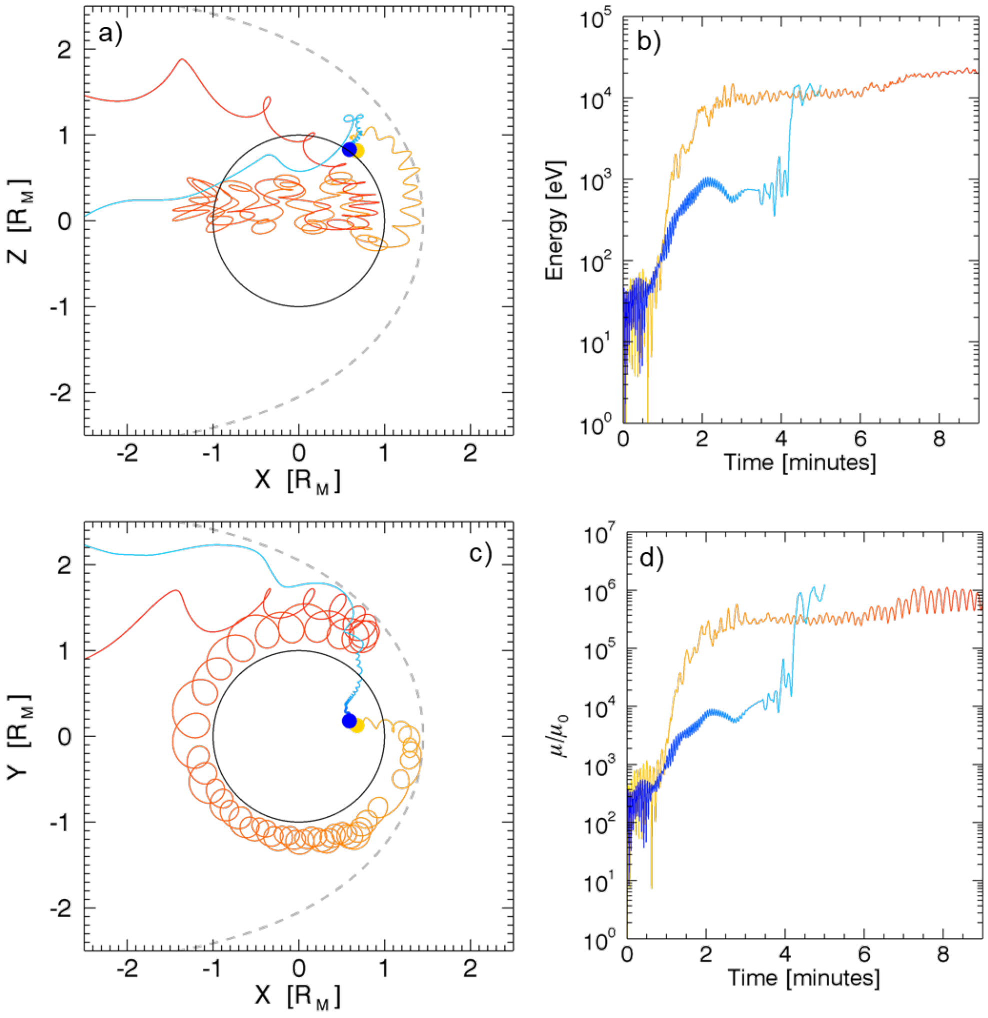

Figure 27: Model test-particle trajectories of Na^+ ions from the Latmos IoniZed Exosphere model (see section 4.3.2). Two test-particle trajectories are shown in the a) MSO XZ- and c) XY-plane on the left, and the time-evolution of the b) ion energy and the d) normalized magnetic moment are shown on the right. The dashed curve shows the location of Mercury's magnetopause. The test-particles are launched near the north pole (blue and yellow dots). The electromagnetic field environment is different between the two test-particle trajectories. The solar wind IMF is strictly northward ($B_z > 0$) in the first case (yellow-red trajectory, the "nominal" case in Chapter 5) and southward for the second test-particle (blue-cyan, "Case 2" in Chapter 5).

Leblanc et al. (2003) studied the ion density distribution of Na^+ and the effect of magnetospheric sputtering on the Na exosphere using the EGM (Leblanc et al., 2003) and the same magnetospheric model as Delcourt et al. (2002, 2003). The authors determined a peak Na^+ density of $\sim 10^2$ Na^+/cm^3 in the morning sector on the dayside. Leblanc et al. (2003) found no apparent effect of the Na^+ sputtering on the neutral Na density distribution in the exosphere due to the small fraction of Na^+ that impact the surface ($\sim$ 15%).

Sarantos and Slavin (2009) investigated the distribution of Na^+ pick-up ions in the magnetosphere. The authors used an exospheric model developed by Mura et al. (2005) and a MHD simulation of Mercury's magnetosphere for solar wind and IMF conditions similar to the first MESSENGER flyby (n=20 cm-3, v= 400 km/s, IMF = -12,12,5 nT) (Benna et al., 2010). Sarantos and Slavin (2009) found a high concentration of Na^+ in the pre-evening sector on the dayside and at dusk. Considering that the solar wind electric field points toward dawn for the given IMF configuration, Sarantos and Slavin (2009) expected to see an enhancement at dawn for southward IMF. They found that the pick-up ions had energies between $\sim 10 - 100$ keV.

Yagi et al. (2010) conducted a statistical study of Na^+ ion trajectories in a MHD model of Mercury's magnetosphere to study the density and pressure distribution of the ion species. The authors found that a ring distribution of high-energy ($E = 1 - 5$ keV) Na^+ can form during northward IMF conditions ($(B_x, B_y, B_z) = (0, 0, 10)$ nT) and nominal solar wind conditions ($n = 35$ cm^{-3}, $v = 400$ km/s). Under these conditions, the Na^+ density is highest in the morning sector ($\sim 10^2$ cm^{-3}) and the Na^+ ion pressure is on the same order as the proton pressure. For higher solar wind ram pressure, the Na^+ density and pressure enhancement is limited to a small region between noon and the dawn terminator. The yellow-red Na^+ test-particle trajectory in Figure 27 resembles the test-particle trajectories in Yagi et al. (2010, Figure 10). The ion is launched at near the north pole (see Figure 27a), follows a magnetic field line toward lower latitudes and then starts to oscillate in the closed field-line region near the equatorial plane (see Figure 27c). The ion energy (see Figure 27b) increases from < 100 eV to ~ 10 keV as it approaches the magnetopause and encounters the strong electric fields near the magnetosheath. The normalized magnetic moment of the test-ion (see Figure 27d) experiences a similar sudden increase as the ion energy during this time period. The ion energy then stays relatively constant as the test-ion drifts dusk-ward in the closed field-line region. Approximately 11 minutes after its injection into the magnetosphere, the test-ion once again encounters the magnetopause (this time on the dusk-side flank) and the strong electric field in its vicinity, and is reflected back toward the magnetotail where it escapes the magnetosphere.

Paral et al. (2010) studied the Na^+ distribution using (Trávníček et al., 2007)'s hybrid model and two sets of IMF and solar wind conditions similar to those during MESSENGER's first and second flyby. The authors found a Na^+ density enhancement located in the predawn region for northward IMF, and that the magnetopause behaved as a more "porous" boundary for southward IMF conditions. The porous boundary allowed Na^+ ions in the simulation to pass from the dayside magnetosphere into the magnetosheath, creating high Na^+ densities (0.1 cm^{-3}) just upstream of the magnetopause. Sarantos and Slavin (2009) also found that Na^+ pickup ions were able to penetrate through the magnetopause boundary, forming an enhancement in the dusk sector of the day- and nightside magnetosphere for northward IMF. Yagi et al. (2010) determined that 1-4 keV Na^+ pick-up ions in the upstream magnetosheath can penetrate the magnetopause and populate the pre-dawn sector even for northward IMF conditions, particularly when the solar wind dynamic pressure is high. Paral et al. (2010) found that the Na^+ ions have a mean energy of 3 keV near closest approach near midnight in the near magnetotail. Ions with energies upward of 10 keV were also found at dawn for northward IMf and in the whole dayside, dusk sector and upstream of the magnetopause for southward IMF.

Seki et al. (2013) found that the conductivity also plays a role in the distribution of the Na^+ ions in the magnetosphere. When a low conductivity surface condition was used together with southward IMF, the ion density distribution showed an ion density enhancement in the predawn sector, similar to Yagi et al. (2010, 2017). For high surface conductivity, the density enhancement region extends far into the nightside plasma sheet ($> 1 - 10$ cm^{-3} up to 1 R_M from the nightside surface). For strong southward IMF ($B_z = -30$ nT), the Na^+ density was less than < 1 cm^{-3} in the whole magnetosphere, likely due to the strong convective field. In all cases, there was a significant Na^+ density dawn-dusk asymmetry toward dawn on the dayside, and toward dusk on the nightside.

There exists hybrid models of Mercury's magnetosphere which treat planetary ions self-consistently (Egan et al., 2019; Exner et al., 2020). Like the solar wind ions, the planetary ions are described as macro-particles, which represent a group of ions with the same macro properties (i.e. position, velocity, mass and charge). The caveat of these models is that the number of test-particles that represent planetary ions is not sufficient to reproduce the observed spatial distribution, with ion density enhancements both at north pole and in the plasma sheet (Raines et al., 2013).

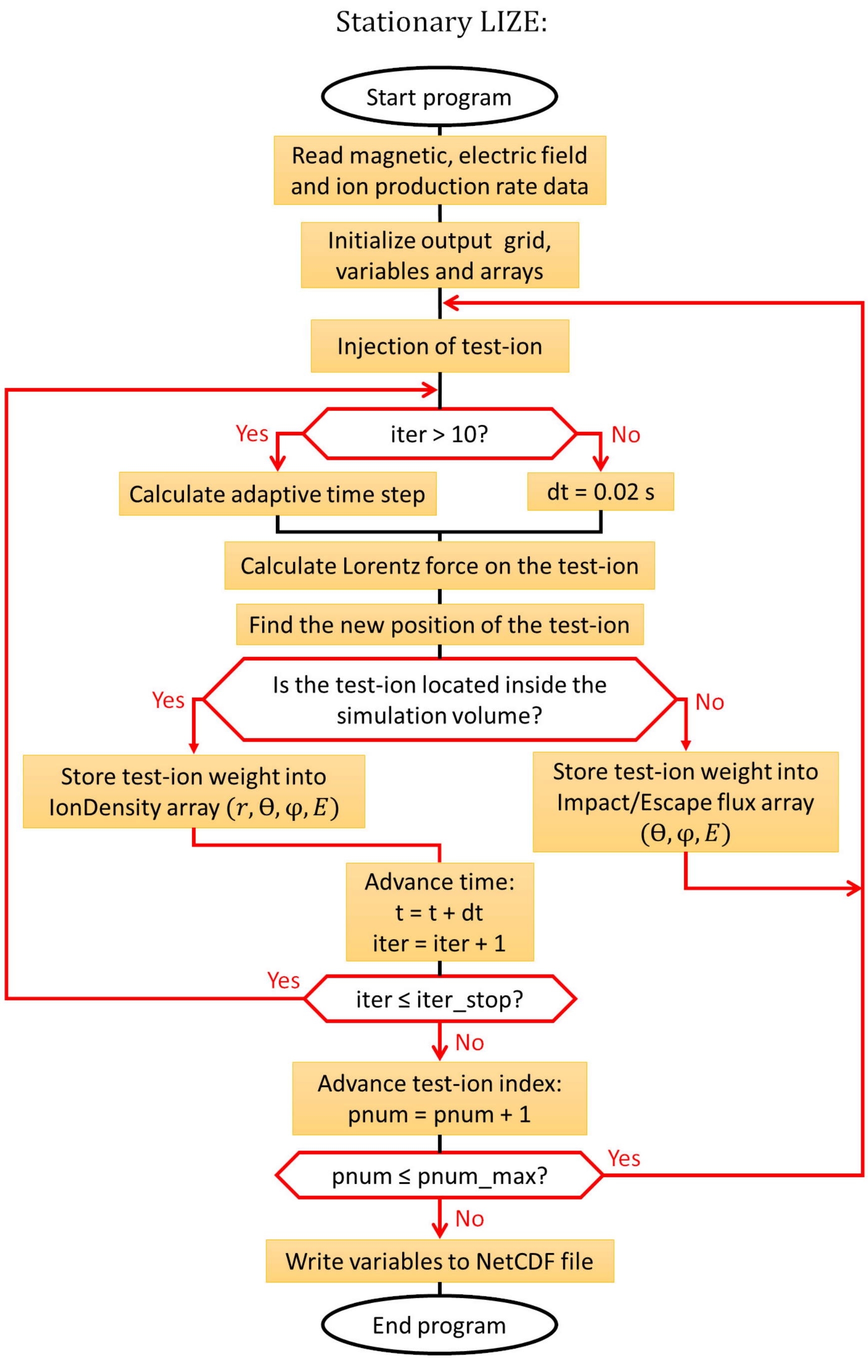

Figure 28: Flowchart of the stationary version of the LIZE model. When 10 iterations have been reached, the model switches from a constant (0.02 s) to an adaptive time step (dt). When the particle has escaped the simulation box or the maximum number of iterations ($iter\_stop$) has been reached, a new test-ion with index $pnum$ is injected. This process is repeated until $pnum\_max$ particles have been reached, after which the output files are produced and the program is completed.

4.3.2 *Latmos IoniZed Exosphere model*

Latmos IoniZed Exosphere (LIZE) model is a test-particle model which can be used to estimate the 3-D ion density distribution of planetary ions in Mercury's magnetosphere.

Each test-particle (or test-ion) represents a large number of planetary ions. This number is the "weight" of the test-ion, determined by the photo-ionization rate of the neutral exosphere. We use the EGM to provide the neutral density. The test-ions are launched from the sunlit portion of Mercury's exosphere and then followed as they move in and outside the magnetosphere under the influence of the Lorentz force.

See Figure 28 for a flowchart which describes the code that makes up the LIZE model. The LIZE code is written in Fortran 90, parallelized using Open MPI and runs on the CICLAD (Calcul Intensif pour le Climat, l'Atmosphère et la Dynamique) data cluster. The model output is given as NetCDF (Network Common Data Form) files.

At the beginning of the LIZE simulation, 100 test-ions are injected into the simulation volume from each cell on the EGM spherical output grid that has a non-zero ion production rate. The test-ions have a weight w_i defined by

$$w_i = \frac{\mathtt{IonProd}_i}{n\Delta V_i}\ [\mathrm{s}^{-1}\mathrm{cm}^{-3}]$$

where $\mathtt{IonProd}_i$ is the ion production rate inside the cell with index i (unit: s^{-1}), n is the number of test-ion produced in the cell and ΔV_i is the volume of cell i. As the simulation progresses, the test-ions will contribute to the ion density computed on the LIZE output grid. The ion density in a cell with index i is determined by,

$$\mathtt{IonDensity}_i = \mathrm{dt}\sum_{j=1}^{N_1}\sum_{k=1}^{N_2} k \cdot w_j$$

where N_1 is the number of test-ions j with weight w_j that passes through cell i, N_2 is the number of iterations that test-ion j spends inside cell i and dt is the time step. The number of injected test-ions per cell ($n = 100$) is a compromise between accuracy and simulation speed. When we compared two simulation runs with identical parameters except for the choice of injected test-particles per cell (10 and 100), we found that the derived ion density in each cell varies with less than 10%.. The IonDensity variable is a 4-D array in the LIZE model (r, θ, ϕ, E), which means that both the 3-D spatial (r, θ, ϕ) and kinetic energy distribution of the ion density can be analyzed.

The Lorentz force is determined by the local magnetic and electric fields. We use a steady-state solution of the global magnetic and electric field computed with LatHyS (Modolo et al., 2016). The model has also been tested with magnetic and electric fields from AIKEF (Müller et al., 2012) and produces similar results regardless of which magnetospheric model is used (see Chapter 5).

The test ions are launched with a zero initial velocity and are quickly accelerated by the electromagnetic fields. The Lorentz equation of motion is solved numerically in the LIZE model,

$$\frac{d\mathbf{v}}{dt} = \frac{q}{m}\left(\mathbf{E} + \mathbf{v} \times \mathbf{B}\right), \quad \mathbf{v}(t_0) = 0$$

with the explicit second-order Runge-Kutta method,

$$\mathbf{v}_{n+1} = \mathbf{v}_n + dt \cdot \left(\frac{q}{m}\right)\left(\mathbf{E} + \mathbf{v}' \times \mathbf{B}\right)$$

where

$$\mathbf{v}' = \mathbf{v}_n + \frac{dt}{2} \cdot \left(\frac{q}{m}\right)\left(\mathbf{E} + \mathbf{v}_n \times \mathbf{B}\right).$$

The test-ion 3-D velocity components are updated at every iteration.

LIZE uses an adaptive time step, which is calculated as

$$dt = \min(\text{GyroP}, \frac{dx}{v_x}, \frac{dy}{v_y}, \frac{dz}{v_z}) \tag{6}$$

where GyroP is the ion gyro period and dx, dy, dz defines the grid cell size of the chosen magnetosphere simulation.

The ion density distribution is calculated on a 4-D grid (r, θ, ϕ, E) in LIZE, where r is the distance from Mercury ($r \in [1, 4]$ R_M), θ is the co-latitude ($\phi \in [0, \pi]$ rad), ϕ is the longitude ($\phi \in [0, 2\pi]$ rad) and E is the kinetic energy ($E \in [1, 10^5]$ eV). The grid cell boundaries are distributed exponentially with respect to r, linearly distributed along θ and ϕ, and are defined as $(E_i - E_{i-1})/E_i = 0.1$ where E_i is the i^{th} energy step.

The test-ion trajectories are followed for 1,000,000 iterations or until they have passed the outermost boundaries of the simulation volume. Less than 1% of the test-ions are still located inside the simulation volume after 1,000,000 iterations. Test-ions which reach the inner ($r < 1$ R_M) or outer boundary ($r > 4$ R_M) of the simulation are considered as impacting and escaping ions respectively. These test-ions leave the main simulation loop but are stored into impact/escape flux arrays (θ, ϕ, E) and can be retrieved from the model output.

It is also possible to use the LIZE model to calculate the mean phase space density distribution inside one or several regions with defined boundaries. This is a useful feature which can be used to compare the modeled ion density distribution with the ion density observed in-situ by a spacecraft instrument that has a limited FOV (see Section 5).

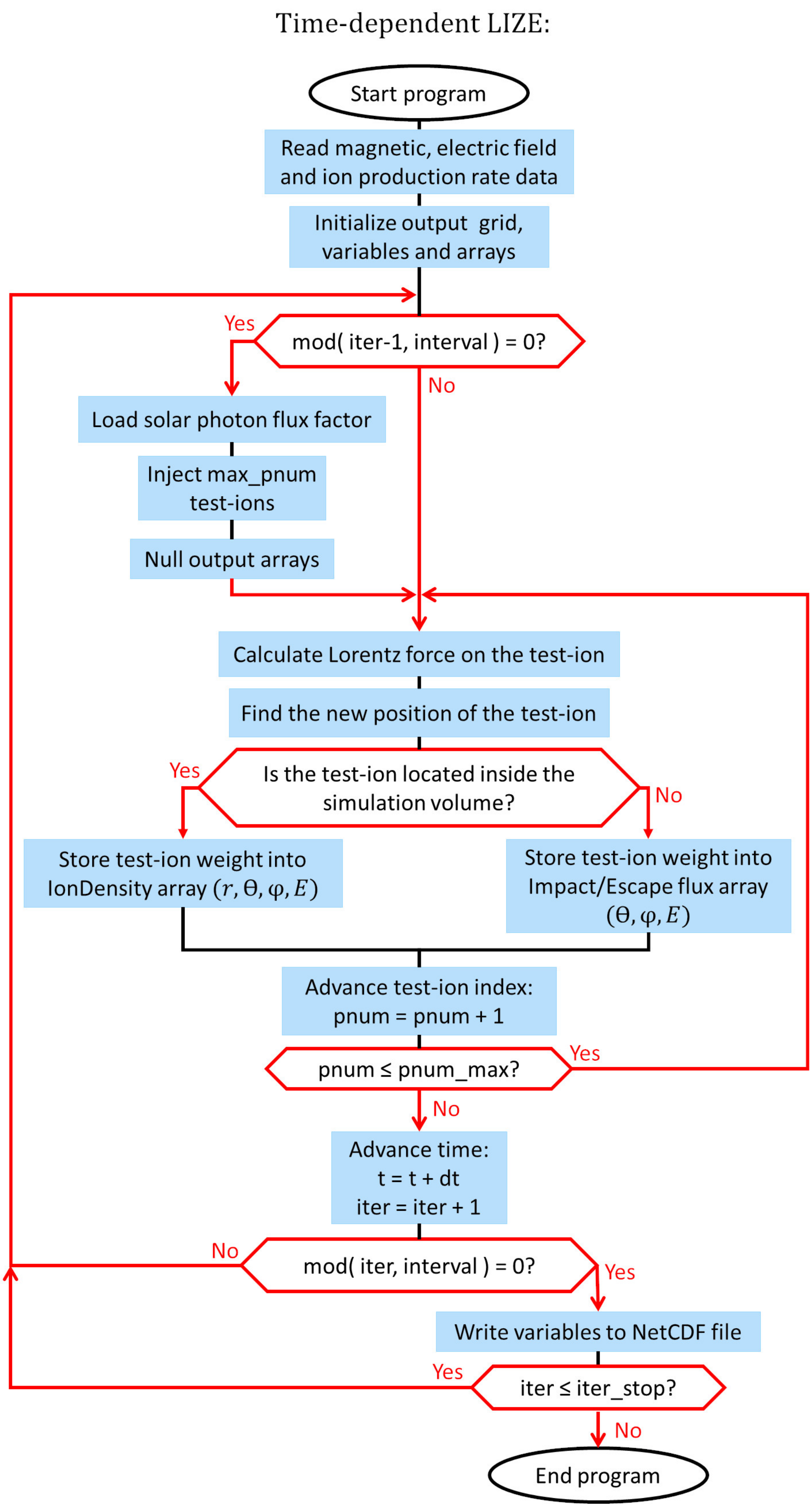

Figure 29: Flowchart of the time-dependent version of the LIZE model.

4.3.2.1 *Time-dependent version*

LIZE can also be run with time-dependent input conditions. In contrast to the standard LIZE code described above, which includes a single test-particle injection at the start of the simulation, the time-dependent version of the LIZE model has repeated particle injections. By changing the test-particle weights, injection velocity or even the spatial distribution of the injected test-particles, one can simulate the impact of changing external conditions on the planetary ion population in Mercury's exosphere.

In Chapter 6 we use this feature to model the impact of strong X-class solar flare on Mercury's ionized exosphere. The simulation volume is first initialized with a long period (~ 30 minutes) of test-particle injections with identical test-particle weights from one injection to the other. "Snapshots" of the ion density distribution are saved to the output at regular intervals. Once the 3-D ion density distribution does not differ more than 10% from one snapshot to the next, we introduce a sequence of solar photon flux factors which are multiplied with the nominal test-particle weights to simulate the real change of the solar photon flux with time during the flare. Compare the flowcharts in Figure 28 and Figure 29 to see the differences between the stationary and the time-dependent version of the LIZE code. For numerical reasons the time step is set to a constant value ($dt = 0.01$ s). For the same reason, the number of ejected test-ions per cell is here set to a lower number (i.e. $n = 50$) than in the static version of the LIZE model ($n = 100$). However, because the time-dependent LIZE model involves many more ejections than the static version, the derived ion density in each cell still varies by less than 10% between different runs.

In the described application of the time-dependent LIZE model, only the solar photon flux changes with time and the neutral density distribution of the exosphere stays relatively constant. If one would instead simulate the impact of a coronal mass ejection on Mercury, the neutral density would likely change. In particular, the distribution of the neutral exosphere may change due to enhanced ion sputtering at the poles, the whole dayside hemisphere due to the compression of the magnetopause and with time, enhanced ion precipitation on the nightside (Orsini et al., 2018). Because the distribution of the neutrals in the exosphere is changing, the ion production rate does too. In addition, one could expect a small change due to daily variations of the solar photon flux.

4.4 SUMMARY

In this chapter we have examined the different types of models which have been applied to explain the distribution and dynamics of the exosphere, magnetosphere and planetary ion environment.

The LIZE model is uniquely suited for the study of planetary ions in the Mercury environment. The model is coupled to a realistic model of the neutral exosphere, which includes all spatial asymmetries and the seasonal cycle for several species, and a magnetospheric model which accounts for ion-kinetic acceleration and plasma transport. The coupling to the EGM exosphere model allows for the study of numerous planetary ion species. To date, 10 neutral species have been implemented in the EGM model for Mercury.

LIZE also introduces several unique model capabilities, such as being able to model the planetary ion phase space density distribution. This is a great tool to study the different acceleration processes which control the motion of planetary ions in Mercury's magnetosphere. LIZE's time-dependent capability also makes it possible to study the impact of short-term variations in the external environment on the planetary ion distribution in the magnetosphere.

In the next two chapters, we will apply the LIZE model to describe the average ion density distribution in the magnetosphere and its response to an extreme solar flare.

.

5

GLOBAL ION DENSITY AND PHASE SPACE DENSITY DISTRIBUTION OF HE$^+$, O$^+$ AND NA$^+$ IN MERCURY'S MAGNETOSPHERE

5.1 INTRODUCTION TO PAPER I

In the previous chapters we have described the observations that exist of the planetary ion environment in Mercury's magnetosphere and the underlying algorithm of the LIZE model. Because of MESSENGER's highly eccentric polar orbit the FIPS observations are restricted to low altitudes in the northern polar region and high altitudes in the south. The FIPS coverage in local time and altitude is also intimately tied to Mercury's TAA. Finally, if the planetary ion distribution is not sufficiently isotropic and subsonic, FIPS limited energy range and field-of-view may not give a representative picture of the true ion density distribution in Mercury's magnetosphere. This means that it is difficult to attribute observed enhancements in the ion density distribution to the exosphere, solar wind and magnetospheric conditions or the FIPS coverage alone.

The LIZE model was developed with these questions in mind and provides a global view of the planetary ion distribution in and outside Mercury's magnetosphere. The coupling to the EGM and LatHyS models allows the LIZE model to account for both the neutral distribution in the exosphere and non-adiabatic ion acceleration mechanisms which may be important to explain the distribution of heavy, energetic ions in Mercury's small magnetosphere. Previous ion density models have been limited to describing the distribution of Na$^+$ ions. There is an interest in investigating the distribution of other ion species (such as He$^+$) to understand how and why these differ from the distribution of Na$^+$. In the article reprinted in the next subsection, we apply the LIZE model to describe the ion density distribution of He$^+$, O$^+$ and Na$^+$ in Mercury's magnetosphere. The results from the LIZE model are compared with the average ion density distribution observed by MESSENGER/FIPS observations during the orbital mission. We study the 3-D phase space density distribution in four different region located inside the magnetosphere. Finally, we investigate how the average ion density computed with LIZE differs for different sets of solar wind and IMF conditions.

5.2 SUMMARY OF PAPER I

Our main findings are the following:

- The spatial distribution of He^+ and the Na^+- and O^+-group ion density seen in the FIPS observations in the equatorial plane are reproduced by the LIZE model. The low-altitude ion density enhancement in the post-dawn sector (6-12 h) exists, as does the low scale height of the ion density near the subsolar point and the extended enhancement at higher altitudes in the dusk-to-midnight sector. The upper boundary of the high ion density region in the noon-to-dusk sector (>12 h) is slightly compressed and shifted toward dawn relative to the average magnetopause location for the relevant solar wind and IMF conditions (computed from Winslow et al., 2013). This is likely due to the strictly northward solar wind IMF in this simulation, which creates a strong solar wind electric field which points toward dawn ($E_y < 0$). This acts to compress/shift the dusk magnetopause flank and the ion distribution. This may also explain why the modeled ion density enhancement at dusk extends all the way to midnight, while the observations do not.

- The absolute magnitude of the modeled ion density is larger by a factor of 2-20 compared to the observations.

- Previous simulations of the Na^+ density in Mercury's magnetosphere give similar estimates of the average ion density. The distribution depends on the solar wind conditions, IMF and surface conductivity. The ion density is commonly a factor of $10^2 - 10^3$ higher than observed by FIPS. Sarantos and Slavin (2009) retrieved a maximum Na^+ ion density of 1 cm^{-3}, which is the only estimate which resembles the results from the FIPS observations. However, Sarantos and Slavin (2009)'s study was limited to Na^+ pickup ions that are born in the magnetosheath region, which is just a fraction of the total Na^+ population.

- The solar wind and IMF is highly variable, and it might be best to study a well selected set of solar wind and IMF conditions to get a better estimate of the average state of the ion density distribution in Mercury's magnetosphere. The high ion density for the northward IMF case may also be due to the common underestimation of the reconnection rate for this type of IMF in magnetospheric models.

- The Na^+ ion density distribution in the magnetosphere has also been inferred from MESSENGER/MAG observations of magnetic field line resonance events. The observations give an estimate of the plasma mass density, which is likely dominated by Na^+ given that solar wind H^+, He^{2+} has a very low mass and other, heavier planetary ion species are relatively scarce compared to Na$^+$. The estimate is limited to closed field-line regions in the magnetosphere, but gives an average ion density which is much closer to the LIZE estimate.

- We get similar results using two different magnetosphere models, AIKEF and LatHyS. AIKEF yields higher ion densities compared to LatHYS but both the magnitude and the spatial distribution of the ions are very similar. The ion density is enhanced in a low-altitude band at all local times for AIKEF.
- A high resolution magnetosphere simulation is needed to avoid islands of high electric field near the planet due to the low plasma density in this region. The ion density and energy distribution are generally very sensitive to the electric field near the planet, since this is where the majority of the ions are formed.
- The phase space density distribution shows an anisotropy in the vx-vz plane in several regions.

This study demonstrates the capability of LIZE to reproduce the MESSENGER/FIPS ion density observations. This opens up the possibility to study parts of the energy distribution and FOV not accessible to FIPS, but which will be viewed by the ion instruments on the BepiColombo spacecraft. This study has also revealed a potential mechanism for ion acceleration of He$^+$ ions in the equatorial plane.

5.3 REPRINT OF PAPER I: ION DENSITY AND PHASE SPACE DENSITY DISTRIBUTION OF PLANETARY IONS NA$^+$, O$^+$ AND HE$^+$ IN MERCURY'S MAGNETOSPHERE

Paper I was accepted for publication in Icarus on 4 October 2021. This section contains the preprint of the accepted article.

Journal Pre-proof

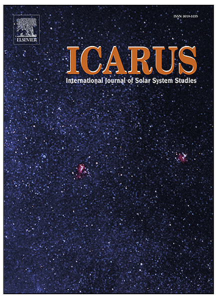

Ion density and phase space density distribution of planetary ions Na^+, O^+ and He^+ in Mercury's magnetosphere

A.L.E. Werner, S. Aizawa, F. Leblanc, J.Y. Chaufray, R. Modolo,
J.M. Raines, W. Exner, U. Motschmann, C. Schmidt

PII: S0019-1035(21)00388-2
DOI: https://doi.org/10.1016/j.icarus.2021.114734
Reference: YICAR 114734

To appear in: *Icarus*

Received date : 9 May 2021
Revised date : 4 October 2021
Accepted date : 4 October 2021

Please cite this article as: A.L.E. Werner, S. Aizawa, F. Leblanc et al., Ion density and phase space density distribution of planetary ions Na^+, O^+ and He^+ in Mercury's magnetosphere. *Icarus* (2021), doi: https://doi.org/10.1016/j.icarus.2021.114734.

Highlights

Ion density and phase space density distribution of planetary ions Na^+, O^+ and He^+ in Mercury's magnetosphere

A. L. E. Werner,S. Aizawa,F. Leblanc,J. Y. Chaufray,R. Modolo,J. M. Raines,W. Exner,U. Motschmann,C. Schmidt

- MESSENGER FIPS ion density observation from the whole orbital phase are analyzed.
- Spatial distribution of Na^+, O^+ and He^+ ion densities are reproduced by our model.
- Simulated Na^+ and He^+ ion densities are overestimated by a factor of 2-20.
- Upstream conditions vary planetary ion densities by almost an order of magnitude.
- Analysis of the ion velocities reveal an anisotropic distribution in the $v_x - v_z$ plane.

Ion density and phase space density distribution of planetary ions Na^+, O^+ and He^+ in Mercury's magnetosphere

A. L. E. Werner[a,*], S. Aizawa[b], F. Leblanc[a], J. Y. Chaufray[c], R. Modolo[c], J. M. Raines[d], W. Exner[e,f], U. Motschmann[f,g] and C. Schmidt[h]

[a] *LATMOS/IPSL, Sorbonne Université, UVSQ, CNRS, Paris, France*
[b] *IRAP, Toulouse, France*
[c] *LATMOS/IPSL, UVSQ Université Paris–Saclay, Sorbonne Université, CNRS, Guyancourt, France*
[d] *Department of Climate and Space Sciences and Engineering, University of Michigan, Ann Arbor, MI, USA*
[e] *Institute for Geophysics and extraterrestrial Physics, TU Braunschweig, Braunschweig, Germany*
[f] *Institute for Theoretical Physics, TU Braunschweig, Braunschweig, Germany*
[g] *DLR Institute of Planetary Research, Berlin, Germany*
[h] *Center for Space Physics, Boston University, USA*

ARTICLE INFO

Keywords:
Mercury, atmosphere
Ionospheres
Magnetospheres
Solar wind

ABSTRACT

Photo-ionization of Mercury's tenuous exosphere contributes to the heavy ion population in the Hermean environment. Observations with the MESSENGER Fast Imaging Plasma Spectrometer (FIPS) have revealed the ion density and spatial distribution of the three most abundant planetary ions or ion groups around Mercury: The Na^+-group (mass-per-charge ratio $\mathrm{m/q} = 21 - 30\ \mathrm{amu/e}$), O^+-group ($\mathrm{m/q} = 16 - 20\ \mathrm{amu/e}$) and He^+. We developed a test-particle model coupled to a neutral exosphere model and two different models of the magnetosphere to simulate the ion density distribution of Na^+, He^+ and O^+. We compare the modeled ion density distribution at aphelion for northward interplanetary magnetic field (IMF) with FIPS observations from the entire orbital phase (23 March 2011 to 30 April 2015). Our model reproduces several observed features but the average ion density is up to 18x too high. However, we find that the discrepancy is less than 3x for other solar wind and exosphere conditions. Comparison with previous simulation studies of the Na^+ ion density and magnetic field line resonance observations give an average Na^+ density which is on the same order as our estimate. Finally, we model the phase space density (PSD) distribution in four different regions. We find that in three out of four regions only a fraction of the PSD distribution can typically be observed by FIPS. This is mainly due the obstruction of the field-of-view caused by the spacecraft's sun shield, which blocks plasma with a high v_x/v_z ratio from entering the instrument.

1. Introduction

Mercury has a tenuous and nearly collisionless atmosphere (exosphere) that is rich in heavy elements. H, He, Na, K, Mg, Ca, Mn, Fe and Al have been detected through ground-based (Potter and Morgan, 1985, 1986; Bida et al., 2000; Doressoundiram et al., 2009; Bida and Killen, 2017) and in-situ observations (Broadfoot et al., 1976; McClintock et al., 2008; Vervack et al., 2016). Space probe Mariner 10 made a tentative detection of the 130.4 nm O emission line during its third flyby past Mercury (Hunten et al., 1988). O could not be observed by the more recent Mercury Surface, Space Environment, Geochemistry, and Ranging (MESSENGER) spacecraft, despite conducting regular observations of the 130 nm line for several years in orbit (Vervack et al., 2016).

The strong solar radiation at Mercury and the intense space weathering causes neutral species to be continuously released from the surface regolith, either thermally (thermal desorption), by individual photons exciting the surface-bound atoms (photo-stimulated desorption), sputtering by solar wind ions or vaporization of whole surface grains by micro-meteoroids. The relative importance of these ejection mechanisms vary depending on species, and is different between volatile species (Na,K,He) and refractory species (Mg, Ca). Because the exosphere is collisionless, the species are not coupled and have their own dynamics. Several models have been developed to determine the relative contribution of the different ejection and loss processes to the overall composition of Mercury's exosphere (Smyth

---

[*] elisabeth.werner@latmos.ipsl.fr
ORCID(s): 0000-0002-1118-9713 (A. L. E. Werner)

and Marconi, 1995; Killen et al., 2001; Wurz and Lammer, 2003; Leblanc and Johnson, 2003, 2010; Schmidt, 2013; Gamborino et al., 2019).

Mercury has a highly eccentric orbit ($\epsilon = 0.2056$) and is trapped in a 3:2 spin-orbit resonance with the Sun. This gives rise to cold and hot longitudes (Soter and Ulrichs, 1967) and a seasonally variable exosphere and sodium ion content (Cassidy et al., 2015, 2016; Jasinski et al., 2021). Some exospheric sources like micro-meteoroid vaporization (Janches et al., 2021) and ion sputtering vary on shorter timescales, which has an impact on both the neutral exosphere (Leblanc et al., 2009; Orsini et al., 2018) and ionized exospheric neutrals (Raines et al., 2018; Jasinski et al., 2020). Meteoroids (as opposed to micrometeoroids) have been detected as large, brief enhancements to the exosphere (Jasinski et al., 2020; Cassidy et al., 2021)

The strong solar radiation at Mercury produces a large flux of heavy ions (on the order of 10^{24} s^{-1}; Raines et al., 2015) from the ionization of the exosphere. Lesser sources of planetary ions include charge exchange and solar wind ion sputtering. MESSENGER Fast Imaging Plasma Spectrometer (FIPS) detected several mass spectrum peaks that may belong to Na$^+$ (mass-per-charge ratio m/q = 23-24 amu/e), O$^+$ and water group ions (16-18 amu/e), S$^+$ and H$_2$S$^+$ (32-36 amu/e), Si$^+$ (28 amu/e), K$^+$ and Ca$^+$ (39-40 amu/e) and He$^+$ (4 amu/e; Zurbuchen et al., 2008). FIPS is a time-of-flight (TOF) mass spectrometer. Due to FIPS TOF uncertainty, ions with similar mass-per-charge ratio were grouped together in so-called ion groups (e.g. Appendix A in Raines et al., 2013). Na$^+$- (m/q = 21-30 amu/e), O$^+$-group (m/q = 16-20 amu/e) ions and He$^+$ (m/q = 4 amu/e) were regularly observed during the mission orbital phase (Zurbuchen et al., 2011; Raines et al., 2013). Ca$^+$ has also been detected by the Mercury Atmospheric and Surface Composition Spectrometer (MASCS) UltraViolet and Visible Spectrometer (UVVS; Vervack et al., 2016).

Observations with the magnetometer (MAG) on MESSENGER have shown that Mercury possesses a weak intrinsic magnetic field that fits the profile of a axially symmetric dipole field with dipole magnetic moment of 195 ± 10 nT-R$_M^3$ (where R$_M$ = 2440 km is the mean Mercury radius) and a 0.2 R$_M$ northward offset (Anderson et al., 2011). The planet takes up a relatively large volume inside the magnetosphere, and the magnetopause standoff distance is typically located at a mere 0.45 R$_M$ from the subsolar point on the surface (Winslow et al., 2013). Despite the weak dipole magnetic moment and the high solar wind ram pressure, the dayside magnetosphere is rarely compressed all the way to the surface (Slavin et al., 2019; Winslow et al., 2020). This is due to the existence of induction currents in Mercury's interior that are driven by solar wind variations (Smith et al., 2012; Slavin et al., 2014; Jia et al., 2015). The Hermean magnetosphere is highly dynamic with a Dungey cycle (Dungey, 1961) time of approximately 2 minutes (Slavin et al., 2009). The same process typically takes 1 hour at Earth (Siscoe et al., 1975).

The comparatively large gyro radius of the heavy ions in relation to the small scale of the Hermean magnetosphere means that non-adiabatic effects are significant almost everywhere in the magnetosphere (Delcourt et al., 2003). Non-adiabatic effects include centrifugal ion acceleration (Delcourt et al., 2002, 2003), which may have a major impact on the ion distribution in the magnetosphere (Raines et al., 2013). The heavy ion population is likely not dense enough to influence the global structure of the Hermean magnetosphere (Exner et al., 2020) but it gives rise to other effects like diamagnetic depression of the magnetic field (Korth et al., 2011), enhancement of the formation of Kelvin-Helmholtz instabilities (Paral et al., 2010) and generation of magnetic field-line-resonances (James et al., 2019).

Analysis of the first few months of FIPS observations in orbit around Mercury revealed several ion density enhancement regions and surprising differences between He$^+$ and the heavier O$^+$- and Na$^+$-group ions. The Na$^+$- and O$^+$-group ions were especially abundant near the northern magnetic cusp with a Na$^+$-group ion abundance four time larger than the solar wind He^{++}. The elliptical polar orbit of MESSENGER did not permit observations at low altitudes in the southern polar region. A later study by Raines et al. (2014) identified two populations of Na$^+$-group ions in the northern cusp: one at low energy (100 – 300 eV) and one at high energy (> 1000 eV). The low-energy ions are believed to be produced locally while the high-energy ions come from photo-ionized escaping neutrals that have been swept into the magnetic cusps by reconnection. The Na$^+$- and O$^+$-group ions also showed smaller enhancements near the dawn terminator in the equatorial plane and at high altitudes (> 2000 km) in the dusk to pre-midnight sector. He$^+$ was much more evenly distributed in the magnetosphere and did not exhibit any particular enhancements in said regions. The density of all species was particularly low near 12 h local time.

The Na$^+$ density enhancement near the dawn terminator may be related to the seasonal dawn enhancement in the neutral exosphere (Potter et al., 2006, 2013; Cassidy et al., 2016; Milillo et al., 2021). If this is true, it could imply a direct link between the neutral surface abundance and the ion density at low altitudes. The dusk enhancement, on the other hand, may be evidence of the non-adiabatic ion acceleration mechanism described in Delcourt et al. (2002, 2003). The difference in spatial distribution between He$^+$ and the heavier ion species may imply that He$^+$ is produced by a different, more diffuse source. The depression at the subsolar point may be an apparent effect caused by the effective energy range (100 eV – 13 keV; Raines et al., 2013).

Raines et al. (2013) also studied the variation of the global average ion density as a function of true anomaly angle. The global averages consist of FIPS data taken at different altitudes, latitudes and local times, and even includes measurements taken inside the solar wind. They found two peaks for the Na^+- and O^+-group ions, a global maximum at TAA = 110° and local maximum at 330°, and a minimum at TAA = 270°. He^+, on the other hand, showed very little variation with TAA. More recently, Jasinski et al. (2021) estimated the TAA variation of the Na^+ production rate from UVVS (Cassidy et al., 2015) and THEMIS observations (Milillo et al., 2021) of the Na exosphere and FIPS Na^+-group ion observations taken inside the northern magnetospheric cusp. They estimated a maximum ion production rate of $3-4\times10^{24}$ s^{-1} between TAA = $0° - 30°$, where FIPS observations are missing.

In this study, we have modeled planetary ions produced from the exosphere by combining different simulations. In Section 2, we describe the models used in this study. In Section 3 we describe the modeled neutral exosphere, magnetic and electric fields in the magnetosphere and the solar wind proton density. Then, we compare the modeled ion density and phase space density distribution with FIPS observations. We discuss the results and their implications in Section 4 and summarize the main findings in Section 5.

2. Models

In order to study the inferred link between the neutral and ionized exospheres we will use a realistic description of Mercury's neutral exosphere consistent with remote and in-situ observations to model the abundance and spatial distribution of Na^+, He^+ and O^+ in and outside Mercury's magnetosphere. We will account for non-adiabatic effects of the heavy planetary ions and their impact on the ion density distribution by coupling our model to two different hybrid models of the magnetosphere.

In the following subsection, we describe the Monte Carlo-model of the neutral exosphere, the two magnetospheric models and our newly developed test-particle model that computes the full equation of motion of the ions.

2.1. Exospheric Global Model (EGM)

The Exospheric Global Model (EGM; Leblanc et al., 2017b) is a parallelized Monte Carlo-model that describes the exosphere around moons and planets. EGM has been previously used to study the exospheres of Mercury (Leblanc and Johnson, 2003, 2010; Leblanc and Doressoundiram, 2011; Leblanc and Chaufray, 2011; Leblanc et al., 2013), Ganymede (Leblanc et al., 2017b), Mars (Leblanc et al., 2017a) and Europa (Oza et al., 2019). In this paper, we use EGM to simulate the density of Na, He and O in the exosphere of Mercury.

EGM reconstructs the exospheric neutral density, average velocity, kinetic temperature and ionization rate in 3-D as well as the amount of exospheric materials trapped in the surface. The quantities are computed on a spherical grid (r, θ, ϕ) where r is the distance from the planet, θ is the co-latitude and ϕ is the longitude. For Mercury, the grid is centered on the planet ($r = 0$) and extends from the surface ($r = 1$ Mercury radius; R_M) up to 5.5 R_M. The grid is divided into cells that are distributed exponentially with r, linearly spaced in ϕ and defined in θ such that all cells at a given altitude have the same volume. For a detailed description of the EGM parallelization scheme see Turc et al. (2014).

A large number of test-particles are ejected from the surface by different mechanisms (see below) and then continuously throughout the simulation. Each test-particle i represents a large number of actual particles, represented by a weight w_i. Each test-particle is followed around Mercury taking into account the various gravity fields (those of Mercury and the Sun) and the effect of the solar radiation pressure. This is done up to the moment when the test-particle is either ionized by the solar radiation flux (calculated taking into account the relative velocity of the test-particles with respect to the Sun and its distance to the Sun), impact the surface or escape from the simulation. In the case of a surface impact, the particles can be either re-ejected or absorbed in the surface, an absorption which duration is estimated for each species and from the local surface temperature (for a detailed description of the simulation scheme, see Leblanc and Johnson, 2010; Leblanc et al., 2017b). The surface temperature is described using a one-dimensional heat conduction model (see Leblanc et al., 2017b). An EGM run last for several Mercury years in order to reach an orbital dependent stationary solution independent from the initial conditions. Once a stationary solution has been reached, the state of the exosphere can be determined at any point along the orbit. To improve the statistics, the 3D density (velocity, ionization rate etc.) at a given TAA is averaged over 20° centered on the TAA in question.

In the following, we assume that the primary origin of the exospheric Na and O atoms is Mercury's surface, either endogenic (internal by regolith diffusion) or exogenic (meteorite origin), while He is primarily coming from implanted

Table 1
Input parameters to the EGM model.

Parameter:	Value:		
Species:	Na	O	He
Ejection processes and surface ejection rate [s^{-1}]:	3.4×10^{25} (PSD) 1.7×10^{23} (MMV) 1.9×10^{23} (SWS)	3.7×10^{22}	5.9×10^{23}
Ionization frequency (at 1 AU in s^{-1}):	5.0×10^{-6}	3.1×10^{-7}	7.5×10^{-8}
Time step:	$\Delta t = 0.81$ s		
Number of cells:	$nr = 80$, $n\theta = 18$ $n\phi = 40$		
Simulation domain:	$1.0 < r < 5.5\ R_{\rm M}$ $0 < \phi < \pi$ rad $0 < \phi < 2\pi$ rad		
Grid resolution:	$\Delta r =$ 5-287 km $\Delta\phi = \frac{\pi}{2}$ rad $\Delta\theta = \frac{\pi}{3}$ - $\frac{\pi}{6}$ rad		
True anomaly angle (TAA):	180°		

solar wind alpha particles. Na and O are launched from the entire surface of Mercury by various ejection mechanisms so that their ejection rate is non uniform, while He is launched from the magnetic cusp regions where solar wind alpha particles can reach the surface. The input parameters to the EGM simulations are listed in Table 1.

2.1.1. Na

We use the same approach as described in Leblanc and Johnson (2010) to model the Na exosphere. Micro-meteoroid impact vaporization (MMV) is described as a source of Na atoms of 5×10^5 Na cm^2 s^{-1} ejected with a Maxwellian-Boltzmann (MB) distribution with a temperature of 3000 K. Photon-stimulated desorption (PSD) is described following a Maxwellian-Boltzmann flux (MBF) distribution with a temperature of 1500 K and an ejection rate determined from a cross-section of 0.68×10^{-17} cm^2 and a dependency with the surface temperature as in Schmidt (2013) using an activation energy set to 0.02 eV. Thermal desorption (TD) is described by a MBF distribution with binding energy between 3.5-4.5 eV and vibrational frequency 2.5×10^{10} s^{-1}. Solar wind ion sputtering (SWS) is described using a yield of 0.15 that is reduced by a factor 2 due to the porosity, a typical solar wind flux corresponding to a velocity of 400 km/s, a density of 10 cm^{-3} and an increase by a factor 4 due to the cusps geometry (defined in Leblanc and Johnson, 2010). The energy distribution of the sputtered Na atoms follows a distribution at $f(E) = UE/(E+U)^3$ with the binding energy U set to 0.27 eV (Leblanc and Johnson, 2003). The ejection rate of each of these processes depends on the Na surface concentration and also on the relative efficiency of each of them (see Leblanc and Johnson, 2003, 2010, for more details and discussions). Column density profiles of the model Na exosphere roughly agrees in both shape and magnitude with UVVS limb scan taken at the south pole and at different local times near the equator (see Figure 4 in Cassidy et al., 2015).

We consider photo-ionization as the main source of the planetary ion population and neglect electron impact ionization as well as ion production caused by solar wind ion sputtering or micro-meteoroid impact vaporization.

Na photo-ionization rate, g-value and radiation pressure are computed as in Leblanc and Johnson (2010), consistent with cometary Na tail observations in the inner heliosphere (Fulle et al., 2007). The calculated Na photo-ionization

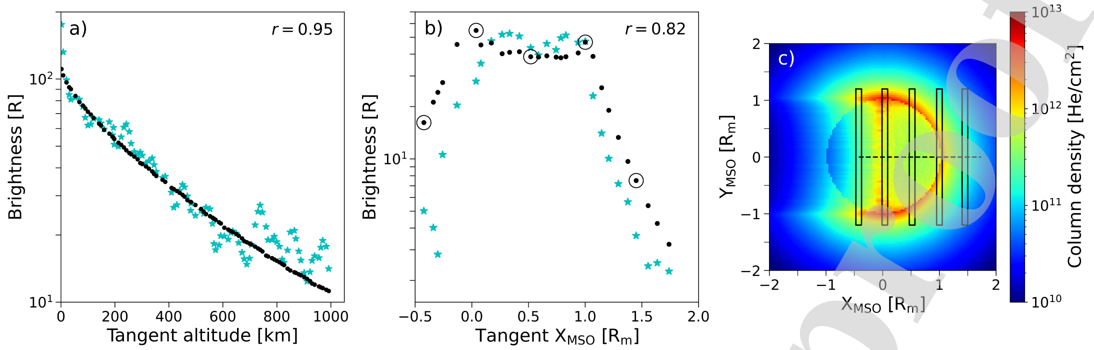

Figure 1: The fit between EGM (black line) and the Mariner 10 He column density observations (green stars) at (a) the subsolar limb and (b) the terminator. Also shown is the (c) simulated 2-D column density map in the equatorial plane and the approximate viewing geometry of Mariner 10 during the terminator observations. The boxes in (c) represent the approximate slit size of the observations. The circled points in (b) show the X_{MSO} coordinates of the boxes in (c). The correlation values r between the best-fit model and the two sets of observations are written in the top right corner of (a) and (b).

rate (5.0×10^{-6} s^{-1} at 1 AU) is close to the value published in Fulle et al. (2007).

2.1.2. He

Following Leblanc and Chaufray (2011), we consider He atoms ejected thermally from the surface. In the version of EGM used by Leblanc and Chaufray (2011) the ejection rate of He was set to 2.3×10^{23} s^{-1} in order to reproduce the Mariner 10 column density profiles of the 58.4 nm He emission line. Leblanc and Chaufray (2011) defined the He source area to the whole surface of Mercury but in this work we limit the He source to the magnetospheric cusps. This is likely more realistic considering that the solar wind bombardment is limited to the cusps during nominal solar wind conditions. We define the location and size of the northern cusp as $27° - 54°$ in latitude (where 0° is the north pole and 90° is the equator) and 10 - 14 h in local time. We define the southern cusp symmetrically in the southern hemisphere. The northern cusp area defined here compares well to the limits of the northern cusp inferred from MAG data (Winslow et al., 2012), although the mean latitudinal extent (11°) of the northern cusp is smaller.

We find that we have to increase the He ejection rate to 5.9×10^{23} s^{-1} to fit the Mariner 10 column density profiles in 1. This is still much smaller than the He^{++} flux during nominal solar wind conditions (Leblanc and Chaufray, 2011). The fit of the new model to the Mariner 10 observations (5.9×10^{23} s^{-1}) gives similar correlation factors to Leblanc and Chaufray (2011), but the fit to the terminator observations is slightly worse ($r = 0.82$ compared to $r = 0.93$ from Leblanc and Chaufray, 2011). In Leblanc and Chaufray (2011) the energy accommodation of the He atoms follow a linear relationship between full accommodation on the dayside ($\alpha = 1$) to weak accommodation with the surface on the nightside ($\alpha = 0.06$ at the terminator and $\alpha = 0.05$ at midnight). The new fit in Figure 1b may imply that the accommodation theory developed for neutral He in Leblanc and Chaufray (2011) may need to be tweaked to better fit this set of observations. Since our study mainly concerns the ion density distribution near the equatorial plane, where the fit to the neutral He observations is good (Figure 1a; $r = 0.95$), we expect that this will have negligible impact on our results. Neutral He could not be observed by MESSENGER due to the limited coverage of the UVVS instrument in the ultraviolet spectral range (McClintock and Lankton, 2007).

The ionization frequency calculation follows the same scheme used for Na and is estimated to 0.1×10^{-6} s^{-1} for He at 1 AU. The solar radiation pressure is also calculated as in Fulle et al. (2007), but for both He and O it is negligible with respect to Mercury's gravity field.

2.1.3. O

As explained in the introduction, the oxygen density in the exosphere of Mercury is not well constrained by observations, only an upper limit could be derived from UVVS observations (Vervack et al., 2016). Moreover, how oxygen could be ejected from the surface into the exosphere is not known. Therefore, due to this lack of observations, oxygen

Table 2
Input parameters to LatHyS and AIKEF.

Parameter:	Lathys value:	AIKEF value:
Time step:	0.02 s	0.01 s
Spatial resolution:	145 km	100 km
Simulation domain:	$-5.4 < x < 5.6$ R_M $-11.3 < y < 11.4$ R_M $-11.3 < z < 11.4$ R_M	$-3.5 < x < 10.5$ R_M $-5.0 < y < 5.0$ R_M $-5.0 < z < 5.0$ R_M
Simulated species:	H^+, He^{++}, Na^+, H^+(planetary)	H^+
Number of solar wind particles per cell:	H^+: 20 He^{++}: 2	H^+: 25
Solar wind number density:	n = 30 cm^{-3}	
Solar wind velocity:	$v = 400$ km/s	
Solar wind magnetic field:	$\mathbf{B} = (B_x, B_y, B_z) = (0, 0, +20)$ nT	
Ram pressure:	$P_{ram} = 8$ nPa	
Alfvén Mach number:	$M_A = 5.2$	

exospheric atoms will be simply simulated starting from a population of ejected atoms from the surface following a MBF distribution at the local surface temperature and proportional to the incident solar radiation flux (that is with a dependency in cosine of the solar zenith angle and no ejection from the nightside). For O we assume a uniform weak thermal accommodation with the surface ($\alpha = 0.11$; Hunten et al., 1988). Hence, when a O test-particle impacts the surface it is immediately re-ejected into the exosphere again. We then scale the O exosphere to fit the upper emission limit (≈ 2 Rayleigh) set by UVVS based on observations of the 130.4 nm O emission line (Vervack et al., 2016; Mcclintock et al., 2018). The O ionization rate at 1 AU is 3.1×10^{-7} s^{-1}.

More recently, Huebner and Mukherjee (2015) re-evaluated the photo-ionization cross-sections, rates and excess energies for a range of atomic species, including the species that we consider in this work. The updated photo-ionization cross sections for Na, O and He are not significantly different from ours and we are using a better resolved solar spectrum compared to Huebner and Mukherjee (2015) (which used the same solar spectrum as in Huebner et al., 1992). For this reason there is a factor $1.6 - 3.2$ difference between our calculated photo-ionization rates and the values published in Huebner and Mukherjee (2015). We will only consider quiet solar wind conditions in this work, but it is noteworthy that in the case of both He and O the photo-ionization rate is a factor of $2 - 3$ higher during high solar activity (Huebner and Mukherjee, 2015). The photo-ionization rate for Na is not nearly as dependent on the solar activity level as O and He (the difference is less than 10 %).

2.2. Models of Mercury's magnetosphere

Both magnetohydrodynamic (MHD; Jia et al., 2015, 2019; Dong et al., 2019) and hybrid (Kallio et al., 2011; Müller et al., 2011; Modolo et al., 2016) models have been employed to describe the electromagnetic field environment around Mercury, which results from the solar wind interaction with Mercury's intrinsic field. Hybrid (electron fluid, ion kinetic) models are particularly well suited to describe plasma processes in systems where the ion Larmor radius is comparable to the length scale of the obstacle itself (Glassmeier et al., 2003; Slavin et al., 2008). Hybrid models have a large computational load compared to MHD models, but they enable higher accuracy in regions where kinetic effects of the ions prevail. We will compare the solar wind H^+ and planetary ion densities using static electric and magnetic fields from two such models: Latmos Hybrid Simulation (LatHyS; Modolo et al., 2016) and Adaptive Ion-Kinetic

Table 3
Input parameters to the LIZE model.

Parameter:	Value:
Time step	Adaptive
Number of cells:	$nr = 65$ $n\theta = 40$ $n\phi = 60$
Simulation domain:	$r = 1.0 - 3.5$ $\mathrm{R_M}$ $\phi = 0 - 2\pi$ rad $\theta = 0 - \pi$ rad
Grid resolution:	$\Delta r = 5 - 600$ km $\Delta\phi = 0.08$ rad $\Delta\theta = 0.1$ rad
Species:	$\mathrm{Na^+}$, $\mathrm{O^+}$, $\mathrm{He^+}$
Number of test-particles/cell:	$n = 100$
Energy range:	$1 - 10^5$ eV
Energy resolution:	$(E_i - E_{i-1})/E_i = 0.1$, where E_i is the ith energy step

Electron-Fluid (AIKEF; Müller et al., 2011).

We use a single set of solar wind ($n = 30$ cm^{-3}, $v = 400$ km/s) and IMF ($\mathbf{B} = B_z = +20$ nT) boundary conditions (see Table 2). This corresponds to "case a" with $B_z > 0$ described in Aizawa et al. (2021) , where B_z is the z-component of the the interplanetary magnetic field (IMF) in the Mercury-Sun Orbital (MSO) system. In MSO coordinates, x points toward the Sun, z points toward the north pole and y completes the right-handed coordinate system (i.e. positive toward dusk).

2.2.1. Latmos Hybrid Simulation (LatHyS)

LatHyS (Modolo et al., 2016) is a hybrid model that describes the 3-D plasma environment around weakly magnetized and unmagnetized planetary bodies. The model has been previously applied to Mercury (Richer et al., 2012), Mars (Modolo et al., 2016; Romanelli et al., 2018a,b), Ganymede (Leclercq et al., 2016) and Titan (Modolo et al., 2007). See Modolo et al. (2016) for further details on LatHyS.

The spatial and temporal resolution used in the LatHyS simulation are $\Delta x = 145$ km and $\Delta t = 0.02$ s. Two solar wind ion ($\mathrm{H^+}$ and $\mathrm{He^{++}}$) and two planetary ion ($\mathrm{Na^+}$ and $\mathrm{H^+}$) species are considered in the simulation. The $\mathrm{Na^+}$ ($\mathrm{H^+}$) ion density distribution in LatHyS is derived from a simple homogeneous Na (H) density model with a surface number density of 10^5/cm^3 (10^4/cm^3) and a scale height of 50 km (1292 km). Macro-particles from the planetary ion distribution are added directly to the total particle count of the simulation.

2.2.2. Adaptive Ion-Kinetic Electron-Fluid (AIKEF)

AIKEF is another hybrid model which has also been used to describe the interaction between magnetized plasma and different types of obstacles, such as planets, moons and comets (Müller et al., 2011). AIKEF has been employed in the past to study Mercury's apparent double magnetopause (Müller et al., 2012), the impact of a temporally variable coronal mass ejection on Mercury's magnetosphere (Exner et al., 2018) and the influence of exospheric $\mathrm{Na^+}$ on the magnetic and electric fields inside Mercury's magnetosphere (Exner et al., 2020).

The AIKEF simulation employs a grid size defined by $\Delta x = 100$ km, a time step $\Delta t = 0.01$ s and a larger number of macro-particles compared to LatHyS (see Table 2). This means that the AIKEF solution have better statistics compared to LatHyS. We only consider solar wind and planetary $\mathrm{H^+}$ in this AIKEF simulation. AIKEF uses so called "ghost particles" with negligible density to fill vacuum regions above Mercury's nightside surface.

2.2.3. *Latmos IoniZed Exosphere (LIZE)*

Even with current high-perfomance computing, it is still not possible to simulate directly the three ion populations in the two hybrid models with good statistics. The global structure of Mercury's magnetosphere is not altered significantly by a tenuous sodium exosphere (Exner et al., 2020). Therefore, a valid method to reconstruct the planetary ion density with sufficient statistics under stationary upstream conditions, is to employ a test-particle model with a static electromagnetic environment.

The Latmos IoniZed Exosphere (LIZE) model is a test-particle model that describes the ion density of planetary ions in the magnetosphere of Mercury. The planetary ion populations are produced by photo-ionization of exospheric neutrals. We use the simulated ion production rate from EGM to define the statistical weights of the test-particles. The full equation of motion of the test-particles is then computed using a Fourth-order Runge-Kutta scheme employing the electromagnetic fields calculated from LatHyS or AIKEF.

The test-ions are injected in the whole 3-D volume and then tracked until they leave the simulation box, impact the surface or exceed a postulated maximum iteration count. 100 test-particles are launched in each cell with zero initial velocity. We find that a non-zero injection velocity that is comparable to the average velocity distribution of the neutrals does not change the results. We use a static spatial grid but an adaptive time step that is limited by the gyro radius and the size of the LatHyS (or AIKEF) spatial grid. We use a spherical coordinate system that is logarithmic in r and uniform in both co-latitude θ and longitude ϕ (see Table 3).

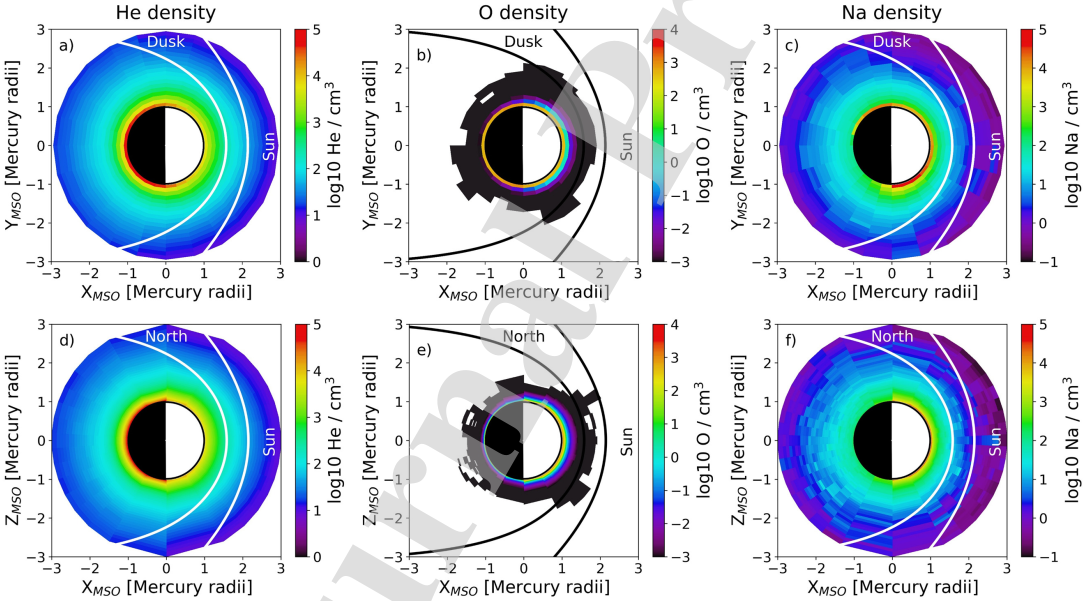

Figure 2: The neutral He, O and Na density computed with EGM, here shown in the equatorial (top row) and the noon-midnight meridional plane (bottom row). The curved lines show the location of the magnetopause and bow shock boundaries (Winslow et al., 2013).

3. Results

3.1. Neutral density

Figure 2 shows the simulated neutral He, O and Na density at aphelion from the EGM in the MSO XY plane (top row) and the MSO XZ plane (bottom row). The neutral density was averaged between $TAA = 170 - 190°$ to give an accurate description of the exosphere at aphelion (TAA = 180°). At this point in the orbit the average neutral density typically reaches its maximum value (Cassidy et al., 2015) and the photo-ionization rate its minimum value. Rather than averaging the neutral density over all possible TAAs with the EGM, computing the ion density at aphelion may be sufficient to give us a broad idea of the average ion density that we can expect over the whole Mercury orbit. The neutral density in the XY (XZ) plane was averaged over a volume segment spanning ±10° in latitude (longitude). The He and Na exospheres are seen to extend well beyond the magnetospheric boundaries while the O exosphere concentrated to low altitudes (see Figure 2).

The location of the magnetopause boundary in Figure 2 was calculated from the Shue et al. (1997) model described in Winslow et al. (2013) that has been fitted to MESSENGER MAG data and then corrected for the solar wind ram pressure of our simulation (P_{ram} = 8 nPa; Table 2). The bow shock location was then determined from the Slavin et al. (2007) model and corrected for the solar wind Alfvén Mach number (M_a = 5.2; Table 2) following the scaling method proposed by Winslow et al. (2013).

The He exosphere is characterized by a higher density on the nightside (see Figure 2a and 2d), which is in agreement with Mariner 10 observations (Broadfoot et al., 1976). The maximum He density is 6.3×10^4 cm^{-3} at the midnight surface. The total He supply rate (5.9×10^{23} s^{-1}) is balanced by 32 % thermal escape (1.9×10^{23} s^{-1}) and 68 % loss by photo-ionization (4.0×10^{23} s^{-1}).

The simulated O ejection rate 3.7×10^{22} s^{-1} was fitted to the upper limit on the average O tangent column density between 0-500 km above the subsolar point ($2.0 \times 10^{10}/cm^2$; Mcclintock et al., 2018) inferred from UVVS observations (Vervack et al., 2016). The O density is highest at noon (9.9×10^2 cm^{-3}). The total O supply rate (3.7×10^{22} s^{-1}) corresponds to 64 % loss by photo-ionization (2.4×10^{22} s^{-1}) and 36 % thermal escape (1.3×10^{22} s^{-1}). We did not study the seasonal variability of the global O ion production rate with EGM.

The Na surface density is lowest on the nightside (9.2×10^1 cm^{-3} at the surface), has a local maximum at the dusk terminator (1.7×10^4 cm^{-3}) and a global maximum at the dawn terminator (5.9×10^4 cm^{-3}). Between TAA $= 170 - 190°$, the Na exosphere is mainly supplied by photo-desorption (3.4×10^{25} s^{-1}) and to a much lesser degree by micro-meteoroid vaporization (1.7×10^{23} s^{-1}) and solar wind ion sputtering (1.9×10^{23} s^{-1}). Thermal desorption is negligible with respect to the other ejection processes at aphelion. The global Na supply rate (3.5×10^{25} s^{-1}) is balanced by 37% loss by photo-ionization (1.3×10^{25} s^{-1}) and 63% thermal escape (2.2×10^{25} s^{-1}). When we compare the global Na^+ ion production rate at different TAA, we find that the maximum photo-ionization loss rate of neutral Na occurs during aphelion (1.3×10^{25} s^{-1}) and the minimum is located at $TAA = 60°$ (1.5×10^{24} s^{-1}). The Na^+ production rate is roughly proportional to the total number of Na atoms in the exosphere (altitude range: 0-2 R_M), which also has a maximum at aphelion (3.1×10^{29} atoms) and a minimum at $TAA = 60°$ (1.4×10^{28} atoms) in our model.

The seasonal variation of the global Na^+ production rate from our model agrees very well with the Jasinski et al. (2021)'s estimates at perihelion and the first part of Mercury's outbound orbit around the Sun (i.e. 3.0×10^{24} s^{-1} at TAA = 0°, 1.5×10^{24} s^{-1} at TAA = 60° and 3.8×10^{24} s^{-1} at TAA = 120°). However, during the inbound orbit our model produces much higher values than Jasinski et al. (2021) (i.e. 1.1×10^{25} s^{-1} at TAA = 240° and 5.1×10^{24} s^{-1} at TAA= 300°). There is no estimate to compare our model to at TAA= 180° due to the lack of UVVS and THEMIS observations near aphelion.

3.2. Mercury's magnetosphere

Figure 3 shows the solar wind H^+ density, the absolute magnetic and electric field ($|B|$, $|E|$), and the H^+ plasma bulk velocity (V_{bulk}) in the equatorial plane from LatHyS and AIKEF.

LatHyS and AIKEF yield very similar solar wind H^+ density distributions, electromagnetic fields and bulk velocities. The bow shock and magnetopause stand-off distances are smaller for AIKEF. The magnetopause boundary is also more compressed toward the tail for AIKEF (see Figure 3a and 3e). There are a few small regions with high electric field ($|E| \approx 5$ mV/m) relative to the surroundings ($|E| \approx 0$) close to the surface in both models (see Figure 3c and 3d). Test-particle ions which encounter these regions in the LIZE model may be subject to sudden particle acceleration. However, we find that these regions are too small ($\sim 200^3$ km^3) to have a substantial impact on the ion velocities. There exists a rather dense nightside ion ring distribution in the AIKEF simulation. The H^+ ions in this region have likely become momentarily trapped in the closed field region of Mercury's intrinsic field and experience a slow azimuthal drift toward the dayside. However, this ion population is unlikely to form a steady ion drift belt due to the small size of the magnetosphere.

In order to check the accuracy of our LIZE model, we simulated the solar wind H^+ density distribution with LIZE using the input parameters of the LatHyS and AIKEF simulations (see Table 2) and compared the results to Figure 3a and 3e to validate the simulated density by LIZE. We launched 250,000 test-particles at X=3.4 R_M uniformly

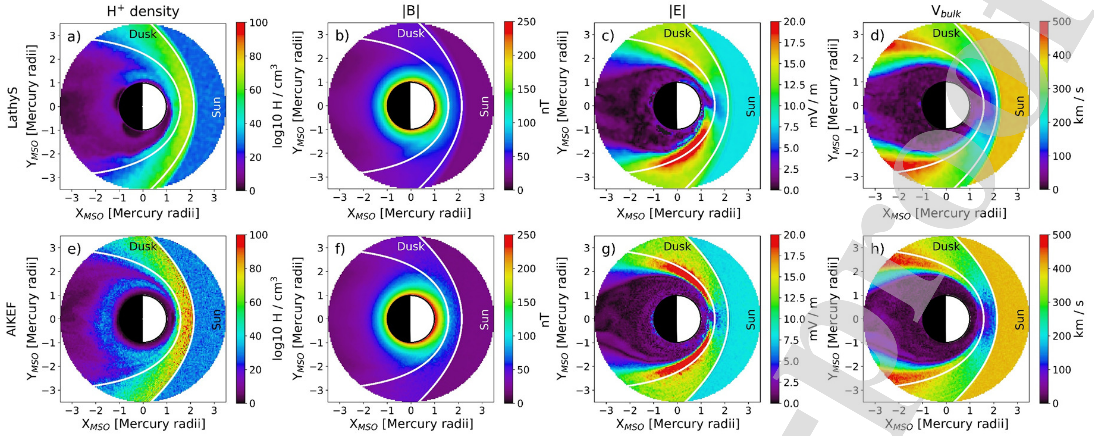

Figure 3: The outputs from two hybrid simulations. (a,e) The solar wind H$^+$ density, (b,f) the total magnetic field, (c,g) the electric field and (d,h) the bulk velocity in the equatorial plane from LatHyS (top row) and AIKEF (bottom row) respectively. The solid white lines in each figure show the location of the magnetopause and bow shock boundaries.

distributed between Y,Z= ±5 R$_M$ with the same density and bulk velocity used as inputs to LatHyS and AIKEF. The H$^+$ ion density distribution simulated with LIZE differ by less than 10% compared to Figure 3a and 3e. This is an indication that our method to reconstruct the ion density in LIZE yields accurate result.

3.3. Ion density

3.3.1. FIPS data analysis

FIPS was a TOF ion mass spectrometer with the ability to detect ions with m/q = 1-40 amu/e and an energy-per-charge E/q between 0.046 - 13.6 keV with 64 exponentially spaced energy channels (Andrews et al., 2007; Gershman et al., 2013). The effective field-of-view (FOV) of the instrument (1.15π sr) permit detection of ions coming from a wide range of directions with an angular resolution of 15°. During normal operation mode FIPS completed a scan of the full E/q range every 65 s. The second operation mode, the burst mode, was used to make frequent scans every 10 s (Gershman et al., 2013).

We extend the analysis by Raines et al. (2013) to the whole set of FIPS ion density (n$_{obs}$) observations accumulated between 23 March 2011 and 30 April 2015. Following Figure 3 in Raines et al. (2013), we plot the average ion density distribution of the Na$^+$- and O$^+$-group ions and He$^+$ as a function of local time and altitude (see the top row of Figure 3.3.1). We restrict our analysis to the latitude range ±30° centered on the equatorial plane. We use a grid with 0.5 h resolution in local time and 100 km in altitude identical to the grid that was used to make Figure 3 in Raines et al. (2013). The color map and color scale in Figure 3.3.1a-c is also identical to Figure 3 in Raines et al. (2013).

There exists two main enhancement regions in Figure 3.3.1a-b. The low-altitude enhancement extends between 6 - 12 local time and up to an altitude of 2000 km. The second, high-altitude enhancement extends between 16.5 - 21 h up to 6000 km. Both enhancement regions roughly follow the altitude profile of the magnetopause, but extends farther into the magnetosheath around noon. He$^+$ exhibits a low-altitude enhancement region at dawn similar to those observed for the Na$^+$ and O$^+$-group ions, but no high-altitude dusk enhancement. There also exists a narrow enhancement region located inside the magnetosheath at 18 h (altitude 5000-8000 km) for all three ion species. This enhancement feature is either missing or not as prominent in the (Raines et al., 2013) data set.

The observed ion density (n_{obs}) by FIPS is defined as

$$\sum_i f_i v_i^2 (\Delta v)_i \Delta\Omega \tag{1}$$

where f is the phase space density (PSD), v is the velocity, Δv is the velocity range, i corresponds to the index of the E/q step in FIPS operation and $\Delta\Omega$ is FIPS solid angle. The product between f_i and $v_i^2(\Delta v)_i$ is summed over each

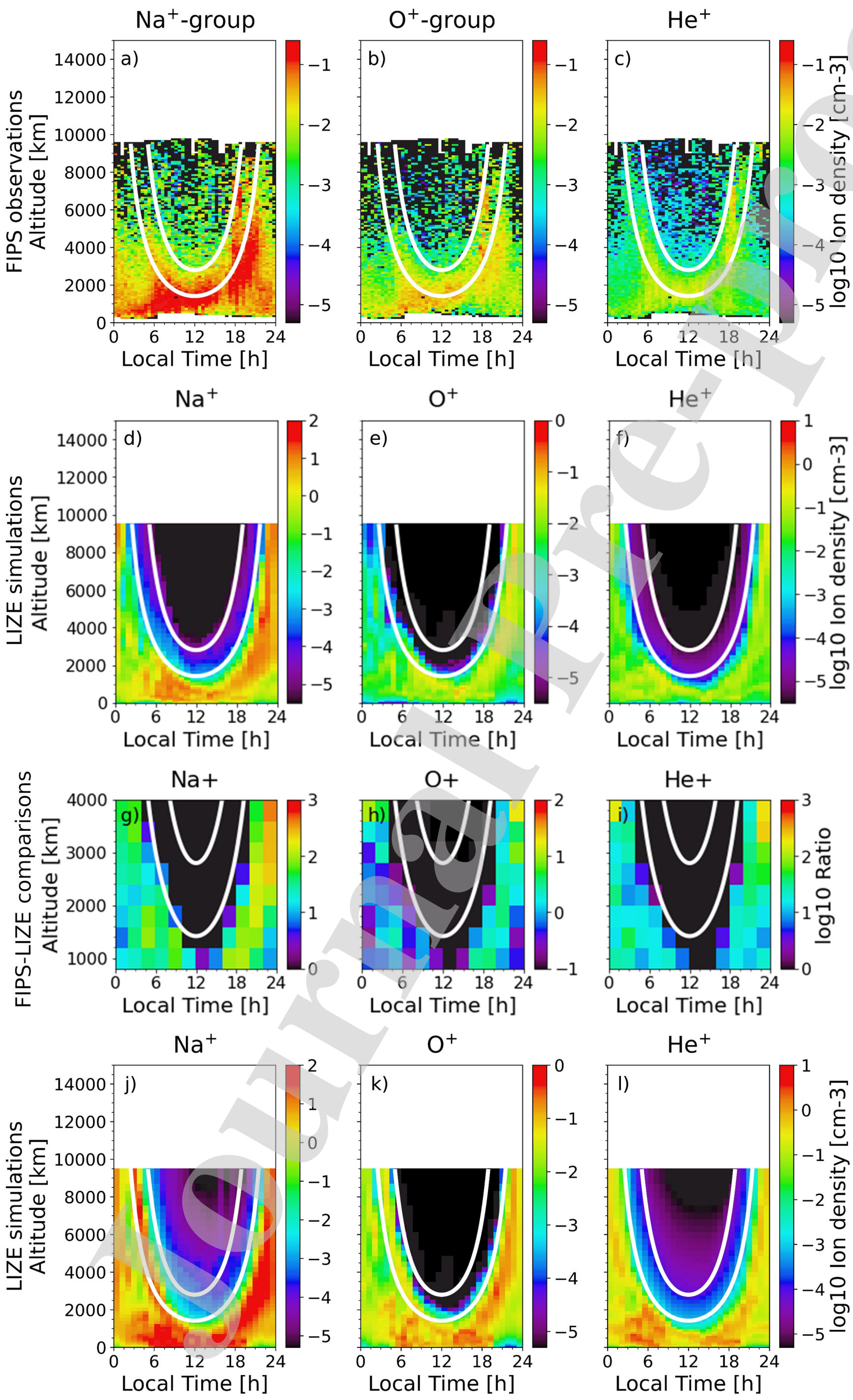
Na+-group
O+-group
He+
a)
b)
c)
FIPS observations
Altitude [km]
0
2000
4000
6000
8000
10000
12000
14000
−1
−2
−3
−4
−5
log10 Ion density [cm-3]
Local Time [h]
0
6
12
18
24
Na+
O+
He+
d)
e)
f)
LIZE simulations
Altitude [km]
2
1
0
−1
−2
−3
−4
−5
log10 Ion density [cm-3]
Na+
O+
He+
g)
h)
i)
FIPS-LIZE comparisons
Altitude [km]
1000
2000
3000
4000
3
2
1
0
−1
log10 Ratio
Na+
O+
He+
j)
k)
l)
LIZE simulations
Altitude [km]
log10 Ion density [cm-3]

Figure 4: (Previous page.) Top row: The average observed ion density by FIPS of the (a) Na^+ group, (b) O^+ group and (c) He^+ in the latitude range ±30°. Second row: Simulated ion density of (d) Na^+, (e) O^+ and (f) He^+ with LIZE using the static magnetic and electric field description by LatHyS, including FIPS energy range and FOV constraints. Third row: Ratio between between the energy range and FOV-corrected simulated ion density and the observed ion density (grid resolution: 400 km, 2 h). The average ion density ratio below the magnetopause is 18 for Na, 0.25 for O and 5.2 for He. Bottom row: the full ion density (no energy range or FOV constraints) simulated with LIZE. The FIPS observations were accumulated between 23 March 2011 and 30 April 2015. The solid white lines show the magnetopause and bow shock boundaries as determined from Winslow et al. (2013). Do note that the sense of the magnetospheric boundaries are reversed in this Figure compared to Figure 3. Thus, points that appear to be located "inside" the parabolas in this Figure are in fact located outside the magnetosphere.

E/q step i in the FIPS energy range and FIPS effective FOV ($\Delta\Omega \approx 1.15\pi\ sr$). n_{obs} is provided for both solar wind ion species (H^+ and He^{++}) and several planetary ion species (Na^+-, O^+-group ions and He^+).

Note that n_{obs} in Raines et al. (2013) was defined slightly differently from Equation 1, in that they did not include the FIPS FOV solid angle in the calculation. Therefore there is at least a 1.15π factor difference in magnitude between Figure 3 in Raines et al. (2013) and 3.3.1 in this paper. The lower energy limit of the FIPS burst observations was decreased from 100 eV to 46 eV in February 2012 (Raines et al., 2013). However, our analysis of the full mission FIPS data set showed very few counts below 100 eV, so the effect of this change is likely very minimal.

Recovered densities from FIPS are also available which make use of techniques to account for the limited FOV under certain assumptions (Raines et al., 2013; Gershman et al., 2013). We did not compare to these densities since they are not available in all regions.

3.3.2. Ion density simulations

The bottom row of Figure 3.3.1 shows the simulated He^+, O^+ and Na^+ ion density from LIZE using the LatHyS electric and magnetic field description. We use the full simulated energy range between $1 - 10^5$ eV. Due to the limited size of the $X > 0$ domain in the AIKEF simulation, we put an upper limit on the simulated ion densities to an altitude of 9500 km. Note that the ion density scale in the top and bottom row of Figure 3.3.1 are different, due to the high simulated densities.

The simulated ion density profiles do not match the absolute magnitude of the FIPS observations. However, both the dawn and the dusk enhancement regions are qualitatively well reproduced. The simulated ion density is highest near the surface (9.3×10^1 Na^+/cm^3, 2.1×10^{-1} O^+/cm^3 and 1.6 He^+cm^{-3}) where the dawn enhancement region is located (04 - 10 h local time). The corresponding FIPS values are: 2.7×10^{-1} Na^+/cm^3, 3.4×10^{-2} O^+/cm^3 and 1.3×10^{-2} He^+/cm^3. The simulated ion density in the magnetosheath is less dense and less extended with altitude compared to the observations. We next consider the effect of FIPS' limited FOV and energy range (0.046 - 13.6 keV) on the simulated ion densities.

The main limitation to FIPS nominal FOV (1.4 π sr) is caused by the sunshade of the spacecraft. The sunshade always points along the positive MSO X-axis irrespective of where the spacecraft is located relative to Mercury. This means that the true FOV extends between 15° from directly behind the sunshade up to 45° from the rear. The FOV is also partially blocked by one of the solar cell panels and other smaller parts on the spacecraft, so that the effective FOV solid angle is 1.15π sr. Since this study considers the ion density distribution averaged over several Mercury years we only consider the main limitations to the FOV along the MSO X-axis (see Figure 5).

The FIPS clock angle, which is defined as the angle between the positive MSO Y-axis and the FIPS boresight, describes the rotation of the spacecraft relative to the MSO frame. Specifically, this defines whether one hemisphere is sampled more than the other. The clock angle distribution for FIPS measurements taken within 0.15 R_{M} of the geometric equator between 2011-2015 is almost equal between the dusk and dawn hemispheres. Therefore, we can assume that FIPS samples both MSO Y-hemispheres in the latitude range ±30°. Due to MESSENGER's highly elliptic polar orbit, the lowest (highest) altitude range in Figure 3.3.1 (top row) will be mostly sampled when the spacecraft is moving toward the north (south) pole. Therefore, the lowest (highest) altitude range may be dominated by ions with $v_z < 0$ ($v_z > 0$). In this study we make the assumption that the FIPS instrument samples MSO $Z > 0$ and $Z < 0$ equally. The ions in our model tend to have small v_z velocities so the specified selection effect is likely not significant near the equatorial plane (see Section 4.4 where we will discuss the ion velocity distribution in greater detail).

The new simulated Na^+, O^+ and He^+ ion density maps that have been corrected for FIPS limited energy range and

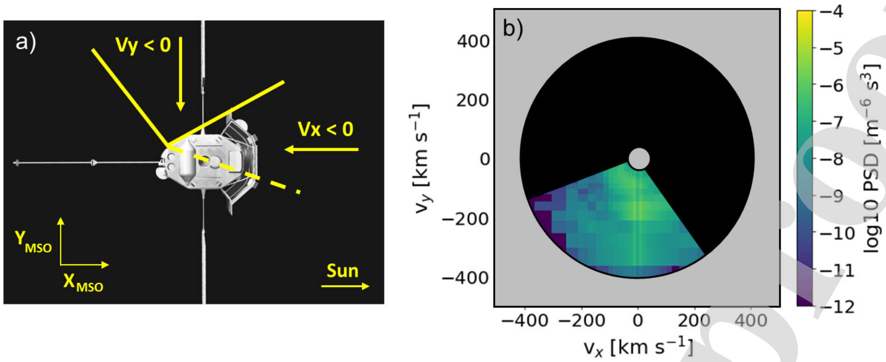

Figure 5: Approximation of (a) FIPS field-of-view (FOV) and the (b) effect of the FIPS energy range (grey) and FOV constraints (black) on an example phase space distribution in the MSO XY plane. The dashed line in (a) shows the extent of FIPS nominal FOV, which is partially obstructed by the sunshade. The model of MESSENGER in Figure 5a was adapted from "Interactive 3D model of the MESSENGER probe" by Fac-tory-o (`https://commons.wikimedia.org/w/index.php?curid=71265802`) under a Creative Commons (CC BY-SA 4.0) licence.

FOV are shown in the second row of Figure 3.3.1. The average ion density has decreased for all species but density enhancement between 18 - 24 h remains. The dawn hemisphere now exhibits a sharp drop-off in ion density before 6 h, similar to what is observed in the FIPS data (top row of Figure 3.3.1). We continue our comparison by making a ratio (see the third row of Figure 3.3.1) between the new simulated and observed ion density. We use a grid with coarser resolution (2 h, 400 km) and reduce the altitude range to 800-6000 km (to exclude bins with few FIPS observations). The average ion density ratio below the magnetopause is 18 for Na$^+$, 5.2 for He$^+$ and 0.25 for O$^+$.

In this study, we have used two hybrid models. On average, AIKEF yields slightly higher ion densities compared to LatHyS but the spatial distribution is nearly identical (see Figure 6). One of the key differences between the two models is a low-altitude (< 1000 km) enhancement region which exists at all local times for AIKEF.

4. Discussion

4.1. Comparison with previous simulations of the Na$^+$ density

When we compare our uncorrected ion density estimate (see Figure 3.3.1d-f) with previous modeling studies of the Na$^+$ ion density distribution in Mercury's magnetosphere (Leblanc et al., 2003; Yagi et al., 2010; Seki et al., 2013; Exner et al., 2020) we find a similar order of discrepancy between the different models and the observations. Leblanc et al. (2003) used the exospheric model described in Leblanc and Johnson (2003) with the analytic magnetospheric model by Delcourt et al. (2003) to trace Na$^+$ ions inside the magnetopause boundary. They found a maximum Na$^+$ density of 10^2/cm^3 at aphelion ($TAA = 180°$), which is close to our uncorrected simulated Na$^+$ density (see Figure 3.3.1). Paral et al. (2010) found a maximum Na$^+$ ion density on the order of 10 cm^{-3} in the equatorial plane for an IMF with a strong northward component. Yagi et al. (2010) modeled the Na$^+$ density for purely northward IMF ($B_z = 10$ nT) with the neutral exosphere model from Leblanc and Johnson (2003) and a MHD magnetospheric model to describe the electromagnetic field environment. Their Case 1 ($n_{sw} = 30$ cm^{-3}, $v_{sw} = 400$ km/s) results gives a similar Na$^+$ density in the dawn hemisphere (10^2 cm^{-3}). Seki et al. (2013) studied the impact of varying southward IMF strength and planetary conductivity on the Na$^+$ ion density distribution using an MHD magnetospheric model. Exner et al. (2020) studied the impact of successively denser versions of a Na$^+$ exosphere on the Mercury field environment. For the standard exosphere they found a maximum Na$^+$ density of 10/cm^3 at the cusps. What is common for all these studies is that the modeled maximum Na$^+$ density is a factor of $10 - 10^3$ times too high compared to the FIPS observations.

Sarantos et al. (2009) used the exospheric Na model from Mura et al. (2007), with a maximum Na surface density of 10^5 cm^{-3} and a MHD simulation with the solar wind IMF profile of the first MESSENGER flyby Benna et al. (2010) to model the distribution of Na$^+$ pickup ions. They studied the ion density distribution of Na$^+$ produced from neutral Na ejected by different source mechanisms. Sarantos et al. (2009) derived a maximum Na$^+$ density of 1 cm^{-3}, which is relatively similar to the observed Na$^+$ ion density by FIPS compared to other modeling studies. The MHD simulation

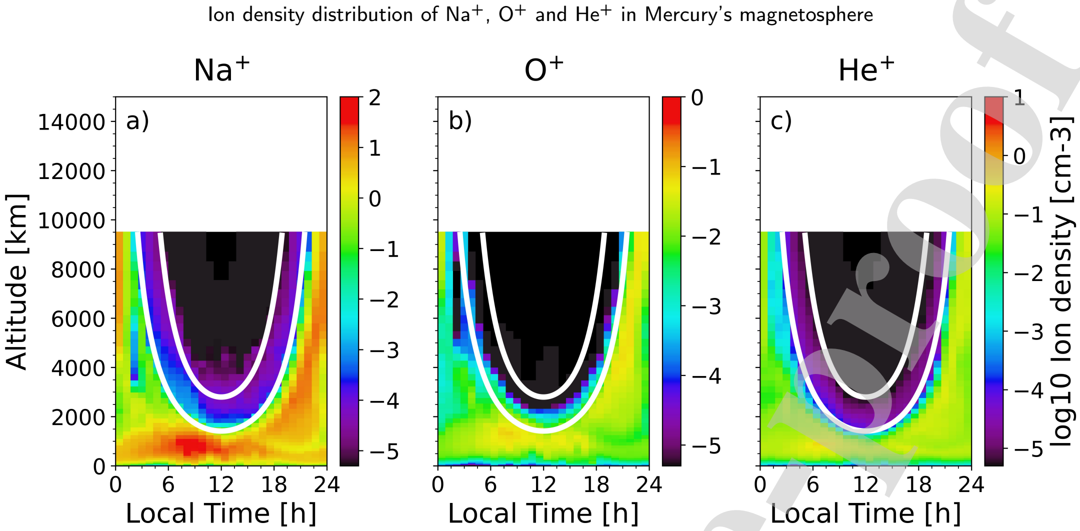

Figure 6: The (a) Na^+, (b) O^+ and (c) He^+ ion density simulated with LIZE using the static magnetic and electric field description by AIKEF.

used in Sarantos et al. (2009) simulation has a lower spatial resolution (122-1952 km) compared to the magnetospheric models in our study. Perhaps for this reason the mean energy of the Na^+ plasma sheet ions in their simulation is 10^2 times higher than in our simulation (see Figure 4 in Sarantos et al., 2009).

4.2. Comparison with other estimates of the ion density

It is also possible to derive the Na^+ density distribution around Mercury from the study of magnetic field-line-resonance (FLR) events (James et al., 2019). FLR events occur when a fast-mode MHD wave converts into a shear Alfvén wave in a non-uniform plasma environment. If this occurs near Mercury's dipole magnetic field, the resonant wave coupling may cause the formation of a standing wave in the closed magnetic field lines, oscillating at the fundamental plasma frequency (Glassmeier et al., 2004). At Mercury a subset of these waves has a frequency that lies below the local Na^+ ion gyro frequency, which indicates that the field line resonance is formed in a plasma dominated by Na^+ ions. James et al. (2019) identified such events using MAG data, the KT17 magnetic field line model (Korth et al., 2015, 2017) and a simple power-law model of the plasma mass density to map the ion density inside the closed field-line-region in the dayside magnetosphere. The plasma density estimate that can be inferred using this method is not limited by a specific energy range or FOV. Using a relaxed Earth-type FLR event criteria James et al. (2019) inferred a maximum plasma mass density of 500 amu/cm^3, which would imply a dayside Na^+ surface density of approximately 22/cm^3 (Exner et al., 2020).

Figure 7 shows the Na^+ ion density in the equatorial plane in units of amu/cm^3 (comparable to Figure 6e in James et al., 2019). The contribution from He^+ and O^+ to the total plasma mass density is negligible. Although our simulated Na^+ density is higher compared to Figure 6e in James et al. (2019), the difference is considerably lower than direct comparison with the FIPS observations. Most importantly, the maximum simulated plasma mass density near the surface (550 amu/cm^3 or 24 Na^+/cm^3) is a close match to James et al. (2019)'s estimate.

Another in-situ observation we could refer to get some clues about the ion density magnitude in the Hermean magnetosphere are the Mariner 10 Mercury flybys. During the Mariner 10 flyby on 1974 March 29, the electrostatic analyzer took electron density measurements in Mercury's plasma wake (Ogilvie et al., 1974). The spacecraft entered the magnetosphere from dusk in the southern magnetospheric lobe and exited at dawn in the north. The spacecraft reached a minimum altitude of 700 km from the surface near midnight local time in the equatorial plane at closest approach.

We model the Na^+, O^+, He^+ and solar wind H^+ ion density with LIZE along the trajectory of Mariner 10. For the electric and magnetic fields, we use the northward B_z LatHyS simulation with n_{sw} = 45.7/cm^3 and v_{sw} = 500 km/s from the end of Section 3. The solar wind properties of this run matches the observed electron energy spectra just

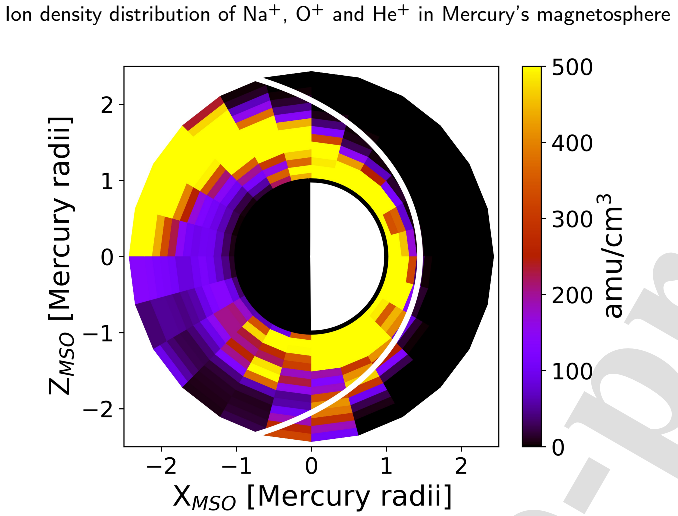

Figure 7: The simulated Na$^+$ ion density in the equatorial plane expressed in amu/cm^3 and plotted with the same color map and in the same scale as Figure 4e and 6e in James et al. (2019).

prior to the spacecraft's entry into the magnetosphere (Ogilvie et al., 1974). We compare the observed electron density with the different simulated ion densities (full energy range and FOV) between 20:41-20:47 UTC which is when the spacecraft first enters the planet's shadow until the time of closest approach. We find that the modeled Na$^+$ ion density in this region is much smaller (0.5-1.0 Na$^+$/cm^3) than the H$^+$ (3.7-9.0 H$^+$/cm^3) or the electron density ($<$ 6.2 e/cm^3). The He$^+$ and O$^+$ densities are negligible. The comparatively low Na$^+$ density implies that the model does not give results which directly contradicts the Mariner 10 electron density observations.

4.3. Intrinsic limits of our simulated ion density

In our EGM simulation of the Na exosphere the near-surface density is $\sim$ 5 times higher at the dawn terminator compared to the subsolar point. The EGM model reproduces the dusk-dawn asymmetry at aphelion observed by UVVS Cassidy et al. (2016). UVVS and THEMIS observations of the Na exosphere near aphelion indicates however that the maximum Na density in the exosphere is located near the subsolar point Milillo et al. (2021); Cassidy et al. (2016). This discrepancy is unlikely to affect the large-scale ion density distribution due to the fast configuration speed of the ions.

Due to the special geometry of the MESSENGER orbit, the ion density at each local time was sampled by FIPS at a particular TAA. The data at 6 - 12 h local time was, for instance, taken when Mercury was located between TAA= $0° - 90°$. The Na exosphere has a strong dawn peak during this part of the orbit (Cassidy et al., 2015, 2016), which might help explain the Na$^+$ enhancement at dawn in Figure 3.3.1a.

The static electromagnetic field environments used in our study may be responsible for the large underestimation of the ion density upstream of the magnetopause (Figure 3.3.1). Without a time-dependent electromagnetic field description it is not possible to account for temporal variations of the position of the magnetic boundaries, magnetic reconnection and other plasma processes.

The average O$^+$ ion density in our simulation is low in comparison to Na$^+$ or He$^+$. Since the O$^+$-group includes several species it is possible that O$^+$ is not the main constituent of the total O$^+$-group ion density (Vervack et al., 2016). It may therefore be necessary to consider the photo-ionization of water ices on Mercury. The Na$^+$-group includes several ion species with similar mass-per-charge ratio to Na$^+$, which includes Mg$^+$, Al$^+$ and Si$^+$. The neutral Mg exosphere is thin (5-50/cm^3 at the surface; Merkel et al., 2017) and the Mg photo-ionization rate (6.5×10^{-7} s^{-1}; Huebner and Mukherjee, 2015) is low compared to Na. Therefore Mg$^+$ is unlikely to make a large contribution to the total Na$^+$-group ion density. Evans et al. (2012) inferred a Si (weight) surface abundance of 24.6% with observations by the Gamma-Ray and Neutron Spectrometer (GRNS) on MESSENGER, which corresponds to a number density that is approximately half that of Na. Al has been observed in Mercury's exosphere with ground-based observations (Bida et al., 2000; Bida and Killen, 2017) and by MESSENGER (Vervack et al., 2016). In adddition, both Al and Si

Table 4
Parameters of the LIZE simulations with different solar wind and IMF conditions. The ion density ratio is defined as the average ratio between the simulated and observed ion density in the altitude range 800-6000 km and below the magnetopause boundary.

Parameter	Nominal case	Case 1	Case 2	Case 3
Time step:	0.02 s	0.05 s	0.05 s	0.05 s
Spatial resolution:	145 km	112 km	112 km	237 km
Number of solar wind particles per cell:	H$^+$: 20 He^{++}: 2	H$^+$: 5 He^{++}: 2	H$^+$: 5 He^{++}: 2	H$^+$: 5 He^{++}: 2
Solar wind number	30 cm^{-3}	50 cm^{-3}	50 cm^{-3}	11 cm^{-3}
Solar wind velocity:	400 km/s	500 km/s	400 km/s	400 km/s
Solar wind magnetic field (B_x, B_y, B_z) [nT]:	(0, 0, 20)	(- 10, 7.5, 13)	(-9.3, 7.7, -13)	(-9.3, 7.7, -13)
Ion density ratio:	Na$^+$: 18 He$^+$: 5.2	Na$^+$: 2.7 He$^+$: 1.1	Na$^+$: 1.6 He$^+$: 0.8	Na$^+$: 0.8 He$^+$: 0.5

have very high photo-ionization rates (Al: 1.2×10^{-3} s^{-1} and Si: 2.29×10^{-5} s^{-1}; Huebner and Mukherjee, 2015) compared to Na. Jasinski et al. (2020)'s estimate of the Al and Si ion production rate (3-7.5/cm^3 at 1500 km) during a large meteoroid impact event can be considered as an upper limit.

Our simulated ion densities reflect a single set of solar wind plasma conditions, IMF orientation and orbital phase. In comparison, the FIPS data displayed in Figure 3.3.1a-c represent an average over 17 Mercury years of observations, and accounts for a wide range of solar wind and exospheric conditions. As the FIPS data reflect the average state of the exosphere, some features may not be as prominent in the FIPS observations as in the simulated ion density. The dusk enhancement region is very dense compared to other regions in our simulation and extends to higher altitudes compared to the observations. This may be an effect of the electric field environment that the test-particle encounter at the flanks of the dayside magnetopause boundary. For solar wind IMF $B_z > 0$ we get $E_y < 0$ in the solar wind (and the magnetosheath). Ions that encounter the duskside magnetopause flank are affected by a strong $E_x < 0$ environment and $E_y < 0$, which will cause these ions to be pushed deep into the low electric field environment of the nightside plasma sheet. The pink-purple Na$^+$ test-particle trajectory in Figure 8 shows an example of this effect. Ions that approach the magnetopause flank from the dawnside experience $E_x > 0$, which makes them more likely to be picked up by the solar wind and quickly escape the Mercury environment. Therefore, for the specific solar wind IMF studied here we will naturally get a low-density, high-energy dawnside ion population and a high-density duskside. The dusk enhancement could also be be due to the non-adiabatic ion acceleration mechanism described in Delcourt et al. (2003), but the northward IMF B_z may inhibit its effects. The blue-cyan Na$^+$ test-particle trajectory in Figure 8 shows a possible example of this acceleration mechanism in action. The sudden increase in energy after 4 minutes when the test-particle was located close the surface near the north pole indicates that it may have experienced centrifugal ion acceleration (compare to Figure 2 in Delcourt et al., 2003).

The strictly northward solar wind IMF and the low solar wind ram pressure of the electromagnetic field environment considered in this work is not necessarily the most commonly observed solar wind environment at Mercury (Sarantos et al., 2007). In order to consider the impact of different solar wind conditions on the modeled ion density, we model Na$^+$, O$^+$ and He$^+$ using three additional LatHyS simulations (see Table 4). We find that the average ion densities computed from these simulations are much closer to the observed values. The difference between model and observations range between a factor of 0.8-1.5 for Na$^+$ and 0.5-1.1 for He$^+$. The O$^+$ density tends to be underestimated. However, although the average ion density ratio is improved the spatial distribution is very different from our nominal case. Following the argument concerning the sign of $E_x, /E_y$ and their impact on the properties of the ion populations on either side of the nightside plasma sheet, we find that Cases 1-3 result in weaker dusk- and stronger dawn enhancement than expected from the FIPS observations. The LatHyS simulations corresponding to Cases 1-3

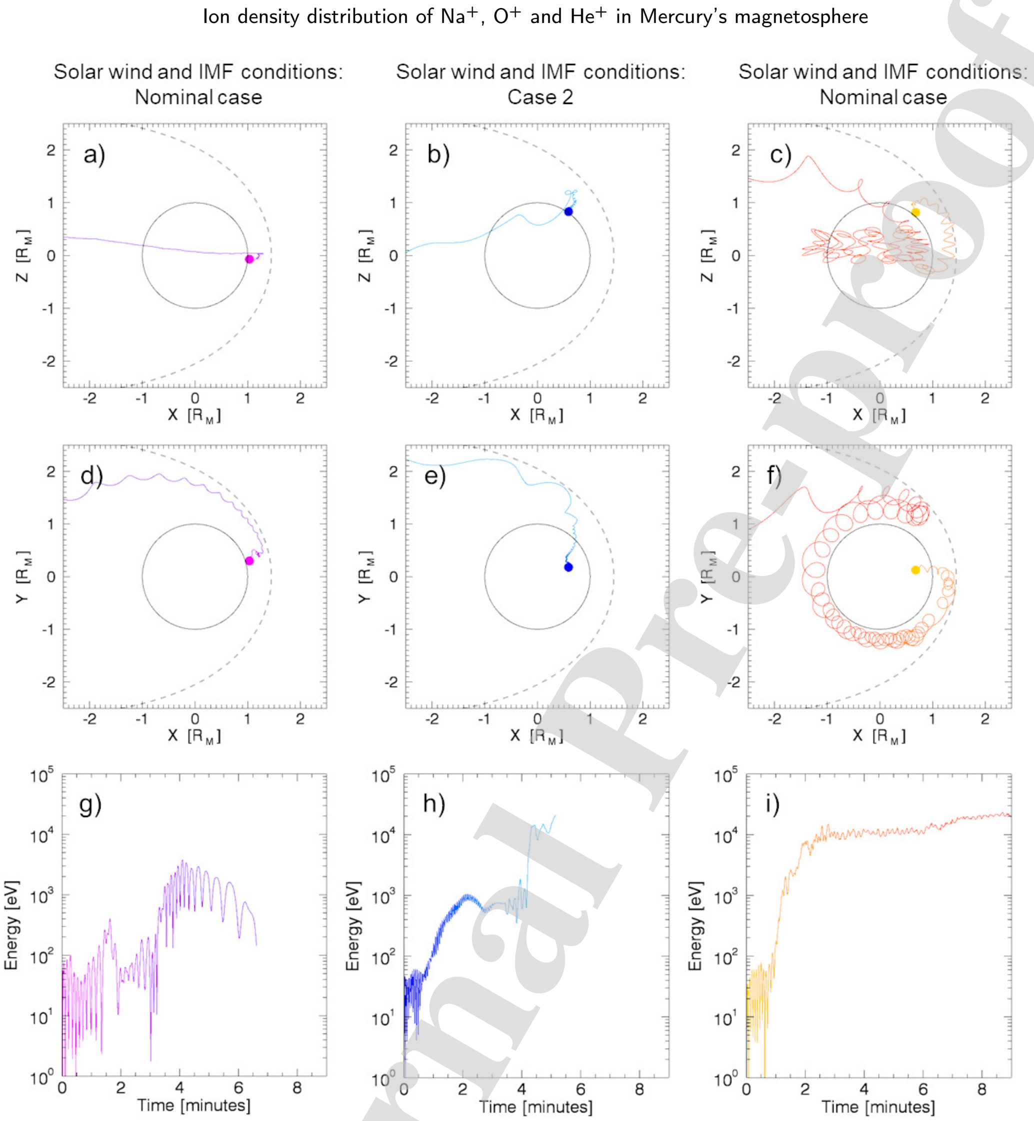

Figure 8: Model test-particle trajectories of Na$^+$ ions from the Latmos IoniZed Exosphere model in the (a-c) MSO XZ-plane and the (d-f) XY-plane. The time-evolution of the test-particle ion energy are shown in (g-i). The dashed curves in (a-f) shows the average location of Mercury's magnetopause. The three test-particles were launched in the dayside magnetosphere (b, c) near the north pole and (a) near the subsolar point (start location shown by the dot markers). The test-particles experience different electromagnetic fields: (a, c) solar wind and IMF conditions corresponding to the nominal case in Table 4 and (b) Case 2 in Table 4. The color gradient in each trajectory shows the evolution of time.

have a lower resolution compared to our nominal case, which may result in higher electric fields in low-density regions inside the magnetosphere which would result in higher test-particle acceleration and lower densities. Regardless, it is clear that the ion density distribution of heavy ions around Mercury have the potential of being highly variable. Since the ion density observations by FIPS discussed in this paper reflects a wide range of solar wind and exosphere conditions, it may be necessary to test more representative solar wind and IMF conditions in order to re-produce the observed distribution as closely as possible.

Global models of Mercury's magnetosphere tend to underestimate the magnetopause reconnection rate for northward solar wind IMF boundary conditions. In effect, this likely causes the average level of Dungey cycle circulation (Dungey, 1961) to be underestimated. Therefore the planetary ion population in our nominal $B_z > 0$ simulation may experience an uncharacteristically weak electric field environment. This aspect could partly explain why we're seeing such a large factor difference between our model results and the FIPS observations for that specific IMF orientation. The low-altitude enhancement in the modeled ion density profiles with AIKEF may be an another effect of the underestimated ion dynamics on the magnetosphere. This ion population is comparatively energetic (10^4 eV) compared to ions at higher altitudes and may be the result of a quasi-trapped ion ring, similar to what has been proposed in Yagi et al. (2010, 2017). Indeed, the the yellow-orange Na$^+$ test-particle trajectory in Figure 8 and other test-particle trajectories in this region show a remarkable similarity to Figure 10 in Yagi et al. (2010) and Figure 3 in Yagi et al. (2017) respectively. The large magnetopause standoff distance during northward IMF and the steady-state magnetospheric fields used in our simulations are likely favorable for the formation of a quasi-steady ring distribution. If the IMF is southward or the short-term variability of the IMF is accounted for the ring distribution may not be as complete as indicated here.

4.4. Reconstruction of the phase space density (PSD)

Judging from Figure 3.3.1j-l the ratio between the simulated and the observed ion densities are not homogeneous. The simulated ion densities tend to diverge more from the observed values with increasing distance from the surface, which is most evident at midnight local time. The ratio is higher in the dusk enhancement region than at dawn, and it is very low near the magnetopause boundary at noon. To investigate the impact of FIPS FOV on the ion density distribution in the magnetosphere in more detail it is necessary to model the phase space density (PSD) distribution.

We model the PSD distribution in four different regions and investigate how FIPS energy range and FOV affects the sampling of the simulated ion density distribution. We select regions located at noon and the dawn enhancement region in the dayside magnetosphere, the dusk enhancement region on the nightside and the dawn magnetosheath (see Figure 9a). The four regions are all centered in the magnetic equatorial plane and range in size between $(\Delta x)^3 = (300\text{km})^3$ to $(\Delta x)^3 = (750\text{km})^3$. Inside the magnetic equatorial plane the FIPS clock angle is such that the boresight of the instrument is predominantly directed toward the dusk hemisphere (approximately 4 times more frequently). Therefore we will only consider the $v_y < 0$ sector in the $v_x - v_y$ plane (see Figure 9). We first compute the PSD on a spherical grid (E, θ, ϕ) with LIZE and then make a transformation to Cartesian velocity coordinates (v_x, v_y, v_z). This allows us to plot $v_x - v_y$ and $v_x - v_z$ slices of the 3-D PSD distribution.

As shown by Figure 9, the Na$^+$ PSD has a distinct spatial distribution in each of the four region. The PSD in Region A is dominated by a dawnward ($v_y < 0$) drift (see Figure 9b). The proximity of Region A to the magnetopause and the strong influence of the dawn- and anti-sunward drift of the solar wind convection field near Region A may be the cause of this particular distribution. Since the FIPS boresight is typically pointing toward the dusk hemisphere in this region, it is well suited to sample a PSD of this type. However, a slice of the same PSD distribution in the $v_x - v_z$ plane reveals that the PSD is concentrated to a narrow region around the MSO X-axis that is blocked from FIPS FOV by the sunshade (Figure 9c). This means that only a fraction of the PSD will be detected by FIPS despite the favorable distribution of the PSD in the $v_x - v_y$ plane. The distribution is far from being isotropic, yet the PSD tends to be more isotropic at lower energies (see Figure 9c).

Region B has a ring-like PSD distribution in the XY plane (Figure 9d) and is rather isotropic in the XZ plane (Figure 9g). Although the maximum of the PSD distribution in Region C (Figure 9e) appears to be located inside FIPS energy range, the global maximum is actually located below FIPS lower energy range (at approximately 10 eV). The PSD in Region D (Figure 9f) resembles a pick-up ion distribution. This implies that the Na$^+$ ions in Region D have been accelerated from outside the magnetopause into the dawn magnetosheath. The PSD distribution of this region peaks at velocities well outside the upper energy range of FIPS in both the $v_x - v_y$ and the $v_x - v_z$ plane, which makes the ions in this region invisible to FIPS.

Although the relative intensity of the PSD differs between the three different species, the spatial distribution is very similar in the MSO XY and XZ plane (see Figure A1-A3 in the appendix). The PSD distribution in Region D has been omitted for O$^+$ due to poor statistics. It is interesting to note that in contrast to Na$^+$, the He$^+$ PSD distribution in Region D falls inside the upper limit of FIPS energy range. In the XZ plane, the PSD distribution is generally concentrated to the non-observable part of phase space for FIPS. The PSD in Region B has the most dispersion in the XZ plane, likely because this region is located far away from the planet and the ions transported here have had more time to disperse. On average LatHyS and AIKEF yields very similar PSD distributions. One key difference between the two models is that

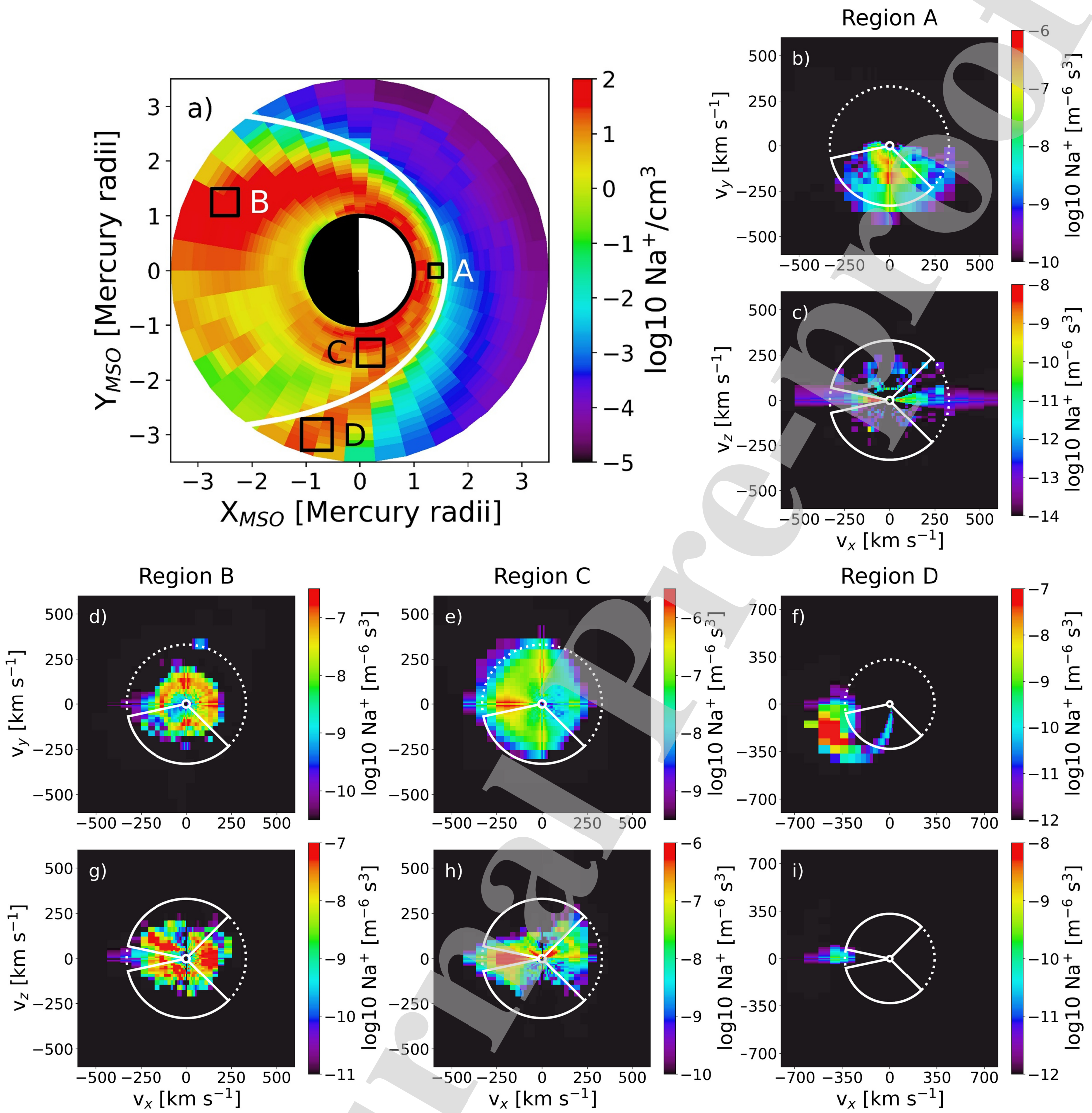

Figure 9: (a) Location of Regions A-D and the uncorrected Na$^+$ ion density in the equatorial plane. Selected cuts of the Na$^+$ PSD in the (b-c) MSO $v_x - v_y$ plane ($v_z = 0$) and the (d-g) $v_x - v_z$ plane ($v_y = 0$). The dotted circles in (b-g) mark the lower and upper energy limit of the FIPS energy range. The circle sectors marked with solid lines illustrate the FIPS limited FOV.

the PSD computed with AIKEF in Region B is concentrated to lower energies in the XY plane and is less dispersed in the XZ plane compared to LatHyS. This suggests that the electric field in Region B is lower in the AIKEF simulation than for LatHyS. Indeed, the anti-sunward component of the electric field in the AIKEF simulation is -0.09 mV/m in Region B compared to -0.8 mV/m for LatHyS.

5. Conclusions

We have analyzed the average ion density and spatial distribution in the equatorial plane inside Mercury's magnetosphere of the Na$^+$-group, O$^+$-group and He$^+$, which were observed by FIPS onboard MESSENGER during the whole orbital mission from 23 March 2011 to 30 April 2015. We developed a test-particle model that describes the full equation of motion of planetary ions produced from photo-ionization of Mercury's neutral exosphere. The model is coupled to a test-particle model of the neutral exosphere (EGM; Leblanc et al., 2017b) and two hybrid models of the electric and magnetic fields in the magnetosphere (LatHyS and AIKEF; Modolo et al., 2016; Müller et al., 2012). We modeled the neutral Na, O and He exospheres at aphelion with EGM and used static electromagnetic field simulations from the two models using the same set of solar wind input parameters to model the ionized Na$^+$, O$^+$ and He$^+$ exospheres for northward IMF conditions. We take the FIPS energy range and FOV constraints into account when we later compare our simulated ion densities with the FIPS ion density observations.

The model reproduces the spatial distribution of the FIPS observations but the average ion density (corrected for FIPS FOV) is between 5-18 times too high compared to the observations. These values were calculated for strictly northward IMF conditions ($B_z = +20$ nT), which might have caused the average Dungey cycle strength to be underestimated (and the ion density to be overestimated). The discrepancy between model and observations is lower (0.8-2.7 for Na$^+$ and 0.5-1.1 for He$^+$) for other solar wind and IMF conditions. The model based on a simple neutral O exosphere tends to underestimate the observed O$^+$ density. The magnitude of the simulated Na$^+$ density uncorrected for the FIPS energy range and field-of-view is roughly in agreement with previous simulation studies (Leblanc et al., 2003; Paral et al., 2010; Yagi et al., 2010; Seki et al., 2013; Exner et al., 2020) even for the nominal case ($B_z = +20$ nT). We also compare our results with plasma mass density measurements inferred from FLR event observations with the MAG instrument (James et al., 2019) and electron density measurements taken by Mariner 10 in the wake of the planet on 29 March 1974 (Ogilvie et al., 1974).

Finally, we model the phase space density distribution in four different regions: at noon and dawn in the dayside magnetosphere, in the dusk magnetotail and the dawn flank of the magnetosheath. We find that the PSD is commonly concentrated to a narrow region surrounding the v_x axis in the $v_x - v_z$ plane. This particular region in phase space is blocked from FIPS FOV due to MESSENGER's sunshade, meaning that only a fraction of the total PSD can be observed. Only the relative magnitude of the PSD distribution appears to be mass-dependent and the distribution in phase space is very similar between the three different species.

The results of this study highlight the limitations of using a steady-state electromagnetic field simulation to model the ion density distribution around Mercury. The phase space density distribution of heavy planetary ions are not necessarily isotropic and vary across different regions around Mercury. One of the largest assets of EGM is its capability to give an accurate description of the exosphere at several points along Mercury's orbit. The results by Raines et al. (2013); Jasinski et al. (2021) on the variation of the global Na$^+$-group ion density along the Mercury year may suggest there is a link between the seasonal neutral Na exosphere and the Na$^+$-group ion distribution in the magnetosphere. We plan to investigate this link with LIZE in more detail in future work.

BepiColombo, which will enter into orbit around Mercury in late 2025, will provide the first in-situ measurements around Mercury since the end of the MESSENGER mission in 2015. Planetary Ion Camera (PICAM) on the Mercury Planetary Orbiter (MPO) has an energy resolution between 1 eV - 3 keV and instantaneous 2π sr FOV (Orsini et al., 2010) and is uniquely suited to study low-energy ions near the surface and ions which have been recently formed. The Mercury Ion Analyzer (MIA) and the Mercury mass Spectrum Analyzer (MSA) on the Mercury Magnetospheric Orbiter (MMO; renamed to MIO after the launch) will be able to sample ions with a wide range of energies (5 eV/e - 30/40 keV/e; Saito et al., 2010). Both instruments have an instantaneous 8-10° × 360° of view, which will also make it possible to obtain the full three-dimensional distribution function of the observed ions. Finally, the UV spectrometer Probing of Hermean Exosphere By Ultraviolet Spectroscopy (PHEBUS; Chassefière et al., 2010) on MPO will make the first in-situ measurements of the neutral He exosphere since Mariner 10 and, for the first time, enable the study of the coupling between the neutral and ionized He exosphere.

6. Acknowledgments

A.L.E.W., F.L., J.-Y.C. and R.M acknowledges the support by ANR of the TEMPETE project (grant ANR-17-CE31-0016). S.A., F.L., J.-Y.C., R.M and A.L.E.W. would like to acknowledge the support of CNES for the Bepi-Colombo mission. W.E. was supported by DFG (German Research Foundation) under contract HE8016/1-1. C.S.

acknowledges NASA's support of this study under grant 80NSSC19K0790. The FIPS_NOBS data set from the entire orbital phase was obtained from the Planetary Data System (`https://pds-ppi.igpp.ucla.edu/search/view/?f=yes&id=pds://PPI/MESS-E_V_H_SW-EPPS-3-FIPS-DDR-V2.0`). A.L.E.W., S.A., F.L., J-Y.C. and R.M thanks the IPSL data center CICLAD for providing access to their computing resources. W.E. and U.M. acknowledge the North-German Supercomputing Alliance (HLRN) for providing HPC resources that have contributed to the research results reported in this paper. LIZE simulation files are available upon request.

A. Appendix

This appendix includes additional figures of the PSD distribution for Na$^+$ (Figure A1), O$^+$ (Figure A2) and He$^+$ (Figure A3). The figures show the PSD distribution in the MSO $v_x - v_y$ and $v_x - v_z$ plane for both the LatHyS and AIKEF. Figure A2 only includes Region A-C.

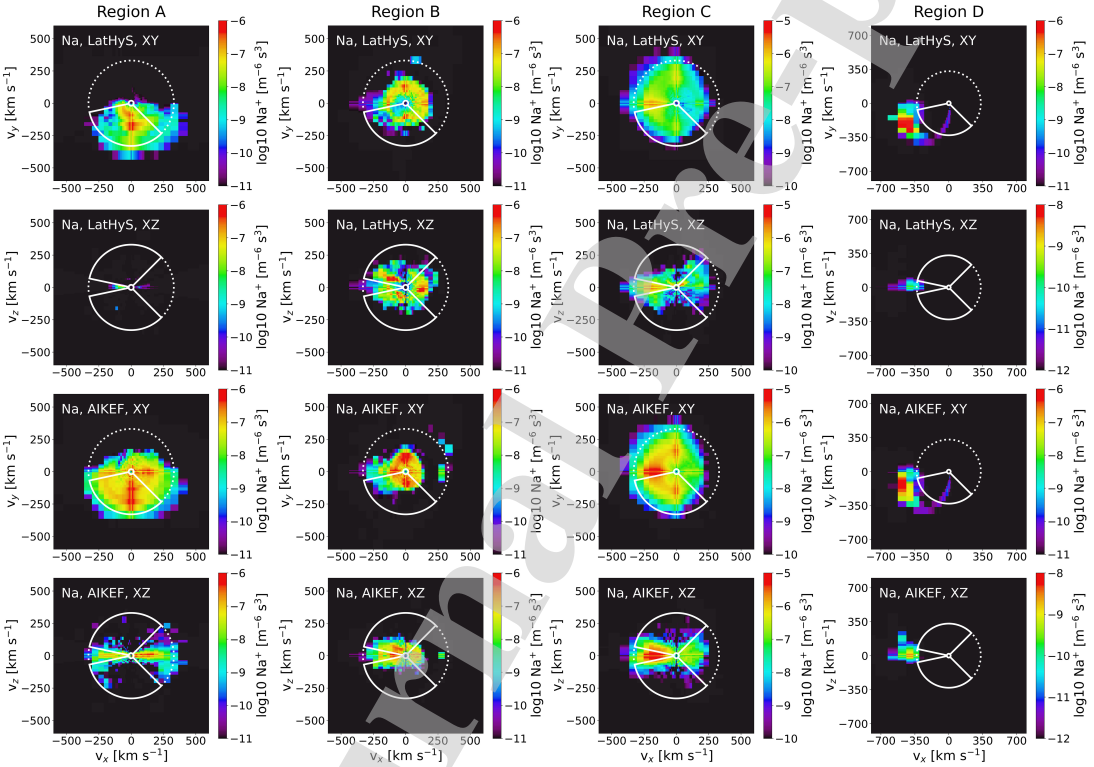

Figure 10: Slices of the Na$^+$ PSD in the MSO $v_x - v_y$ plane ($v_z = 0$) and the $v_x - v_z$ plane ($v_y = 0$) in Regions A-D computed with the magnetic and electric fields supplied by LatHyS and AIKEF.

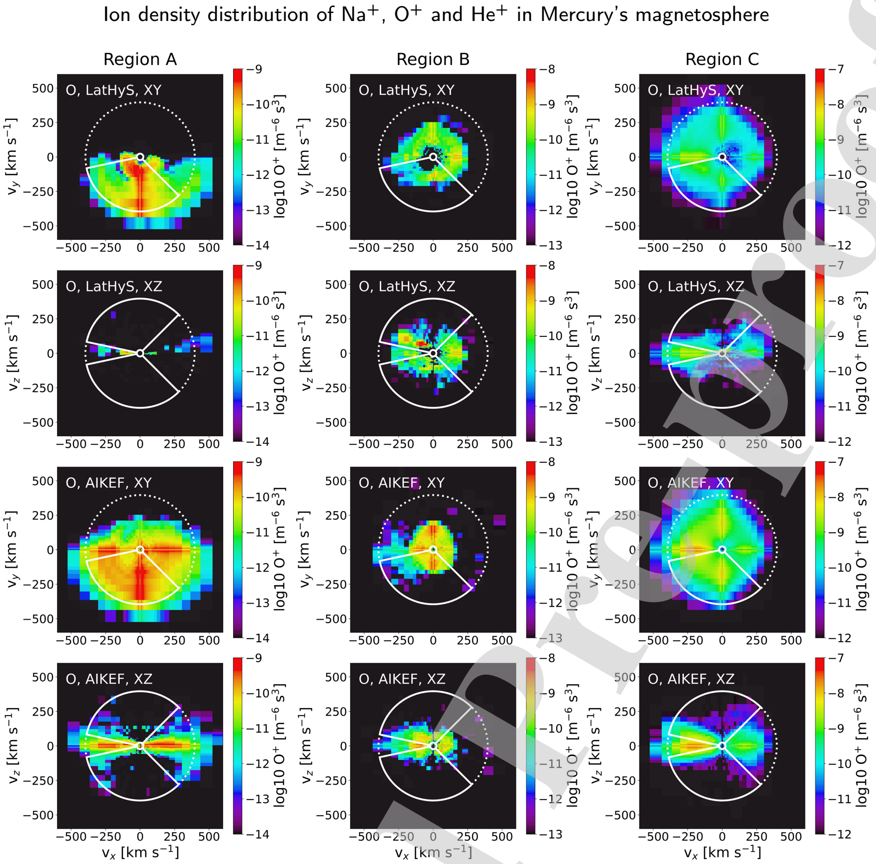

Figure 11: Slices of the O$^+$ PSD in the MSO $v_x - v_y$ plane ($v_z = 0$) and the $v_x - v_z$ plane ($v_y = 0$) in Regions A-C computed with the magnetic and electric fields supplied by LatHyS and AIKEF.

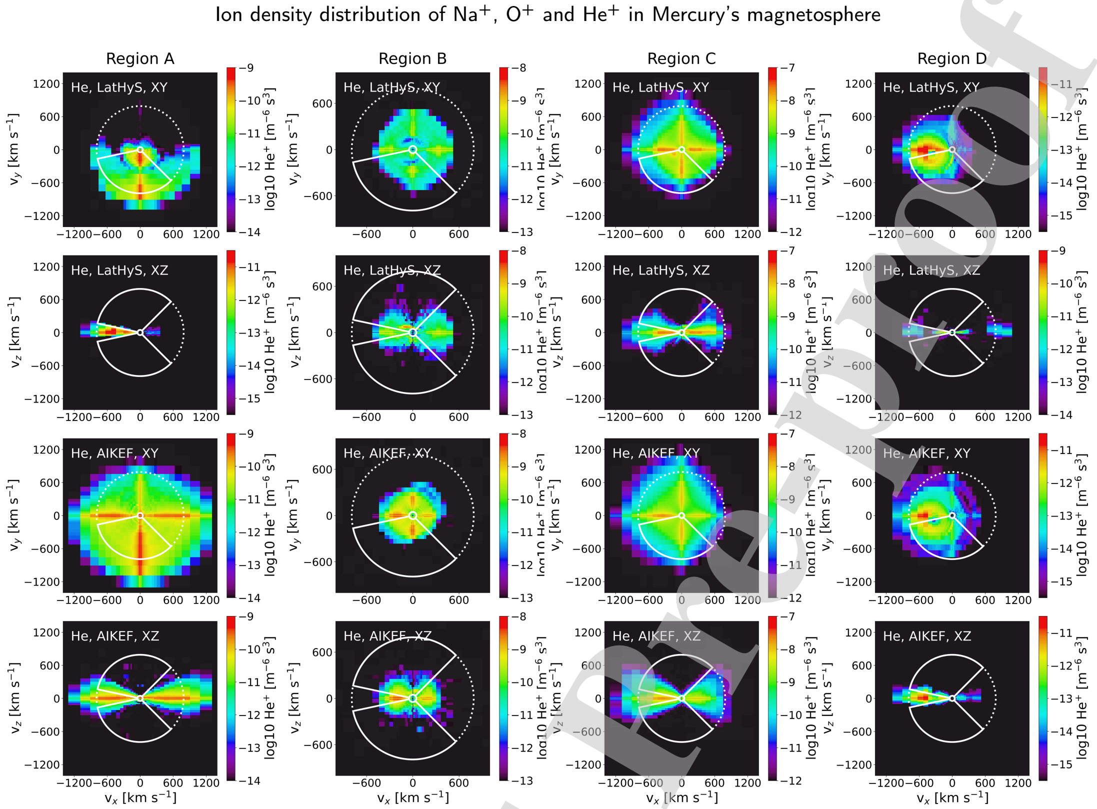

Figure 12: Slices of the He$^+$ PSD in the MSO $v_x - v_y$ plane ($v_z = 0$) and the $v_x - v_z$ plane ($v_y = 0$) in Regions A-D computed with the magnetic and electric fields supplied by LatHyS and AIKEF.

References

Aizawa, S., Griton, L.S., Fatemi, S., Exner, W., Deca, J., Pantellini, F., Yagi, M., Heyner, D., Génot, V., André, N., Amaya, J., Murakami, G., Beigbeder, L., Gangloff, M., Bouchemit, M., Budnik, E., Usui, H., 2021. Cross-comparison of global simulation models applied to Mercury's dayside magnetosphere. Planetary and Space Science 198, 105176. doi:10.1016/j.pss.2021.105176.

Anderson, B.J., Johnson, C.L., Korth, H., Purucker, M.E., Winslow, R.M., Slavin, J.A., et al., 2011. The Global Magnetic Field of Mercury from MESSENGER Orbital Observations. Science 333, 1859. doi:10.1126/science.1211001.

Andrews, G.B., Zurbuchen, T.H., Mauk, B.H., Malcom, H., Fisk, L.A., Gloeckler, G., Ho, G.C., Kelley, J.S., Koehn, P.L., Lefevere, T.W., Livi, S.S., Lundgren, R.A., Raines, J.M., 2007. The Energetic Particle and Plasma Spectrometer Instrument on the MESSENGER Spacecraft. Space Science Reviews 131, 523–556. doi:10.1007/s11214-007-9272-5.

Benna, M., Anderson, B.J., Baker, D.N., Boardsen, S.A., Gloeckler, G., Gold, R.E., et al., 2010. Modeling of the magnetosphere of Mercury at the time of the first MESSENGER flyby. Icarus 209, 3–10. doi:10.1016/j.icarus.2009.11.036.

Bida, T.A., Killen, R.M., 2017. Observations of the minor species Al and Fe in Mercury's exosphere. Icarus 289, 227–238. doi:10.1016/j.icarus.2016.10.019.

Bida, T.A., Killen, R.M., Morgan, T.H., 2000. Discovery of calcium in Mercury's atmosphere. Nature 404, 159–161. doi:10.1038/35004521.

Broadfoot, A.L., et al., 1976. Mariner 10: Mercury atmosphere. Geophysical Research Letters 3, 577–580. doi:10.1029/GL003i010p00577.

Cassidy, T.A., McClintock, W.E., Killen, R.M., Sarantos, M., Merkel, A.W., Vervack, R.J., Burger, M.H., 2016. A cold-pole enhancement in Mercury's sodium exosphere. Geophysical Research Letters 43, 11,121–11,128. doi:10.1002/2016GL071071.

Cassidy, T.A., Merkel, A.W., Burger, M.H., Sarantos, M., Killen, R.M., McClintock, W.E., Vervack, R.J., 2015. Mercury's seasonal sodium exosphere: MESSENGER orbital observations. Icarus 248, 547–559. doi:10.1016/j.icarus.2014.10.037.

Cassidy, T.A., Schmidt, C.A., Merkel, A.W., Jasinski, J.M., Burger, M.H., 2021. Detection of Large Exospheric Enhancements at Mercury due to Meteoroid Impacts. The Planetary Science Journal 2. doi:10.3847/PSJ/ac1a19.

Chassefière, E., Maria, J.L., Goutail, J.P., Quémerais, E., Leblanc, F., Okano, S., Yoshikawa, I., Korablev, O., Gnedykh, V., Naletto, G., Nicolosi, P., Pelizzo, M.G., Correia, J.J., Gallet, S., Hourtoule, C., Mine, P.O., Montaron, C., Rouanet, N., Rigal, J.B., Muramaki, G., Yoshioka, K., Kozlov, O., Kottsov, V., Moisseev, P., Semena, N., Bertaux, J.L., Capria, M.T., Clarke, J., Cremonese, G., Delcourt, D., Doressoundiram, A., Erard, S., Gladstone, R., Grande, M., Hunten, D., Ip, W., Izmodenov, V., Jambon, A., Johnson, R., Kallio, E., Killen, R., Lallement, R., Luhmann, J., Mendillo, M., Milillo, A., Palme, H., Potter, A., Sasaki, S., Slater, D., Sprague, A., Stern, A., Yan, N., 2010. PHEBUS: A double ultraviolet spectrometer to observe Mercury's exosphere. Planetary and Space Science 58, 201–223. doi:10.1016/j.pss.2008.05.018.

Delcourt, D.C., Grimald, S., Leblanc, F., Berthelier, J.J., Millilo, A., Mura, A., et al., 2003. A quantitative model of the planetary Na+ contribution to MercuryÂ's magnetosphere. Annales Geophysicae 21, 1723–1736. doi:10.5194/angeo-21-1723-2003.

Delcourt, D.C., Moore, T.E., Orsini, S., Millilo, A., Sauvaud, J.A., 2002. Centrifugal acceleration of ions near Mercury. Geophysical Research Letters 29. doi:10.1029/2001GL013829.

Dong, C., Wang, L., Hakim, A., Bhattacharjee, A., Slavin, J.A., DiBraccio, G.A., Germaschewski, K., 2019. Global Ten-Moment Multifluid Simulations of the Solar Wind Interaction with Mercury: From the Planetary Conducting Core to the Dynamic Magnetosphere. Geophysical Research Letters 46, 11,584–11,596. doi:10.1029/2019GL083180.

Doressoundiram, A., Leblanc, F., Foellmi, C., Erard, S., 2009. Metallic Species in Mercury's Exosphere: EMMI/New Technology Telescope Observations. The Astrophysical Journal 137, 3859–3863. doi:10.1088/0004-6256/137/4/3859.

Dungey, J.W., 1961. Interplanetary Magnetic Field and the Auroral Zones. Physical Review Letters 6, 47–48. doi:10.1103/PhysRevLett.6.47.

Evans, L.G., Peplowski, P.N., Rhodes, E.A., Lawrence, D.J., McCoy, T.J., Nittler, L.R., Solomon, S.C., Sprague, A.L., Stockstill-Cahill, K.R., Starr, R.D., Weider, S.Z., Boynton, W.V., Hamara, D.K., Goldsten, J.O., 2012. Major-element abundances on the surface of Mercury: Results from the MESSENGER Gamma-Ray Spectrometer. Journal of Geophysical Research (Planets) 117. doi:10.1029/2012JE004178.

Exner, W., Heyner, D., Liuzzo, L., Motschmann, U., Shiota, D., Kusano, K., Shibayama, T., 2018. Coronal mass ejection hits mercury: A.I.K.E.F. hybrid-code results compared to MESSENGER data. Planetary and Space Science 153, 89–99. doi:10.1016/j.pss.2017.12.016.

Exner, W., Simon, S., Heyner, D., Motschmann, U., 2020. Influence of Mercury's Exosphere on the Structure of the Magnetosphere. Journal of Geophysical Research: Space Physics 125. doi:10.1029/2019JA027691.

Fulle, M., Leblanc, F., Harrison, R.A., Davis, C.J., Eyles, C.J., Halain, J.P., Howard, R.A., Bockelée-Morvan, D., Cremonese, G., Scarmato, T., 2007. Discovery of the Atomic Iron Tail of Comet MCNaught Using the Heliospheric Imager on STEREO. The Astrophysical Journal 661, L93–L96. doi:10.1086/518719.

Gamborino, D., Vorburger, A., Wurz, P., 2019. Mercury's subsolar sodium exosphere: an ab initio calculation to interpret MASCS/UVVS observations from MESSENGER. Annales Geophysicae 37, 455–470. doi:10.5194/angeo-37-455-2019.

Gershman, D.J., Slavin, J.A., Raines, J.M., Zurbuchen, T.H., Anderson, B.J., Korth, H., Baker, D.N., Solomon, S.C., 2013. Magnetic flux pileup and plasma depletion in Mercury's subsolar magnetosheath. Journal of Geophysical Research: Space Physics 118, 7181–7199. doi:10.1002/2013JA019244.

Glassmeier, K.H., Klimushkin, D., Othmer, C., Mager, P., 2004. ULF waves at Mercury: Earth, the giants, and their little brother compared. Advances in Space Research 33, 1875–1883. doi:10.1016/j.asr.2003.04.047.

Glassmeier, K.H., Mager, P.N., Klimushkin, D., 2003. Concerning ULF pulsations in Mercury's magnetosphere. Geophysical Research Letters 30. doi:10.1029/2003GL017175.

Huebner, W.F., Keady, J.J., Lyon, S.P., 1992. Solar Photo Rates for Planetary Atmospheres and Atmospheric Pollutants. Astrophysics and Space Science 195, 1–294. doi:10.1007/BF00644558.

Huebner, W.F., Mukherjee, J., 2015. Photoionization and photodissociation rates in solar and blackbody radiation fields. Planetary and Space Science 106, 11–45. doi:10.1016/j.pss.2014.11.022.

Hunten, D.M., Morgan, T.H., Shemansky, D.E., 1988. The Mercury atmosphere, in: Vilas, F., Chapman, C.R., Matthews, M.S. (Eds.), Mercury. University of Arizona Press, Tucson, Arizona, USA, pp. 562–612.

James, M.K., Imber, S.M., Yeoman, T.K., Bunce, E.J., 2019. Field Line Resonance in the Hermean Magnetosphere: Structure and Implications for

Plasma Distribution. Journal of Geophysical Research: Space Physics 124, 211–228. doi:10.1029/2018JA025920.

Janches, D., Berezhnoy, A.A., Christou, A.A., Cremonese, G., Hirai, T., Horányi, M., Jasinski, J.M., Sarantos, M., 2021. Meteoroids as One of the Sources for Exosphere Formation on Airless Bodies in the Inner Solar System. Space Science Reviews 217. doi:10.1007/s11214-021-00827-6.

Jasinski, J.M., Cassidy, T.A., Raines, J.M., Milillo, A., Regoli, L.H., Dewey, R., Slavin, J.A., Mangano, V., Murphy, N., 2021. Photoionization Loss of Mercury's Sodium Exosphere: Seasonal Observations by MESSENGER and the THEMIS Telescope. Geophysical Research Letters 48. doi:10.1029/2021GL092980.

Jasinski, J.M., Regoli, L.H., Cassidy, T.A., Dewey, R.M., Raines, J.M., Slavin, J.A., Coates, A.J., Gershman, D.J., Nordheim, T.A., Murphy, N., 2020. A transient enhancement of Mercury's exosphere at extremely high altitudes inferred from pickup ions. Nature Communications 11. doi:10.1038/s41467-020-18220-2.

Jia, X., Slavin, J.A., Gombosi, T.I., Daldorff, L.K.S., Toth, G., Holst, B., 2015. Global MHD simulations of Mercury's magnetosphere with coupled planetary interior: Induction effect of the planetary conducting core on the global interaction. Journal of Geophysical Research (Space Physics) 120, 4763–4775. doi:10.1002/2015JA021143.

Jia, X., Slavin, J.A., Poh, G., DiBraccio, G.A., Toth, G., Chen, Y., Raines, J.M., Gombosi, T.I., 2019. MESSENGER Observations and Global Simulations of Highly Compressed Magnetosphere Events at Mercury. Journal of Geophysical Research (Space Physics) 124, 229–247. doi:10.1029/2018JA026166.

Kallio, E., Chaufray, J.Y., Modolo, R., Snowden, D., Winglee, R., 2011. Modeling of Venus, Mars, and Titan. Space Science Reviews 162, 267–307. doi:10.1007/s11214-011-9814-8.

Killen, R.M., Potter, A.E., Reiff, P., Sarantos, M., Jackson, B.V., Hick, P., Giles, B., 2001. Evidence for space weather at Mercury. Journal of Geophysical Research 106, 20509–20526. doi:10.1029/2000JE001401.

Korth, H., Anderson, B.J., Raines, J.M., Slavin, J.A., Zurbuchen, T.H., Johnson, C.L., et al., 2011. Plasma pressure in Mercury's equatorial magnetosphere derived from MESSENGER Magnetometer observations. Geophysical Research Letters 38. doi:10.1029/2011GL049451.

Korth, H., Johnson, C.L., Philpott, L., Tsyganenko, N.A., Anderson, B.J., 2017. A Dynamic Model of Mercury's Magnetospheric Magnetic Field. Geophysical Research Letters 44, 10,147–10,154. doi:10.1002/2017GL074699.

Korth, H., Tsyganenko, N.A., Johnson, C.L., Philpott, L.C., Anderson, B.J., Al Asad, M.M., Solomon, S.C., McNutt, R.L., 2015. Modular model for Mercury's magnetospheric magnetic field confined within the average observed magnetopause. Journal of Geophysical Research: Space Physics 120, 4503–4518. doi:10.1002/2015JA021022.

Leblanc, F., Chaufray, J.Y., 2011. Mercury and Moon He exospheres: Analysis and modeling. Icarus 216, 551–559. doi:10.1016/j.icarus.2011.09.028.

Leblanc, F., Chaufray, J.Y., Doressoundiram, A., Berthelier, J.J., Mangano, V., López-Ariste, A., Borin, P., 2013. Mercury exosphere. III: Energetic characterization of its sodium component. Icarus 223, 963–974. doi:10.1016/j.icarus.2012.08.025.

Leblanc, F., Chaufray, J.Y., Modolo, R., Leclercq, L., Curry, S., Luhmann, J., et al., 2017a. On the Origins of Mars' Exospheric Nonthermal Oxygen Component as Observed by MAVEN and Modeled by HELIOSARES. Journal of Geophysical Research: Planets 122, 2401–2428. doi:10.1002/2017JE005336.

Leblanc, F., Delcourt, D., Johnson, R.E., 2003. Mercury's sodium exosphere: Magnetospheric ion recycling. Journal of Geophysical Research (Planets) 108. doi:10.1029/2003JE002151.

Leblanc, F., Doressoundiram, A., 2011. Mercury exosphere. II. The sodium/potassium ratio. Icarus 211, 10–20. doi:10.1016/j.icarus.2010.09.004.

Leblanc, F., Doressoundiram, A., Schneider, N., Massetti, S., Wedlund, M., López Ariste, A., et al., 2009. Short-term variations of Mercury's Na exosphere observed with very high spectral resolution. Geophysical Research Letters 36. doi:10.1029/2009GL038089.

Leblanc, F., Johnson, R.E., 2003. Mercury's sodium exosphere. Icarus 164, 261–281. doi:10.1016/S0019-1035(03)00147-7.

Leblanc, F., Johnson, R.E., 2010. Mercury exosphere I. Global circulation model of its sodium component. Icarus 209, 280–300. doi:10.1016/j.icarus.2010.04.020.

Leblanc, F., Oza, A.V., Leclercq, L., Schmidt, C., Cassidy, T., Modolo, R., et al., 2017b. On the orbital variability of Ganymede's atmosphere. Icarus 293, 185–198. doi:10.1016/j.icarus.2017.04.025.

Leclercq, L., Modolo, R., Leblanc, F., Hess, S., Mancini, M., 2016. 3D magnetospheric parallel hybrid multi-grid method applied to planet-plasma interactions. Journal of Computational Physics 309, 295–313. doi:10.1016/j.jcp.2016.01.005.

McClintock, W.E., Bradley, E.T., Vervack, R.J., Killen, R.M., Sprague, A.L., Izenberg, N.R., Solomon, S.C., 2008. Mercury's Exosphere: Observations During MESSENGER's First Mercury Flyby. Science 321, 92. doi:10.1126/science.1159467.

Mcclintock, W.E., Cassidy, T.A., Merkel, A.W., Killen, R.M., Burger, M.H., Vervack, R.J., 2018. Observations of mercury's exosphere: Composition and structure, in: Solomon, S.C., Nittler, L.R., Anderson, B.J. (Eds.), Mercury: The view after MESSENGER. Cambridge Planetary Science, Cambridge. chapter 14, pp. 371–403.

McClintock, W.E., Lankton, M.R., 2007. The Mercury Atmospheric and Surface Composition Spectrometer for the MESSENGER Mission. Space Science Reviews 131, 481–521. doi:10.1007/s11214-007-9264-5.

Merkel, A.W., Cassidy, T.A., Vervack, R.J., McClintock, W.E., Sarantos, M., Burger, M.H., Killen, R.M., 2017. Seasonal variations of Mercury's magnesium dayside exosphere from MESSENGER observations. Icarus 281, 46–54. doi:10.1016/j.icarus.2016.08.032.

Milillo, A., Mangano, V., Massetti, S., Mura, A., Plainaki, C., Alberti, T., Ippolito, A., Ivanovski, S.L., Aronica, A., De Angelis, E., Kazakov, A., Noschese, R., Orsini, S., Rispoli, R., Sordini, R., Vertolli, N., 2021. Exospheric Na distributions along the Mercury orbit with the THEMIS telescope. Icarus 355. doi:10.1016/j.icarus.2020.114179.

Modolo, R., Chanteur, G.M., Wahlund, J.E., Canu, P., Kurth, W.S., Gurnett, D., Matthews, A.P., Bertucci, C., 2007. Plasma environment in the wake of Titan from hybrid simulation: A case study. Geophysical Research Letters 34. doi:10.1029/2007GL030489.

Modolo, R., Hess, S., Mancini, M., Leblanc, F., Chaufray, J.Y., Brain, D., et al., 2016. Mars-solar wind interaction: LatHyS, an improved parallel 3-D multispecies hybrid model. Journal of Geophysical Research (Space Physics) 121, 6378–6399. doi:10.1002/2015JA022324.

Müller, J., Simon, S., Motschmann, U., Schüle, J., Glassmeier, K.H., Pringle, G.J., 2011. A.I.K.E.F.: Adaptive hybrid model for space plasma simulations. Computer Physics Communications 182, 946–966. doi:`10.1016/j.cpc.2010.12.033`.

Müller, J., Simon, S., Wang, Y.C., Motschmann, U., Heyner, D., Schüle, J., Ip, W.H., Kleindienst, G., Pringle, G.J., 2012. Origin of Mercury's double magnetopause: 3D hybrid simulation study with A.I.K.E.F. Icarus 218, 666–687. doi:`10.1016/j.icarus.2011.12.028`.

Mura, A., Milillo, A., Orsini, S., Massetti, S., 2007. Numerical and analytical model of Mercury's exosphere: Dependence on surface and external conditions. Planetary and Space Science 55, 1569–1583. doi:`10.1016/j.pss.2006.11.028`.

Ogilvie, K.W., Scudder, J.D., Hartle, R.E., Siscoe, G.L., Bridge, H.S., Lazarus, A.J., et al., 1974. Observations at Mercury Encounter by the Plasma Science Experiment on Mariner 10. Science 185, 145–151. doi:`10.1126/science.185.4146.145`.

Orsini, S., Livi, S., Torkar, K., Barabash, S., Milillo, A., Wurz, P., di Lellis, A.M., Kallio, E., SERENA Team, 2010. SERENA: A suite of four instruments (ELENA, STROFIO, PICAM and MIPA) on board BepiColombo-MPO for particle detection in the Hermean environment. Planetary and Space Science 58, 166–181. doi:`10.1016/j.pss.2008.09.012`.

Orsini, S., Mangano, V., Milillo, A., Plainaki, C., Mura, A., Raines, J.M., De Angelis, E., Rispoli, R., Lazzarotto, F., Aronica, A., 2018. Mercury sodium exospheric emission as a proxy for solar perturbations transit. Scientific Reports 8. doi:`10.1038/s41598-018-19163-x`.

Oza, A.V., Leblanc, F., Johnson, R.E., Schmidt, C., Leclercq, L., Cassidy, T.A., Chaufray, J.Y., 2019. Dusk over dawn O_2 asymmetry in Europa's near-surface atmosphere. Planetary and Space Science 167, 23–32. doi:`10.1016/j.pss.2019.01.006`.

Paral, J., Trávníček, P.M., Rankin, R., Schriver, D., 2010. Sodium ion exosphere of Mercury during MESSENGER flybys. Geophysical Research Letters 37. doi:`10.1029/2010GL044413`.

Potter, A.E., Killen, R.M., Reardon, K.P., Bida, T.A., 2013. Observation of neutral sodium above Mercury during the transit of November 8, 2006. Icarus 226, 172–185. doi:`10.1016/j.icarus.2013.05.029`.

Potter, A.E., Killen, R.M., Sarantos, M., 2006. Spatial distribution of sodium on Mercury. Icarus 181, 1–12. doi:`10.1016/j.icarus.2005.10.026`.

Potter, A.E., Morgan, T.H., 1985. Discovery of Sodium in the Atmosphere of Mercury. Science 229, 651–653. doi:`10.1126/science.229.4714.651`.

Potter, A.E., Morgan, T.H., 1986. Potassium in the atmosphere of Mercury. Icarus 67, 336–340. doi:`10.1016/0019-1035(86)90113-2`.

Raines, J.M., DiBraccio, G.A., Cassidy, T.A., Delcourt, D.C., Fujimoto, M., Jia, X., Mangano, V., Milillo, A., Sarantos, M., Slavin, J.A., Wurz, P., 2015. Plasma Sources in Planetary Magnetospheres: Mercury. Space Science Reviews 192, 91–144. doi:`10.1007/s11214-015-0193-4`.

Raines, J.M., Gershman, D.J., Slavin, J.A., Zurbuchen, T.H., Korth, H., Anderson, B.J., Solomon, S.C., 2014. Structure and dynamics of Mercury's magnetospheric cusp: MESSENGER measurements of protons and planetary ions. Journal of Geophysical Research: Space Physics 119, 6587–6602. doi:`10.1002/2014JA020120`.

Raines, J.M., Gershman, D.J., Zurbuchen, T.H., Sarantos, M., Slavin, J.A., Gilbert, J.A., et al., 2013. Distribution and compositional variations of plasma ions in Mercury's space environment: The first three Mercury years of MESSENGER observations. Journal of Geophysical Research: Space Physics 118, 1604–1619. doi:`10.1029/2012JA018073`.

Raines, J.M., Wallace, K.L., Sarantos, M., Jasinksi, J.M., Tracy, P.J., Dewey, R.M., et al., 2018. First In-Situ Observations of Exospheric Response to CME Impact at Mercury, in: Mercury: Current and Future Science of the Innermost Planet, Proceedings of the conference held 1-3 May, 2018 in Columbia, Maryland.

Richer, E., Modolo, R., Chanteur, G.M., Hess, S., Leblanc, F., 2012. A global hybrid model for Mercury's interaction with the solar wind: Case study of the dipole representation. Journal of Geophysical Research (Space Physics) 117. doi:`10.1029/2012JA017898`.

Romanelli, N., Modolo, R., Leblanc, F., Chaufray, J.Y., Hess, S., Brain, D., Connerney, J., et al., 2018a. Effects of the Crustal Magnetic Fields and Changes in the IMF Orientation on the Magnetosphere of Mars: MAVEN Observations and LatHyS Results. Journal of Geophysical Research (Space Physics) 123, 5315–5333. doi:`10.1029/2017JA025155`.

Romanelli, N., Modolo, R., Leblanc, F., Chaufray, J.Y., Martinez, A., Ma, Y., et al., 2018b. Responses of the Martian Magnetosphere to an Interplanetary Coronal Mass Ejection: MAVEN Observations and LatHyS Results. Geophysical Research Letters 45, 7891–7900. doi:`10.1029/2018GL077714`.

Saito, Y., Sauvaud, J.A., Hirahara, M., Barabash, S., Delcourt, D., Takashima, T., Asamura, K., BepiColombo MMO/MPPE Team, 2010. Scientific objectives and instrumentation of Mercury Plasma Particle Experiment (MPPE) onboard MMO. Planetary and Space Science 58, 182–200. doi:`10.1016/j.pss.2008.06.003`.

Sarantos, M., Killen, R.M., Kim, D., 2007. Predicting the long-term solar wind ion-sputtering source at Mercury. Planetary and Space Science 55, 1584–1595. doi:`10.1016/j.pss.2006.10.011`.

Sarantos, M., Slavin, J.A., Benna, M., Boardsen, S.A., Killen, R.M., Schriver, D., Trávníček, P., 2009. Sodium-ion pickup observed above the magnetopause during MESSENGER's first Mercury flyby: Constraints on neutral exospheric models. Geophysical Research Letters 36. doi:`10.1029/2008GL036207`.

Schmidt, C.A., 2013. Monte Carlo modeling of north-south asymmetries in Mercury's sodium exosphere. Journal of Geophysical Research (Space Physics) 118, 4564–4571. doi:`10.1002/jgra.50396`.

Seki, K., Terada, N., Yagi, M., Delcourt, D.C., Leblanc, F., Ogino, T., 2013. Effects of the surface conductivity and the IMF strength on the dynamics of planetary ions in Mercury's magnetosphere. Journal of Geophysical Research (Space Physics) 118, 3233–3242. doi:`10.1002/jgra.50181`.

Shue, J.H., Chao, J.K., Fu, H.C., Russell, C.T., Song, P., Khurana, K.K., Singer, H.J., 1997. A new functional form to study the solar wind control of the magnetopause size and shape. Journal of Geophysical Research 102, 9497–9512. doi:`10.1029/97JA00196`.

Siscoe, G.L., Ness, N.F., Yeates, C.M., 1975. Substorms on Mercury? Journal of Geophysical Research 80, 4359. doi:`10.1029/JA080i031p04359`.

Slavin, J.A., Acuña, M.H., Anderson, B.J., Baker, D.N., Benna, M., Boardsen, S.A., Gloeckler, G., Gold, R.E., Ho, G.C., Korth, H., Krimigis, S.M., McNutt, R.L., Raines, J.M., Sarantos, M., Schriver, D., Solomon, S.C., Trávníček, P., Zurbuchen, T.H., 2009. MESSENGER Observations of Magnetic Reconnection in Mercury's Magnetosphere. Science 324, 606. doi:`10.1126/science.1172011`.

Slavin, J.A., Acuña, M.H., Anderson, B.J., Baker, D.N., Benna, M., Gloeckler, G., et al., 2008. Mercury's Magnetosphere After MESSENGER's

First Flyby. Science 321, 85. doi:10.1126/science.1159040.

Slavin, J.A., DiBraccio, G.A., Gershman, D.J., Imber, S.M., Poh, G., Raines, J.M., Zurbuchen, T.H., Jia, X., Baker, D.N., Glassmeier, K.H., Livi, S.A., Boardsen, S.A., Cassidy, T.A., Sarantos, M., Sundberg, T., Masters, A., Johnson, C.L., Winslow, R.M., Anderson, B.J., Korth, H., McNutt, R.L., Solomon, S.C., 2014. MESSENGER observations of Mercury's dayside magnetosphere under extreme solar wind conditions. Journal of Geophysical Research: Space Physics 119, 8087–8116. doi:10.1002/2014JA020319.

Slavin, J.A., Krimigis, S.M., Acuña, M.H., Anderson, B.J., Baker, D.N., Koehn, P.L., Korth, H., Livi, S., Mauk, B.H., Solomon, S.C., Zurbuchen, T.H., 2007. MESSENGER: Exploring Mercury's Magnetosphere. Space Science Reviews 131, 133–160. doi:10.1007/s11214-007-9154-x.

Slavin, J.A., Middleton, H.R., Raines, J.M., Jia, X., Zhong, J., Sun, W.J., Livi, S., Imber, S.M., Poh, G.K., Akhavan-Tafti, M., Jasinski, J.Â.M., DiBraccio, G.A., Dong, C., Dewey, R.M., Mays, M.L., 2019. MESSENGER Observations of Disappearing Dayside Magnetosphere Events at Mercury. Journal of Geophysical Research: Space Physics 124, 6613–6635. doi:10.1029/2019JA026892.

Smith, D.E., Zuber, M.T., Phillips, R.J., Solomon, S.C., Hauck, S.A., Lemoine, F.G., Mazarico, E., Neumann, G.A., Peale, S.J., Margot, J.L., Johnson, C.L., Torrence, M.H., Perry, M.E., Rowlands, D.D., Goossens, S., Head, J.W., Taylor, A.H., 2012. Gravity Field and Internal Structure of Mercury from MESSENGER. Science 336, 214. doi:10.1126/science.1218809.

Smyth, W.H., Marconi, M.L., 1995. Theoretical Overview and Modeling of the Sodium and Potassium Atmospheres of Mercury. The Astrophysical Journal 441, 839. doi:10.1086/175407.

Soter, S., Ulrichs, J., 1967. Rotation and Heating of the Planet Mercury. Nature 214, 1315–1316. doi:10.1038/2141315a0.

Turc, L., Leclercq, L., Leblanc, F., Modolo, R., Chaufray, J.Y., 2014. Modelling Ganymede's neutral environment: A 3D test-particle simulation. Icarus 229, 157–169. doi:10.1016/j.icarus.2013.11.005.

Vervack, R.J., Killen, R.M., McClintock, W.E., Merkel, A.W., Burger, M.H., Cassidy, T.A., Sarantos, M., 2016. New discoveries from MESSENGER and insights into Mercury's exosphere. Geophysical Research Letters 43, 11,545–11,551. doi:10.1002/2016GL071284.

Winslow, R.M., Anderson, B.J., Johnson, C.L., Slavin, J.A., Korth, H., Purucker, M.E., Baker, D.N., Solomon, S.v., 2013. Mercury's magnetopause and bow shock from MESSENGER Magnetometer observations. Journal of Geophysical Research: Space Physics 118, 2213–2227. doi:10.1002/jgra.50237.

Winslow, R.M., Johnson, C.L., Anderson, B.J., Korth, H., Slavin, J.A., Purucker, M.E., Solomon, S.C., 2012. Observations of Mercury's northern cusp region with MESSENGER's Magnetometer. Geophysical Research Letters 39. doi:10.1029/2012GL051472.

Winslow, R.M., Lugaz, N., Philpott, L., Farrugia, C.J., Johnson, C.L., Anderson, B.J., Paty, C.S., Schwadron, N.A., Asad, M., 2020. Observations of Extreme ICME Ram Pressure Compressing Mercury's Dayside Magnetosphere to the Surface. The Astrophysical Journal 889. doi:10.3847/1538-4357/ab6170.

Wurz, P., Lammer, H., 2003. Monte-Carlo simulation of Mercury's exosphere. Icarus 164, 1–13. doi:10.1016/S0019-1035(03)00123-4.

Yagi, M., Seki, K., Matsumoto, Y., Delcourt, D.C., Leblanc, F., 2010. Formation of a sodium ring in Mercury's magnetosphere. Journal of Geophysical Research (Space Physics) 115. doi:10.1029/2009JA015226.

Yagi, M., Seki, K., Matsumoto, Y., Delcourt, D.C., Leblanc, F., 2017. Global Structure and Sodium Ion Dynamics in Mercury's Magnetosphere With the Offset Dipole. Journal of Geophysical Research (Space Physics) 122, 10,990–11,002. doi:10.1002/2017JA024082.

Zurbuchen, T.H., Raines, J.M., Gloeckler, G., Krimigis, S.M., Slavin, J.A., Koehn, P.L., et al., 2008. MESSENGER Observations of the Composition of Mercury's Ionized Exosphere and Plasma Environment. Science 321, 90. doi:10.1126/science.1159314.

Zurbuchen, T.H., Raines, J.M., Slavin, J.A., Gershman, D.J., Gilbert, J.A., Gloeckler, G., Anderson, B.J., Baker, D.N., Korth, H., Krimigis, S.M., Sarantos, M., Schriver, D., McNutt, R.L., Solomon, S.C., 2011. MESSENGER Observations of the Spatial Distribution of Planetary Ions Near Mercury. Science 333, 1862. doi:10.1126/science.1211302.

6

IMPACT OF A STRONG X-CLASS SOLAR FLARE ON THE PLANETARY ION COMPOSITION IN MERCURY'S MAGNETOSPHERE

6.1 INTRODUCTION TO PAPER II

The previous chapter demonstrated LIZE capabilities for the steady-state exosphere and magnetosphere. This chapter concerns the short-term variability of the ion density distribution. We use the time-dependent version of the LIZE code to study the impact of a real solar flare event (i.e. the X9.3-class solar flare which erupted on 6 September 2017) on different planetary ion species (He^+, O^+, Na^+ and Mg^+). We use a model spectra from the Flare Irradiance Spectral Model (FISM, Chamberlin et al., 2020) to simulate the impact of the solar flare on the time-dependent photo-ionization rate.

6.2 SUMMARY TO PAPER II

We make the following findings:

- Solar flares have their greatest impact in the X-ray to EUV wavelengths, and little to no impact above $\lambda = 200$ nm. The studied solar flare event, and likely solar flares in general, have very little effect on the photo-ionization rate of Na. This is due to the wavelength-dependence of the Na photo-ionization cross-section, which is dominated by longer wavelengths ($\lambda > 200$ nm) where the flare has a negligible effect. However, for O, He and Mg the photo-ionization rate is raised by as much as 80% just because of the flare. The wavelength-dependence of the photo-ionization cross-sections of these species differ from that of Na and have relatively low photo-ionization thresholds compared to Na (see Table 3 in Chapter 4), which means that the solar flare has a relatively large impact on the total photo-ionization rates of said species.

- The ion density distribution at noon at low altitudes contains two ion populations separated by energy. The low-energy ion population is likely produced locally, while the high-energy ions is part of an ion ring distribution. The relative intensity of the high-energy population is higher for low-mass ions such as He^+. The nightside contains a single ion population at keV energies for all species.

- The time delay between the time of maximum photo-ionization and the time of maximum ion density in a given region differs between different regions and for different species. On the dayside, the low-energy ions reach their maximum intensity just 2 minutes after the flare, while the high-energy population reach their maximum 14-15 minutes later. In region C, the maximum ion density occurs 7-8 minutes after the maximum ion density in region A.

- The different peak times for the low-energy and high-energy He^+ ions causes the He^+ ion density in Region A to decay more slowly during the first 10 minutes after the main peak than expected.

- The distribution of the surface impact flux follows the general evolution of the ion density distribution. When the ion density peaks in a given region, the impact flux peaks just ~ 2 minutes later.

- Due to the difference in optical thickness of the solar atmosphere in X-ray and EUV wavelengths, the intensity of the gradual phase will depend on where the source region of the flare is located on the solar disk. For center-of-disk flares, the Mg density peaks before He and O. For limb flares, all three species reach their maximum photo-ionization rate at the same time, and the He, O photo-ionization rate is a little bit lower, the recovery a bit faster.

In conclusion, we find that the response of the planetary ion distribution in the magnetosphere is non-linear with respect to different locations inside the magnetosphere, energy and species.

6.3 REPRINT OF PAPER II: MODELING THE IMPACT OF A STRONG X-CLASS SOLAR FLARE ON THE PLANETARY ION COMPOSITION IN MERCURY'S MAGNETOSPHERE

Paper II has been submitted to Geophysical Research Letters and is currently under review (last updated: 9 December 2021). This section contains the draft version of the article that is currently under review.

Modeling the impact of a strong X-class solar flare on the planetary ion composition in Mercury's magnetosphere

A. L. E. Werner[1]*, F. Leblanc[1], J. Y. Chaufray[2], R. Modolo[2], S. Aizawa[3], L. Z. Hadid[4], C. Baskevitch[2]

[1]LATMOS/IPSL, Sorbonne Université, UVSQ, CNRS, Paris, France
[2]LATMOS/IPSL, UVSQ Université Paris–Saclay, Sorbonne Université, CNRS, Guyancourt, France
[3]IRAP, Toulouse, France
[4]Laboratoire de Physique des Plasmas (LPP), CNRS, Observatoire de Paris, Sorbonne Université, Université Paris Saclay, Ecole polytechnique, Institut Polytechnique de Paris, 91120 Palaiseau, France

Key Points:

- A strong X-class flare can boost the photoionization frequencies of Mercury's Mg, O and He exospheres with $40-80\%$.
- The dayside magnetosphere contains two ion populations for each species which respond to the flare on different time scales.
- Depending on the flare geometry, there may be a time delay between the maximum Mg^+, O^+ and He^+ ion densities in the magnetosphere.

---

*Current affiliation: Swedish Institute of Space Physics, Uppsala, Sweden

Corresponding author: Elisabeth Werner, `elisabeth.werner@latmos.ipsl.fr`

Abstract

We model the impact of an extreme solar flare on the Mg^+, Na^+, O^+ and He^+ ion density distribution in Mercury's magnetosphere. The Flare Irradiance Spectral Model of the solar irradiance during the X9.3-class flare on 6 September 2017 is used as input to the time-dependent Latmos Ionized Exosphere ion density model. We find that the time-evolution of the planetary ion distribution differs with respect to energy, location and species. There exist two ion energy populations on the dayside that experience different dynamical evolution. The peak ion density in the nightside plasma sheet is delayed by $\sim 7-8$ minutes compared to the dayside. The maximum Mg^+ density occurs ~ 4 minutes before He^+ and O^+ in the whole magnetosphere. The time delay between different species does not necessarily occur for solar flares that erupt near the apparent solar limb, where the optical depth is large.

Plain Language Summary

A solar flare is a sudden outburst on the Sun which releases radiation and energetic particles. The abrupt radiation enhancement can strongly increase the frequency by which neutral atoms in Mercury's thin atmosphere are ionized. We use a model of the flare radiation spectrum and a new ion density model to study how a strong solar flare impacts the distribution of planetary ions in Mercury's magnetosphere. We select the strongest solar flare of solar cycle 24, which occurred on 6 September 2017. We find that the time-evolution of the ion density varies depending on the planetary ion species, the location inside the magnetosphere, the ion energy and the location of the flare on the Sun with respect to Mercury. The maximum Mg^+ density occurs ~ 4 minutes before He^+ and O^+ in the whole magnetosphere. This only happens for solar flares which erupt near the center of the solar disk as seen from Mercury. There are two ion populations with different energies on the dayside, and a single ion population on the nightside. For all species, the peak ion density in Mercury's shadow occurs $\sim 7-8$ minutes after the corresponding peak on the dayside.

1 Introduction

Mercury has a tenuous, collision-less atmosphere (i.e. a surface-bounded exosphere) that consists of H, He, Na, K, Mg, Ca, Mn, Fe and Al (Broadfoot et al., 1974; Potter & Morgan, 1985, 1986; Bida et al., 2000; McClintock et al., 2008; Bida & Killen, 2017; Vervack et al., 2016). The exosphere is maintained over time by different source and loss mechanisms. Mercury's exosphere is mainly sourced from the surface regolith, diffusion of gases from Mercury's interior and surface bombardment by solar wind ions (Killen et al., 2007). The species are released from the regolith into the exosphere by a variety of ejection processes, such as thermal desorption, photon-stimulated desorption, solar wind ion sputtering and meteoroid impact vaporization (Leblanc & Johnson, 2003, 2010; Killen et al., 2007). Neutrals are then lost from the exosphere by thermal (Jeans) escape, acceleration of the atoms by the solar radiation pressure to escape velocity and photoionization.

Mercury has a small magnetosphere that is the result of the interaction between the interplanetary magnetic field (IMF) and the intrinsic dipole magnetic field (Anderson et al., 2011). The magnetospheric ion population mainly consists of solar wind ions, but planetary ions may contribute to as much as 10% of the total ion pressure (Yagi et al., 2010). The planetary ions that exist in Mercury's magnetosphere are primarily sourced from photoionization of the neutral exosphere. The Fast Imaging Plasma Spectrometer (FIPS; Andrews et al., 2007) onboard the Mercury Surface, Space Environment, Geochemistry, and Ranging (MESSENGER) spacecraft has mapped the distribution of planetary ions in Mercury's magnetosphere. Na^+-group (mass-per charge ratio m/q = 21 - 30 amu/e), O^+-group (m/q = 16 - 20 amu/e) ions and He^+ were among the most commonly observed ion species by FIPS inside the magnetosphere (Zurbuchen et al., 2011; Raines et al., 2013). The planetary ions were found to be particularly abundant in the central plasma sheet on the nightside and near the northern cusp on the dayside (Raines et al., 2013).

Both Mercury's exosphere (Burger et al., 2014; Cassidy et al., 2015, 2016; Merkel et al., 2017, 2018) and the planetary ion environment (Raines et al., 2013; Jasinski et al., 2021) have been shown to vary as a function of true anomaly angle (TAA). Ground-based observations of the Na exosphere have shown variations with a timescale on the order of hours (Leblanc et al., 2008, 2009; Mangano et al., 2009, 2013, 2015; Orsini et al., 2018) to minutes (Massetti et al., 2017). Changes in the Na emission distribution have been attributed to variations in the solar wind IMF and solar transient events (Mangano et al., 2013, 2015; Orsini et al., 2018; Milillo et al., 2021). Jasinski et al. (2020) determined that a large meteoroid impact event was responsible behind the FIPS observation of a sudden (< 10 minute) enhancement of the Na^+-group ion flux ($\sim 10^4$ cm^{-2} s^{-1} at $\sim$5300 km). Raines et al. (2018) reported an enhancement of the He^+ density (up to 0.1 cm^{-3}) in the northern cusp following the transit of a CME at Mercury.

There have been a number of intense solar flare events in modern time. Noteworthy examples include the Bastille Day event on 14 July 2000 (Aulanier et al., 2000), the Halloween solar storms in 2003 (Tsurutani et al., 2005) and more recently, a set of strong X-class flares in September 2017 (Yan et al., 2018). On Earth, extreme solar flares can give rise to solar radiation storms, which can have severe biological effects and disrupt satellite operations, and radio blackouts, which affects positioning and satellite navigation (National Oceanic and Atmospheric Administration, 2011). Solar flares have also been shown to enhance X-ray emission at Jupiter (Maurellis et al., 2000), Saturn (Bhardwaj et al., 2005) and disturb Mars's ionosphere (Mendillo et al., 2006; Fallows et al., 2015). To our knowledge, the impact of solar flares on Mercury has not been studied before. Considering Mercury's short heliocentric distance and the unique composition of heavy species in Mercury's exosphere, it is a particularly interesting case to consider.

We have developed a model to simulate the impact of a strong X-class solar flare on the ion density distribution of Mg^+, Na^+, O^+ and He^+ in Mercury's magnetosphere. The solar flare event and the model are described in Section 2. We describe the key results in Section 3 and discuss their implications in Section 4. Finally, we summarize our findings in Section 5.

2 Model and Method

2.1 The X9.3-class Solar Flare on 6 September 2017

Between 4-10 September 2017 the active region (AR) 12673 on the Sun released a series of solar flares and CMEs that impacted Earth and the planet Mars. Two special issues in the Space Weather journal (Knipp, D., 2018) and the Geophysical Research Letters (Diffenbaugh, N., 2018) review the observations that were made from these events and the impact they had on the two planets.

The strongest solar flare of this period (and solar cycle 24) started at 11:53 Universal Time (UT) on 6 September 2017 and reached peak emission at 12:02 UT. The flare was detected by the Geostationary Operational Environmental Satellites (GOES) and ranked as the 14th most intense solar flare observed since measurements began in 1975 (Berdermann et al., 2018). Solar flares are classified by their maximum energy output, which is estimated from measurements in the wavelength range $\lambda = 0.1$ - 0.8 nm by GOES X-ray sensor (XRS). The 6 September flare had a peak energy output of 9.3×10^{-4} $\mathrm{W/m^2}$ and was therefore classified as an X9.3-class event. The strongest solar flare detected to date occurred on 4 November 2003 and was estimated to X28, which makes it at least three times stronger than the 6 September 2017 flare.

A flare of similar strength (X8.2) erupted on 10 September 2017 from the same active region and hit the planet Mars. Spacecraft observations of Mars's upper atmosphere after the flare showed signs of heating and expansion of the upper atmosphere (Jain et al., 2018), which caused the exosphere and ion density at a given altitude to increase (Elrod et al., 2018; Thiemann et al., 2018). The photochemical escape of O was also shown to be enhanced as a result of the flare (Thiemann et al., 2018). The 6 and 10 September 2017 flares likely also affected Mercury but there were no spacecraft in orbit around Mercury that could study its effects.

2.2 The Flare Irradiance Spectral Model-Version 2

The Flare Irradiance Spectral Model-Version 2 (FISM2; Chamberlin et al., 2020) is an empirical model of the solar spectral irradiance. The solar spectral irradiance is estimated at a heliocentric distance of 1 AU in the wavelength range 0.05 to 189.95 nm with a spectral cadence of 0.1 nm. FISM2 uses data from the X-Ray Photometer System (XPS) on the Solar Radiation and Climate Experiment (SORCE) in the wavelength range 0-6 nm, the EUV Variability Experiment (EVE) on Solar Dynamics Observatory (SDO) between 6-105 nm and the Solar Stellar Irradiance Comparison Experiment (SOLSTICE; also on SORCE) between 115-190 nm. The FISM2 output is given in a "daily" and "flare" version. The daily output contains the daily average of the solar spectrum for any given day since 1947 until the present. The flare product consists of a modeled spectrum for every 60 s of the selected day (from 2003 until the present). The FISM2 solar irradiance spectra are available at `http://lasp.colorado.edu/lisird/data/fism`.

The FISM2 model relies on a set of proxies to represent the irradiance variability in the full wavelength range (0-190 nm) caused by the solar cycle, solar rotation and solar flares. The solar spectral irradiance variability due to solar flares is estimated using two separate proxies. Measurements from the GOES/XRS B-channel (0.1-0.8 nm) are used to model the gradual (thermal) phase of the solar flare (Priest, 1981). The time-derivative of the GOES/XRS-B measurements are used to represent the impulsive (non-thermal) phase (Neupert, 1968). Only the irradiance variation due to the solar cycle and solar rotation is accounted for in the daily product, while the flare product also accounts for the irradiance variation due to real solar flare events.

We use the FISM2 flare output on 6 September 2017 in order to estimate the time-evolution of the photoionization flux for different species during the specified flare event. The FISM2 model has been used in the past to study the 6 and 10 September 2017 X-class flares (Chamberlin et al., 2018). To calculate the Mg, Na, O and He photoionization frequencies we merge the FISM2 spectra (0-190 nm) with the solar flux model from Killen et al. (2009) between 190-1300 nm and use the theoretical photoionization cross sections from Verner et al. (1996).

2.3 The Latmos Ionized Exosphere Model

The Latmos IoniZed Exosphere (LIZE) model is a test-particle model which describes the 3-D ion density distribution of photo-ions derived from Mercury's exosphere. The model is coupled to a Monte Carlo model of the exosphere (EGM; Leblanc & Johnson, 2010; Leblanc et al., 2017) and a hybrid model of the magnetosphere (LatHyS; Modolo et al., 2016, 2018). We make a separate LIZE simulation for each ion species (Mg^+, O^+ and He^+). For the O and He exospheres, we used the results of EGM described in Werner et al. (2022), whereas for the Mg exosphere those described in Chaufray et al. (2021a, 2021b). The EGM model of the Na exosphere has been described previously in Leblanc and Johnson (2010) and the He exosphere in Leblanc and Chaufray (2011). We find that the 6 September 2017 flare did not cause the Na surface ejection rate by photo-stimulated desorption to increase or Mercury's surface temperature to rise (which controls the rate of thermal desorption). Surface ejection by ion sputtering or micro-meteoroid vaporization are not affected by the solar radiation conditions. Therefore we make the assumption that the neutral Mg, O and He exosphere density does not change significantly during the flare. We use the EGM output at true anomaly angle $TAA = 180°$ (i.e. at aphelion) for all species. For the simulation of the magnetosphere, we use the same set of solar wind and IMF boundary conditions as "case a" described in Aizawa et al. (2021). The LIZE model has been used previously to determine the average ion density and phasespace density distribution of Na^+, O^+ and He^+ inside Mercury's magnetosphere (Werner et al., 2022). The model gives a similar average density and spatial distribution as the Na^+-group, O^+-group and He^+ ion density observations made by MESSENGER/FIPS (Raines et al., 2013).

For the purpose of this study, we have implemented the capability to use time-dependent input conditions with the LIZE model. We make repeated test-particle injections in the whole simulation volume with a test-particle weight that depends on the nominal 3-D ion production rate and the time-dependent photoionization frequency calculated with the FISM2 model. We use a 4-D grid (r, ϕ, θ, E) where r is the distance from the planet, θ is the co-latitude, ϕ is the longitude and E is the kinetic energy. The grid is centered on the planet and the simulation volume is bounded between $r = 1.0 - 3.5$ Mercury radii (R_M), $\theta = 0 - \pi$ rad and $\phi = 0 - 2\pi$ rad. The grid is divided into 65 exponentially distributed cells along r ($\Delta r = 5 - 600$ km), 40 cells along θ ($\Delta\theta = 0.08$ rad) and 60 cells along ϕ ($\Delta\phi = 0.1$ rad). The energy range is $E = 1 - 10^5$ eV and the energy resolution is described by the formula $(E_i - E_{i-1})/E_i = 0.1$ where E_i is the ith energy step. All test-particles inside the simulation are synchronously advanced in space after every time step ($dt = 0.01$ s). Every 60 s we inject 50 test-particles with zero initial velocity from random positions within each cell on the grid that has a non-zero ion production rate (as defined in the corresponding EGM simulation). The output consists of "snapshots" of the 3-D ion density distribution. Before triggering the solar flare we initialize the simulation volume with 30 minutes of test-particle injections with weights which correspond to the nominal photoionization frequency (for each species) in order to have a steady state situation of the magnetospheric environment. After this time, the deviation between snapshots taken 60 s apart is less than 10%.

3 Results

3.1 Time-evolution of the Mg, Na, O and He photoionization frequency

Figure 1*a* shows the integrated solar spectral irradiance during the first 30 minutes of the 6 September 2017 flare event. To make this particular plot we have used the wavelength range 0-190 nm as opposed to the whole wavelength range (0-1300 nm), to more clearly show the peaks of the impulsive ($t = 3$ min) and gradual ($t = 6$ - 7 min) phases of the flare. The flare emission that occurs during the impulsive phase is believed to be due to non-thermal acceleration of high speed electrons and protons inside magnetic loops in the solar atmosphere, while the gradual phase is dominated by thermal radiation or bremsstrahlung from the hot gas nested inside the magnetic loops (Dennis & Schwartz, 1989). Figure 1*b* shows the solar spectral irradiance at two discrete wavelengths: $\lambda = 12$ nm and $\lambda = 180$ nm. The spectral irradiance at $\lambda = 12$ nm is dominated by the gradual phase while the relatively cool, impulsive phase typically dominates at longer wavelengths. Figure 1c shows the time evolution of the photoionization frequency for He, O, Mg and Na normalized to their values before the start of the flare.

Na has the highest nominal photoionization frequency of the four species (5.0×10^{-6} s^{-1}), but the solar flare has a negligible effect on Na (see the inset plot in Figure 1*c*). The Mg photoionization frequency is an order of magnitude smaller compared to Na ($4.5{\times}10^{-7}$ s^{-1}) but increases with up to 87% as a result of the flare. The He and O photoionization frequencies have a similar time-evolution during the flare (see Figure 1*c*) but have different magnitude (He: $7.5{\times}10^{-8}$ s^{-1}; O: $3.1{\times}10^{-7}$ s^{-1}). The He den-

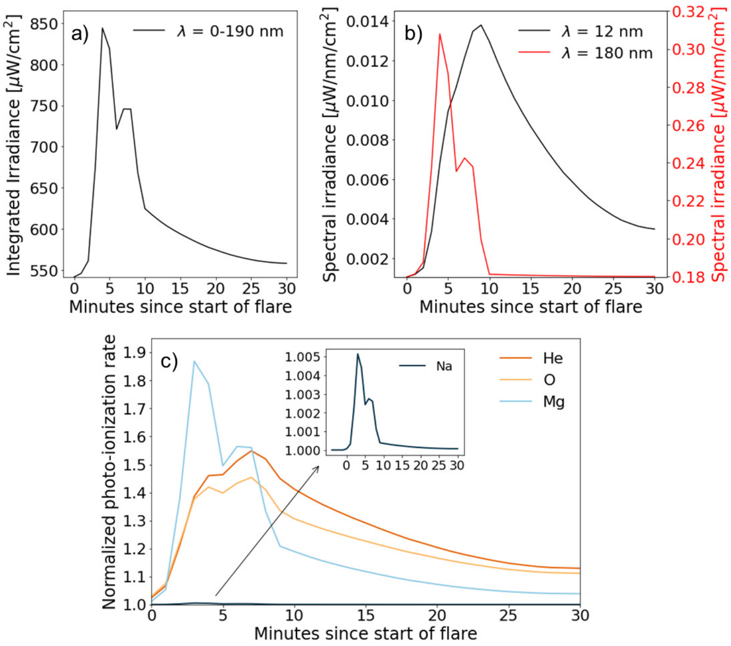

Figure 1. The (*a*) integrated solar irradiance during the first 30 minutes of the 6 September 2017 flare in the wavelength interval λ = 0 - 190 nm calculated using the FISM2 model, (*b*) the spectral solar irradiance at the wavelengths λ = 12 nm and λ = 80 nm and (*c*) the normalized photoionization frequency for Na, He, O and Mg.

sity from the EGM, which is used as input to the LIZE model, is much higher and have a larger scale height compared to the O density (Werner et al., 2022). The Mg photoionization frequency is highest after 3 minutes, while the maximum He and O photoionization frequencies occurs 7 minutes after the start of the flare. This implies that the impulsive flare phase is most effective in raising the Mg photoionization frequency while the gradual phase is more important for He and O. The different time-evolution of the photoionization frequency for each species and their distribution in the exosphere have the potential to create large differences between their ion counterparts in the magnetosphere.

3.2 Time-evolution of the ion density separated by energy

3.2.1 The ion energy spectrum before the flare

Figure 2*a*−*c* show the average He^+, O^+ and Mg^+ ion density in the latitude range ±30° centered on the geometric equatorial plane. We study the evolution of the He^+, O^+ and Mg^+ ion density as a function of time and energy (Figure 2d-l) inside three different regions in the magnetosphere (white boxes in 2*a*-2*c*). The energy spectra in Figure 2d-l shows the ion density separated per energy bin and has the unit $\text{cm}^{-3} \cdot dE^{-1}$, where the energy bin width dE is given by $dE = 0.1E_i$ and $E_0 = 1$ eV. The first region (i.e. Region A) is located near the surface (Altitude: 0-500 km) on the dayside (Local time: 10:30-12:00 h). Region B is located at higher altitudes (Altitude: 100-1100 km) near the dawn terminator (Local time: 05:00-06:30 h), and Region C is located near midnight in the nightside plasma sheet (Altitude: 700-1500 km; Local time: 23:00-01:00 h). Figure 2*d*−*l* show the ion energy distributions (energy spectra) for He^+, O^+ and Mg^+ in Region A-C as a function of time.

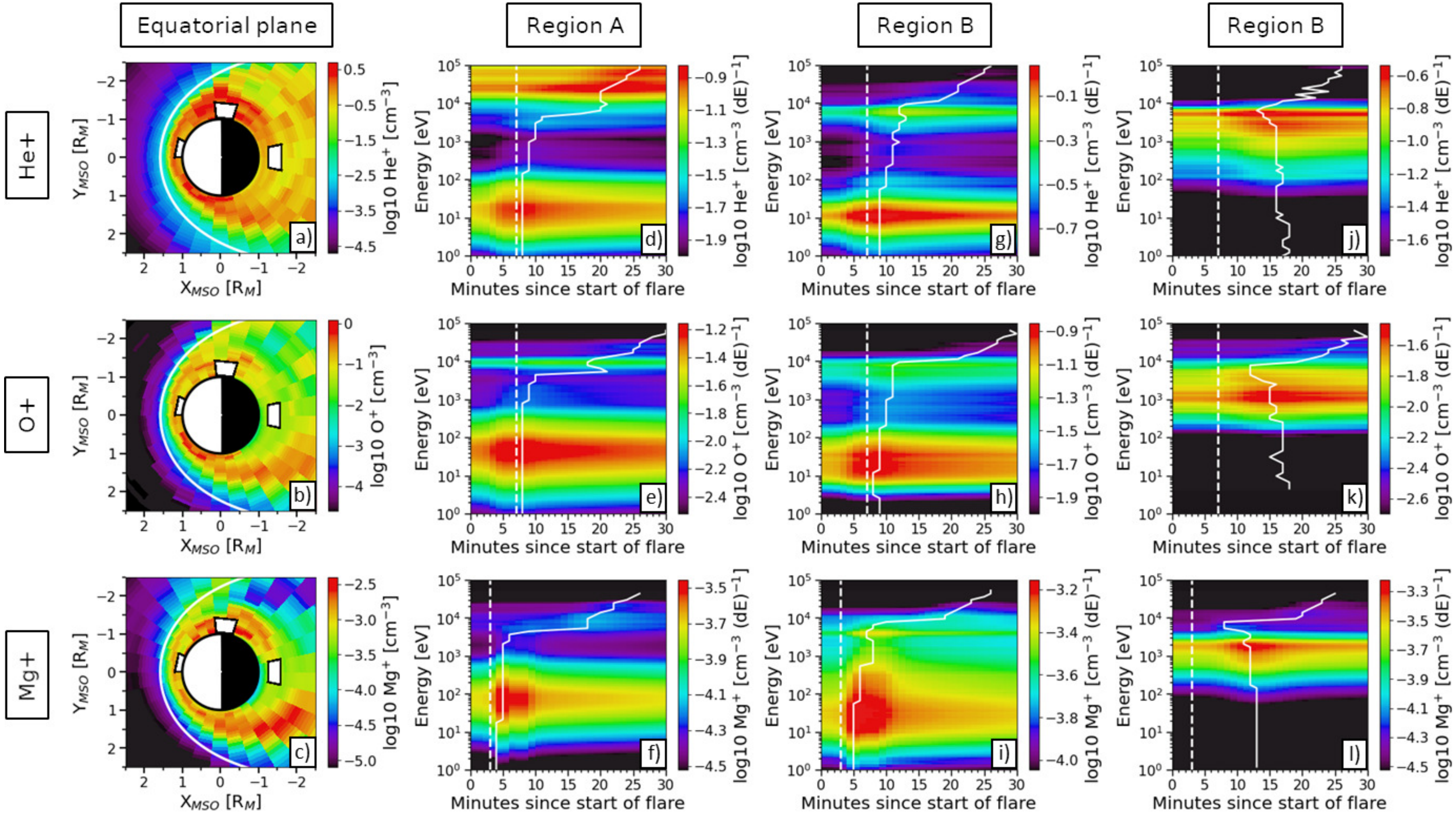

Figure 2. The (a) He$^+$ (t = 8 min), (b) O$^+$ (t = 8 min) and (c) Mg$^+$ (t = 5 min) ion density in the equatorial plane (average over latitude range ±30°) and (d - l) the time-evolution of the energy spectra in Region A - C separated by species. In Figure a - c, X_{MSO} points toward the Sun and Y_{MSO} points toward dusk. The solid white hyperbolas in panels a - c show the location of the magnetopause boundary, which has been calculated and corrected for the solar wind ram pressure of our simulation (P_{ram} = 8 nPa) following the scheme described in Winslow et al. (2013). The white boxes show the location of Region A - C. The dashed white lines in Figure d - l highlights the time when the photoionization frequency for each species reaches its maximum value. The solid white curves identifies the time when the ion density is highest in each energy channel.

Before the flare ($t = 0$), the energy spectra in Region A-B exhibits two distinctive peaks (Population 1 and 2). Population 1 consists of low-energy ions ($E = 0$ - 100 eV) while Population 2 contains much hotter ions ($E > 10$ keV). The low energy of the ions in Population 1 indicate that they have recently been photo-ionized and were likely created inside or near Region A-B. On the contrary, Population 2 must either contain ions which have been created elsewhere and/or have experienced a different dynamical evolution compared to the ions in Population 1 (see Section 4 for an in-depth discussion). For He^+ in Region A, Population 1 has a maximum at $E = 20$ eV and Population 2 at $E = 20$ keV. The energy spectra for O^+ and Mg^+ in Region A (see Figure 2e-2f) also consists of two ion populations. Population 1 (2) has a mean energy of $E = 40$ eV ($E = 10$ keV) for O^+ and $E = 80$ eV ($E = 8$ keV) for Mg^+. The density of the Population 1 and 2 He^+ ions in Region A are quite similar, with Population 1 being just ~40% more abundant than Population 2. However, for O^+ and Mg^+ Population 1 completely dominates the energy spectrum and Population 2 only accounts for ~10% of the total ion density. The mean energy of the two ion populations are generally lower in Region B: Population 1 (2) has a mean energy of $E = 10$ eV ($E = 5$ keV) for He^+, $E = 30$ eV ($E = 8$ keV) for O^+ and $E = 30$ eV ($E = 4$ keV) for Mg^+. Region C appears to be populated by a single ion population with a relatively high average energy of $E =$ 5 keV for He^+, $E = 1$ keV for O^+ and $E = 2$ keV for Mg^+.

3.2.2 Time-evolution of the ion energy spectrum

The difference between the dashed line and the solid curves in Figure 2d - 2l illustrates the time delay between the maximum photoionization frequency and the maximum ion density in each energy channel. The time delay for Population 1 in Region A is $\Delta t = 1{-}2$ minutes for all modeled species. The time delay for Population 2 is longer, approximately $\Delta t = 14{-}15$ minutes. Similar values are found in Region B. Inside region C the maximum ion density occurs at $t = 14 - 15$ minutes for He^+, O^+ and at $t = 11$ minutes for Mg^+. If we compare the dashed and the solid curves in Figure 2j - l we find that the time delay is $\Delta t = 7 - 8$ minutes irrespective of the species.

Population 1 typically dominates the total ion density in both Region A and B during the entire simulation for all modeled species. However, the He^+ Population 1 ($E = 0{-}100$ eV) in Region A varies between being twice as dense as Population 2 ($E > 10$ keV) at $t = 8$ minutes, to only 20% more abundant compared to Population 2 at $t =$ 22 minutes. In effect, this causes the average He^+ density to decay more slowly in Region A. The average He^+ density is elevated by ~25% compared to the background value for almost 10 minutes shortly after the main peak ($t = 8$ min). This is not the case for O^+ and Mg^+, that do not possess such a large population of high-energy ions in this region.

4 Discussion

The photoionization frequency for different neutral species reach their maximum value at different times during a flare. This depends on the photoionization energy threshold and in particular on the wavelength-dependence of the photoionization cross-section for each species. This may cause the impulsive or the gradual flare phase to be the most effective in raising the overall photoionization frequency. The time-evolution of the Mg (and Na) photoionization frequency exhibit a strong correlation with the impulsive phase of the 6 September 2017 flare (see Figure 1c) while the He and O photoionization frequencies reach their maximum values during the gradual flare phase. This result implies that a spacecraft (which carries a plasma mass spectrometer) in orbit around Mercury during a strong X-class flare event will first detect an increase of the Mg^+ density followed by He^+ and O^+ several minutes later, regardless of where the spacecraft is located inside the magnetosphere. Calculations show that most species that have been observed in Mercury's exosphere (Bida et al., 2000; Bida & Killen, 2017; Broadfoot et al., 1974; McClintock et al., 2008; Potter & Morgan, 1985, 1986; Vervack et al., 2016) or are expected based on observations of Mercury's surface composition (Evans et al., 2012, 2015; Nittler et al., 2011; Peplowski et al., 2012, 2015) are most affected by the impulsive phase of the 6 September 2017 flare (i.e. H, C, Na, Mg, Al, Si, S, Ar, Ca, Fe). The strength of the impulsive and gradual phase vary on an event-to-event basis. The impulsive flare phase tends to be the dominant phase for small flares, while strong flares like the 6 September 2017 flare often exhibit a relatively strong gradual phase which can last for over an hour (Dennis & Schwartz, 1989).

At most, there are 2.4×10^{26} (He^+: 43% increase), 4.5×10^{25} (O^+: 38% increase) 5×10^{23} (Mg^+: 49% increase) additional He^+, O^+ and Mg^+ ions being produced respectively in and outside Mercury's magnetosphere. The maximum He^+, O^+ and Mg^+ ion production during the flare is equal to barely 0.1% of the plasma mass density of the Na^+ ion population however, and therefore does not cause any significant mass loading of Mercury's magnetosphere.

Analysis of test-particle trajectories for Population 2 ions reveal that they experience a different dynamical evolution compared to Population 1. Population 2 largely consists of ions which have become quasi-trapped in the closed field line region near Mercury's magnetic equator. Figure 3 shows an example Mg^+ test-particle trajectory from the LIZE model which is typical to Population 2. The Mg^+ test-particle is ejected in the southern hemisphere and travels toward the dayside equatorial region (see Figure 3a-d and f). As the test-particle moves into the dayside hemisphere it approaches the magnetopause (see Figure 3e), and encounters the strong electric field near the magnetosheath (see the red part of the trajectory in Figure 3a-d and g). This causes the ion energy to increase from a few hundred eV to > 10 keV (see Figure 3h) and the test-particle starts to drift around the planet toward the nightside, where it eventually impacts the planet. The small size of Mercury's magnetosphere prevents the formation of a steady ion drift belt. Low-mass ions like He^+ can make 1-2 complete orbits before impacting the planet or escaping, while heavier ions like Na^+ are typically not able to pass the dayside magnetosphere because of their large gyro radii.

The test-particle trajectory in Figure 3 seems to suggest that the Population 2 ions in Region A does not belong to the Type 0 or Type 1 ion populations described in Glass et al. (2021), but could be part of Type 3. Glass et al. (2021) identified different types of Na^+ test-particle trajectories which could be responsible for the population of > 1 keV Na^+ ions observed in Mercury's northern magnetospheric cusp by FIPS (Raines et al., 2014). Type 3 consists of Na^+ ions which comes close to the magnetopause but do not cross into the magnetosheath before passing through the northern cusp. The Mg^+ ion in Figure 3 is energized to > 10 keV before its closest approach to the magnetopause (see Figure 3e and h). It is possible that Type 3 ions are rare at high latitudes simply because they are easily (quasi-)trapped in the closed field line region near the equator and therefore remain at mid-latitudes.

The magnetopause is located farther away from the surface at the dawn terminator compared to the subsolar point due to solar wind aberration. This implies that the solar wind convective electric field have less influence over the ions in Region B compared to Region A, which leads to overall lower ion energies in this region. Region C is located in Mercury's shadow, where there is no local ion production and ions can only be transported here from elsewhere in the magnetosphere. This explains the lack of a low-energy ion population in Region C and the time delay between the peak ion density in Region A and Region C. The ions in Region C are mainly sourced by magnetospheric convection from the dayside and the quasi-trapped ion drift belt.

The two peaks in the solar irradiance from the 6 September flare are relatively pronounced compared to the X8.2-class flare on the 10 September. This is caused by the

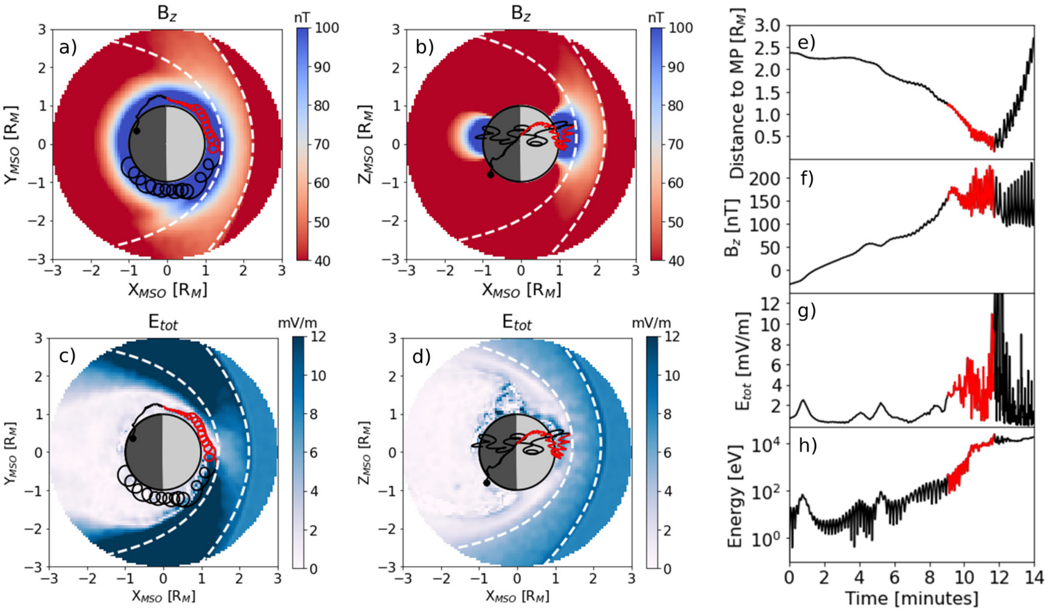

Figure 3. Example test-particle trajectory of a Na^+ ion from the LIZE model in the (a,c) MSO XY-plane and the (b,d) XZ-plane. Also shown is the magnetic field component B_z (a,b) and the total electric field E_{tot} (c,d) from the LathyS simulation. (e) shows the distance of the Na^+ ion from the planet, (f) the time-evolution of B_z experienced by the Na^+ ion, (f) the total electric field and (h) the ion energy. The part of the test-particle trajectory highlighted in red indicates a short time period when the ion energy increases from ~100 eV to >10 keV. The white dashed curves in (a-d) show the approximate location of the magnetopause and bow shock calculated from Winslow et al. (2013).

difference in the optical thickness of the flare emission during the impulsive and gradual phase. The 6 September flare occurred when the active region was located near the center of the solar disk (S09W34) as seen from Earth, while the 10 September flare occurred when the active region was located near the solar limb (S08W88). The emission during the gradual phase of the flare is optically thick and more easily absorbed by the Sun's atmosphere than the impulsive emission which is optically thin. Because the optical path between an observer and the apparent solar limb is longer compared to the center of the solar disk, the intensity of the gradual flare phase emission may change considerably depending on the location of the flare source region. This means that for species like He^+ and O^+ the time of the peak photoionization frequency will also change. The Mg^+ photoionization frequency is mainly controlled by the impulsive flare phase and is therefore less sensitive to the location of the flare source region. It should be noted that the FISM2 flare model is based on GOES observations made at Earth, and will not reflect the true flare radiation profile at Mercury if the planet is located far away from the Sun-Earth line. The 6 September 2017 flare, for instance, erupted closer to the apparent center of the solar disk as seen from Mercury and may have caused the gradual phase flare emission to be even stronger than suggested here.

5 Conclusions

We have used a test-particle model of the planetary ion density distribution in Mercury's magnetosphere which accepts time-dependent input conditions. We use this time-dependent capability to model the impact of a real flare event (the X9.3-class flare on 6 September 2017) on different planetary ion species. We find the following:

- The photoionization frequency of Na was not significantly affected, while the photoionization frequencies of Mg, O and He were increased with up to $40 - 80\%$.
- The maximum He and O photoionization frequencies are delayed by $\sim$4 minutes after the maximum Mg photoionization frequency. This is because the photoionization process for these species are mostly affected by the emission released during the gradual flare phase. Consequently, the photoionization frequency of Mg displays a relatively quick decay after the main peak compared to O and He.
- In the dayside magnetosphere, the low-energy ion population experiences a quicker evolution than the high-energy ions. At low altitudes on the dayside, $\sim$20 keV energy ions take up to 14 minutes to show a flare enhancement. This comes to show that the planetary ion population experiences different dynamical evolution which have different characteristic timescales.
- In the nightside plasma sheet, there is no local ion production and ions can only be transported here from elsewhere in the magnetosphere. For this reason there is no low-energy ion population in this region. There is a time delay between the maximum ion density on the dayside and the maximum ion density in the nightside of $\sim$7 - 8 minutes for all species.

This study shows that predicting the response of Mercury's magnetosphere to a strong solar flare is an intricate problem. What a mass spectrum analyzer on a spacecraft inside Mercury's magnetosphere will measure depends on a number of factors: the species, the location of the flare on the solar disk, the location of the spacecraft and the energy range of the instrument.

Acknowledgments

A.L.E.W., F.L., J.-Y.C. and R.M acknowledges the support by ANR of the TEMPETE project (grant ANR-17-CE31-0016). S.A., F.L., J.-Y.C., R.M and A.L.E.W. would like to acknowledge the support of CNES for the BepiColombo mission. The FISM2 model output for 6 September 2017 was obtained from the LASP Interactive Solar Irradiance Datacenter (`https://lasp.colorado.edu/lisird/data/fism_flare_hr/`). The LatHyS, EGM and LIZE simulation simulation results are publicly available through the IMPEx web-interface (`http://impex.latmos.ipsl.fr/`). To view the EGM and LIZE files, first select a LatHyS file (e.g. Data tree>Mercury>Simulations>`LatHyS_Merc_02_05_20`), then any LatHyS, EGM or LIZE file. The files can also be downloaded directly from: `http://impex.latmos.ipsl.fr/Hybrid/Merc_02_05_20/Magw_02_05_20_t00600.nc` (LatHyS magnetic field), `http://impex.latmos.ipsl.fr/Hybrid/Merc_02_05_20/Elew_02_05_20_t00600.nc` (LatHyS electric field), `http://impex.latmos.ipsl.fr/EGM/Mercury_05_10_21A/EGM_Mercury_170_190_00000278_10072021.nc` (EGM He), `http://impex.latmos.ipsl.fr/EGM/Mercury_05_10_21B/EGM_Mercury_049_049_00800000_10072021.nc` (EGM O), `http://impex.latmos.ipsl.fr/EGM/Mercury_05_10_21C/EGM_Mercury_180_180_23609999_10072021.nc` (EGM Mg), `http://impex.latmos.ipsl.fr/LIZE/Merc_02_05_20A/LIZE_tdep_flare_He_LatHyS_020520_EGM_170_190_00000278_t00.nc` (LIZE He$^+$), `http://impex.latmos.ipsl.fr/LIZE/Merc_02_05_20B/LIZE_tdep_flare_O_LatHyS_020520_EGM_049_049_00800000_t00.nc` (LIZE O$^+$) and `http://impex.latmos.ipsl.fr/LIZE/Merc_02_05_20C/LIZE_tdep_flare_Mg_LatHyS_020520_EGM_180_180_23609999_t00.nc` (LIZE Mg$^+$). A.L.E.W., F.L., J-Y.C. and R.M thanks the IPSL data center CICLAD for providing access to their computing resources.

References

Aizawa, S., Griton, L. S., Fatemi, S., Exner, W., Deca, J., Pantellini, F., . . . Usui,

H. (2021). Cross-comparison of global simulation models applied to Mercury's dayside magnetosphere. *Planetary and Space Science*, *198*. doi: 10.1016/j.pss.2021.105176

Anderson, B. J., Johnson, C. L., Korth, H., Purucker, M. E., Winslow, R. M., Slavin, J. A., ... Zurbuchen, T. H. (2011). The Global Magnetic Field of Mercury from MESSENGER Orbital Observations. *Science*, *333*(6051), 1859. doi: 10.1126/science.1211001

Andrews, G. B., Zurbuchen, T. H., Mauk, B. H., Malcom, H., Fisk, L. A., Gloeckler, G., ... Raines, J. M. (2007). The Energetic Particle and Plasma Spectrometer Instrument on the MESSENGER Spacecraft. *Space Science Reviews*, *131*(1-4), 523-556. doi: 10.1007/s11214-007-9272-5

Aulanier, G., DeLuca, E. E., Antiochos, S. K., McMullen, R. A., & Golub, L. (2000). The Topology and Evolution of the Bastille Day Flare. *The Astrophysical Journal*, *540*(2), 1126-1142. doi: 10.1086/309376

Berdermann, J., Kriegel, M., Banyś, D., Heymann, F., Hoque, M. M., Wilken, V., ... Jakowski, N. (2018). Ionospheric Response to the X9.3 Flare on 6 September 2017 and Its Implication for Navigation Services Over Europe. *Space Weather*, *16*(10), 1604-1615. doi: 10.1029/2018SW001933

Bhardwaj, A., Elsner, R. F., Waite, J., J. Hunter, Gladstone, G. R., Cravens, T. E., & Ford, P. G. (2005). Chandra Observation of an X-Ray Flare at Saturn: Evidence of Direct Solar Control on Saturn's Disk X-Ray Emissions. *The Astrophysical Journal*, *624*(2), L121-L124. doi: 10.1086/430521

Bida, T. A., & Killen, R. M. (2017). Observations of the minor species Al and Fe in Mercury's exosphere. *Icarus*, *289*, 227-238. doi: 10.1016/j.icarus.2016.10.019

Bida, T. A., Killen, R. M., & Morgan, T. H. (2000). Discovery of calcium in Mercury's atmosphere. *Nature*, *404*(6774), 159-161. doi: 10.1038/35004521

Broadfoot, A. L., Kumar, S., Belton, M. J. S., & McElroy, M. B. (1974). Mercury's Atmosphere from Mariner 10: Preliminary Results. *Science*, *185*(4146), 166-169. doi: 10.1126/science.185.4146.166

Burger, M. H., Killen, R. M., McClintock, W. E., Merkel, A. W., Vervack, R. J., Cassidy, T. A., & Sarantos, M. (2014). Seasonal variations in Mercury's dayside calcium exosphere. *Icarus*, *238*, 51-58. doi: 10.1016/j.icarus.2014.04.049

Cassidy, T. A., McClintock, W. E., Killen, R. M., Sarantos, M., Merkel, A. W., Vervack, R. J., & Burger, M. H. (2016). A cold-pole enhancement in Mercury's sodium exosphere. *Geophysical Research Letters*, *43*(21), 11,121-11,128. doi: 10.1002/2016GL071071

Cassidy, T. A., Merkel, A. W., Burger, M. H., Sarantos, M., Killen, R. M., McClintock, W. E., & Vervack, R. J. (2015). Mercury's seasonal sodium exosphere: MESSENGER orbital observations. *Icarus*, *248*, 547-559. doi: 10.1016/j.icarus.2014.10.037

Chamberlin, P. C., Eparvier, F. G., Knoer, V., Leise, H., Pankratz, A., Snow, M., ... Woods, T. N. (2020). The Flare Irradiance Spectral Model-Version 2 (FISM2). *Space Weather*, *18*(12). doi: 10.1029/2020SW002588

Chamberlin, P. C., Woods, T. N., Didkovsky, L., Eparvier, F. G., Jones, A. R., Machol, J. L., ... Woodraska, D. L. (2018). Solar Ultraviolet Irradiance Observations of the Solar Flares During the Intense September 2017 Storm Period. *Space Weather*, *16*(10), 1470-1487. doi: 10.1029/2018SW001866

Chaufray, J.-. Y., Leblanc, F., Werner, A. L. E., Modolo, R., & Aizawa, S. (2021a). Seasonal variations of Mg and Ca in the exosphere of Mercury. In *Agu fall meeting abstracts 2021.*

Chaufray, J.-. Y., Leblanc, F., Werner, E., Modolo, R., & Aizawa, S. (2021b). Seasonal variations of Mg and Ca in the exosphere of Mercury. *Icarus*, *Under review*.

Dennis, B. R., & Schwartz, R. A. (1989). Solar Flares - the Impulsive Phase. *Solar Physics*, *121*(1-2), 75-94. doi: 10.1007/BF00161688

Diffenbaugh, N. (Ed.). (2018). *Impact of the Sept. 10, 2017, solar event on Mars [Special issue]. Geophysical Research Letters.* `https://agupubs.onlinelibrary.wiley.com/doi/toc/10.1002/(ISSN)1944-8007.MARS_SOLAR1.`

Elrod, M. K., Curry, S. M., Thiemann, E. M. B., & Jain, S. K. (2018). September 2017 Solar Flare Event: Rapid Heating of the Martian Neutral Upper Atmosphere From the X-Class Flare as Observed by MAVEN. *Geophysical Research Letters*, *45*(17), 8803-8810. doi: 10.1029/2018GL077729

Evans, L. G., Peplowski, P. N., McCubbin, F. M., McCoy, T. J., Nittler, L. R., Zolotov, M. Y., ... Solomon, S. C. (2015). Chlorine on the surface of Mercury: MESSENGER gamma-ray measurements and implications for the planet's formation and evolution. *Icarus*, *257*, 417-427. doi: 10.1016/j.icarus.2015.04.039

Evans, L. G., Peplowski, P. N., Rhodes, E. A., Lawrence, D. J., McCoy, T. J., Nittler, L. R., ... Goldsten, J. O. (2012). Major-element abundances on the surface of Mercury: Results from the MESSENGER Gamma-Ray Spectrometer. *Journal of Geophysical Research (Planets)*, *117*. doi: 10.1029/2012JE004178

Fallows, K., Withers, P., & Gonzalez, G. (2015). Response of the Mars ionosphere to solar flares: Analysis of MGS radio occultation data. *Journal of Geophysical Research (Space Physics)*, *120*(11), 9805-9825. doi: 10.1002/2015JA021108

Glass, A. N., Raines, J. M., Jia, X., Tensihev, V., Shou, Y., Aizawa, S., & A., S. J. (2021). A 3D MHD-Particle Tracing Model of Na+ Energization on Mercury's Dayside. *Planetary and Space Science*, *126*. doi: 10.1029/2021JA029587

Jain, S. K., Deighan, J., Schneider, N. M., Stewart, A. I. F., Evans, J. S., Thiemann, E. M. B., ... Jakosky, B. M. (2018). Martian Thermospheric Response to an X8.2 Solar Flare on 10 September 2017 as Seen by MAVEN/IUVS. *Geophysical Research Letters*, *45*(15), 7312-7319. doi: 10.1029/2018GL077731

Jasinski, J. M., Cassidy, T. A., Raines, J. M., Milillo, A., Regoli, L. H., Dewey, R., ... Murphy, N. (2021). Photoionization Loss of Mercury's Sodium Exosphere: Seasonal Observations by MESSENGER and the THEMIS Telescope. *Geophysical Research Letters*, *48*(8). doi: 10.1029/2021GL092980

Jasinski, J. M., Regoli, L. H., Cassidy, T. A., Dewey, R. M., Raines, J. M., Slavin, J. A., ... Murphy, N. (2020). A transient enhancement of Mercury's exosphere at extremely high altitudes inferred from pickup ions. *Nature Communications*, *11*. doi: 10.1038/s41467-020-18220-2

Killen, R., Cremonese, G., Lammer, H., Orsini, S., Potter, A. E., Sprague, A. L., ... Mura, A. (2007). Processes that Promote and Deplete the Exosphere of Mercury. *Space Science Reviews*, *132*(2-4), 433-509. doi: 10.1007/s11214-007-9232-0

Killen, R., Shemansky, D., & Mouawad, N. (2009). Expected Emission from Mercury's Exospheric Species, and their Ultraviolet-Visible Signatures. *The Astrophysical Journal Supplement*, *181*(2), 351-359. doi: 10.1088/0067-0049/181/2/351

Knipp, D. (Ed.). (2018). *Space Weather Events of 4-10 September 2017 [Special issue]. Space Weather.* `https://agupubs.onlinelibrary.wiley.com/doi/toc/10.1002/(ISSN)1542-7390.SW-SEPT2017.`

Leblanc, F., & Chaufray, J. Y. (2011). Mercury and Moon He exospheres: Analysis and modeling. *Icarus*, *216*(2), 551-559. doi: 10.1016/j.icarus.2011.09.028

Leblanc, F., Doressoundiram, A., Schneider, N., Mangano, V., López Ariste, A., Lemen, C., ... Cremonese, G. (2008). High latitude peaks in Mercury's sodium exosphere: Spectral signature using THEMIS solar telescope. *Geophysical Research Letters*, *35*(18). doi: 10.1029/2008GL035322

Leblanc, F., Doressoundiram, A., Schneider, N., Massetti, S., Wedlund, M., López Ariste, A., ... Cremonese, G. (2009). Short-term variations of Mercury's Na exosphere observed with very high spectral resolution. *Geophysical Research Letters*, *36*(7). doi: 10.1029/2009GL038089

Leblanc, F., & Johnson, R. E. (2003). Mercury's sodium exosphere. *Icarus*, *164*(2), 261-281. doi: 10.1016/S0019-1035(03)00147-7

Leblanc, F., & Johnson, R. E. (2010). Mercury exosphere I. Global circulation model of its sodium component. *Icarus*, *209*(2), 280-300. doi: 10.1016/j.icarus.2010.04.020

Leblanc, F., Oza, A. V., Leclercq, L., Schmidt, C., Cassidy, T., Modolo, R., … Johnson, R. E. (2017). On the orbital variability of Ganymede's atmosphere. *Icarus*, *293*, 185-198. doi: 10.1016/j.icarus.2017.04.025

Mangano, V., Leblanc, F., Barbieri, C., Massetti, S., Milillo, A., Cremonese, G., & Grava, C. (2009). Detection of a southern peak in Mercury's sodium exosphere with the TNG in 2005. *Icarus*, *201*(2), 424-431. doi: 10.1016/j.icarus.2009.01.016

Mangano, V., Massetti, S., Milillo, A., Mura, A., Orsini, S., & Leblanc, F. (2013). Dynamical evolution of sodium anisotropies in the exosphere of Mercury. *Planetary and Space Science*, *82*, 1-10. doi: 10.1016/j.pss.2013.03.002

Mangano, V., Massetti, S., Milillo, A., Plainaki, C., Orsini, S., Rispoli, R., & Leblanc, F. (2015). THEMIS Na exosphere observations of Mercury and their correlation with in-situ magnetic field measurements by MESSENGER. *Planetary and Space Science*, *115*, 102-109. doi: 10.1016/j.pss.2015.04.001

Massetti, S., Mangano, V., Milillo, A., Mura, A., Orsini, S., & Plainaki, C. (2017). Short-term observations of double-peaked Na emission from Mercury's exosphere. *Geophysical Research Letters*, *44*(7), 2970-2977. doi: 10.1002/2017GL073090

Maurellis, A. N., Cravens, T. E., Gladstone, G. R., Waite, J. H., & Acton, L. W. (2000). Jovian X-ray emission from solar X-ray scattering. *Geophysical Research Letters*, *27*(9), 1339-1342. doi: 10.1029/1999GL010723

McClintock, W. E., Bradley, E. T., Vervack, R. J., Killen, R. M., Sprague, A. L., Izenberg, N. R., & Solomon, S. C. (2008). Mercury's Exosphere: Observations During MESSENGER's First Mercury Flyby. *Science*, *321*(5885), 92. doi: 10.1126/science.1159467

Mendillo, M., Withers, P., Hinson, D., Rishbeth, H., & Reinisch, B. (2006). Effects of Solar Flares on the Ionosphere of Mars. *Science*, *311*(5764), 1135-1138. doi: 10.1126/science.1122099

Merkel, A. W., Cassidy, T. A., Vervack, R. J., McClintock, W. E., Sarantos, M., Burger, M. H., & Killen, R. M. (2017). Seasonal variations of Mercury's magnesium dayside exosphere from MESSENGER observations. *Icarus*, *281*, 46-54. doi: 10.1016/j.icarus.2016.08.032

Merkel, A. W., Vervack, R. J., Killen, R. M., Cassidy, T. A., McClintock, W. E., Nittler, L. R., & Burger, M. H. (2018). Evidence Connecting Mercury's Magnesium Exosphere to Its Magnesium-Rich Surface Terrane. *Geophysical Research Letters*, *45*(14), 6790-6797. doi: 10.1029/2018GL078407

Milillo, A., Mangano, V., Massetti, S., Mura, A., Plainaki, C., Alberti, T., … Vertolli, N. (2021). Exospheric Na distributions along the Mercury orbit with the THEMIS telescope. *Icarus*, *355*. doi: 10.1016/j.icarus.2020.114179

Modolo, R., Hess, S., Génot, V., Leclercq, L., Leblanc, F., Chaufray, J. Y., … Holmström, M. (2018). The LatHyS database for planetary plasma environment investigations: Overview and a case study of data/model comparisons. *Planetary and Space Science*, *150*, 13-21. doi: 10.1016/j.pss.2017.02.015

Modolo, R., Hess, S., Mancini, M., Leblanc, F., Chaufray, J.-Y., Brain, D., … Mazelle, C. (2016). Mars-solar wind interaction: LatHyS, an improved parallel 3-D multispecies hybrid model. *Journal of Geophysical Research (Space Physics)*, *121*(7), 6378-6399. doi: 10.1002/2015JA022324

National Oceanic and Atmospheric Administration. (2011). *NOAA Space Weather Scales.* `https://www.swpc.noaa.gov/sites/default/files/images/NOAAscales.pdf`. (Last updated on 7 April 2011. Accessed on 6 September

2021)

Neupert, W. M. (1968). Comparison of Solar X-Ray Line Emission with Microwave Emission during Flares. *Astrophysical Journal*, *153*, L59. doi: 10.1086/180220

Nittler, L. R., Starr, R. D., Weider, S. Z., McCoy, T. J., Boynton, W. V., Ebel, D. S., … Sprague, A. L. (2011). The Major-Element Composition of Mercury's Surface from MESSENGER X-ray Spectrometry. *Science*, *333*(6051), 1847. doi: 10.1126/science.1211567

Orsini, S., Mangano, V., Milillo, A., Plainaki, C., Mura, A., Raines, J. M., … Aronica, A. (2018). Mercury sodium exospheric emission as a proxy for solar perturbations transit. *Scientific Reports*, *8*. doi: 10.1038/s41598-018-19163-x

Peplowski, P. N., Lawrence, D. J., Evans, L. G., Klima, R. L., Blewett, D. T., Goldsten, J. O., … Weider, S. Z. (2015). Constraints on the abundance of carbon in near-surface materials on Mercury: Results from the MESSENGER Gamma-Ray Spectrometer. *Planetary and Space Science*, *108*, 98-107. doi: 10.1016/j.pss.2015.01.008

Peplowski, P. N., Lawrence, D. J., Rhodes, E. A., Sprague, A. L., McCoy, T. J., Denevi, B. W., … Weider, S. Z. (2012). Variations in the abundances of potassium and thorium on the surface of Mercury: Results from the MESSENGER Gamma-Ray Spectrometer. *Journal of Geophysical Research (Planets)*, *117*. doi: 10.1029/2012JE004141

Potter, A. E., & Morgan, T. H. (1985). Discovery of Sodium in the Atmosphere of Mercury. *Science*, *229*(4714), 651-653. doi: 10.1126/science.229.4714.651

Potter, A. E., & Morgan, T. H. (1986). Potassium in the atmosphere of Mercury. *Icarus*, *67*(2), 336-340. doi: 10.1016/0019-1035(86)90113-2

Priest, E. R. (1981). *Solar flare magnetohydrodynamics.* New York: Gordon and Breach.

Raines, J. M., Gershman, D. J., Slavin, J. A., Zurbuchen, T. H., Korth, H., Anderson, B. J., & Solomon, S. C. (2014). Structure and dynamics of Mercury's magnetospheric cusp: MESSENGER measurements of protons and planetary ions. *Journal of Geophysical Research (Space Physics)*, *119*(8), 6587-6602. doi: 10.1002/2014JA020120

Raines, J. M., Gershman, D. J., Zurbuchen, T. H., Sarantos, M., Slavin, J. A., Gilbert, J. A., … Solomon, S. C. (2013). Distribution and compositional variations of plasma ions in Mercury's space environment: The first three Mercury years of MESSENGER observations. *Journal of Geophysical Research: Space Physics*, *118*(4), 1604-1619. doi: 10.1029/2012JA018073

Raines, J. M., Wallace, K. L., Sarantos, M., Jasinksi, J. M., Tracy, P. J., Dewey, R. M., … Slavin, J. A. (2018). First In-Situ Observations of Exospheric Response to CME Impact at Mercury. In *Mercury: Current and future science of the innermost planet* (Vol. 2047).

Thiemann, E. M. B., Andersson, L., Lillis, R., Withers, P., Xu, S., Elrod, M., … Deighan, J. (2018). The Mars Topside Ionosphere Response to the X8.2 Solar Flare of 10 September 2017. *Geophysical Research Letters*, *45*(16), 8005-8013. doi: 10.1029/2018GL077730

Tsurutani, B. T., Judge, D. L., Guarnieri, F. L., Gangopadhyay, P., Jones, A. R., Nuttall, J., … Viereck, R. (2005). The October 28, 2003 extreme EUV solar flare and resultant extreme ionospheric effects: Comparison to other Halloween events and the Bastille Day event. *Geophysical Research Letters*, *32*(3). doi: 10.1029/2004GL021475

Verner, D. A., Ferland, G. J., Korista, K. T., & Yakovlev, D. G. (1996). Atomic Data for Astrophysics. II. New Analytic FITS for Photoionization Cross Sections of Atoms and Ions. *The Astrophysical Journal*, *465*, 487. doi: 10.1086/177435

Vervack, R. J., Killen, R. M., McClintock, W. E., Merkel, A. W., Burger, M. H., Cassidy, T. A., & Sarantos, M. (2016). New discoveries from MESSENGER and insights into Mercury's exosphere. *Geophysical Research Letters*, *43*(22), 11,545-11,551. doi: 10.1002/2016GL071284

Werner, A. L. E., Aizawa, S., Leblanc, F., Chaufray, J.-. Y., Modolo, R., Raines, J. M., … Schmidt, C. (2022). Ion density and phase space density distribution of planetary ions Na^+, O^+ and He^+ in Mercury's magnetosphere. *Icarus*, *372*. doi: 10.1016/j.icarus.2021.114734

Winslow, R. M., Anderson, B. J., Johnson, C. L., Slavin, J. A., Korth, H., Purucker, M. E., … Solomon, S. C. (2013). Mercury's magnetopause and bow shock from MESSENGER Magnetometer observations. *Journal of Geophysical Research (Space Physics)*, *118*(5), 2213-2227. doi: 10.1002/jgra.50237

Yagi, M., Seki, K., Matsumoto, Y., Delcourt, D. C., & Leblanc, F. (2010). Formation of a sodium ring in Mercury's magnetosphere. *Journal of Geophysical Research (Space Physics)*, *115*(A10). doi: 10.1029/2009JA015226

Yan, X. L., Wang, J. C., Pan, G. M., Kong, D. F., Xue, Z. K., Yang, L. H., … Feng, X. S. (2018). Successive X-class Flares and Coronal Mass Ejections Driven by Shearing Motion and Sunspot Rotation in Active Region NOAA 12673. *The Astrophysical Journal*, *856*(1), 79. doi: 10.3847/1538-4357/aab153

Zurbuchen, T. H., Raines, J. M., Slavin, J. A., Gershman, D. J., Gilbert, J. A., Gloeckler, G., … Solomon, S. C. (2011). MESSENGER Observations of the Spatial Distribution of Planetary Ions Near Mercury. *Science*, *333*(6051), 1862. doi: 10.1126/science.1211302

7

CONCLUSIONS

In this thesis, we have described the development of a novel test-particle model and its successful application to Mercury's ionized environment.

We have demonstrated that the LIZE model succeed to describe the ion density distribution in the magnetosphere with high precision with respect to existing MESSENGER/FIPS ion density observations. We have also shown the model's capability to describe the phase space density distribution of the planetary ion population in different regions. Finally, we extended the model to accept time-dependent input conditions, and apply this new model capability to study the impact of a strong solar flare event on the planetary ion population.

The results from our model leads us to the following conclusions and topics of future study.

The LIZE model successfully reproduces the average local time-altitude distribution of the He^+, O^+-group and Na^+-group ion density observed by FIPS during the orbital phase of the MESSENGER mission. For nominal solar wind conditions and a strictly northward IMF profile, the magnitude of the average ion density is overestimated by a factor of 5-18. When we test different solar wind conditions, we find that the difference is just a factor of 0.5-2.7 but the spatial distribution does not match as well as for the nominal case. This would imply that the spatial distribution of the planetary ions are highly dependent on the solar wind and IMF conditions at Mercury. To make a better estimate of the average observed ion density and its spatial distribution, it is likely necessary to simulate more representative solar wind and IMF conditions with high statistics.

Our ion density estimates are likely affected by the steady-state magnetic and electric field description. The modeled ion density outside the magnetopause is too low, and for strictly northward IMF, the ion density inside the magnetosphere is too high. It is possible that the large dayside magnetopause during northward IMF conditions and the steady-state magnetic and electric fields used in these models may influence the formation of the ion ring distribution that we see in the model results. The real solar wind is variable, which means that the formation of an ion ring may not occur except under very special conditions.

The response of Mercury's planetary ion environment to a solar flare depends on the ion species, energy range, location in the magnetosphere and the location of the flare source region with respect to Mercury. We find two different ion populations in the dayside magnetosphere which experience different dynamical evolution. We also find a delayed response time on the order of several minutes between the dayside and the nightside plasma sheet. Depending on the flare geometry there may also be a time delay between the different ion species.

The seasonal cycle cycle of the Na^+ density distribution is a topic of interest. Raines et al. (2013) studied the average observed ion density at different TAA for He^+ and O^+- and Na^+-group ions. Jasinski et al. (2021) analyzed FIPS observations taken near the northern cusp at different TAA. Due to the special geometry of the MESSENGER orbit, the ion density at each local time was sampled by FIPS at a particular TAA. This makes it difficult to separate regional and seasonal variations in the FIPS data. For this reason it is not straight-forward to resolve the orbital variation of the ion population, much less over the course of an entire solar activity cycle. UVVS observations of the neutral Na exosphere were also missing near aphelion due to limitations on the viewing geometry. LIZE will be useful to compensate for the lack of observations at certain Mercury TAAs.

The next step of the LIZE model development is to accurately simulate the impact of a CME on the planetary ion density distribution in Mercury's magnetosphere (Raines et al., 2018). The development of the time-dependent LIZE algorithm and its first successful application to describe the impact of a solar flare, both described in this thesis, are crucial to accomplish this task. The time-dependent LIZE model will be used to simulate the different phases of an ICME (shock, sheath and magnetic cloud; Zurbuchen and Richardson, 2006). We will simulate the impact of the changing magnetospheric configuration and solar wind composition on the planetary ion population. To accomplish this, LIZE will need to take time-dependent input conditions from both the EGM and LatHyS. Time-dependent input conditions have already been implemented in EGM as a part of this PhD, and will be for LatHyS in the near future. This coupling between the three models will also help understand the impact of the planetary ion population on the exosphere and the magnetosphere. The coupling to the EGM model will make it possible to simulate the impact the increased ion precipitation on the neutral exosphere, and how this in turn may add to the existing time-variability of the ion density distribution inside the magnetosphere. This makes the LIZE model ideal to support several observation objectives of the BepiColombo mission.

In this thesis we have attempted to answer what the distribution of different planetary ion species looks like in the magnetosphere, their phase space density distribution and their response to short-term, extreme changes in the solar radiation spectrum. The LIZE model clearly puts the ion density distribution in the context of the solar wind and solar radiation conditions, the magnetosphere and the exosphere as a coupled system. The model results presented in this thesis and future LIZE simulations can be used to better understand future observations of Mercury's planetary ion environment. The BepiColombo/MPO and Mio carries several ion mass spectrometers which together will cover a much larger energy range than previous planetary ion observations. LIZE model capabilities may become critical to properly analyze measurements made from two different positions in space and instruments with different spatial, temporal and energy coverage.

BIBLIOGRAPHY

Aizawa, S. et al. (2021). “Cross-comparison of global simulation models applied to Mercury’s dayside magnetosphere.” In: *Planetary and Space Science* 198, 105176. doi: `10.1016/j.pss.2021.105176`.

Aizawa, S., Delcourt, D. and Terada, N. (2018). “Sodium Ion Dynamics in the Magnetospheric Flanks of Mercury.” In: *Geophysical Research Letters* 45.2, pp. 595–601. doi: `10.1002/2017GL076586`.

Anderson, B. J. et al. (2007). “The Magnetometer Instrument on MESSENGER.” In: *Space Science Reviews* 131.1-4, pp. 417–450. doi: `10.1007/s11214-007-9246-7`.

Anderson, B. J. et al. (2008). “The Structure of Mercury’s Magnetic Field from MESSENGER’s First Flyby.” In: *Science* 321.5885, p. 82. doi: `10.1126/science.1159081`.

Anderson, B. J. et al. (2011). “The Global Magnetic Field of Mercury from MESSENGER Orbital Observations.” In: *Science* 333.6051, p. 1859. doi: `10.1126/science.1211001`.

Anderson, B. J. et al. (2012). “Low-degree structure in Mercury’s planetary magnetic field.” In: *Journal of Geophysical Research (Planets)* 117, E00L12. doi: `10.1029/2012JE004159`.

Andrews, G. B. et al. (2007). “The Energetic Particle and Plasma Spectrometer Instrument on the MESSENGER Spacecraft.” In: *Space Science Reviews* 131.1-4, pp. 523–556. doi: `10.1007/s11214-007-9272-5`.

Baumgardner, J., Wilson, J. and Mendillo, M. (2008). “Imaging the sources and full extent of the sodium tail of the planet Mercury.” In: *Geophysical Research Letters* 35.3, L03201. doi: `10.1029/2007GL032337`.

Benna, M. et al. (2010). “Modeling of the magnetosphere of Mercury at the time of the first MESSENGER flyby.” In: *Icarus* 209.1, pp. 3–10. doi: `10.1016/j.icarus.2009.11.036`.

Bida, T. A., Killen, R. M. and Morgan, T. H. (2000). “Discovery of calcium in Mercury’s atmosphere.” In: *Nature* 404.6774, pp. 159–161. doi: `10.1038/35004521`.

Bida, T. A. and Killen, R. M. (2017). “Observations of the minor species Al and Fe in Mercury’s exosphere.” In: *Icarus* 289, pp. 227–238. doi: `10.1016/j.icarus.2016.10.019`.

Birn, J. et al. (2001). “Geospace Environmental Modeling (GEM) magnetic reconnection challenge.” In: *Journal of Geophysical Research* 106.A3, pp. 3715–3720. doi: `10.1029/1999JA900449`.

Bishop, J. and Chamberlain, J. W. (1989). “Radiation pressure dynamics in planetary exospheres: A “natural” framework.” In: *Icarus* 81.1, pp. 145–163. doi: `10.1016/0019-1035(89)90131-0`.

Boardsen, S. A. et al. (2010). "Observations of Kelvin-Helmholtz waves along the dusk-side boundary of Mercury's magnetosphere during MESSENGER's third flyby." In: *Geophysical Research Letters* 37.12, L12101. DOI: 10.1029/2010GL043606.

Broadfoot, A. L., Shemansky, D. E. and Kumar, S. (1976). "Mariner 10: Mercury atmosphere." In: *Geophysical Research Letters* 3.10, pp. 577–580. DOI: 10.1029/GL003i010p00577.

Broadfoot, A. L. et al. (1974). "Mercury's Atmosphere from Mariner 10: Preliminary Results." In: *Science* 185.4146, pp. 166–169. DOI: 10.1126/science.185.4146.166.

Burger, M. H. et al. (2010). "Monte Carlo modeling of sodium in Mercury's exosphere during the first two MESSENGER flybys." In: *Icarus* 209.1, pp. 63–74. DOI: 10.1016/j.icarus.2010.05.007.

Burger, M. H. et al. (2012). "Modeling MESSENGER observations of calcium in Mercury's exosphere." In: *Journal of Geophysical Research (Planets)* 117, E00L11, E00L11. DOI: 10.1029/2012JE004158.

Burger, M. H. et al. (2014). "Seasonal variations in Mercury's dayside calcium exosphere." In: *Icarus* 238, pp. 51–58. DOI: 10.1016/j.icarus.2014.04.049.

Burlaga, L. F. (2001). "Magnetic fields and plasmas in the inner heliosphere: Helios results." In: *Planetary and Space Science* 49.14-15, pp. 1619–1627. DOI: 10.1016/S0032-0633(01)00098-8.

Cassidy, T. A. et al. (2015). "Mercury's seasonal sodium exosphere: MESSENGER orbital observations." In: *Icarus* 248, pp. 547–559. DOI: 10.1016/j.icarus.2014.10.037.

Cassidy, T. A. et al. (2016). "A cold-pole enhancement in Mercury's sodium exosphere." In: *Geophysical Research Letters* 43.21, pp. 11,121–11,128. DOI: 10.1002/2016GL071071.

Chamberlain, J. W. (1961). *Physics of the Aurora and Airglow*. American Geophysical Union (AGU). ISBN: 9781118668047. DOI: https://doi.org/10.1029/SP041.

Chamberlain, J. W. (1963). "Planetary coronae and atmospheric evaporation." In: *Planetary and Space Science* 11.8, pp. 901–960. DOI: 10.1016/0032-0633(63)90122-3.

Chamberlain, J. W. and Campbell, F. J. (1967). "Rate of Evaporation of a Non-Maxwellian Atmosphere." In: *Astrophysical Journal* 149, p. 687. DOI: 10.1086/149298.

Chamberlin, P. C. et al. (2020). "The Flare Irradiance Spectral Model-Version 2 (FISM2)." In: *Space Weather* 18.12, e02588. DOI: 10.1029/2020SW002588.

Christensen, U. R. (2006). "A deep dynamo generating Mercury's magnetic field." In: *Nature* 444.7122, pp. 1056–1058. DOI: 10.1038/nature05342.

Christou, A. A., Killen, R. M. and Burger, M. H. (2015). "The meteoroid stream of comet Encke at Mercury: Implications for MErcury Surface, Space ENvironment, GEochemistry, and Ranging observations of the exosphere." In: *Geophysical Research Letters* 42.18, pp. 7311–7318. DOI: 10.1002/2015GL065361.

Cremonese, G. et al. (2005). "Release of neutral sodium atoms from the surface of Mercury induced by meteoroid impacts." In: *Icarus* 177.1, pp. 122–128. DOI: 10.1016/j.icarus.2005.03.022.

Dandouras, I. et al. (2020). "Future Missions Related to the Determination of the Elemental and Isotopic Composition of Earth, Moon and the Terrestrial Planets." In: *Space Science Reviews* 216.8, 121. DOI: 10.1007/s11214-020-00736-0.

Delcourt, D. C. (2013). "On the supply of heavy planetary material to the magnetotail of Mercury." In: *Annales Geophysicae* 31.10, pp. 1673–1679. DOI: 10.5194/angeo-31-1673-2013.

Delcourt, D. C. et al. (2002). "Centrifugal acceleration of ions near Mercury." In: *Geophysical Research Letters* 29.12, p. 1591. DOI: 10.1029/2001GL013829.

Delcourt, D. C. et al. (2003). "A quantitative model of the planetary Na+ contribution to MercuryÂ's magnetosphere." In: *Annales Geophysicae* 21.8, pp. 1723–1736. DOI: 10.5194/angeo-21-1723-2003.

Delcourt, D. C. et al. (2012). "Centrifugally stimulated exospheric ion escape at Mercury." In: *Geophysical Research Letters* 39.22, L22105. DOI: 10.1029/2012GL054085.

DiBraccio, G. A. et al. (2015). "MESSENGER observations of flux ropes in Mercury's magnetotail." In: *Planetary and Space Science* 115, pp. 77–89. DOI: 10.1016/j.pss.2014.12.016.

Domingue, D. L. et al. (2007). "Mercury's Atmosphere: A Surface-Bounded Exosphere." In: *Space Science Reviews* 131.1-4, pp. 161–186. DOI: 10.1007/s11214-007-9260-9.

Doressoundiram, A. et al. (2009). "Metallic Species in Mercury's Exosphere: EMMI/New Technology Telescope Observations." In: *The Astrophysical Journal* 137.4, pp. 3859–3863. DOI: 10.1088/0004-6256/137/4/3859.

Doressoundiram, A. et al. (2010). "Spatial variations of the sodium/potassium ratio in Mercury's exosphere uncovered by high-resolution spectroscopy." In: *icarus* 207.1, pp. 1–8. DOI: 10.1016/j.icarus.2009.11.020.

ESA/ATG medialab (2020). *BepiColombo MPO's science instruments & BepiColombo Mio's science instruments*. [Online; accessed 2021-08-26]. URL: https://sci.esa.int/web/bepicolombo/-/59934-spacecraft-duo.

ESA/Sebastian Besse (2016). *Relationship of BepiColombo and MESSENGER orbits to Mercury's magnetic field*. [Online; accessed 2021-08-26]. URL: https://www.planetary.org/space-images/relationship-of-bepicolombo.

Egan, H. et al. (2019). "Planetary magnetic field control of ion escape from weakly magnetized planets." In: *Monthly Notices of the Royal*

Astronomical Society 488.2, pp. 2108–2120. DOI: 10.1093/mnras/stz1819.

Evans, L. G. et al. (2012). "Major-element abundances on the surface of Mercury: Results from the MESSENGER Gamma-Ray Spectrometer." In: *Journal of Geophysical Research (Planets)* 117, E00L07. DOI: 10.1029/2012JE004178.

Evans, L. G. et al. (2015). "Chlorine on the surface of Mercury: MESSENGER gamma-ray measurements and implications for the planet's formation and evolution." In: *Icarus* 257, pp. 417–427. DOI: 10.1016/j.icarus.2015.04.039.

Exner, W. et al. (2020). "Influence of Mercury's Exosphere on the Structure of the Magnetosphere." In: *Journal of Geophysical Research (Space Physics)* 125.7, e27691. DOI: 10.1029/2019JA027691.

Gamborino, D., Vorburger, A. and Wurz, P. (2019). "Mercury's subsolar sodium exosphere: an ab initio calculation to interpret MASCS/UVVS observations from MESSENGER." In: *Annales Geophysicae* 37.4, pp. 455–470. DOI: 10.5194/angeo-37-455-2019.

Genova, A. et al. (2019). "Geodetic Evidence That Mercury Has A Solid Inner Core." In: *Geophysical Research Letters* 46.7, pp. 3625–3633. DOI: 10.1029/2018GL081135.

Gershman, D. J. et al. (2013). "Magnetic flux pileup and plasma depletion in Mercury's subsolar magnetosheath." In: *Journal of Geophysical Research (Space Physics)* 118.11, pp. 7181–7199. DOI: 10.1002/2013JA019244.

— (2014). "Ion kinetic properties in Mercury's pre-midnight plasma sheet." In: *Geophysical Research Letters* 41.16, pp. 5740–5747. DOI: 10.1002/2014GL060468.

Gershman, D. J. et al. (2015). "MESSENGER observations of multiscale Kelvin-Helmholtz vortices at Mercury." In: *Journal of Geophysical Research (Space Physics)* 120.6, pp. 4354–4368. DOI: 10.1002/2014JA020903.

Gingell, P. W., Sundberg, T. and Burgess, D. (2015). "The impact of a hot sodium ion population on the growth of the Kelvin-Helmholtz instability in Mercury's magnetotail." In: *Journal of Geophysical Research (Space Physics)* 120.7, pp. 5432–5442.

Gombosi, T. I. et al. (2000). "MHD Simulations of Current Systems in Planetary Magnetospheres: Mercury and Saturn." In: *Washington DC American Geophysical Union Geophysical Monograph Series* 118, p. 363. DOI: 10.1029/GM118p0363.

Grava, C. et al. (2021). "Volatiles and Refractories in Surface-Bounded Exospheres in the Inner Solar System." In: *Space Science Reviews* 217.5, 61, p. 61. DOI: 10.1007/s11214-021-00833-8.

Hauck, S. A. et al. (2013). "The curious case of Mercury's internal structure." In: *Journal of Geophysical Research (Planets)* 118.6, pp. 1204–1220. DOI: 10.1002/jgre.20091.

Hodges, R. R. (1980). “Methods for Monte Carlo simulation of the exospheres of the moon and mercury.” In: *Journal of Geophysical Research* 85.A1, pp. 164–170. DOI: 10.1029/JA085iA01p00164.

Huebner, W. F., Keady, J. J. and Lyon, S. P. (1992). “Solar Photo Rates for Planetary Atmospheres and Atmospheric Pollutants.” In: *Astrophysics and Space Science* 195.1, pp. 1–294. DOI: 10.1007/BF00644558.

Huebner, W. F. and Mukherjee, J. (2015). “Photoionization and photodissociation rates in solar and blackbody radiation fields.” In: *Planetary and Space Science* 106, pp. 11–45. DOI: 10.1016/j.pss.2014.11.022.

Hunten, D. M., Morgan, T. H. and Shemansky, D. E. (1988). “The Mercury atmosphere.” In: *Mercury*. Ed. by F. Vilas, C. R. Chapman and M. S. Matthews. Tucson, Arizona, USA: University of Arizona Press, pp. 562–612.

Hunten, D. M., Roach, F. E. and Chamberlain, J. W. (1956). “A photometric unit for the airglow and aurora.” In: *Journal of Atmospheric and Terrestrial Physics* 8.6, pp. 345–346. DOI: 10.1016/0021-9169(56)90111-8.

Hunten, D. M. and Sprague, A. L. (1997). “Origin and character of the lunar and mercurian atmospheres.” In: *Advances in Space Research* 19.10, pp. 1551–1560. DOI: 10.1016/S0273-1177(97)00368-2.

— (2002). “Diurnal variation of Na and K at Mercury.” In: *Meteoritics and Planetary Science* 37.9, pp. 1191–1195. DOI: 10.1111/j.1945-5100.2002.tb00888.x.

Ip, W. H. (1986). “The sodium exosphere and magnetosphere of Mercury.” In: *Geophysical Research Letters* 13.5, pp. 423–426. DOI: 10.1029/GL013i005p00423.

Ip, W. H. and Kopp, A. (2004). “Mercury’s Birkeland current system.” In: *Advances in Space Research* 33.12, pp. 2172–2175. DOI: 10.1016/S0273-1177(03)00444-7.

Ip, W.-H. (1997). “Time-variable phenomena in the magnetosphere and exosphere of Mercury.” In: *Advances in Space Research* 19.10, pp. 1615–1620. DOI: 10.1016/S0273-1177(97)00375-X.

Ip, W.-H. and Kopp, A. (2002). “MHD simulations of the solar wind interaction with Mercury.” In: *Journal of Geophysical Research (Space Physics)* 107.A11, 1348. DOI: 10.1029/2001JA009171.

James, M. K. et al. (2019). “Field Line Resonance in the Hermean Magnetosphere: Structure and Implications for Plasma Distribution.” In: *Journal of Geophysical Research: Space Physics* 124.1, pp. 211–228. DOI: 10.1029/2018JA025920.

James, M. K. et al. (2017). “Interplanetary magnetic field properties and variability near Mercury’s orbit.” In: *Journal of Geophysical Research (Space Physics)* 122.8, pp. 7907–7924. DOI: 10.1002/2017JA024435.

Jasinski, J. M. et al. (2017). “Mercury’s Solar Wind Interaction as Characterized by Magnetospheric Plasma Mantle Observations With

MESSENGER." In: *Journal of Geophysical Research (Space Physics)* 122.12, pp. 12,153–12,169. DOI: 10.1002/2017JA024594.

Jasinski, J. M. et al. (2020). "A transient enhancement of Mercury's exosphere at extremely high altitudes inferred from pickup ions." In: *Nature Communications* 11, 4350. DOI: 10.1038/s41467-020-18220-2.

Jasinski, J. M. et al. (2021). "Photoionization Loss of Mercury's Sodium Exosphere: Seasonal Observations by MESSENGER and the THEMIS Telescope." In: *Geophysical Research Letters* 48.8, e92980. DOI: 10.1029/2021GL092980.

Jia, X. et al. (2015). "Global MHD simulations of Mercury's magnetosphere with coupled planetary interior: Induction effect of the planetary conducting core on the global interaction." In: *Journal of Geophysical Research (Space Physics)* 120.6, pp. 4763–4775. DOI: 10.1002/2015JA021143.

Johnson, R. E. (1994). "Plasma-Induced Sputtering of an Atmosphere." In: *Space Science Reviews* 69.3-4, pp. 215–253. DOI: 10.1007/BF02101697.

Johnson, R. E. et al. (2002). "Energy Distributions for Desorption of Sodium and Potassium from Ice: The Na/K Ratio at Europa." In: *Icarus* 156.1, pp. 136–142. DOI: 10.1006/icar.2001.6763.

Kabin, K. et al. (2000). "Interaction of Mercury with the Solar Wind." In: *Icarus* 143.2, pp. 397–406. DOI: 10.1006/icar.1999.6252.

Kabin, K. et al. (2008). "Global MHD modeling of Mercury's magnetosphere with applications to the MESSENGER mission and dynamo theory." In: *Icarus* 195.1, pp. 1–15. DOI: 10.1016/j.icarus.2007.11.028.

Kallio, E. and Janhunen, P. (2003). "Solar wind and magnetospheric ion impact on Mercury's surface." In: *Geophysical Research Letters* 30.17, 1877. DOI: 10.1029/2003GL017842.

— (2004). "The response of the Hermean magnetosphere to the interplanetary magnetic field." In: *Advances in Space Research* 33.12, pp. 2176–2181. DOI: 10.1016/S0273-1177(03)00447-2.

Killen, R. M. and Morgan, T. H. (1993). "Maintaining the Na Atmosphere of Mercury." In: *Icarus* 101.2, pp. 293–312. DOI: 10.1006/icar.1993.1026.

Killen, R. M., Potter, A. E. and Morgan, T. H. (1990). "Spatial distribution of sodium vapor in the atmosphere of Mercury." In: *Icarus* 85.1, pp. 145–167. DOI: 10.1016/0019-1035(90)90108-L.

Killen, R. M. et al. (2001). "Evidence for space weather at Mercury." In: *Journal of Geophysical Research* 106.E9, pp. 20509–20526. DOI: 10.1029/2000JE001401.

Killen, R. M. et al. (2018). "Understanding Mercury's Exosphere: Models Derived from MESSENGER Observations." In: *Mercury: The View after MESSENGER*. Ed. by S. C. Solomon, L. R. Nittler and B. J. Anderson. Cambridge: Cambridge University Press. Chap. 15, pp. 407–429.

Killen, R. M. (2016). “Pathways for energization of Ca in Mercury’s exosphere.” In: *Icarus* 268, pp. 32–36. DOI: 10.1016/j.icarus.2015.12.035.

Killen, R. M., Bida, T. A. and Morgan, T. H. (2005). “The calcium exosphere of Mercury.” In: *Icarus* 173.2, pp. 300–311. DOI: 10.1016/j.icarus.2004.08.022.

Killen, R. M. and Hahn, J. M. (2015). “Impact vaporization as a possible source of Mercury’s calcium exosphere.” In: *Icarus* 250, pp. 230–237. DOI: 10.1016/j.icarus.2014.11.035.

Killen, R. M. et al. (1999). “Sodium D2 line profiles: clues to the temperature structure of Mercury’s exosphere.” In: *Planetary and Space Science* 47.12, pp. 1449–1458. DOI: 10.1016/S0032-0633(99)00071-9.

Killen, R. M. et al. (2010). “Observations of metallic species in Mercury’s exosphere.” In: *Icarus* 209.1, pp. 75–87. DOI: 10.1016/j.icarus.2010.02.018.

Killen, R. et al. (2007). “Processes that Promote and Deplete the Exosphere of Mercury.” In: *Space Science Reviews* 132.2-4, pp. 433–509. DOI: 10.1007/s11214-007-9232-0.

Korth, H. et al. (2004). “Determination of the properties of Mercury’s magnetic field by the MESSENGER mission.” In: *Planetary and Space Science* 52.8, pp. 733–746. DOI: 10.1016/j.pss.2003.12.008.

Korth, H. et al. (2011). “The interplanetary magnetic field environment at Mercury’s orbit.” In: *Planetary and Space Science* 59.15, pp. 2075–2085. DOI: 10.1016/j.pss.2010.10.014.

Korth, H. et al. (2012). “Characteristics of the plasma distribution in Mercury’s equatorial magnetosphere derived from MESSENGER Magnetometer observations.” In: *Journal of Geophysical Research (Space Physics)* 117.A12, A00M07. DOI: 10.1029/2012JA018052.

Korth, H. et al. (2014). “Plasma distribution in Mercury’s magnetosphere derived from MESSENGER Magnetometer and Fast Imaging Plasma Spectrometer observations.” In: *Journal of Geophysical Research (Space Physics)* 119.4, pp. 2917–2932. DOI: 10.1002/2013JA019567.

Korth, H. et al. (2015). “Modular model for Mercury’s magnetospheric magnetic field confined within the average observed magnetopause.” In: *Journal of Geophysical Research (Space Physics)* 120.6, pp. 4503–4518. DOI: 10.1002/2015JA021022.

Kunc, J. A. and Shemansky, D. E. (1981). “The interaction of helium with α-quartz.” In: *The Journal of Chemical Physics* 75.5, pp. 2406–2411. DOI: 10.1063/1.442304.

Kunc, J. A. and Shemansky, D. E. (1985). “The potential curve of the He-α-quartz surface interaction.” In: *Surface Science* 163.1, pp. 237–248. DOI: 10.1016/0039-6028(85)90861-1.

Leblanc, F. and Chaufray, J. Y. (2011). “Mercury and Moon He exospheres: Analysis and modeling.” In: *Icarus* 216.2, pp. 551–559. DOI: `10.1016/j.icarus.2011.09.028`.

Leblanc, F., Delcourt, D. and Johnson, R. E. (2003). “Mercury’s sodium exosphere: Magnetospheric ion recycling.” In: *Journal of Geophysical Research (Planets)* 108.E12, 5136. DOI: `10.1029/2003JE002151`.

Leblanc, F. and Johnson, R. E. (2003). “Mercury’s sodium exosphere.” In: *Icarus* 164.2, pp. 261–281. DOI: `10.1016/S0019-1035(03)00147-7`.

Leblanc, F. et al. (2008). “High latitude peaks in Mercury’s sodium exosphere: Spectral signature using THEMIS solar telescope.” In: *Geophysical Research Letters* 35.18, L18204. DOI: `10.1029/2008GL035322`.

Leblanc, F. et al. (2009). “Short-term variations of Mercury’s Na exosphere observed with very high spectral resolution.” In: *Geophysical Research Letters* 36.7, L07201. DOI: `10.1029/2009GL038089`.

Leblanc, F. et al. (2017). “On the orbital variability of Ganymede’s atmosphere.” In: *Icarus* 293, pp. 185–198. DOI: `10.1016/j.icarus.2017.04.025`.

Leblanc, F. and Johnson, R. E. (2010). “Mercury exosphere I. Global circulation model of its sodium component.” In: *Icarus* 209.2, pp. 280–300. DOI: `10.1016/j.icarus.2010.04.020`.

Liljeblad, E. et al. (2014). “Statistical investigation of Kelvin-Helmholtz waves at the magnetopause of Mercury.” In: *Journal of Geophysical Research (Space Physics)* 119.12, pp. 9670–9683. DOI: `10.1002/2014JA020614`.

López Ariste, A., Rayrole, J. and Semel, M. (2000). “First results from THEMIS spectropolarimetric mode.” In: *Astronomy and Astrophysics Supplement* 142, pp. 137–148. DOI: `10.1051/aas:2000144`.

Luhmann, J. G. and Friesen, L. M. (1979). “A simple model of the magnetosphere.” In: *Journal of Geophysical Research* 84.A8, pp. 4405–4408. DOI: `10.1029/JA084iA08p04405`.

Luhmann, J. G., Russell, C. T. and Tsyganenko, N. A. (1998). “Disturbances in Mercury’s magnetosphere: Are the Mariner 10 “substorms” simply driven?” In: *Journal of Geophysical Research* 103.A5, pp. 9113–9120. DOI: `10.1029/97JA03667`.

Lukyanov, A. V. et al. (2001). “Energetic neutral atom imaging of Mercury’s magnetosphere 2. Distribution of energetic charged particles in a compact magnetosphere.” In: *Planetary and Space Science* 49.14-15, pp. 1677–1684. DOI: `10.1016/S0032-0633(01)00106-4`.

Madey, T. E. et al. (1998). “Desorption of alkali atoms and ions from oxide surfaces: Relevance to origins of Na and K in atmospheres of Mercury and the Moon.” In: *Journal of Geophysical Research* 103.E3, pp. 5873–5888. DOI: `10.1029/98JE00230`.

Mangano, V. et al. (2007). “The contribution of impulsive meteoritic impact vapourization to the Hermean exosphere.” In: *Planetary* *and Space Science* 55.11, pp. 1541–1556. DOI: 10.1016/j.pss.2006.10.008.

Mangano, V. et al. (2009). "Detection of a southern peak in Mercury's sodium exosphere with the TNG in 2005." In: *Icarus* 201.2, pp. 424–431. DOI: 10.1016/j.icarus.2009.01.016.

Mangano, V. et al. (2013). "Dynamical evolution of sodium anisotropies in the exosphere of Mercury." In: *Planetary and Space Science* 82, pp. 1–10. DOI: 10.1016/j.pss.2013.03.002.

Mangano, V. et al. (2015). "THEMIS Na exosphere observations of Mercury and their correlation with in-situ magnetic field measurements by MESSENGER." In: *Planetary and Space Science* 115, pp. 102–109. DOI: 10.1016/j.pss.2015.04.001.

Margot, J. L. et al. (2007). "Large Longitude Libration of Mercury Reveals a Molten Core." In: *Science* 316.5825, p. 710. DOI: 10.1126/science.1140514.

Marsch, E. et al. (1982). "Solar wind protons: Three-dimensional velocity distributions and derived plasma parameters measured between 0.3 and 1 AU." In: *Journal of Geophysical Research* 87.A1, pp. 52–72. DOI: 10.1029/JA087iA01p00052.

Massetti, S. et al. (2003). "Mapping of the cusp plasma precipitation on the surface of Mercury." In: *Icarus* 166.2, pp. 229–237. DOI: 10.1016/j.icarus.2003.08.005.

Massetti, S. et al. (2017). "Short-term observations of double-peaked Na emission from Mercury's exosphere." In: *Geophysical Research Letters* 44.7, pp. 2970–2977. DOI: 10.1002/2017GL073090.

McClintock, W. E. et al. (2018). "Observations of Mercury's Exosphere: Composition and Structure." In: *Mercury: The View after MESSENGER*. Ed. by S. C. Solomon, L. R. Nittler and B. J. Anderson. Cambridge: Cambridge University Press. Chap. 14, pp. 371–406.

McClintock, W. E. and Lankton, M. R. (2007). "The Mercury Atmospheric and Surface Composition Spectrometer for the MESSENGER Mission." In: *Space Science Reviews* 131.1-4, pp. 481–521. DOI: 10.1007/s11214-007-9264-5.

McClintock, W. E. et al. (2008). "Mercury's Exosphere: Observations During MESSENGER's First Mercury Flyby." In: *Science* 321.5885, p. 92. DOI: 10.1126/science.1159467.

McClintock, W. E. et al. (2009). "MESSENGER Observations of Mercury's Exosphere: Detection of Magnesium and Distribution of Constituents." In: *Science* 324.5927, p. 610. DOI: 10.1126/science.1172525.

McGrath, M. A., Johnson, R. E. and Lanzerotti, L. J. (1986). "Sputtering of sodium on the planet Mercury." In: *Nature* 323.6090, pp. 694–696. DOI: 10.1038/323694a0.

Merkel, A. W. et al. (2017). "Seasonal variations of Mercury's magnesium dayside exosphere from MESSENGER observations." In: *Icarus* 281, pp. 46–54. DOI: 10.1016/j.icarus.2016.08.032.

Merkel, A. W. et al. (2018). “Evidence Connecting Mercury’s Magnesium Exosphere to Its Magnesium-Rich Surface Terrane.” In: *Geophysical Research Letters* 45.14, pp. 6790–6797. DOI: `10.1029/2018GL078407`.

Modolo, R. et al. (2018). “The LatHyS database for planetary plasma environment investigations: Overview and a case study of data/-model comparisons.” In: *Planetary and Space Science* 150, pp. 13–21. DOI: `10.1016/j.pss.2017.02.015`.

Modolo, R. et al. (2016). “Mars-solar wind interaction: LatHyS, an improved parallel 3-D multispecies hybrid model.” In: *Journal of Geophysical Research (Space Physics)* 121.7, pp. 6378–6399. DOI: `10.1002/2015JA022324`.

Müller, J. et al. (2012). “Origin of Mercury’s double magnetopause: 3D hybrid simulation study with A.I.K.E.F.” In: *Icarus* 218.1, pp. 666–687. DOI: `10.1016/j.icarus.2011.12.028`.

Mura, A. et al. (2005). “Dayside H^+ circulation at Mercury and neutral particle emission.” In: *Icarus* 175.2, pp. 305–319. DOI: `10.1016/j.icarus.2004.12.010`.

Mura, A. et al. (2007). “Numerical and analytical model of Mercury’s exosphere: Dependence on surface and external conditions.” In: *Planetary and Space Science* 55.11, pp. 1569–1583. DOI: `10.1016/j.pss.2006.11.028`.

Mura, A. (2012). “Loss rates and time scales for sodium at Mercury.” In: *Planetary and Space Science* 63, pp. 2–7. DOI: `10.1016/j.pss.2011.08.012`.

Mura, A. et al. (2009). “The sodium exosphere of Mercury: Comparison between observations during Mercury’s transit and model results.” In: *Icarus* 200.1, pp. 1–11. DOI: `10.1016/j.icarus.2008.11.014`.

NASA Space Science Data Coordinated Archive (2021). *Labelled diagram of Mariner 10*. [Online; accessed 2021-06-09]. URL: `https://nssdc.gsfc.nasa.gov/planetary/image/mariner10_labelled.jpg`.

NASA (2017). *Full Moon Photographed From Apollo 11 Spacecraft*. [Online; accessed 2021-08-30]. URL: `https://www.nasa.gov/mission_pages/apollo/40th/images/apollo_image_25.html`.

NASA/JPL (2008). *Mercury as Never Seen Before*. [Online; accessed 2021-08-30]. URL: `https://images.nasa.gov/details-PIA11245`.

NASA/Karen Northon (2017). *NASA Captures "EPIC" Earth Image*. [Online; accessed 2021-08-30]. URL: `https://www.nasa.gov/image-feature/nasa-captures-epic-earth-image`.

Ness, N. F. et al. (1974). “Magnetic Field Observations near Venus: Preliminary Results from Mariner 10.” In: *Science* 183.4131, pp. 1301–1306. DOI: `10.1126/science.183.4131.1301`.

Ness, N. F. et al. (1975). “The magnetic field of Mercury, 1.” In: *Journal of Geophysical Research* 80.19, p. 2708. DOI: `10.1029/JA080i019p02708`.

— (1976). "Observations of Mercury's Magnetic Field." In: *Icarus* 28.4, pp. 479–488. DOI: `10.1016/0019-1035(76)90121-4`.

Nguyen, H. D. (1960). "Variations AU cours du crepuscule du rapport des intensites des raies D du sodium atmospherique." In: *Publications of the Observatoire Haute-Provence* 5.29.

Nittler, L. R. et al. (2011). "The Major-Element Composition of Mercury's Surface from MESSENGER X-ray Spectrometry." In: *Science* 333.6051, p. 1847. DOI: `10.1126/science.1211567`.

Nittler, L. R. et al. (2018). "The Chemical Composition of Mercury." In: *Mercury: The View after MESSENGER*. Ed. by S. C. Solomon, L. R. Nittler and B. J. Anderson. Cambridge: Cambridge University Press. Chap. 2, pp. 30–51.

Ogilvie, K. W. et al. (1974). "Observations at Mercury Encounter by the Plasma Science Experiment on Mariner 10." In: *Science* 185.4146, pp. 145–151. DOI: `10.1126/science.185.4146.145`.

Ogilvie, K. W. et al. (1977). "Observations at the planet Mercury by the Plasma Electron Experiment: Mariner 10." In: *Journal of Geophysical Research* 82.13, p. 1807. DOI: `10.1029/JA082i013p01807`.

Oppenheimer, M. (1980). "Sodium D-line emission in comet West (1975n) and the sodium source in comets." In: *Astrophysical Journal* 240, pp. 923–928. DOI: `10.1086/158305`.

Orsini, S. et al. (2018). "Mercury sodium exospheric emission as a proxy for solar perturbations transit." In: *Scientific Reports* 8, 928. DOI: `10.1038/s41598-018-19163-x`.

Paral, J. et al. (2010). "Sodium ion exosphere of Mercury during MESSENGER flybys." In: *Geophysical Research Letters* 37.19, L19102. DOI: `10.1029/2010GL044413`.

Peplowski, P. N. et al. (2011). "Radioactive Elements on Mercury's Surface from MESSENGER: Implications for the Planet's Formation and Evolution." In: *Science* 333.6051, p. 1850. DOI: `10.1126/science.1211576`.

Peplowski, P. N. et al. (2012). "Variations in the abundances of potassium and thorium on the surface of Mercury: Results from the MESSENGER Gamma-Ray Spectrometer." In: *Journal of Geophysical Research (Planets)* 117, E00L04. DOI: `10.1029/2012JE004141`.

Peplowski, P. N. et al. (2015a). "Constraints on the abundance of carbon in near-surface materials on Mercury: Results from the MESSENGER Gamma-Ray Spectrometer." In: *Planetary and Space Science* 108, pp. 98–107. DOI: `10.1016/j.pss.2015.01.008`.

Peplowski, P. N. et al. (2015b). "Geochemical terranes of Mercury's northern hemisphere as revealed by MESSENGER neutron measurements." In: *Icarus* 253, pp. 346–363. DOI: `10.1016/j.icarus.2015.02.002`.

Pettengill, G. H. and Dyce, R. B. (1965). "A Radar Determination of the Rotation of the Planet Mercury." In: *Nature* 206.4990, p. 1240. DOI: `10.1038/2061240a0`.

Pilipp, W. G. et al. (1987). "Variations of electron distribution functions in the solar wind." In: *Journal of Geophysical Research* 92.A2, pp. 1103–1118. DOI: 10.1029/JA092iA02p01103.

Pokorný, P., Sarantos, M. and Janches, D. (2017). "Reconciling the Dawn-Dusk Asymmetry in Mercury's Exosphere with the Micrometeoroid Impact Directionality." In: *The Astrophysical Journal Letters* 842.2, L17. DOI: 10.3847/2041-8213/aa775d.

— (2018). "A Comprehensive Model of the Meteoroid Environment around Mercury." In: *The Astrophysical Journal* 863.1, 31. DOI: 10.3847/1538-4357/aad051.

Potter, A. E. and Killen, R. M. (2008). "Observations of the sodium tail of Mercury." In: *Icarus* 194.1, pp. 1–12. DOI: 10.1016/j.icarus.2007.09.023.

Potter, A. E., Killen, R. M. and Morgan, T. H. (1999). "Rapid changes in the sodium exosphere of Mercury." In: *Planetary and Space Science* 47.12, pp. 1441–1448. DOI: 10.1016/S0032-0633(99)00070-7.

— (2002). "The sodium tail of Mercury." In: *Meteoritics and Planetary Science* 37.9, pp. 1165–1172. DOI: 10.1111/j.1945-5100.2002.tb00886.x.

— (2007). "Solar radiation acceleration effects on Mercury sodium emission." In: *Icarus* 186.2, pp. 571–580. DOI: 10.1016/j.icarus.2006.09.025.

Potter, A. E., Killen, R. M. and Sarantos, M. (2006). "Spatial distribution of sodium on Mercury." In: *Icarus* 181.1, pp. 1–12. DOI: 10.1016/j.icarus.2005.10.026.

Potter, A. E. and Morgan, T. H. (1985). "Discovery of Sodium in the Atmosphere of Mercury." In: *Science* 229.4714, pp. 651–653. DOI: 10.1126/science.229.4714.651.

— (1986). "Potassium in the atmosphere of Mercury." In: *Icarus* 67.2, pp. 336–340. DOI: 10.1016/0019-1035(86)90113-2.

— (1987). "Variation of sodium on mercury with solar radiation pressure." In: *Icarus* 71.3, pp. 472–477. DOI: 10.1016/0019-1035(87)90041-8.

— (1990). "Evidence for Magnetospheric Effects on the Sodium Atmosphere of Mercury." In: *Science* 248.4957, pp. 835–838. DOI: 10.1126/science.248.4957.835.

Potter, A. E. et al. (2013). "Observation of neutral sodium above Mercury during the transit of November 8, 2006." In: *Icarus* 226.1, pp. 172–185. DOI: 10.1016/j.icarus.2013.05.029.

Potter, A. E. and Morgan, T. H. (1997). "Evidence for suprathermal sodium on Mercury." In: *Advances in Space Research* 19.10, pp. 1571–1576. DOI: 10.1016/S0273-1177(97)00370-0.

Raines, J. M. et al. (2014). "Structure and dynamics of Mercury's magnetospheric cusp: MESSENGER measurements of protons and planetary ions." In: *Journal of Geophysical Research: Space Physics* 119.8, pp. 6587–6602. DOI: 10.1002/2014JA020120.

Raines, J. M. et al. (2015). “Plasma Sources in Planetary Magnetospheres: Mercury.” In: *Space Science Reviews* 192.1-4, pp. 91–144. DOI: 10.1007/s11214-015-0193-4.

Raines, J. M. et al. (2018). “First In-Situ Observations of Exospheric Response to CME Impact at Mercury.” In: *Mercury: Current and Future Science of the Innermost Planet, Proceedings of the conference held 1-3 May, 2018 in Columbia, Maryland*. Vol. LPI Contribution No. 2047, 6038.

Raines, J. M. et al. (2013). “Distribution and compositional variations of plasma ions in Mercury’s space environment: The first three Mercury years of MESSENGER observations.” In: *Journal of Geophysical Research (Space Physics)* 118.4, pp. 1604–1619. DOI: 10.1029/2012JA018073.

Robinson, M. S. and Lucey, P. G. (1997). “Recalibrated Mariner 10 color mosaics: Implications for mercurian volcanism.” In: *Science* 275, pp. 197–200. DOI: 10.1126/science.275.5297.197.

Russell, C. T., Baker, D. N. and Slavin, J. A. (1988). “The magnetosphere of Mercury.” In: *Mercury*. Ed. by F. Vilas, C. R. Chapman and M. S. Matthews. Accessible online at: https://www.researchgate.net/publication/23925868_The_magnetosphere_of_Mercury. University of Arizona Press, pp. 514–561.

Sarantos, M. and Tsavachidis, S. (2020). “The Boundary of Alkali Surface Boundary Exospheres of Mercury and the Moon.” In: *Geophysical Research Letters* 47.16, e88930. DOI: 10.1029/2020GL088930.

Sarantos, M., Killen, R. M. and Kim, D. (2007). “Predicting the long-term solar wind ion-sputtering source at Mercury.” In: *Planetary and Space Science* 55.11, pp. 1584–1595. DOI: 10.1016/j.pss.2006.10.011.

Sarantos, M. and Slavin, J. A. (2009). “On the possible formation of Alfvén wings at Mercury during encounters with coronal mass ejections.” In: *Geophysical Research Letters* 36.4, L04107. DOI: 10.1029/2008GL036747.

Sarantos, M. et al. (2001). “A B_x-interconnected magnetosphere model for Mercury.” In: *Planetary and Space Science* 49.14-15, pp. 1629–1635. DOI: 10.1016/S0032-0633(01)00100-3.

Sarantos, M. et al. (2011). “Limits to Mercury’s magnesium exosphere from MESSENGER second flyby observations.” In: *Planetary and Space Science* 59.15, pp. 1992–2003. DOI: 10.1016/j.pss.2011.05.002.

Schaefer, B. E. (2007). “The Latitude and Epoch for the Origin of the Astronomical Lore in MUL.APIN.” In: *American Astronomical Society Meeting Abstracts #210*. Vol. 210. American Astronomical Society Meeting Abstracts, 42.05.

Schleicher, H. et al. (2004). “Detection of neutral sodium above Mercury during the transit on 2003 May 7.” In: *Astronomy and Astrophysics* 425, pp. 1119–1124. DOI: 10.1051/0004-6361:20040477.

Schmidt, C. A. (2013). "Monte Carlo modeling of north-south asymmetries in Mercury's sodium exosphere." In: *Journal of Geophysical Research (Space Physics)* 118.7, pp. 4564–4571. DOI: 10.1002/jgra.50396.

Seki, K. et al. (2013). "Effects of the surface conductivity and the IMF strength on the dynamics of planetary ions in Mercury's magnetosphere." In: *Journal of Geophysical Research (Space Physics)* 118.6, pp. 3233–3242. DOI: 10.1002/jgra.50181.

Shemansky, D. E. (1980). "Comment of 'Methods of Monte Carlo simulation of the exospheres of the moon and Mercury' by R. R. Hodges, Jr." In: *Journal of Geophysical Research* 85.A1, pp. 221–222. DOI: 10.1029/JA085iA01p00221.

Shemansky, D. E. and Broadfoot, A. L. (1977). "Interaction of the surfaces of the Moon and Mercury with their exospheric atmospheres." In: *Reviews of Geophysics and Space Physics* 15.491-499, pp. 27–89. DOI: 10.1029/RG015i004p00491.

Shemansky, D. E. and Morgan, T. H. (1991). "Source processes for the alkali metals in the atmosphere of Mercury." In: *Geophysical Research Letters* 18.9, pp. 1659–1662. DOI: 10.1029/91GL02000.

Slade, M. A., Butler, B. J. and Muhleman, D. O. (1992). "Mercury Radar Imaging: Evidence for Polar Ice." In: 258.5082, pp. 635–640. DOI: 10.1126/science.258.5082.635.

Slavin, J. A. and Holzer, R. E. (1981). "Solar wind flow about the terrestrial planets, 1. Modeling bow shock position and shape." In: *Journal of Geophysical Research* 86.A13, pp. 11401–11418. DOI: 10.1029/JA086iA13p11401.

Slavin, J. A. et al. (2003). "Geotail observations of magnetic flux ropes in the plasma sheet." In: *Journal of Geophysical Research (Space Physics)* 108.A1, 1015. DOI: 10.1029/2002JA009557.

Slavin, J. A. et al. (2008). "Mercury's Magnetosphere After MESSENGER's First Flyby." In: *Science* 321.5885, p. 85. DOI: 10.1126/science.1159040.

Slavin, J. A. et al. (2009). "MESSENGER Observations of Magnetic Reconnection in Mercury's Magnetosphere." In: *Science* 324.5927, p. 606. DOI: 10.1126/science.1172011.

Slavin, J. A. et al. (2010). "MESSENGER Observations of Extreme Loading and Unloading of Mercury's Magnetic Tail." In: *Science* 329.5992, p. 665. DOI: 10.1126/science.1188067.

Slavin, J. A. et al. (2014). "MESSENGER observations of Mercury's dayside magnetosphere under extreme solar wind conditions." In: *Journal of Geophysical Research (Space Physics)* 119.10, pp. 8087–8116. DOI: 10.1002/2014JA020319.

Smith, G. R. et al. (1978). "Monte carlo modeling of exospheric bodies: Mercury." In: *Journal of Geophysical Research* 83.A8, pp. 3783–3790. DOI: 10.1029/JA083iA08p03783.

Smyth, W. H. (1983). “Io’s sodium cloud - Explanation of the east-west asymmetries. II.” In: *Astrophysical Journal* 264, pp. 708–725. DOI: `10.1086/160644`.

— (1986). “Nature and variability of Mercury’s sodium atmosphere.” In: *Nature* 323.6090, pp. 696–699. DOI: `10.1038/323696a0`.

Speiser, T. W. (1965). “Particle Trajectories in Model Current Sheets, 1, Analytical Solutions.” In: *Journal of Geophysical Research* 70.17, pp. 4219–4226. DOI: `10.1029/JZ070i017p04219`.

Sprague, A. L. et al. (1997). “Distribution and Abundance of Sodium in Mercury’s Atmosphere, 1985-1988.” In: *Icarus* 129.2, pp. 506–527. DOI: `10.1006/icar.1997.5784`.

Sundberg, T. et al. (2012). “MESSENGER orbital observations of large-amplitude Kelvin-Helmholtz waves at Mercury’s magnetopause.” In: *Journal of Geophysical Research (Space Physics)* 117.A4, A04216. DOI: `10.1029/2011JA017268`.

Trávníček, P. M. et al. (2010). “Mercury’s magnetosphere-solar wind interaction for northward and southward interplanetary magnetic field: Hybrid simulation results.” In: *Icarus* 209.1, pp. 11–22. DOI: `10.1016/j.icarus.2010.01.008`.

Trávníček, P., Hellinger, P. and Schriver, D. (2007). “Structure of Mercury’s magnetosphere for different pressure of the solar wind: Three dimensional hybrid simulations.” In: *Geophysical Research Letters* 34.5, L05104. DOI: `10.1029/2006GL028518`.

Tyler, A. L., Kozlowski, R. W. and Schneider, N. M. (1987). “Mercury’s Atmosphere: Latitudinal Asymmetries in Sodium and Potassium.” In: *Bulletin of the American Astronomical Society*. Vol. 19, p. 862.

Vervack R. J., J. et al. (2011). “Early MESSENGER Results for Less Abundant or Weakly Emitting Species in Mercury’s Exosphere.” In: *EPSC-DPS Joint Meeting 2011*, p. 1131.

Vervack, R. J. et al. (2009). “MESSENGER Observations of Mercury’s Exosphere: Discoveries and Surprises from the First Two Flybys.” In: *Lunar and Planetary Science Conference*. Lunar and Planetary Science Conference, 2220.

Vervack, R. J. et al. (2016). “New discoveries from MESSENGER and insights into Mercury’s exosphere.” In: *Geophysical Research Letters* 43.22, pp. 11,545–11,551. DOI: `10.1002/2016GL071284`.

Vervack, R. J. et al. (2010). “Mercury’s Complex Exosphere: Results from MESSENGER’s Third Flyby.” In: *Science* 329.5992, p. 672. DOI: `10.1126/science.1188572`.

Wang, Y. C. et al. (2010). “A hybrid simulation of Mercury’s magnetosphere for the MESSENGER encounters in year 2008.” In: *Icarus* 209.1, pp. 46–52. DOI: `10.1016/j.icarus.2010.05.020`.

Weider, S. Z. et al. (2015). “Evidence for geochemical terranes on Mercury: Global mapping of major elements with MESSENGER’s X-Ray Spectrometer.” In: *Earth and Planetary Science Letters* 416, pp. 109–120. DOI: `10.1016/j.epsl.2015.01.023`.

Werner, A. L. E. et al. (2021a). “Ion density and phase space density distribution of planetary ions Na^+, O^+ and He^+ in Mercury’s magnetosphere.” In: *Icarus* Submitted.

Werner, A. L. E. et al. (2021b). “Modeling the impact of a strong X-class solar flare on the heavy ion composition in Mercury’s magnetosphere.” In: *Geophysical Research Letters* Submitted.

Whang, Y. C. (1977). “Magnetospheric magnetic field of Mercury.” In: *Journal of Geophysical Research* 82.7, p. 1024. DOI: `10.1029/JA082i007p01024`.

Wiens, R. C. et al. (1997). “Sputtering Products of Sodium Sulfate: Implications for Io’s Surface and for Sodium-Bearing Molecules in the Io Torus.” In: *Icarus* 128.2, pp. 386–397. DOI: `10.1006/icar.1997.5758`.

Winslow, R. M. et al. (2012). “Observations of Mercury’s northern cusp region with MESSENGER’s Magnetometer.” In: *Geophysical Research Letters* 39.8, L08112. DOI: `10.1029/2012GL051472`.

Winslow, R. M. et al. (2013). “Mercury’s magnetopause and bow shock from MESSENGER Magnetometer observations.” In: *Journal of Geophysical Research (Space Physics)* 118.5, pp. 2213–2227. DOI: `10.1002/jgra.50237`.

Winslow, R. M. et al. (2014). “Mercury’s surface magnetic field determined from proton-reflection magnetometry.” In: *Geophysical Research Letters* 41.13, pp. 4463–4470. DOI: `10.1002/2014GL060258`.

Wurz, P. and Lammer, H. (2003). “Monte-Carlo simulation of Mercury’s exosphere.” In: *Icarus* 164.1, pp. 1–13. DOI: `10.1016/S0019-1035(03)00123-4`.

Yagi, M. et al. (2010). “Formation of a sodium ring in Mercury’s magnetosphere.” In: *Journal of Geophysical Research (Space Physics)* 115.A10, A10253. DOI: `10.1029/2009JA015226`.

— (2017). “Global Structure and Sodium Ion Dynamics in Mercury’s Magnetosphere With the Offset Dipole.” In: *Journal of Geophysical Research (Space Physics)* 122.11, pp. 10,990–11,002. DOI: `10.1002/2017JA024082`.

Yakshinskiy, B. V. and Madey, T. E. (1999). “Photon-stimulated desorption as a substantial source of sodium in the lunar atmosphere.” In: *Nature* 400.6745, pp. 642–644. DOI: `10.1038/23204`.

Yakshinskiy, B. V. and Madey, T. E. (2005). “Temperature-dependent DIET of alkalis from SiO_2 films: Comparison with a lunar sample.” In: *Surface Science* 593.1-3, pp. 202–209. DOI: `10.1016/j.susc.2005.06.062`.

Yoshikawa, I. et al. (2008). “Observation of Mercury’s sodium exosphere during the transit on November 9, 2006.” In: *Planetary and Space Science* 56.13, pp. 1676–1680. DOI: `10.1016/j.pss.2008.07.026`.

Zurbuchen, T. H. et al. (2004). “On the space environment of Mercury.” In: *Advances in Space Research* 33.11, pp. 1884–1889. DOI: `10.1016/j.asr.2003.04.048`.

Zurbuchen, T. H. and Richardson, I. G. (2006). “In-Situ Solar Wind and Magnetic Field Signatures of Interplanetary Coronal Mass Ejections.” In: *Space Science Reviews* 123.1-3, pp. 31–43. DOI: `10.1007/s11214-006-9010-4`.

Zurbuchen, T. H. et al. (2008). “MESSENGER Observations of the Composition of Mercury’s Ionized Exosphere and Plasma Environment.” In: *Science* 321.5885, p. 90. DOI: `10.1126/science.1159314`.

Zurbuchen, T. H. et al. (2011). “MESSENGER Observations of the Spatial Distribution of Planetary Ions Near Mercury.” In: *Science* 333.6051, p. 1862. DOI: `10.1126/science.1211302`.

van Helden, A. (1976). “The Importance of the Transit of Mercury of 1631.” In: *Journal for the History of Astronomy* 7, p. 1. DOI: `10.1177/002182867600700101`.